Thermodynamic and experimental investigations of the phosphorus removal from molten silicon for photovoltaic applications

Simon Favre

Communauté
UNIVERSITÉ Grenoble Alpes

THÈSE

Pour obtenir le grade de

DOCTEUR DE L'UNIVERSITE GRENOBLE ALPES

Spécialité : **Matériaux, Mécanique, Génie civil, Électrochimie**

Arrêté ministériel : 25 mai 2016

Présentée par

Simon FAVRE

Thèse dirigée par **Guy CHICHIGNOUD**, Chargé de recherche, CNRS, codirigée par **Ioana NUTA**, Chargée de recherche, CNRS et **Kader ZAÏDAT**, Maître de conférences, Grenoble INP

préparée au sein du **Laboratoire SIMaP**
dans **l'École Doctorale I-MEP²**

Étude thermodynamique et expérimentale de la déphosphoration du silicium liquide pour des applications photovoltaïques

Thèse soutenue publiquement le **28 novembre 2017**, devant le jury composé de :

Mme Anne KAMINSKI-CACHOPO	
Professeur, IMEP – LAHC Grenoble	Présidente
M. Erwann FOURMOND	
Maître de conférences, INSA Lyon	Rapporteur
Mme Christine GUÉNEAU	
Directrice de recherche, CEA Saclay	Rapporteur
M. Mimoun EL MARSSI	
Professeur, Université de Picardie Jules Verne	Examinateur
M. Mustapha LEMITI	
Professeur, INSA Lyon	Examinateur
M. Guy CHICHIGNOUD	
Chargé de recherche, SIMaP Grenoble	Directeur de thèse
Mme Ioana NUTA	
Chargée de recherche, SIMaP Grenoble	Invité
M. Kader ZAÏDAT	
Maître de conférences, SIMaP Grenoble	Invité

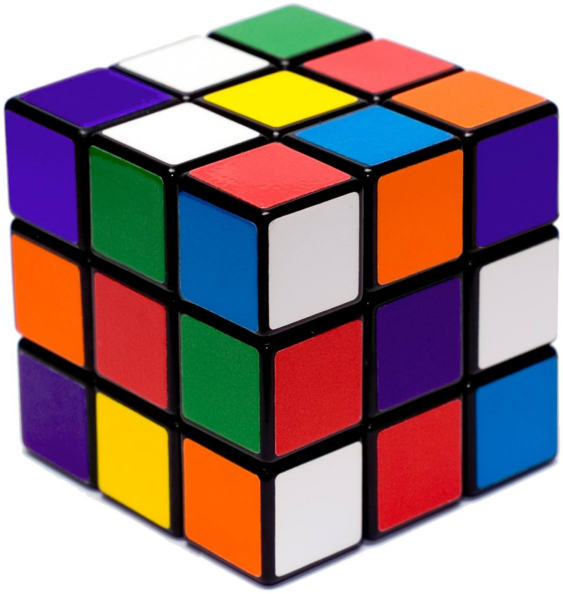

Remerciements

NOMBREUSES sont les personnes avec qui j'ai partagé ces plus de trois années de vie. D'une façon ou d'une autre, ce manuscrit est le fruit de leur collaboration. Aussi, je souhaiterais adresser un grand merci :

à Christian Chatillon, qui a su me transmettre avec passion sa connaissance encyclopédique de la thermodynamique. Je ne saurais assez le remercier pour son dévouement et pour m'avoir donné goût à cette matière;

à Ioana Nuta, pour m'avoir précieusement aiguillé sur les multiples aspects de ce domaine, et particulièrement lors de la rédaction d'articles;

à Kader Zaïdat, qui m'a apporté un soutien bienveillant tout au long de la thèse et sur tous les plans;

à Guy Chichignoud, pour son investissement dans la mise en place et pratique de la nouvelle version de SPYCE;

aux membres du jury : à Erwann Fourmond et Christine Guéneau d'avoir accepté d'être rapporteurs de ce manuscrit, Mimoun El Marssi et Mustapha Lemiti d'en avoir été les examinateurs et Anne Kaminski-Cachopo de l'avoir présidé.

à Christian Garnier, pour m'avoir aidé à surmonter les moindres difficultés d'ordre expérimental avec patience et gentillesse;

à Évelyne Fischer, sans qui l'optimisation thermodynamique n'aurait jamais pu aboutir;

à Benjamin Pichat, Denis Bon, Nadine Vidal, qui ont apporté leurs expertises dans les modifications de SPYCE;

à Laurent Artaud, Roman Reboud, Stéphane Massucci, Hervé Collas, Bruno Mallery, pour leurs nombreux diagnostics concernant les problèmes de vide;

à la communauté Wikipédia pour m'avoir aidé à combler mes lacunes.

à mes amis thésards et stagiaires Leslie, Mathieu, Juju, Maxime, Benzou, Ahmed, Patouille, Nico, Hamza, Rémi, Pr. Jawichian, Julian, Julie, Cyril, Tianjiao, Anas;

à mes colocagières Xavier, Ben, Colin, Marmoule, Xiao-Yann, Jérém, Guigui, Flavien, PZ, Louis;

à Zazou, Clémence, Élodie et Jérôme;

à Pizza Totor;

à mon coiffeur Maximilien;

à mes amis limougeauds, mes amis lisséens.

Merci à ma famille, et plus particulièrement à Papa, Maman et Camille.

Merci Marion.

Nomenclature

Symbol	Description	Unit
Units		
[Ω]	Ohm	
[A]	Ampere	
[amu]	Atomic mass unit	1 amu $\approx 1.661 \cdot 10^{-27}$ kg
[at.%]	Atomic percentage	
[atm]	Atmosphere	1 atm $= 1.01325 \cdot 10^{5}$ Pa
[bar]	Bar	1 bar $= 10^{5}$ Pa
[°C]	Celcius degree	
[C]	Coulomb	
[eV]	Electronvolt	1 eV $\approx 1.6 \cdot 10^{-19}$ J
[Gtoe]	Giga tonne of oil equivalent	1 Gtoe $\approx 4.19 \cdot 10^{19}$ J
[H]	Henry	
[Hz]	Hertz	
[J]	Joule	
[K]	Kelvin	
[kg]	Kilogram	
[m]	Metre	
[mmHg]	Millimetre of mercury	1 mmHg $\approx$ 133.322 Pa
[mol]	Mole	
[N]	Newton	
[Pa]	Pascal	
[ppb]	Parts per billion	1 ppb $= 10^{-7}$ %
[ppm]	Parts per million	1 ppm $= 10^{-4}$ %
[ppmw]	Parts per million by weight	1 ppmw $= 10^{-4}$ wt.%
[S]	Siemens	
[s]	Second	
[sr]	Steradian	
[T]	Tesla	
[Torr]	Torr	1 Torr = 133.322 Pa
[V]	Volt	
[W]	Watt	
[wt.%]	Weight percentage	

Constants

$\mu_0 = 4\pi \cdot 10^{-7}$ H.m^{-1}	Permeability constant
$c = 2.99792458 \cdot 10^{8}$ m.s^{-1}	Speed of light in vacuum
$F = 9.648533289 \cdot 10^{4}$ C.mol^{-1}	Faraday constant
$g_n \approx 9.80665$ m.s^{-2}	Standard gravity
$h = 6.62607004 \cdot 10^{-34}$ m^2.kg.s^{-1}	Planck constant
$k_B = 1.38064852 \cdot 10^{-23}$ J.K^{-1}	Boltzmann constant
$\mathcal{N}_A \approx 6.0221415 \cdot 10^{23}$ mol^{-1}	Avogadro constant
$R = 8.3144598$ J.K^{-1}.mol^{-1}	Gas constant

Photovoltaic technology

ν	Photon frequency	[s^{-1}]
η	Solar cell efficiency	[–]
E_e	Irradiance	[W.m^{-2}]
E_g	Energy gap	[eV]
I	Current	[A]
I_d	Diode current	[A]
I_d	Photogenerated current	[A]
k_0	Segregation coefficient	[–]
R_s	Resistance	[Ω]
R_{sh}	Shunt resistance	[Ω]
S	Surface of the cell	[m^2]
V	Voltage	[V]

Thermodynamics

γ_i	Activity coefficient of species i	[–]
γ_i^∞	Activity coefficient of species i at infinite dilution	[–]
ε_i^j	Wagner interaction coefficient between species i and j	[–]
μ_i	Chemical potential of species i	[J.mol^{-1}]
ν_i	Stoichiometric coefficient of species i	[–]
ρ_i	Density of species i	[kg.m^{-3}]
ϕ	Phase	
Ω	Microstates of the system	[–]
a_i	Activity of species i	[–]
C_p	Heat capacity at constant pressure	[J.K^{-1}]
C_V	Heat capacity at constant volume	[J.K^{-1}]
F	Helmholtz free energy	[J]
G	Gibbs free energy	[J]
H	Enthalpy	[J]
K_{eq}	Equilibrium constant (also K_c, K_d, K_p)	[–]
K_{H_i}	Henry's constant of species i	[Pa]
${}^kL$	Redlich-Kister interaction coefficient of order k	[–]

M_i		Atomic mass of species i	$[\mathrm{kg.mol^{-1}}]$
n_i	●	Chemical amount of species i	[mol]
p	●	Pressure	[Pa]
p^*	●	Vapour pressure	[Pa]
p_h	●	Hydrostatic pressure	[Pa]
p_i	●	Partial pressure of species i	[Pa]
p^{up}	●	Pressure upstream the needle valve	[Pa]
Q		Heat	[J]
Q_r		Reaction quotient	[–]
S	●	Entropy	$[\mathrm{J.K^{-1}}]$
T	●	Temperature	[K]
U		Internal energy	[J]
V	●	Volume	$[\mathrm{m^3}]$
W		Work	[J]
x_i	●	Mole fraction of species i	[–]

ΔZ	Quantity of change
$\Delta_f Z$	Quantity of formation
$\Delta_r Z$	Quantity of reaction
${}^{\mathrm{E}}Z$	Excess quantity
${}^{\mathrm{id}}Z$	Ideal quantity
${}^{\mathrm{ref}}Z$	Reference quantity
Z^0	Standard quantity
Z^ϕ	Quantity of phase ϕ

Kinetic gas theory

α_e	Empirical evaporation coefficient	[–]
ϕ	Impingement rate	$[\mathrm{m^{-2}.s^{-1}}]$
Φ	Hertz-Knudsen flow	$[\mathrm{m^{-2}.s^{-1}}]$
$\Phi^{\searrow}$	Condensation Hertz-Knudsen flow	$[\mathrm{m^{-2}.s^{-1}}]$
$\Phi^{\nearrow}$	Evaporation Hertz-Knudsen flow	$[\mathrm{m^{-2}.s^{-1}}]$
c	Velocity of a particle	$[\mathrm{m.s^{-1}}]$
$\vec{c}$	Velocity vector of a particle	$[\mathrm{m.s^{-1}}]$
d	Diameter of a particle	[m]
E^{kin}	Kinetic energy	[J]
$f(\vec{c})$	Maxwell-Boltzmann distribution of speeds	$[\mathrm{s.m^{-1}}]$
$f(\vec{c},\vec{r},t)$	Distribution function	
$f(E)$	Probability density function	
k_0	Partition coefficient	[–]
L	Length	[m]
ℓ	Mean free path of a particle	[m]
m	Mass	[kg]
N	Number of particles	[–]
$\vec{r}$	Position vector of a particle	[m]

S	Surface of the silicon droplet	[m^2]
T	Temperature	[K]
T_0	Wall temperature	[K]
t	Time	[s]

Electromagnetism

δ	Skin depth	[m]
μ	Magnetic permeability	[H.m^{-1}]
σ	Electrical conductivity	[S.m^{-1}]
Φ_B	Magnetic flux	[T.m^2]
ω	Angular frequency	[Hz]
$\vec{B}$	Magnetic field	[T]
$\vec{E}$	Electrical field	[V.m^{-1}]
$\mathcal{E}$	Electromotive force	[V]
f	Frequency	[Hz]
$\vec{F}_L$	Lorentz force	[N]
G	Force function	[−]
H	Heat function	[−]
$\vec{j}$	Induced current density	
P	Power absorbed by the sample	[W]
q	Radius-to-skin-depth ratio	[−]
r	Radius of the sample	[m]
t	Time	[s]
v_A	Alfvén speed	[m.s^{-1}]

Mass transfer

α^*	Mass diffusivity	[m^2.s^{-1}]
β^*	Coefficient of mass expansion	[m^3.mol^{-1}]
ν	Kinematic viscosity	[m^2.s^{-1}]
Φ_m	Mass flux	[mol.m^{-2}.s^{-1}]
C_d	Concentration of the silicon droplet on the surface	[mol.m^{-3}]
C_∞	Concentration of the silicon droplet far afield	[mol.m^{-3}]
$\mathcal{D}$	Diffusion coefficient	[m^2.s^{-1}]
$\overline{k}$	Global mass transfer coefficient	[m.s^{-1}]
Kn	Knudsen number	[−]
L	Characteristic length	[m]
Pr	Prandtl number	[−]
Ra	Rayleigh number	[−]
$\overline{\mathrm{Sh}}$	Mean Sherwood number	[−]

Acronyms

2DS	2℃ Scenario
Calphad	Calculation of phase diagrams
CSP	Concentrated solar power
DC	Differential conductivity
DSC	Differential scanning calorimetry
DTA	Differential thermal analysis
EBSD	Electron backscatter diffraction
ECU	Electronics control unit
EG-Si	Electronic grade silicon
EML	Electromagnetic levitation
FBR	Fluidized bed reactor
FC	Faraday cup
FKM	Fluoroelastomer
GDMS	Glow discharge mass spectrometry
HDI	Human development index
HE	Hall effect
HF	High frequency
IR	Infrared
IUPAC	International Union of Pure and Applied Chemistry
IVR	Induction vacuum refining
KCMS	Knudsen cell mass spectrometry
MG-Si	Metallurgical grade silicon
MH	Microhardness
NAA	Neutron activation analysis
OM	Optical microscopy
$[P]_{(Si)}$	Solubility of phosphorus in silicon
PDF	Probability density function
PL	Photoluminescence
PV	Photovoltaic
QMS	Quadrupole mass spectrometer
RBS	Rutherford backscattering spectrometry
RF	Radio frequency
RGA	Residual gas analyzer
SGTE	Scientific Group Thermodata Europe
SIMS	Secondary ion mass spectrometry
SNMS	Secondary neutral mass spectrometry
SoG-Si	Solar grade silicon
SPYCE	Silicon purity controlled under electromagnetic levitation
SR	Sheet resistivity
TEM	Transmission electron microscopy
TG-DTA	Thermogravimetric - differential thermal analysis
TGA	Thermogravimetric analysis
UMG-Si	Upgraded metallurgical grade silicon
UV	Ultraviolet
XRD	X-ray diffraction

XRT	X-ray topography

Contents

Introduction

PHOTOVOLTAIC cells are overwhelmingly elaborated from extremely pure silicon, which cannot be found as such in nature. Fortunately silica is plentiful: a carbothermic reduction merely enables to obtain the element in question. Purification steps are however required to obtain from this metallurgical grade a solar grade silicon.

Energy intensive processes for the electronics industries are currently the most common ways to achieve such a standard, but by their very nature, an alternative means has to be developed. Among the impurities in silicon, phosphorus is challenging to remove: standard segregations are inconceivable as its corresponding segregation coefficient is too high ($k_0 = 0.35$).

Vacuum refining in a furnace is a solution developed at the industrial scale by several companies, yet some phenomena occurring at this stage remain unclear. The impact of residual oxygen is for example unknown as it has never been considered in the hypotheses of previous authors. It would be a great help to understand the roles of thermodynamic parameters in order to optimize this process.

This thesis takes place within the ISOPEM project framework: it aims to implement on an industrial scale in Savoie a metallurgical process to produce solar grade silicon. This project is coordinated by Photosil Industries, a subsidiary of FerroPem, itself subsidiary of FerroSolar, the world largest producer of metallurgical silicon. It brings together several partners that are FerroPem, Apollon Solar, INES and the CNRS-SIMaP laboratory.

The study is based on two major parts: following a bibliographic review, a thermodynamic modeling of interactions between different involved elements nourishes a program created to simulate the dephosphorization process of molten silicon in the presence of oxygen. Additionally experimental investigations are conducted with a silicon levitation pilot under controlled atmosphere. The objective is to validate the predictions with very clean experimental conditions and to find the best settings to apply with the industrial furnace.

The first chapter is dedicated to the state of art of photovoltaic materials and the ways of producing a pure enough silicon. It will help to comprehend the purpose of the present study and locate its impact in the production line.

The second is twofold: it gives the scientific tools required to fully understand the remainder of the study, and also contains the review of the investigated thermodynamic system.

The third chapter describes the functioning of the simulation program dedicated to the phosphorus removal from liquid silicon, and takes into account the impact of oxygen on this process.

The fourth chapter presents the implemented experimental procedures on an electromagnetic levitation device and its development.

1

Silicon in the energy field

ALBEIT energy is omnipresent, it is a very complex notion to comprehend. *Enérgeia* means in Ancient Greek "being in action"; as a philosophical concept Aristotle conceived it as the transition of potentiality into actuality. Yet its common use in a scientific context only dates from the middle of the 19th century.

In 1892 Poincaré discussed the difficulty in defining it in the preface of a collection of his lectures [36] and the only statement he could ultimately make about it is: "*There is something, that remains constant*". It surely is constant but can transform or transfer[1]: apart from its own physical strength, humanity uses surrounding energy for its needs as so.

The following section states on the worldwide energy use and the ensuing energy challenge of the 21st century.

1.1 Global energy background

1.1.1 Overarching worldwide challenge

Global use of energy is exponentially increasing (Figure 1.1): at the beginning of the 19th century it was estimated at 0.25 Gtoe[2]. At the beginning of the 20th century it was worth 1 Gtoe, and doubled in 1950 to 2 Gtoe. Nowadays, humanity has used over 13 Gtoe.

[1] Talking about energy *production* or *consumption* is then improper as such.

[2] **G**iga **t**onne of **o**il **e**quivalent, corresponding to the chemical energy contained in a giga tonne of oil.

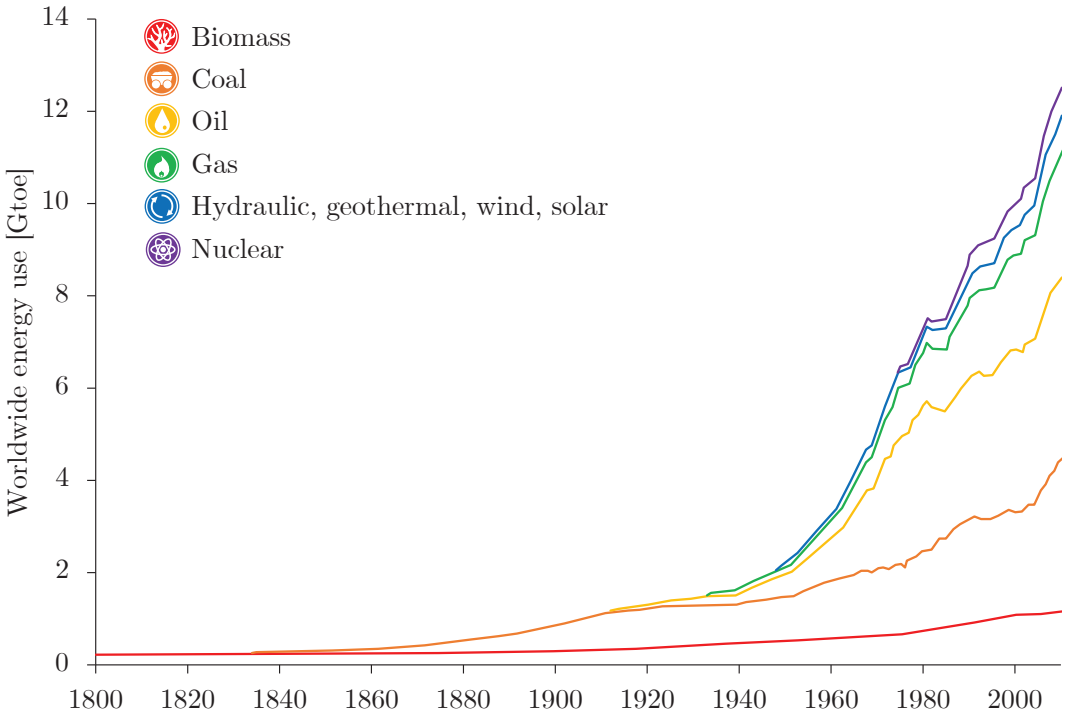

Figure 1.1: Global accumulated energy use between 1800 and 2010 [16]

Despite all the energy restraint efforts that would be possible to make, one will have to face growing energy needs as worldwide population will increase by 30% by 2050 [32], and as one billion people strive as of now to increase their energy use.

As an example 17% of global population lacks access to electricity while 38% has electricity supply problems [22]. Yet accessing to it is known to have advantages thereof such as education and health.

It exists a linear correlation between electricity access and the human development index[3] (HDI) of countries outlining the importance of having access to this commodity (Figure 1.2).

1.1.2 Main energy resources

Energy is thus a crucial parameter for every human being aspiring to an acceptable quality of life. Its presence on Earth is evidently proteiform, hence the different ways of using it.

Biomass is the first external energy ever used by mankind when 400 000 years ago it mastered fire. Chemical energy stored in the chemical bonds of organic combustible – in that case wood, but also straw, crop waste or biogas – is released mainly forming $CO_{2(g)}$ or $CH_{4(g)}$ and thus used either as a fuel or simply for heating.

[3]This indicator compiles life expectancy, education and gross national income factors.

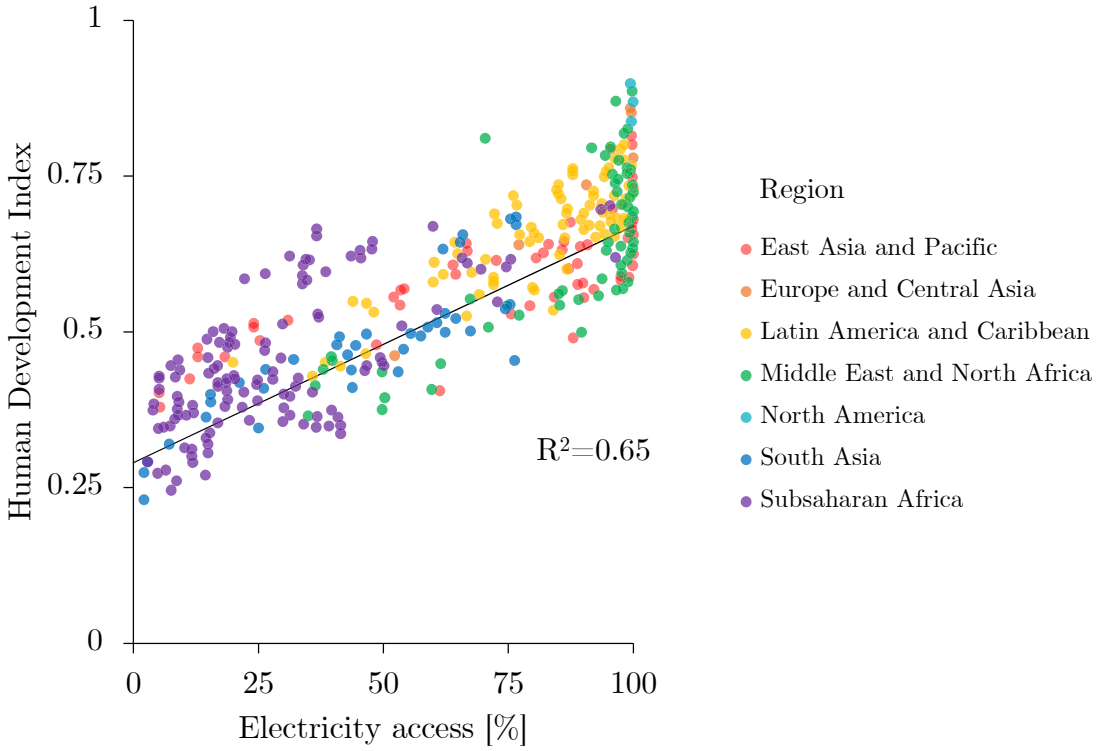

Figure 1.2: Relationship between HDI and access to electricity for 2000-2010 [2]

Coal is a sedimentary rock formed by carbonization of dead vegetation over hundred of millions of years, making it a fossil fuel. Its combustion releases much more chemical energy than biomass, explaining its wide use mainly in heating and producing electricity with thermal power plants.

Oil, in the energy meaning of the term, refers to liquid hydrocarbons formed by dead microorganisms. Trapped in geological formations dating from tens of millions of years, it has undergone high temperatures and pressures. Its use became increasingly important when internal combustion engine was invented. As an energy source, it covers the vast majority of the transports needs.

Natural gases commonly refer to hydrocarbon gas mixtures – mostly $CH_{4(g)}$, $C_3H_{8(g)}$ and $C_4H_{10(g)}$ – and originate from the disaggregation of the same ancient microorganisms which produced oil. They are flammable and then are either used for heating or for producing electricity with thermal power plants.

Nuclear energy is released when uranium U^{235} and plutonium Pu^{239} nuclei underwent fission. In practice it acts like thermal energy as it produces heat in the reactor. Nuclear power plants emerged in the 1960s and produce solely electricity. Storage of resulting radioactive waste is its main topic of debate as their lifetime is estimated to be several hundreds of thousands of years.

Geothermal energy, as it name suggests it, is thermal energy from the Earth. Tectonic plate boundaries and volcanic areas are more easily exploitable because magma is there more serviceable. It provides heat and electricity with geothermal

power plants. In 2012 it represents 0.5% of the worldwide energy use.

Hydraulic is converting mechanical energy from water into electricity. River flows, waves, tides, or waterfalls are exploited respectively by watermills, wave energy converters, tide mills and dams. The common criticism of its use is that construction of dams often create physical and social changes in the concerned area. It covers 2.4% of the worldwide energy needs.

Mechanical energy from **wind** can also be converted into electricity with wind turbines. This technology exponentially increased for the last twenty years, but only represents 0.3% of the worldwide energy use.

Solar heating or solar photovoltaic systems convert respectively thermal energy and light energy into heat and electricity. In total it only represents 0.1% of the worldwide energy use, but is exponentially growing as it can be seen in Figure 1.3.

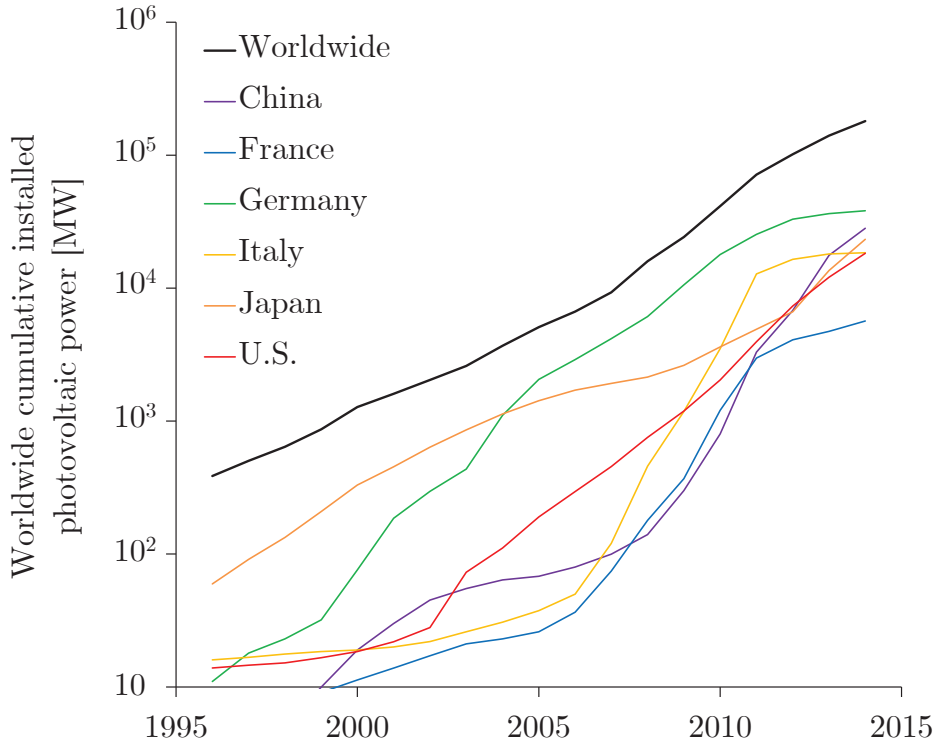

Figure 1.3: Growth of worldwide installed photovoltaics [8]

By their very nature, a comparison of energy resources is hard to draw. They differ in terms of energy intensity, availability, price, payback time, efficiency, CO_2 emissions, water consumption and so on. What is a paramount stack for humanity is to agree on a sustainable energy model that minimizes its irreversible environmental impact.

1.1.3 Future energy model

The outlook for the overall energy system is difficult to assess. Different scenarios of evolution are suggested, mainly depending on how rigorously every economic and political actors will apply the policy decisions of intergovernmental organizations.

The 2℃ Scenario (2DS) is the most optimistic of the three presented by International Energy Agency [23]: decreasing by 60% the total CO_2 emissions by 2050 with a drastic environmental guideline would limit the average global temperature increase to 2℃. Figure 1.4 presents in this scenario the possible evolution of the worldwide energy use.

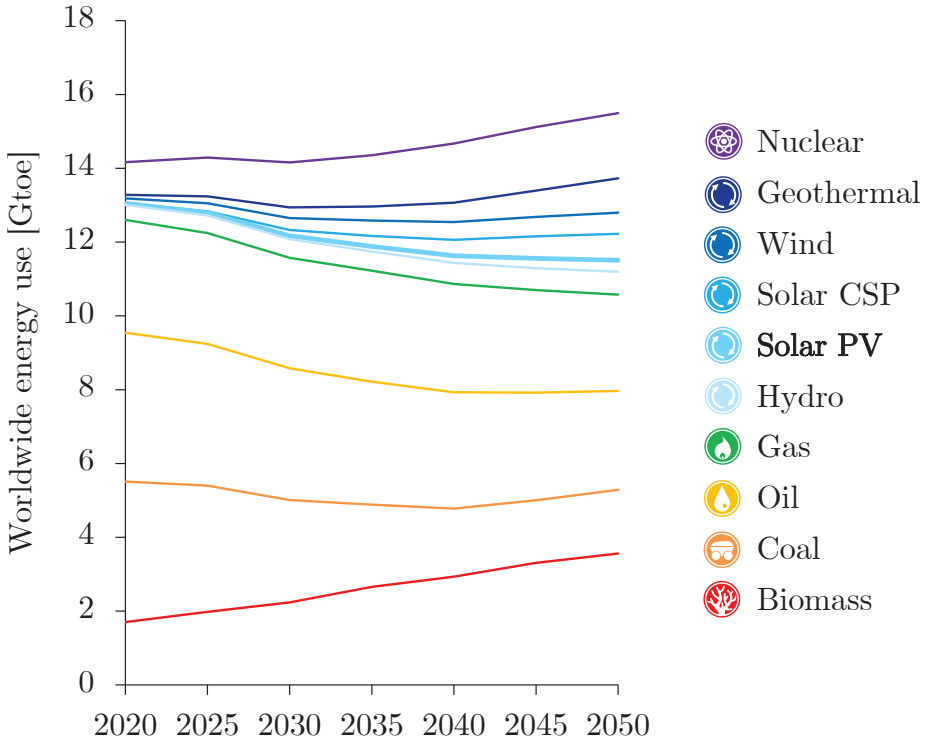

Figure 1.4: Predictions of the global accumulated energy use according to the 2DS. PV stands for photovoltaics and CSP for concentrated solar power.

It appears that curbing its exponential increase and developing alternative energies instead of fossil energies are the key criteria for carrying out this objective.

1.2 Field of photovoltaics

Sun annually provides 2.8 to 90.6 times more[4] thermal and light energy to Earth lands than the current worldwide energy use [41].

[4]This wide range reflects different assumptions on annual weather conditions and available land area.

Light energy can be converted into electricity by means of a semiconducting material: this phenomenon is called the photovoltaic effect. It was firstly revealed by Becquerel in 1839, but was anecdotal until 1954 when the first practical solar cell was conceived for spatial industry.

Here its operation is described in the case of the most used semiconductor, namely silicon.

1.2.1 Operating principle of a photovoltaic solar cell

Semiconductor definition

In an atom (Figure 1.5.a), electrons are arranged on different quantified energy levels around its nucleus. Two neighbouring atoms interact by means of their electrons, causing a shift of energy levels according to Pauli exclusion principle (Figure 1.5.b). But for a greater number of atoms, the numerous shifts of discrete levels necessitate to introduce the concept of bands relative to the band theory, that are continuums of those close energy levels (Figure 1.5.c).

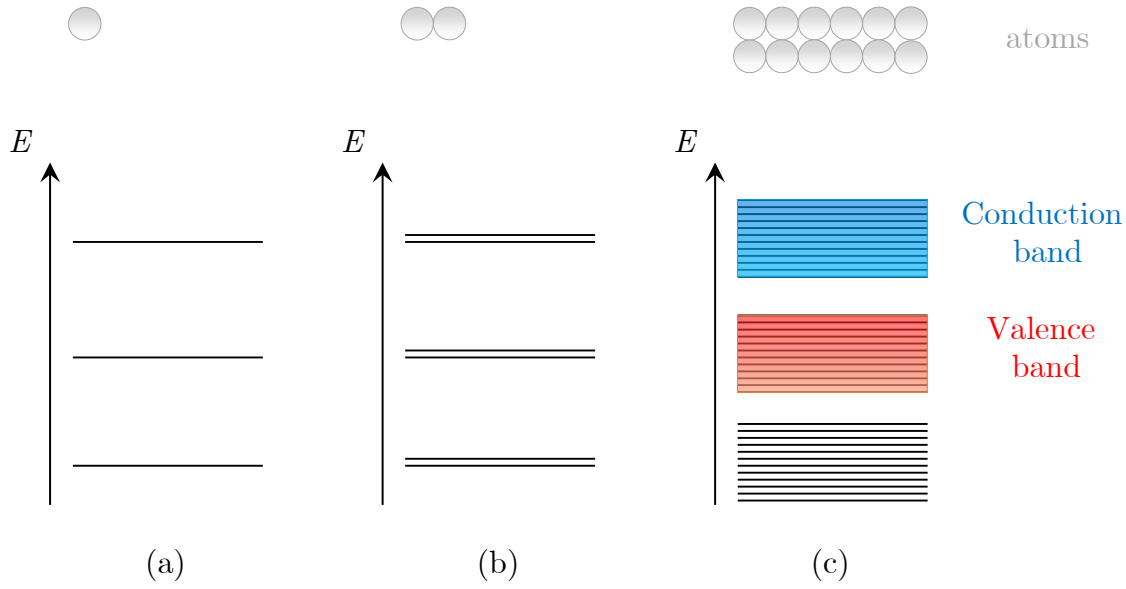

Figure 1.5: Introduction to band theory for understanding the semiconductors principle

Low energy bands of the core electrons do not participate in bonding. The most energetic complete energy band is called the valence band, while the first incomplete band following it is called the conduction band.

A conducting crystal has no gap between those two bands, therefore valence electrons can move to the conducting band without any external energy supply. Conversely, an insulator has a great gap band impassable by electrons with a reasonable amount of energy.

The band gap of semiconductors exists, however it is thinner thus crossable if an external energy is supplied. For silicon, this gap is $E_g = 1.1$ eV so photon energy

$E = h\nu$ from sunlight can rise a valence electron to the conduction band. In other terms, silicon is conducting solely when lighted up by the sun.

In order to create electricity, one needs to have on the one hand an electron excess and on the other hand an electron deficit, which is obtainable by doping silicon respectively with phosphorus and boron.

Semiconductor doping

Silicon atoms have four valence electrons, while phosphorus has five and boron three. Doping silicon means to introduce one of the two latter at a small amount to alter its electronic density. For n-type Si – doped with P – the electrons in excess are mobile in the lattice; for p-type Si – doped with B – the electrons in deficit are materialized by electron holes also mobile in the lattice.

By bringing those two types of semiconductors in contact, electrons diffuse to the p-type and holes diffuse to the n-type. Electron-hole pairs fade out and P^+ and B^- are formed from either side of the junction, creating a depletion region with an electric field.

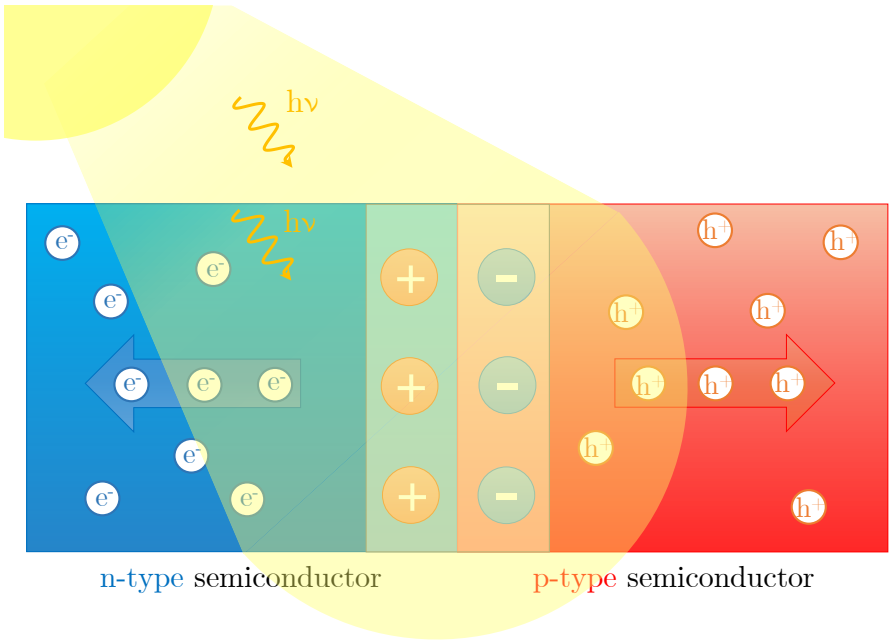

Figure 1.6: Depletion region of a pn junction sunlit

When this pn junction is lighted (Figure 1.6), photons transfer electrons from the valence band to the conduction band: electron-hole pairs are created and the electric field of the depletion region guides electrons to the n zone and holes to the p zone, thereby creating electricity.

1.2.2 Photovoltaic technologies

Limiting factors of photovoltaic conversion

The incident solar radiation is composed of photons with wavelengths comprised between 250 to 2500 nm (Figure 1.7), that is from the ultraviolet to the infrared range; but mostly in the visible spectrum. Only photons with an energy greater than 1.1 eV – the silicon band gap energy – are absorbed and create electron-hole pairs. The thermodynamic efficiency limit[5] is about 86%, but this limit is far from being reached.

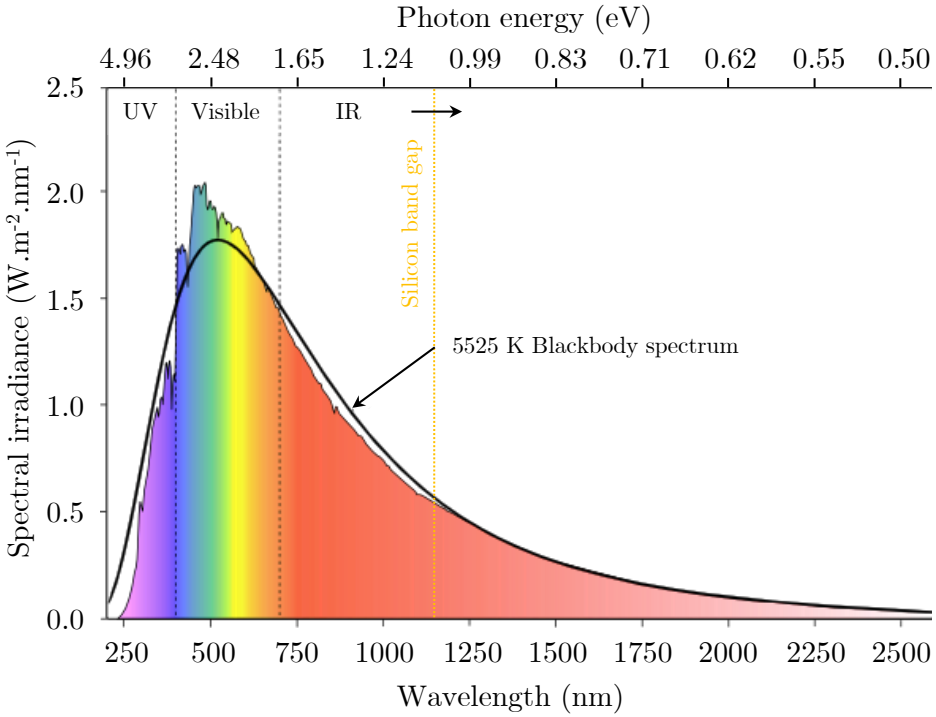

Figure 1.7: Solar radiation at the top of the atmosphere, adapted from [10]

Apart from the conversion losses due to the cells arrangement – for example the shading of each other – and its connections – ohmic losses –, some come from the inherent nature of the chosen semiconductor. For simple junction cells, photons with an energy less than E_g do not serve conversion. According to Figure 1.7 it represents 17% of the total amount of photons for silicon. In addition to this, when their energy exceeds E_g they transfer this extra energy to the crystal lattice in the form of heat in a very short time: this phenomenon is called thermalization. By taking into account those aspects, the theoretical conversion efficiency limit has been established by Shockley and Queisser at 32% for silicon cells and is called the ultimate efficiency [39].

[5] Carnot theoretical efficiency applied to the conversion of sunlight into electricity.

Solar cell principle

The equivalent circuit of a solar cell presented in Figure 1.8 consists of a current source with its photogenerated current I_{ph} depending on the lighting. In parallel a diode with a current I_d represents the pn junction. The current $I = I_{ph} - I_d$ flows in the external circuit passing through the series resistor R_s. Values of R_s and shunt resistor R_{sh} shall be respectively low and high.

The efficiency η of a solar cell is defined as the ratio between the maximum power point produced by the cell and the power of the incident radiation:

$$\eta = \frac{I_{\max} V_{\max}}{E_e S} \tag{1.1}$$

where E_e is the irradiance expressed in W.m^{-2} and S the surface of the cell expressed in m^2.

Those individual cells are assembled in series (adding voltages) or parallel (adding currents) to form a photovoltaic module.

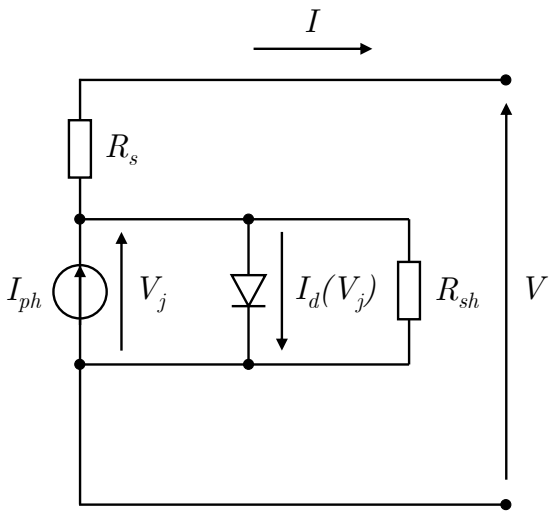

Figure 1.8: Solar cell electrical model

Main types of solar cells

Significant cost reductions and increased uptake of photovoltaics have been observed in the last few years. Even if ongoing improvements are reported in other photovoltaic materials, silicon has a stranglehold on this industry.

Silicon solar cells are the first generation of photovoltaic material to emerge. Taking advantage of this technological maturity, those represent more than 90% of the cells global production (Figure 1.9). Alternative photovoltaic materials subsequently arose, ranging from thin films semiconductors – CdTe or CIGS[6] – to organic,

[6]Respectively stands for cadmium telluride and copper indium gallium selenide solar cells.

dye sensitized or more recently organic-inorganic perovskites. Their performances are currently growing and promising but in overall at the development stage.

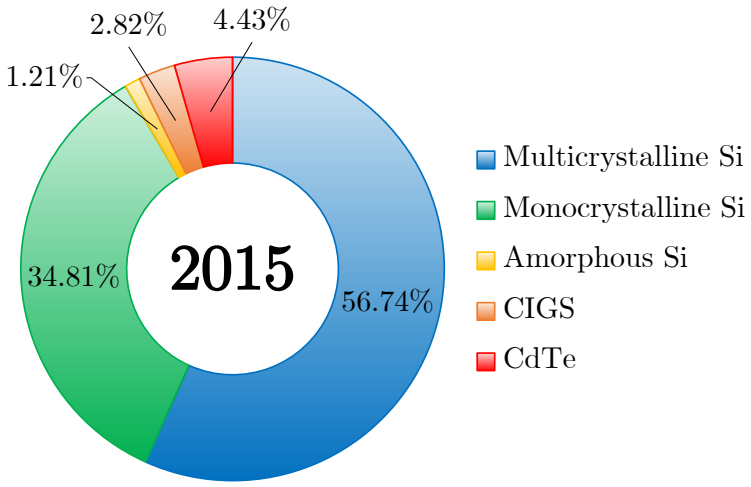

Figure 1.9: Photovoltaic market shares in W produced during the year 2015 according to [18]

Depending on manufacturing processes, silicon in solar cells can be of several kinds:

- monocrystalline silicon[7] is mainly obtained by Czochralski process. A monocrystalline seed is dipped in the molten silicon; the solidification is then initiated by slowly pulling it up while rotating, and reproduces the crystal orientation of the seed. It features a general efficiency of 18-20% albeit laboratories reached up to 25.6% [19];
- multicrystalline silicon consists of small crystals obtained by solidifying directionally molten silicon downward a two-zone furnace, that is to say the heat-exchanger method. Resulting ingots have the cuboid shape of their vessel, thus skipping the cutting step of cylindrical ingots required for obtaining wafers. This time and energy saving process is counterbalanced by its lower efficiency – nowadays ranging from 16 to 18% – due to lattice defects emanating from its very nature;
- amorphous silicon is oppositely unstructured at the nanoscopic scale with dangling bonds saturated by hydrogenation. Deposited in thin films onto flexible substrates, it provides a micrometer scale thickness for a low energy process. Its efficiency does not exceed 10%, making it generally a niche market for devices requiring little power such as pocket calculators.

Among the alternatives to silicon, CdTe and CGIS thin films are the most advanced technologies that are developed at the industrial stage:

[7] Also known as single-crystal silicon.

- the principle of CdTe solar cells is based on an heterojunction between n-type CdS of high band gap (2.4 eV) and p-type CdTe (1.45 eV). The first hampers the thermalization phenomenon while the second absorbs almost all the solar spectrum. Its structural simplicity justifies a relatively fast and low energy manufacturing process, however its availability and recycling are the main drawbacks;
- CGIS – or more accurately $CuIn_xGa_{1-x}Se_2$ – has a band gap ranging continuously from 1.0 to 1.7 eV and is used as the p-type semiconductor of the heterojunction, CdS being the n-type. Given its quaternary character the manufacturing is more complex than for CdTe, but has then a higher absorption coefficient.

1.3 Producing solar grade silicon

High purity silicon is required for photovoltaic cells. If it meets the requirement of a 99.999(9)% purity, it can be called solar grade silicon – SoG-Si. Such a high quality is the result of several elaboration steps.

Silicon can be found profusely in earth crust: it is the second most present element – 25.7 wt.% – after oxygen. It mainly exists in the form of sand or quartz, namely silica SiO_2. The first step is then the reduction of silica to obtain metallurgical grade silicon – MG-Si. The resulting liquid silicon will contain too many impurities to be used as such, therefore a purification step is necessary, followed by a solidification.

1.3.1 Reduction of silica

Silica is carbothermally reduced inside electric arc furnaces according to the following global reaction:

$$SiO_{2(l)} + 2C_{(s)} \rightleftharpoons Si_{(l)} + 2CO_{(g)} \tag{1.2}$$

The resulting MG-Si has a purity level of approximately 98 to 99%. The remaining impurities are either intrinsic ones or reacting intermediates.

In order to obtain MG-Si, quartz gravels are introduced in the furnace with charcoal, coke and wood chips. A very high voltage is applied between the graphite electrodes and the raw materials, inducing an electric arc. This latter heats the enclosure up to 1700 - 2200 K.

Filsinger and Bourrie [15] identified experimentally the intermediate steps involved in the process. The main reactions, neither independent nor consecutive are as follows:

$$SiO_{2(l)} + 3C_{(s)} \rightleftharpoons SiC_{(s)} + 2CO_{(g)} \tag{1.3}$$

$$2SiO_{2(l)} + SiC_{(s)} \rightleftharpoons 3SiO_{(g)} + CO_{(g)} \tag{1.4}$$

$$SiO_{(g)} + 2C_{(s)} \rightleftharpoons SiC_{(s)} + CO_{(g)} \tag{1.5}$$

$$SiO_{(g)} + SiC_{(s)} \rightleftharpoons 2Si_{(l)} + CO_{(g)} \tag{1.6}$$

The resulting CO recombines with atmospheric O_2 to form CO_2.

Melted MG-Si is then poured into ladles and separated from the slag before being cast in ingot molds.

The overwhelming majority of the worldwide MG-Si is produced by this process, however several studies have been recently conducted to open an alternative path somewhat cheaper and more ecological. Amongst these studies shall be mentioned the electrolytic reduction in molten salt [43], the carbothermic reduction in presence of nitrogen followed by a solar dissociation of the resulting nitride Si_3N_4 [30], the aluminothermic reduction in an inductive furnace [29], or more recently the gaseous reduction [25]. It reveals that processing MG-Si is not an outdated research topic, and perhaps the carbothermic reduction of silica will be soon in competition if those researches rise to an industrial scale.

1.3.2 Purification of silicon

The average 2% impurities included in MG-Si are limiting the solar cells efficiency (Figure 1.10) and shall then be reduced below the ppm. They mainly consist of metallic elements, light impurities, and also dopants like boron and phosphorus.

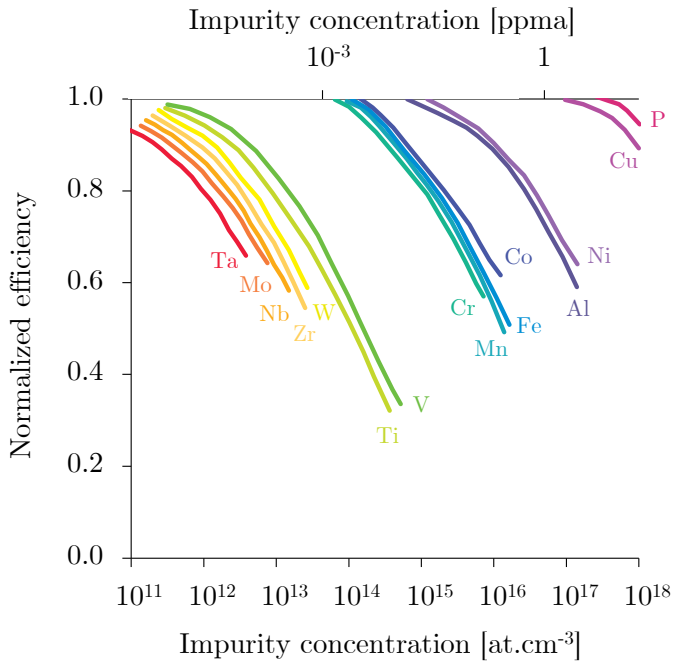

Figure 1.10: Effect of impurities content on the efficiency of p-type Si solar cells [12]

Requirements of some impurities content are presented in Table 1.1. They are given on an indicative basis as they may vary from one source to another.

Table 1.1: Several impurities content of silicon at different purification stages, given in ppm

Element	**MG-Si** [17]	**UMG-Si** [38]	**SoG-Si** [27, 38]	**EG-Si** [27]
Si	99%	3 – 4N	5 – 6N	9 – 11N
Al	1500 – 4000	< 50	< 0.1	< 0.0008
Fe	2000 – 3000	< 150	< 0.3	< 0.01
Ca	500 – 600	< 500	< 0.1	< 0.003
Cr	50 – 200	< 15	< 0.1	–
Ti	160 – 200	< 5	< 0.01	< 0.003
C	600	< 250	< 3	< 0.5
O	3000	< 2000	< 10	–
B	40 – 80	< 30	< 0.3	< 0.0002
P	**20 – 50**	$\mathbf{< 15}$	$\mathbf{< 0.1}$	$\mathbf{< 0.0008}$

Phosphorus contamination during the manufacturing steps of high purity silicon are presented in Figure 1.11. To obtain ultimately such low ratios, different purification processes can be operated: an overview of those is presented below in order to lay out the thesis approach.

a. Chemical approach

Siemens process Nowadays the dominant process to purify silicon is the Siemens process based on the hydrogenous reduction of trichlorosilane $SiHCl_3$.

The first step is the hydrochlorination of MG-Si at 623 K to form $SiHCl_3$:

$$Si_{(s)} + 3HCl_{(g)} \rightleftharpoons SiHCl_{3(g)} + H_{2(g)} \tag{1.7}$$

In parallel MG-Si forms also silicon tetrachloride $SiCl_4$:

$$Si_{(s)} + 4HCl_{(g)} \rightleftharpoons SiCl_{4(g)} + 2H_{2(g)} \tag{1.8}$$

Then follows a series of distillations for purifying $SiHCl_3$. The latter is introduced in a reactor containing silicon rods at 1373 K playing the role of seeds. The general reaction is then:

$$SiHCl_{3(g)} + H_{2(g)} \rightleftharpoons Si_{(s)} + 3HCl_{(g)} \tag{1.9}$$

This method is designed for the electronics industry which demands a very high purity silicon – 9 to 11N[8] Si –, namely electronic grade silicon or EG-Si. A large energy input is understandably needed to obtain such a pure silicon.

[8]Number of nines in the purity grade percentage.

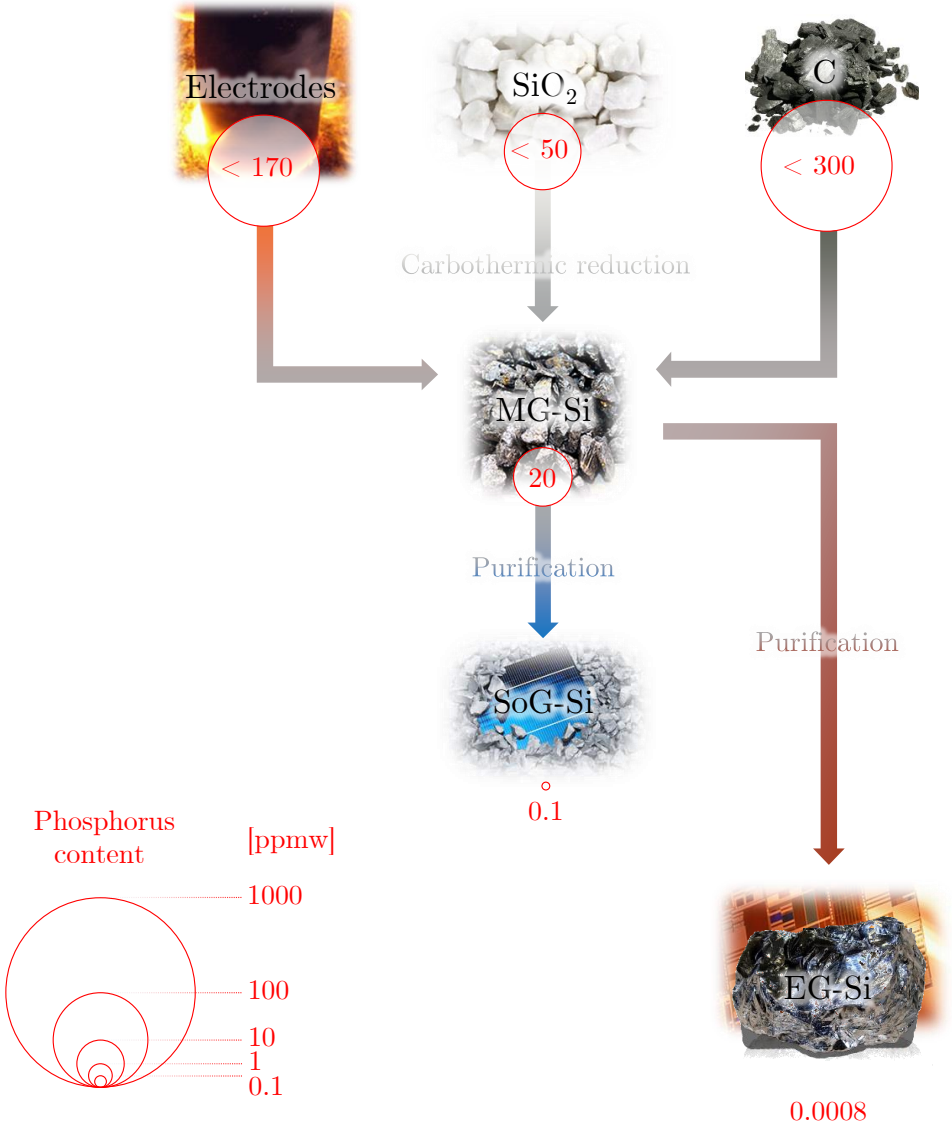

Figure 1.11: Different phosphorus contents in the refinement scheme. Fraction values are taken from Yuge et al. [45] and Dal Martello [11]

Fluidized Bed Reactor process This more recent alternative can be used to directly produce SoG-Si. It has the advantage of running continuously, contrary to the Siemens process.

It first hydrogenates $SiCl_4$ through a mass bed of silicon in a fluidized bed reactor (FBR):

$$3SiCl_{4(g)} + 2H_{2(g)} + Si_{(l)} \rightleftharpoons 4SiHCl_{3(g)} \tag{1.10}$$

After distillation, $SiHCl_3$ is treated through fixed bed columns filled with catalysts as so:

$$2SiHCl_{3(g)} \rightleftharpoons SiH_2Cl_{2(g)} + SiCl_{4(g)} \tag{1.11}$$

$$3SiH_2Cl_{2(g)} \rightleftharpoons SiH_{4(g)} + 2SiHCl_{3(g)} \tag{1.12}$$

Silane SiH_4 is purified by distillation and pyrolyzed in a reactor to produce silicon onto heated silicon rods:

$$SiH_{4(g)} \rightleftharpoons 2H_{2(g)} + Si_{(s)} \tag{1.13}$$

Even if this method proves to be a closed-loop process – as the intermediates reactants are recycled within it – its cost is still high given the numerous steps required for converting $SiHCl_3$ into SiH_4.

b. Electrochemical approach

The three-layer electrorefining of silicon exists at the laboratory scale and is currently in the development stage by NTNU and SINTEF [34]. The electrochemical cell is maintained above the melting point of pure silicon 1685 K: at the bottom is an anode made of a liquid MG-Si/Cu alloy, upon which a less dense liquid layer of CaF_2/BaF_2 lies. The top layer is the resulting SoG-Si.

When an electric current is provided, MG-Si of the alloy is dissolved anodically into the electrolyte, passes through as a complex ion up to the top layer. Also all less noble metals – Na, K, Ca, Ba... – oxidize and dissolve into the electrolyte as complex fluoride ions.

This method is efficient for the removal of impurities in MG-Si, except for boron. That is why it can be conceivable to use it for treating the silicon waste of the sawing of wafers, which is an issue in the photovoltaic field.

c. Metallurgical approach

This refining approach aims to avoid the high capital and energy cost of the usual Siemens process by using well known procedures at the industrial scale. Instead of getting rid of every types of impurities at once via sublimation, this approach involves different processes depending on their nature. This is the context in which the present dephosphorization problematic takes place.

Metallic impurities removal

The starting feedstock is an upgraded metallurgical grade silicon – UMG-1 Si – obtained by directional solidification of the liquid MG-Si. It melts in an inductive furnace and is submitted to another segregation: it results a so-called UMG-2 Si.

This crystallization step is a crucial part of the purification process: a large part of the impurities tends to segregate into the liquid phase, including the metallic impurities as it is shown in Table 1.2. The segregation coefficient k_0 of a given

Table 1.2: Segregation coefficient of some impurities in Czochralski grown silicon observed by Davis et al. [12], except Ca from Ceccaroli and Pizzini [9], C, N and O from Yatsurugi et al. [44].

Type	Element	k_0
Transition metals	Co	$1.0 \cdot 10^{-5}$
	Cr	$1.1 \cdot 10^{-5}$
	Cu	$8.0 \cdot 10^{-4}$
	Fe	$6.4 \cdot 10^{-6}$
	Mn	$1.3 \cdot 10^{-5}$
	Mo	$4.5 \cdot 10^{-8}$
	Nb	10^{-7}
	Ni	$3.2 \cdot 10^{-5}$
	Ta	$2.1 \cdot 10^{-8}$
	Ti	$2.0 \cdot 10^{-6}$
	V	$4 \cdot 10^{-6}$
	W	$1.7 \cdot 10^{-8}$
	Zn	10^{-5}
	Zr	$< 1.5 \cdot 10^{-7}$
Alkaline	Mg	$3.2 \cdot 10^{-6}$
	Ca	$1.6 \cdot 10^{-3}$
Light	C	$7 \cdot 10^{-2}$
	N	$7 \cdot 10^{-4}$
	O	1.25
Dopants	B	0.8
	P	0.35

element quantifies this tendency: it is defined by the ratio of impurity concentration between the solid and the liquid silicon.

The remaining liquid part of UMG-Si, which contains a large amount of impurities with low k_0, is separated by pouring it into a waste container.

As indicated in Table 1.2, this process is not effective for removing every contaminants. Other techniques shall then complement it.

Alkali and alkaline earth removal

A slag process is considered for removing these kinds of impurities. This method is based on the pyrometallurgical refining of MG-Si. A slag consisting of silica sand, $CaO/CaCO_3$ as well as MgO is formed from oxidizing gas, additives and melted silicon. The slag is nonreactive with molten silicon – which has a low solubility – and has a different density so it can be removed by gravity or mechanically.

If impurities contained in MG-Si have a higher affinity with oxygen than with silicon, they oxidize and migrate to the slag.

Boron removal

Different processes have been studied to remove boron: either by slag process [42], cold gas blowing [33] or plasma refining [31].

In the last case, molten silicon is purified with a plasma torch created by induction that blows onto its surface several reactive species such as O_2 and H_2 (Figure 1.12).

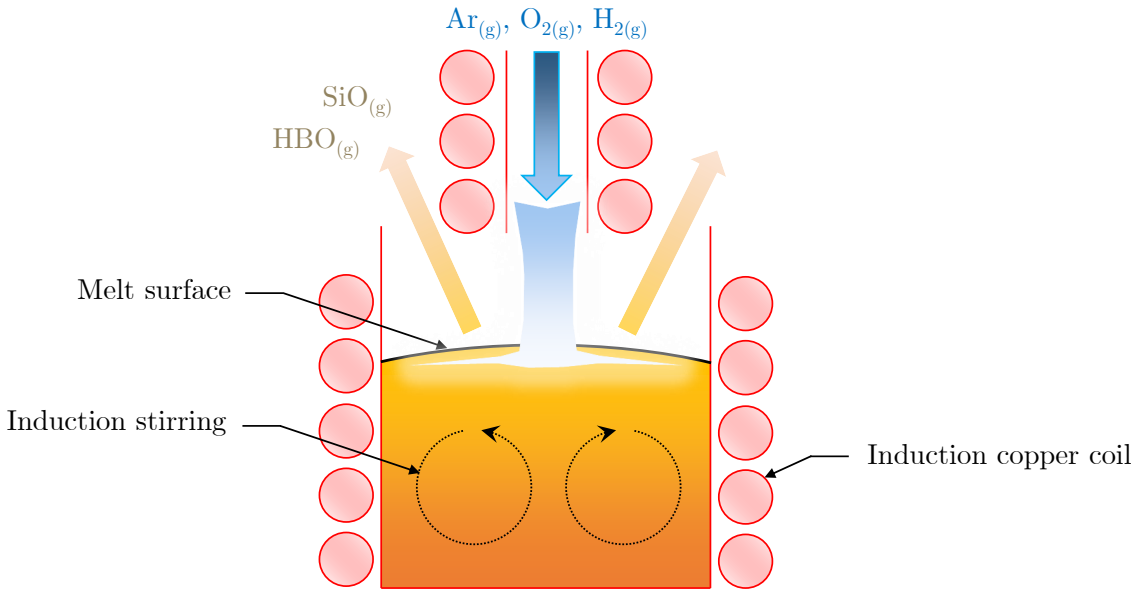

Figure 1.12: Schema of an inductively coupled plasma

The melt is electromagnetically stirred so that the surface can be constantly renewed. The plasma gas volatilizes some remaining impurities which have a high segregation coefficient: for instance boron is mainly removed as $HBO_{(g)}$, and carbon as $CO_{(g)}$. The resulting high velocity of the gas induces a complex flow with reactive boundary layers. In ongoing processes, a high quantity of H_2 is used and gases are heated to achieve the plasma state [1, 31, 33].

In the case of phosphorus, the removal by this inductive plasma refining technique is unfruitful: only a reduction by half has been observed [1].

The overall metallurgical process efficiency depends directly on the boron removal: the purification time decreases with the oxygen concentration, however after a certain amount a layer of SiO_2 is formed at the surface of the melt and highly hampers the process.

Light impurities removal

Silicon contamination by light elements like carbon, nitrogen and oxygen stems from different sources. In general the precipitation of such light elements is induced by high temperature processes.

Oxygen originates from the dissolution of silica crucibles where silicon crystallizes, but also from is transported in the growth furnace [26]. It constitutes various defect complexes in silicon that lower the performance of resulting solar cells.

The carbothermic reduction of silica evidently incorporates carbon impurities, and so do the graphite parts and the remaining atmosphere of the growth furnace. It can merely form SiC, but also combines with oxygen into precipitates.

Nitrogen is often introduced by gas dissolution or by partial decomposition of the Si_3N_4 coating layer on the inner wall of the silica crucibles used.

Another segregation follows the plasma purification in order to remove those impurities.

ISOPEM project

The metallurgical purification is an integral part of the ISOPEM project in which this thesis takes place. Driven by Photosil Industries since 2006, it focuses on several techniques among those mentioned: segregation of impurities during solidification, inductive plasma process inducing volatile boron compounds and crystallization of silicon ingots [14].

Within the SIMaP laboratory several related topics were broached, among which should be mentioned the 2D-mapping of the plasma technique in concentration ratio and temperature [3], its viability by electrical characterization of the resulting wafers [13], or nitrogen and carbon reaction with silicon during solidification [5, 7] and its growth model [6]. With respect to the present study, it also addresses the problem of molten silicon dephosphorization.

1.3.3 Phosphorus removal in the metallurgical purification

In the reduction process of MG-Si, silica and carbon raw materials used unavoidably contain phosphorus. This grade of silicon presents a concentration range of 10 to 50 ppm of P. Upstream of the whole purification approach described above, the method used to refine liquid MG-Si is the evaporation in an induction vacuum refining (IVR) furnace: it lowers in a melt of several hundreds kilograms the amount of phosphorus to about 0.1 ppm. This required maximum limit is based on its impact on the conversion efficiency of solar cells [4, 20]. Other volatile impurities such as Al, Ca, Mg, or Na are also removed by this refining method.

Experimental works have been carried out in the last two decades to demonstrate the efficiency of this technique: Suzuki et al. [40] found that phosphorus decreased from 32 to 6 – 7 ppmw with one hour of $2.7 \cdot 10^{-2}$ Pa vacuum treatment between 1723 and 1823 K, Yuge et al. [46] to less than the required 0.1 ppmw within two hours, and Zheng et al. [47] from 15 to 0.08 ppmw after 2 hours.

Zheng et al. [47, 48] developed a dephosphorization model for their experiment. According to them, phosphorus removal by IVR includes five steps that are shown in Figure 1.13:

① Phosphorus is carried through the melt near the liquid boundary layer;

② It crosses the layer to reach the melt surface;

③ Phosphorus evaporates from the melt surface into the gas phase above;

④ The gaseous phosphorus goes higher in the chamber;
⑤ It condensates on the walls or is carried away by the pump.

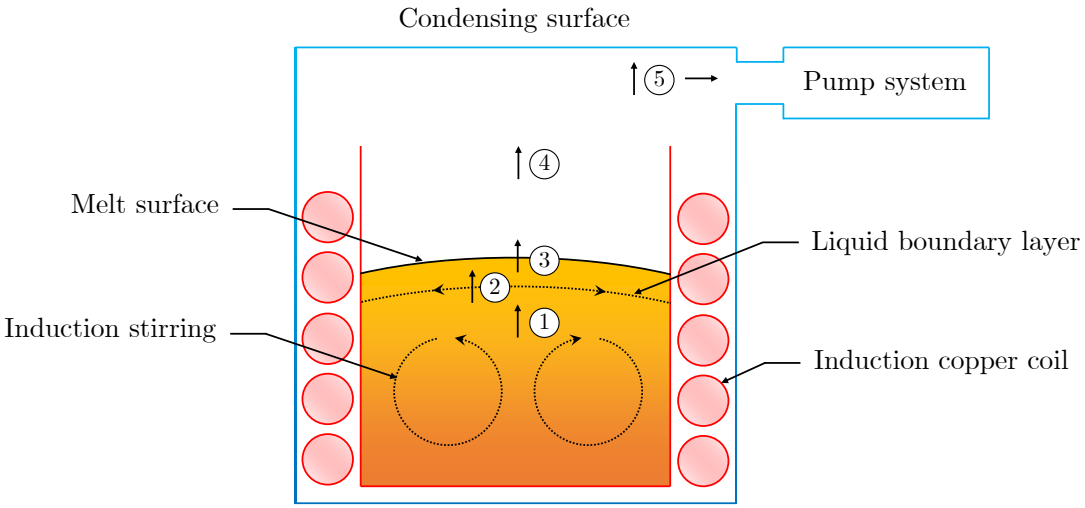

Figure 1.13: Schema of an inductive vacuum refining furnace, adapted from [48]

Irradiating the silicon surface with an electron beam is an alternative that has been proposed, yet the cost of such a process must be the main downside. Ikeda and Maeda [24] reported a decrease down to 3 ppmw by this technique after refining 30 minutes under 10^{-2} Pa of vacuum pressure. Hanazawa et al. [21] observed a decrease to 0.1 ppmw at an industrial scale, Pires et al. [35] from 38 to 0.39 ppmw within 20 minutes under 10^{-4} – 10^{-2} Pa, and Miyake et al. [28] decreased it from 200 to 1 ppmw for one hour under high vacuum.

The removal rate of phosphorus is influenced by different factors that have been experimentally identified: a high temperature [40, 46] and a low pressure [21, 46] favor the dephosphorization time. The species evaporating during this step have been studied by Zheng et al. [48], however an important assumption is made: no other impurities have been taken into account in the model. This hypothesis is also formulated in the experiment of Safarian and Tangstad [37] that studied the kinetics of phosphorus removal at 0.5 Pa, decreasing from 17 to 1.5 ppmw in five hours.

1.4 Positioning of the thesis

Aforementioned chemical purification steps of MG-Si are mostly energy intensive processes with strong environmental impacts, and are rather designed for the upscale EG-Si. The metallurgical route is a more appropriate procedure but is still at the development stage as scientific obstacles remain unsolved.

One of them is the lack of understanding the thermodynamic phenomena involved in the vacuum refining to master the key parameters at the industrial scale. In particular, the impact of other impurities in this dephosphorization step have not been considered so far.

Oxygen is one of the main contaminant element, present both in the crucible used and in the residual atmosphere of the furnace. It will therefore be primarily investigated.

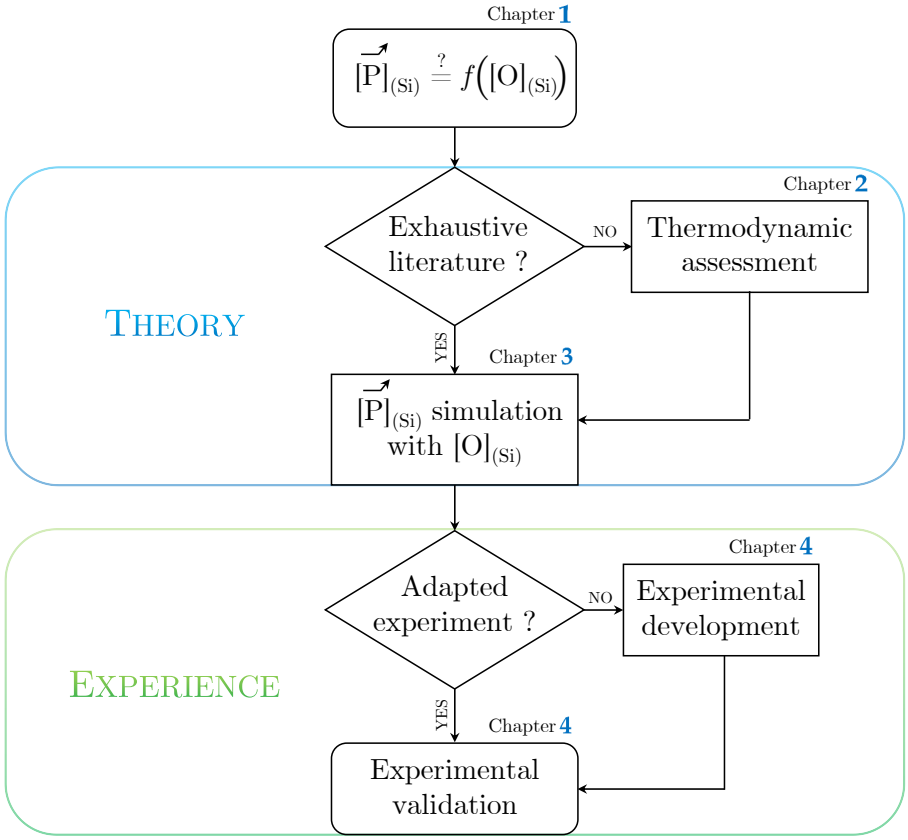

Figure 1.14: Global approach of the thesis

The adopted strategy in the study is presented in Figure 1.14, where the chapters content is specified. First of all, a comprehensive literature survey on the Si – P system is foreseen. An array of relevant articles is the most essential element for investigating theoretically the dephosphorization process of silicon.

If the thermodynamic system is proved to be clearly defined – and specifically in the high-temperature and Si-rich region –, it will be directly implemented in a program that shall predict the distillation time of a given Si-O-P alloy. The associated time factor will be appended by means of adequate kinetic gas theory equations.

Otherwise, a Calphad assessment should be planned to fill that need. This is a computational method employed to model thermodynamic properties for each phase

and simulate multicomponent multi-phase behaviour in binary or more complex systems.

An experimental validation of the theoretical outcomes is required. The electromagnetic levitation will be the main considered technique since it operates in a clean environment without any crucible. An apparatus is available in the SIMaP laboratory, and the experimental conditions may differ: several modifications are possibly required.

Bibliography

[1] C. ALEMANY, C. TRASSY, B. PATEYRON, K.-I. LI, AND Y. DELANNOY, *Refining of metallurgical-grade silicon by inductive plasma*, Solar energy materials and solar cells, 72 (2002), pp. 41–48.

[2] P. ALSTONE, D. GERSHENSON, AND D. M. KAMMEN, *Decentralized energy systems for clean electricity access*, Nature Climate Change, 5 (2015), pp. 305–314.

[3] J. ALTENBEREND, G. CHICHIGNOUD, AND Y. DELANNOY, *Atomic emission spectroscopy method for mixing studies in high power thermal plasmas*, Spectrochimica Acta Part B: Atomic Spectroscopy, 89 (2013), pp. 93–102.

[4] B. BATHEY AND M. CRETELLA, *Solar-grade silicon*, Journal of Materials Science, 17 (1982), pp. 3077–3096.

[5] M. BEAUDHUIN, G. CHICHIGNOUD, P. BERTHO, T. DUFFAR, M. LEMITI, AND K. ZAIDAT, *Carbon reaction with levitated silicon–experimental and thermodynamic approaches*, Materials Chemistry and Physics, 133 (2012), pp. 284–288.

[6] M. BEAUDHUIN, T. DUFFAR, M. LEMITI, AND K. ZAIDAT, *One-dimensional model of the equiaxed grain formation in multi-crystalline silicon*, Journal of crystal growth, 319 (2011), pp. 106–113.

[7] M. BEAUDHUIN, K. ZAIDAT, T. DUFFAR, AND M. LEMITI, *Nitrogen reaction with silicon: Investigation of si undercooling and si 3 n 4 growth*, Journal of Crystal Growth, 336 (2011), pp. 77–81.

[8] BP, *Bp statistical review of world energy*, 2015.

[9] B. CECCAROLI AND S. PIZZINI, *Processes*, Advanced Silicon Materials for Photovoltaic Applications, (2012), pp. 21–78.

[10] C. CHANDLER, *Solar spectrum*, 2012.

[11] E. DAL MARTELLO, *Impurity distribution and reduction behaviour of quartz in the production of high purity silicon*, (2012).

[12] J. DAVIS, A. ROHATGI, R. H. HOPKINS, P. D. BLAIS, P. RAI-CHOUDHURY, J. R. MCCORMICK, AND H. MOLLENKOPF, *Impurities in silicon solar cells*, IEEE Transactions on Electron Devices, 27 (1980), pp. 677–687.

[13] J. DEGOULANGE, I. PERICHAUD, C. TRASSY, AND S. MARTINUZZI, *Multicrystalline silicon wafers prepared from upgraded metallurgical feedstock*, Solar Energy Materials and Solar Cells, 92 (2008), pp. 1269–1273.

[14] R. Einhaus, J. Kraiem, F. Cocco, Y. Caratini, D. Bernou, D. Sarti, G. Rey, R. Monna, C. Trassy, J. Degoulange, et al., *Photosil–simplified production of solar silicon from metallurgical silicon*, Proceedings of the 21st European PVSEC, Dresden, (2006), pp. 580–583.

[15] D. H. Filsinger and D. B. Bourrie, *Silica to silicon: key carbothermic reactions and kinetics*, Journal of the American Ceramic Society, 73 (1990), pp. 1726–1732.

[16] R. Fouquet et al., *A brief history of energy*, International Handbook on the Economics of Energy, (2009).

[17] M. A. Green, *Solar cells: operating principles, technology, and system applications*, (1982).

[18] ——, *Commercial progress and challenges for photovoltaics*, Nature Energy, 1 (2016).

[19] M. A. Green, K. Emery, Y. Hishikawa, W. Warta, and E. D. Dunlop, *Solar cell efficiency tables (version 45)*, Progress in photovoltaics: research and applications, 23 (2015), pp. 1–9.

[20] B. Gribov and K. Zinov'ev, *Preparation of high-purity silicon for solar cells*, Inorganic materials, 39 (2003), pp. 653–662.

[21] K. Hanazawa, N. Yuge, and Y. Kato, *Evaporation of phosphorus in molten silicon by an electron beam irradiation method*, Materials Transactions, 45 (2004), pp. 844–849.

[22] IEA, *World Energy Outlook 2015*, World Energy Outlook, IEA Publications, 2015.

[23] ——, *Energy Technology Perspectives 2016*, Energy Technology Perspectives, IEA Publications, 2016.

[24] T. Ikeda and M. Maeda, *Purification of metallurgical silicon for solar-grade silicon by electron beam button melting*, ISIJ international, 32 (1992), pp. 635–642.

[25] M. S. Islam, M. A. Rhamdhani, G. A. Brooks, et al., *Solar-grade silicon: current and alternative production routes*, Chemeca 2011: Engineering a Better World: Sydney Hilton Hotel, NSW, Australia, 18-21 September 2011, (2011), p. 1826.

[26] K. Kakimoto, A. Tashiro, T. Shinozaki, H. Ishii, and Y. Hashimoto, *Mechanisms of heat and oxygen transfer in silicon melt in an electromagnetic czochralski system*, Journal of crystal growth, 243 (2002), pp. 55–65.

[27] D. Lynch and M. Lynch, *The search for a low cost solar-grade silicon*, Silicon for the chemical industry VII, (2004), pp. 21–24.

[28] V. M. Miyake, T. Hiramatsu, and M. Maeda, *Removal of phosphorus and antimony in silicon by electron beam melting at low*, Journal of the Japan Institute of Metals, 70 (2006), pp. 43–46.

[29] B. Mukashev, K. Abdullin, M. Tamendarov, T. Turmagambetov, B. Beketov, M. Page, and D. Kline, *A metallurgical route to produce upgraded silicon and monosilane*, Solar energy materials and solar cells, 93 (2009), pp. 1785–1791.

[30] J. P. Murray, G. Flamant, and C. J. Roos, *Silicon and solar-grade silicon production by solar dissociation of si_3n_4*, Solar energy, 80 (2006), pp. 1349–1354.

[31] N. Nakamura, H. Baba, Y. Sakaguchi, S. Hiwasa, and Y. Kato, *Boron removal in molten silicon with steam added plasma melting method*, Journal of the Japan Institute of Metals, 67 (2003), pp. 583–589.

[32] U. Nations, *World population 2015 wallchart*, Department of Economic and Social Affairs, Population Division, (2015).

[33] E. F. Nordstrand and M. Tangstad, *Removal of boron from silicon by moist hydrogen gas*, Metallurgical and Materials Transactions B, 43 (2012), pp. 814–822.

[34] E. Olsen and S. Rolseth, *Three-layer electrorefining of silicon*, Metallurgical and Materials Transactions B, 41 (2010), pp. 295–302.

[35] J. Pires, J. Otubo, A. Braga, and P. Mei, *The purification of metallurgical grade silicon by electron beam melting*, Journal of Materials Processing Technology, 169 (2005), pp. 16–20.

[36] H. Poincare, *Thermodynamique*, vol. 3, Association Amicale des Eleves et Anciens Eleves de la Faculte des Sciences, georges carre ed., 1892.

[37] J. Safarian and M. Tangstad, *Kinetics and mechanism of phosphorus removal from silicon in vacuum induction refining*, High Temperature Materials and Processes, 31 (2012), pp. 73–81.

[38] D. Sarti and R. Einhaus, *Silicon feedstock for the multi-crystalline photovoltaic industry*, Solar energy materials and solar cells, 72 (2002), pp. 27–40.

[39] W. Shockley and H. J. Queisser, *Detailed balance limit of efficiency of p-n junction solar cells*, Journal of applied physics, 32 (1961), pp. 510–519.

[40] K. Suzuki, K. Sakaguchi, T. Nakagiri, and N. Sano, *Gaseous removal of phosphorus and boron from molten silicon*, Journal of the Japan Institute of Metals, 54 (1990), pp. 161–167.

[41] UNDP, *World Energy Assessment: Energy and the challenge of sustainability*, World Energy Outlook, UNDP, 2000.

[42] J.-j. Wu, Y.-l. Li, K.-x. WEI, Y. Bin, Y.-n. DAI, et al., *Boron removal in purifying metallurgical grade silicon by cao–sio2 slag refining*, Transactions of Nonferrous Metals Society of China, 24 (2014), pp. 1231–1236.

[43] K. Yasuda, T. Nohira, Y. H. Ogata, and Y. Ito, *Direct electrolytic reduction of solid silicon dioxide in molten licl–kcl–cacl$_2$ at 773 k*, Journal of the Electrochemical Society, 152 (2005), pp. D208–D212.

[44] Y. Yatsurugi, N. Akiyama, Y. Endo, and T. Nozaki, *Concentration, solubility, and equilibrium distribution coefficient of nitrogen and oxygen in semiconductor silicon*, Journal of the electrochemical society, 120 (1973), pp. 975–979.

[45] N. Yuge, M. Abe, K. Hanazawa, H. Baba, N. Nakamura, Y. Kato, Y. Sakaguchi, S. Hiwasa, and F. Aratani, *Purification of metallurgical-grade silicon up to solar grade*, Progress in Photovoltaics: Research and Applications, 9 (2001), pp. 203–209.

[46] N. Yuge, K. Hanazawa, K. Nishikawa, and H. Terashima, *Removal of phosphorus, aluminum and calcium by evaporation in molten silicon*, Journal of the Japan Institute of Metals(Japan), 61 (1997), pp. 1086–1093.

[47] S.-S. Zheng, W.-H. Chen, J. Cai, J.-T. Li, C. Chen, and X.-T. Luo, *Mass transfer of phosphorus in silicon melts under vacuum induction refining*, Metallurgical and Materials Transactions B, 41 (2010), pp. 1268–1273.

[48] S.-S. Zheng, T. A. Engh, M. Tangstad, and X.-T. Luo, *Separation of phosphorus from silicon by induction vacuum refining*, Separation and purification technology, 82 (2011), pp. 128–137.

2

Theoretical study of the Si – P system

INVESTIGATING the theoretical dephosphorization process of molten silicon needs to set up an array of relevant thermodynamic data relative to the Si – P system. An analysis of the available literature is performed, including both experimental and optimization studies.

Before starting with the theoretical investigation, some basic thermodynamic notions must be reminded. Due to the large number of thermodynamic variables used throughout the manuscript, a color code is suggested to help the reading along.

2.1 Preliminary thermodynamic concepts

Thermodynamics is all about **energy**[1]. It focuses on its different forms, its conservation and conversions, but also the relation between energy and properties of matter. The term originates from the Greek *thermo* and *dynamis* respectively meaning heat and movement[2], which is a hint for the content of the following part.

2.1.1 Energies

The **first law of thermodynamics** is about the conservation of energy, therefore states that the **internal energy** U of an isolated system is constant:

$$dU = 0 \tag{2.1}$$

[1] In fact, it is the first branch of science to use the notion of energy as a scientific concept.

[2] It will consequently not broach other aspects of energy, such as electric or electromagnetic issues.

The energy of a closed system may however vary due to an exchange of heat Q or work W with the outside environment. **Heat** is the transfer of thermal energy between two bodies at different temperatures while **work** is the transfer of mechanical energy between two bodies at different pressures.

Furthermore if different types of its particles react chemically, their numbers may not be constant. In this general case:

$$dU = \delta Q + \delta W + \sum_i \mu_i dn_i \tag{2.2}$$

One needs to underline that each term of equation 2.2 is a form of energy and is expressed in Joule: it is respectively the thermal (Q), mechanical (W) and chemical ($\mu_i n_i$) aspect of the energy. In the last term n_i is the amount of substance of the species i and μ_i is the chemical potential of this species. These variables are introduced in the next part.

In practice the first law is of utmost importance in engineering as it rules out the perpetual motion machine of the first kind.

2.1.2 State variables

A thermodynamic system is characterized by several variables corresponding to macroscopic properties (Figure 2.1). They can be of two kinds: **intensive** (■) or **extensive** (□). The size of the system does not affect the value of the first, contrary to the second.

Each aspect of the thermodynamic system – thermal, mechanical, chemical – is described by one intensive and one extensive variable (Table 2.1).

Table 2.1: Fundamental properties describing a thermodynamic system

Kind of energy	**Intensive aspect ■**	**Extensive aspect □**
Thermal Q	Temperature T	Entropy S
Mechanical W	Pressure p	Volume V
Chemical $\mu_i n_i$	Chemical potential μ_i	Chemical amount n_i

Thermal energy Q

■ **Temperature** expressed in K describes the microscopic kinetic agitation degree of the particles in the system.

□ Given in J.K^{-1}, **entropy** was defined in statistical mechanics in 1877 by Ludwig Boltzmann as a logarithmic function of the number of ways Ω the particles can be arranged in the system:

$$S = k_B \ln \Omega \tag{2.3}$$

The number of possible states Ω existing in the system depends on its size, hence the extensive property of entropy. This function is not purely logarithmic: it is weighted by the Boltzmann constant[3] k_B that is equal to 1.38065 $\cdot 10^{-23}$ J.K^{-1}. This relation helps to understand why entropy is generally referred as a measure of molecular disorder within a macroscopic system beyond the thermal aspect.

For a given closed system, a heat variation is depicted as a combination of a temperature and entropy variation:

$$\delta Q = TdS \tag{2.4}$$

As the first law of thermodynamics defines energy and its conservation, the **second law** defines the concept of entropy to explain that without external work performed on the system, heat flows from hotter to colder bodies and not the other way around. The irreversibility of this process states that dS cannot be negative in such a system.

The second law rules out so-called perpetual machines of the second kind, *i.e.* engines that respect the conservation of energy but try to generate work either by withdrawing heat from one hot body without rejecting it to a colder body, or by cooling down a thermal reservoir.

Mechanical energy W

▪ **Pressure** expressed in Pa is the force applied to the surface of the system per unit of this area. This latter weighting makes it intensive.

□ The corresponding extensive quantity is the **volume** of the system.

For a given closed system, a work variation is depicted as a combination of a pressure and volume variation:

$$\delta W = -pdV \tag{2.5}$$

The convention is that negative sign is applied to the work contribution to specify that it is done *on* the system.

Chemical energy $\mu_i n_i$

▪ **Chemical potential** expressed in J.mol^{-1} is the energetic cost for introducing a mole of a species i in the system. This intensive variable is to chemical conversion what temperature is to thermal conversion or what pressure is to mechanical conversion, in that if the system is chemically inhomogeneous, particles tend to move from higher to lower chemical potential.

□ The corresponding extensive quantity is the **chemical amount** of the species i.

[3] Multiplying it by the Avogadro number $\mathcal{N}_A$ gives the ideal gas constant R that is used thereafter.

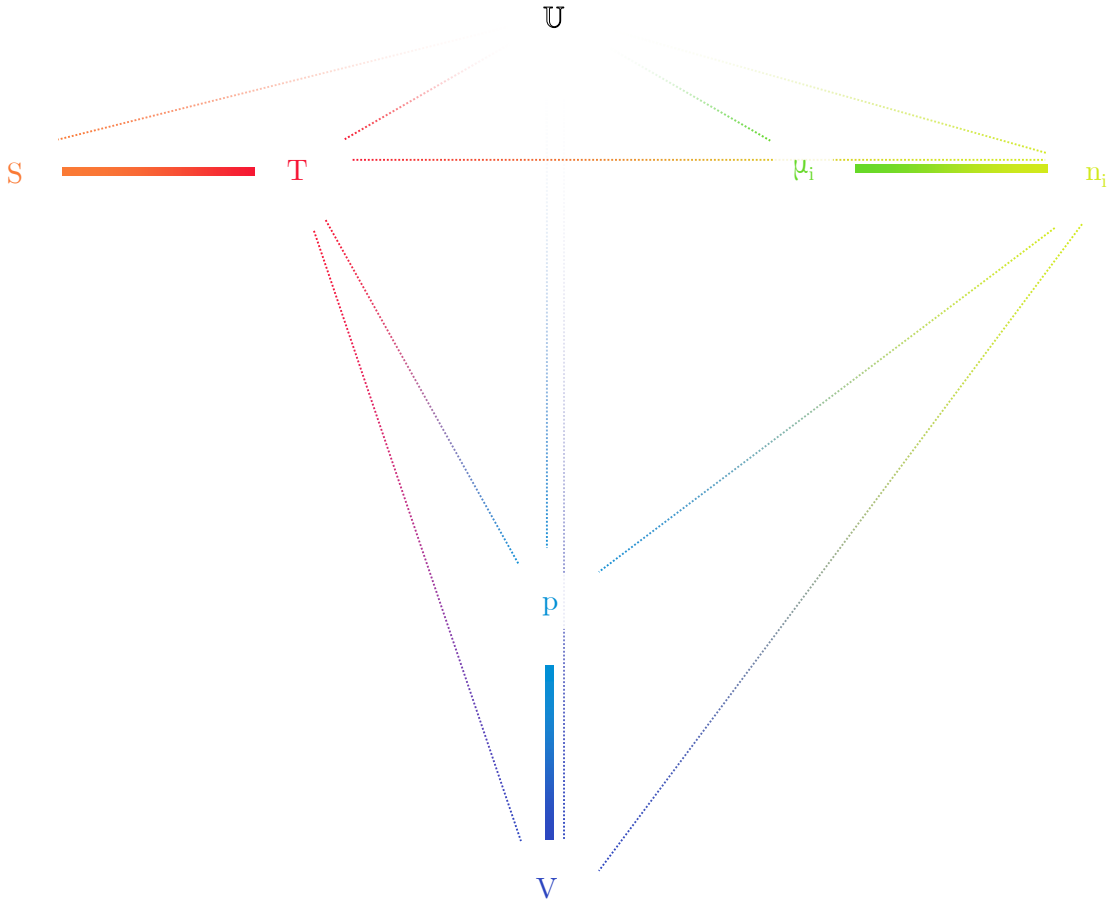

$$dU = TdS - pdV + \sum_i \mu_i dn_i \qquad \text{First law of thermodynamics}$$

$$pV = nRT \qquad \text{Ideal gas law}$$

Figure 2.1: Map of the different thermodynamic **state variables** and the main relations connecting them. The ideal gas law is properly discussed Chapter 3.

In a closed system, equation 2.2 can be rewritten for relating the internal energy of the system to those state variables:

$$dU = TdS - pdV + \sum_i \mu_i dn_i \tag{2.6}$$

The state variables presented enable to fully identify the condition at a specific time of a system *i.e.* its **thermodynamic state**. It is said to be **at equilibrium** if no macroscopic flows of matter or of energy are observed over a certain time[4]. In order to quantify the thermodynamic state of a system, thermodynamic potentials are employed.

2.1.3 Thermodynamic potentials

Under certain conditions the value of a thermodynamic potential decreases during a transformation to finally reach a minimum at equilibrium. Internal energy is such a potential: according to equation 2.6 it tends to a minimum value in a closed system for a constant volume and entropy. However, due to the second law of thermodynamics the last condition is unrealistic, so U cannot be used as such in practice.

To overcome this problem, three thermodynamic potentials have been set up: **enthalpy**, **Helmholtz free energy** and **Gibbs free energy** (Figure 2.2). They are the result of different Legendre transformations[5] used to replace extensive variables S and V – inappropriate experimentally speaking – by intensive variables p and T, and are consequently all expressed in Joule[6].

Enthalpy

Enthalpy H is the result of a Legendre transformation of U where the change of variable is the pressure in place of the volume, so H is expressed as:

$$H = U + pV \tag{2.7}$$

As $d(pV) = Vdp + pdV$ it is possible to write for a closed system:

$$dH = TdS + Vdp + \sum_i \mu_i dn_i \tag{2.8}$$

It occurs from this equation that enthalpy plays the same role for a constant pressure as internal energy for constant volume. H is associated with the concept of heat – it stands for that word, and derives from the Greek *thalpein* meaning

[4]The notion of time in this definition is debated: the most telling example to illustrate this point is the case of a glass window. For a decade scale it seems at equilibrium, but over millennia it will ultimately melt.

[5]To put it simply the new function is the difference between the original function and the product of the original and new variables.

[6]In practice, molar equivalents ($J.mol^{-1}$) are also used.

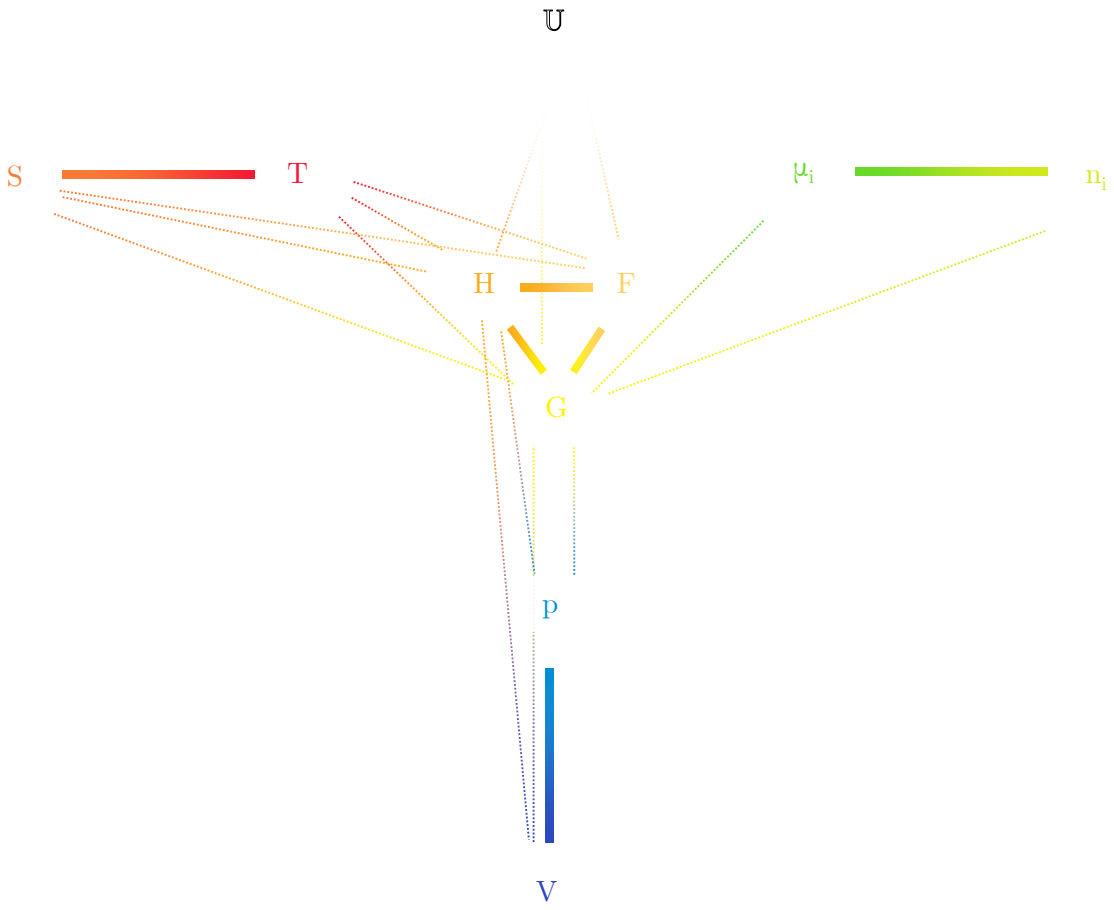

$$H = U + pV \qquad \text{Enthalpy definition}$$

$$F = U - TS \qquad \text{Helmholtz free energy definition}$$

$$G = U + pV - TS \qquad \text{Gibbs free energy definition}$$

$$H = \sum_i \mu_i n_i + TS \qquad \text{Enthalpy and state variables}$$

$$F = \sum_i \mu_i n_i - pV \qquad \text{Helmholtz free energy and state variables}$$

$$G = \sum_i \mu_i n_i \qquad \text{Gibbs free energy and state variables}$$

Figure 2.2: Map of the different **thermodynamic potentials** and the main relations connecting them

"to heat" – because for a closed system where the pressure and the number of particles are constant, the variation of enthalpy is nothing but the variation of heat according to equation 2.8.

Measuring the enthalpy of a system is not conceivable, instead one seeks enthalpy change ΔH between final and initial enthalpies. If a chemical reaction gives off heat, it is said to be **exothermic** and $\Delta H < 0$. It occurs when the energy released from forming new chemical bonds is more than the energy required to break initial bonds. On the contrary if a chemical reaction requires energy, it is said to be **endothermic** and $\Delta H > 0$.

Helmholtz free energy

Helmholtz free energy F is the result of a Legendre transformation of U where the change of variable is the temperature in place of the entropy, so F is expressed as:

$$F = U - TS \tag{2.9}$$

As $d(TS) = SdT + TdS$ it is possible to write for a closed system:

$$dF = -SdT - pdV + \sum_i \mu_i dn_i \tag{2.10}$$

F can be used for studying pressure changes in isothermal transformations such as explosions, but investigating chemical equilibria requires using a potential that relates isothermal *and* isobaric systems; this being the case of Gibbs free energy.

Gibbs free energy

Gibbs free energy G is the result of a Legendre transformation of U where the change of variable is twofold: p in place of V and T in place of S. It is then expressed as:

$$G = U + pV - TS \tag{2.11}$$

Then if one reconciles with equation 2.6 it appears that:

$$G = \sum_i \mu_i n_i \tag{2.12}$$

In other words, when p and T are kept constant the energy previously mentioned to introduce the notion of μ_i is nothing else than the Gibbs free energy.

Indeed for a closed system it is possible to write:

$$dG = -SdT + Vdp + \sum_i \mu_i dn_i \tag{2.13}$$

This relation implies that a closed isobaric and isothermal system minimizes its Gibbs free energy when equilibrium is reached. One needs to realize the significance of this thermodynamic potential in practice: it depends on experimentally measurable (unlike S and μ_i) and manageable (unlike V) variables.

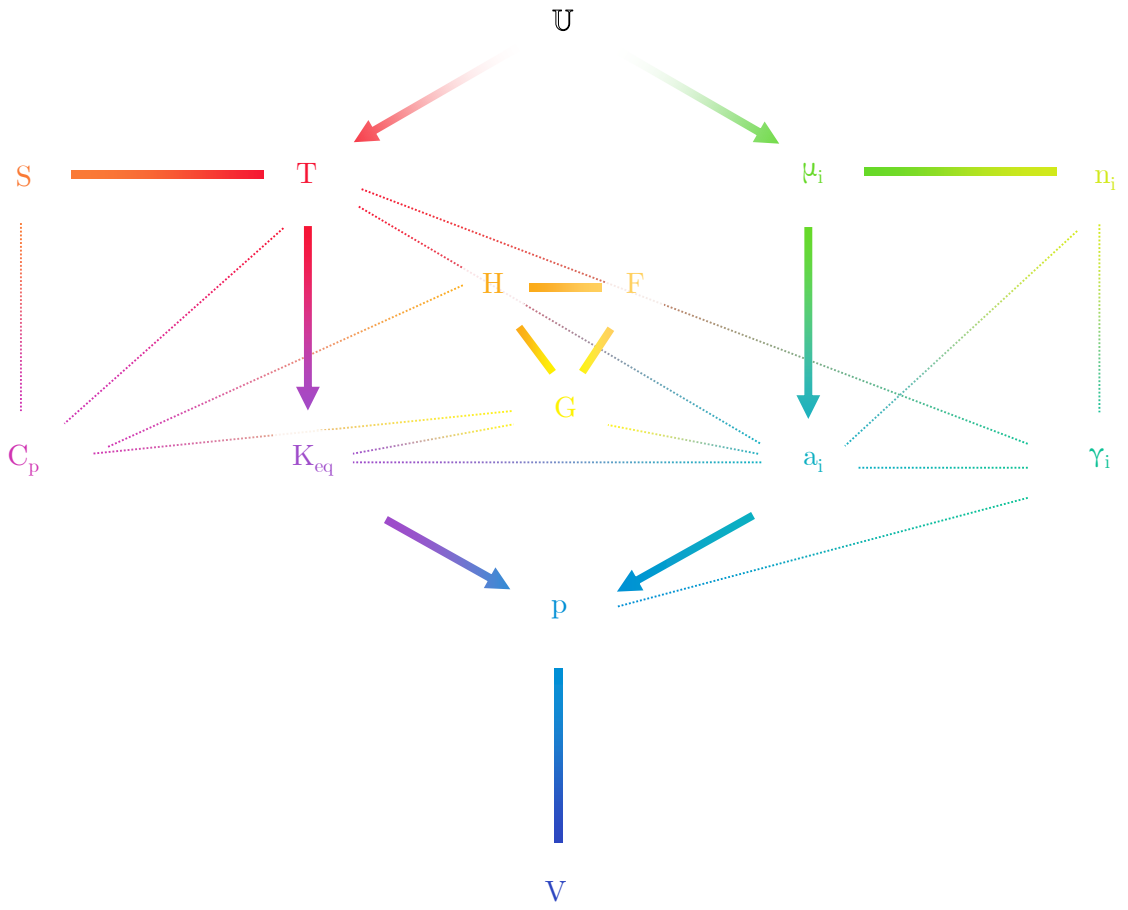

$$C_p = T\left(\frac{\partial S}{\partial T}\right)_{p,n_i}$$ Heat capacity definition

$$a_i = e^{\frac{\mu_i - \mu_i^0}{RT}}$$ Activity definition

$$a_i = \gamma_i x_i$$ Activity coefficient definition

$$K_{\text{eq}} = 10^{\frac{A}{T}+B}$$ Equilibrium constant experimental fit

$$K_{\text{eq}} = e^{-\frac{\Delta G^0}{RT}}$$ Equilibrium constant related to ΔG^0

$$K_{\text{eq}}(j) = \frac{p_j}{\prod_i a_i^{\nu_i}}$$ Equilibrium constant for vaporization reactions

Figure 2.3: Map of the other useful variables for the thermodynamic study (**dilution concepts**, **thermal coefficients**) and the main relations connecting them

Considering equation 2.11 Gibbs free energy change can be written as a function of temperature, enthalpy change and entropy change:

$$\Delta G = \Delta H - T\Delta S \tag{2.14}$$

If $\Delta G < 0$ the chemical reaction is spontaneous. To be so it shall be either exothermic, or endothermic with a sufficiently positive entropy change.

To approach more deeply thermodynamics, other variables shall be introduced (Figure 2.3). Dilution concepts will help to investigate phosphorus as an impurity element in silicon, while thermal coefficients will provide a better thermodynamic description of the system.

2.1.4 Dilution concepts

From now onwards, the next variables involve notions that need to be clarified.

- A **solution**, firstly, is a solid or liquid phase in which the composition can be modified continuously by adding or removing components. It is said to be **ideal** if the interactions between its components, regardless of their nature, are identical.
- To determine its properties, the **standard state** of a material – such as a solution – is defined as a reference point. The IUPAC convention states that the **standard pressure** $p^0 = 10^5$ Pa $= 1$ bar characterizes it for any temperature T, although $T = 298$ K is often used as a *reference* temperature.

Activity

This notion was later introduced as a result of the lack of understanding non ideal chemical systems. It is historically derived from the chemical potential. By considering dG for a pure substance at constant temperature it comes $d\mu = Vdp$ and for an ideal gas, by integrating this equation from the standard state (μ^0, p^0) to a non standard state (μ, p) one gets:

$$\mu - \mu^0 = RT \ln \frac{p}{p^0} \tag{2.15}$$

The notion of activity arises then from the willingness to have a similar behaviour regarding the chemical potential in the case of real gases. More generally the following activity definition is applicable for any solution:

$$a_i = e^{\frac{\mu_i - \mu_i^0}{RT}} \tag{2.16}$$

In concrete terms, the chemical activity a_i of a species i is a dimensionless quantity ranging from 0 to 1 reflecting the availability of i to interact with other species in a reaction system, which therefore depends on its amount. To put it differently, a_i is the *active* fraction of i.

Activity coefficient

Activity coefficient γ_i is also dimensionless and quantifies the deviation from ideal behaviour of a species i in a real solution. It informs how different activity a_i is from the *real* mole fraction x_i. $\gamma_i < 1$ means that contacts between species of different nature are favored, whereas $\gamma_i > 1$ means the opposite: there is a tendancy to form agglomerates of species of the same nature. That being said one can write for liquid phase:

$$a_i = \gamma_i x_i \tag{2.17}$$

As species i tends towards ideality, γ_i approaches 1.

In the case of ideal solutions, **Raoult's law** states that partial vapour pressure p_i above the solution is related to its mole fraction by the partial vapour pressure of the pure species i as so:

$$p_i = p_i^0 x_i \tag{2.18}$$

By definition, a_i is the ratio between p_i and p_i^0 in the gas phase so according to this law, activity coefficient γ_i is 1 in ideal solutions.

However in dilute solutions, one applies instead **Henry's law**. It states that partial vapour pressure p_i above the solution is related to its mole fraction by experimentally defined Henry's constant K_{H_i} of species i instead of p_i^0.

In infinite dilutions, activity coefficient γ_i^∞ is related to Henry's constant by:

$$\gamma_i^\infty = \frac{K_{H_i}}{p_i^0} \tag{2.19}$$

Figure 2.4 sheds light on those two extreme cases.

2.1.5 Thermal coefficients

Equilibrium constant

This dimensionless constant K_{eq} is the familiar reaction quotient of products over reactants Q_r, but at equilibrium. When $K_{\text{eq}} \gg 1$, the equilibrium lies to the right of the chemical equation and vice versa. The quantities used for defining K_{eq} are partial pressures p_i for gas phases and activities a_i for non ideal solutions[7].

It does not depend on initial concentrations, or on the reaction mechanism, but solely on temperature and stoichiometry. It is thus experimentally described by:

$$K_{\text{eq}} = 10^{\frac{A}{T}+B} \tag{2.20}$$

At equilibrium, thermodynamic potentials tend to a minimum so they shall be related to the notion of K_{eq}. As at p and T constant, μ_i is the partial Gibbs free energy G_i, according to equation 2.16 one gets:

[7] Sometimes this constant is referred as K_p or K_c when it merely uses pressures or concentrations.

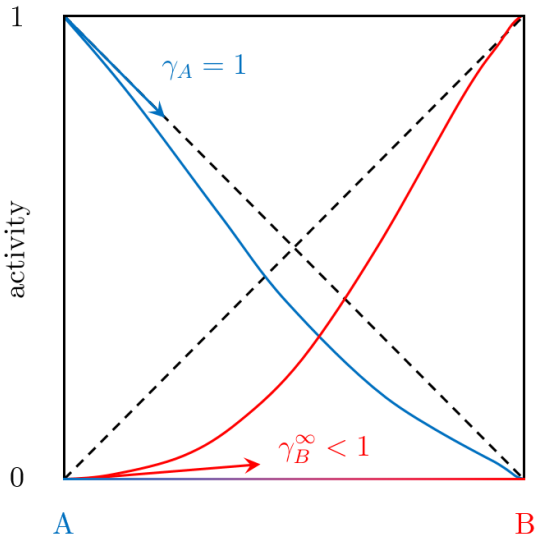

Figure 2.4: General appearance of a_A and a_B activities of a binary solution A,B at constant p and T in the case of $\gamma_i < 1$. Raoult's law applies for A when concentrated whereas Henry's law applies for B when infinitely diluted.

$$\Delta G = \sum_i (G_i^0 + RT \ln a_i) = \Delta G^0 + RT \ln Q_r \tag{2.21}$$

ΔG reaches zero at equilibrium, consequently:

$$\Delta G^0 = -RT \ln K_{\text{eq}} \tag{2.22}$$

Heat capacity

This extensive variable corresponds to the amount of heat Q needed to raise by 1 K the temperature of a system, thus is expressed in J.K^{-1}.

In a closed system at chemical equilibrium[8], one can define **heat capacity at constant volume** C_V from equation 2.6 by deriving internal energy with respect to temperature:

$$C_V = \left(\frac{\partial Q}{\partial T}\right)_V = \left(\frac{\partial U}{\partial T}\right)_V \tag{2.23}$$

In practice, **heat capacity at constant pressure** C_p is rather used as it derives from enthalpy. According to 2.7 one can write:

$$C_p = \left(\frac{\partial Q}{\partial T}\right)_p = \left(\frac{\partial H}{\partial T}\right)_p \tag{2.24}$$

Moreover this latter quantity is related to entropy and Gibbs free energy by deriving it twice:

[8] $dn_i = 0$.

$$\left(\frac{\partial^2 G}{\partial T^2}\right)_{p,n_i} = -\left(\frac{\partial S}{\partial T}\right)_{p,n_i} = -\frac{C_p}{T} \tag{2.25}$$

Heat capacity is experimentally obtainable with calorimeters, and is generally fitted as a function of T as so:

$$C_p = \underbrace{a + b \cdot T - \frac{c}{T^2}}_{\text{Maier-Kelley equation}} + d \cdot T^2 + e \cdot T^3 ... \tag{2.26}$$

Then obtaining enthalpy and entropy changes between two temperatures (usually from 298 K) is conceivable by integrating equation 2.24 and 2.25:

$$\Delta H^T_{298\ \mathrm{K}} = \Delta_f H^0_{298\ \mathrm{K}} + \int_{298\ \mathrm{K}}^{T} C_p dT \tag{2.27}$$

$$\Delta S^T_{298\ \mathrm{K}} = S^0_{298\ \mathrm{K}} + \int_{298\ \mathrm{K}}^{T} \frac{C_p}{T} dT \tag{2.28}$$

All the previously introduced thermodynamic concepts are key variables for the following theoretical study as they can be related to liquid or gas phases. The links established between one another provide a better overall picture of the reasoning mechanisms to unroll for the next sections.

2.1.6 Thermodynamic databases

Thermodynamics is increasingly used as technology advances and innovative processes are investigated. Studying thermodynamic properties of substances by critically analyzing the available literature is therefore essential to provide reliable and consistent data to scientists and engineers from various backgrounds.

Historically, the project of constituting such reference books started for different reasons – applied or normative –, in different geographical areas – US, Europe, USSR – and in various scientific fields – metallurgy, geoscience, or else nuclear.

As accumulating thermodynamic data is a long and fastidious work, the objective of unifying the various data banks with an international cooperation is far from being reached.

A reference data bank should present a broad and coherently selected set of substances, and contain thermochemical data and thermal functions mutually consistent and selected as the result of critical analysis of *all* available literature data. An estimation of the reliability of the values, an explicative text about the origin of these results and a bibliography should be included.

Two kinds of reference books then exist: critical reference books and compilation handbooks. The first type meets most of the requirements mentioned above, but they are few. The second type forms the majority of the reference books as they mainly consist of reproduced data from other reference articles; they are generally

less reliable as they might content uncritical data of periodicals and inconsistent values.

The most commonly used thermodynamic databases are listed in Table 2.2. They differ according to the notation used, the choice of standard states, the kind of elements and compounds considered, or the quantities evaluated. Broadly speaking though, the JANAF and Gurvich tables are considered to be the most reliable.

Table 2.2: A non-exhaustive list of the reference books and data banks used in thermodynamics. The compilation handbooks shortlisted here are deemed the most reliable in their own category.

Type of database	**Format**	**Tables – *Electronic Base***	**First author**
Critical	Tabular, electronic	TPIS – *IVTANTERMO*	Gurvich [19]
	Tabular, electronic	JANAF	Chase [11]
	Tabular, functional	US Bureau of Mines	Pankratz [43]
	Tabular	NBS	Wagman [72]
	Tabular	TCS	Glushko [18]
	Tabular	CODATA	Cox [12]
	Tabular	SVTPE	Hultgren [21]
Compilation	Functional, electronic	SGTE – *THERMODATA*	Dinsdale [13]
	Tabular	TPIS	Barin, Knacke [5]
	Tabular	TPRMS	Robie [46]

In spite of the scientific community best efforts, a wide-ranging experimental investigation has not been performed for many systems thus far. In such instances, a comprehensive analysis is conceivable through thermodynamic assessment.

2.1.7 Calphad approach

The Calphad approach[9] involves two steps (Figure 2.5). It firstly consists of gathering relevant data from the literature and modeling parameters for each phase of the system. The second step is then to put these models into the fragmentary experimental data from the literature in an extrapolation perspective.

It can be performed by different software packages, such as Thermo-Calc [2], FactSage [4], PANDAT [9] or Lukas BINGSS and BINFKT programs [32].

□ Step 1: Critical analysis

Modeling the phases ϕ amounts to give an analytical description of the Gibbs free energy G^{ϕ} for each of them with respect to T, x_i and less frequently p_i. This first step is of utmost importance as it afterwards allows to estimate phase equilibria and thermodynamic properties *beyond* the regions of experimental data: G^{ϕ} indeed holds all other properties within as previously pointed out.

[9] **Cal**culation of **pha**se **d**iagrams, also referred as thermodynamic assessment, thermodynamic modeling or thermodynamic optimization.

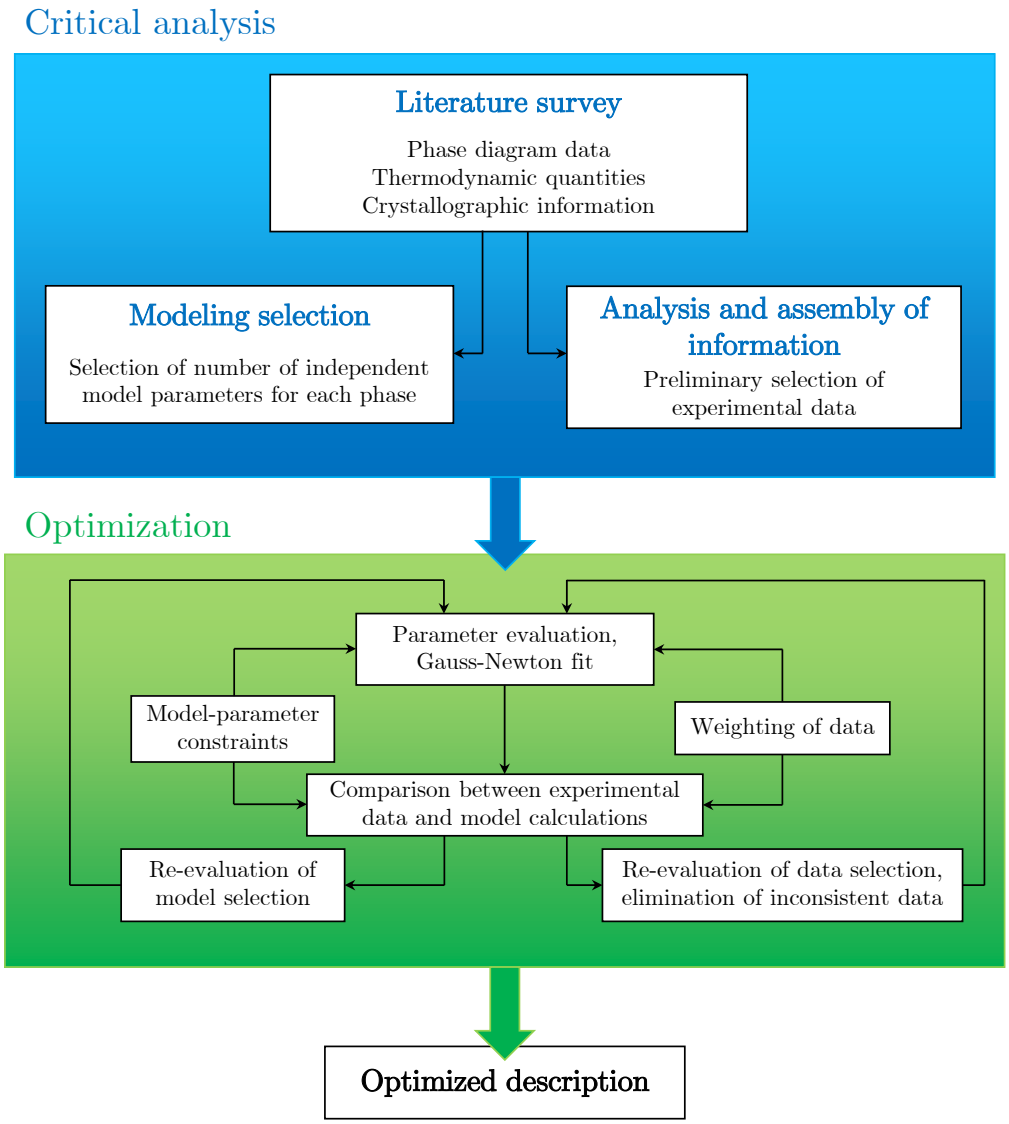

Figure 2.5: A schematic diagram of the general Calphad approach, inspired from [33]. Indications in gray are not realized in this study.

For pure elements or stoichiometric compounds, the composition is fixed. G^{ϕ} is then generally deduced from experimental C_p^{ϕ} and consequently expressed with the following SGTE[10] formalism:

$$G^{\phi} = a + b \cdot T + c \cdot T \ln T + d \cdot T^2 + e \cdot T^{-1} + f \cdot T^3 \tag{2.29}$$

For solutions, the composition is variable. If ϕ is considered as a **regular solu-**

[10] **S**cientific **G**roup **T**hermodata **E**urope.

tion[11] G^{ϕ} is then described by a triple-faceted expression:

$$G^{\phi} = \underbrace{\sum_{i} x_i \cdot {}^{0}G_i^{\phi}}_{{}^{\mathrm{ref}}G} + \underbrace{RT \sum_{i} x_i \ln x_i}_{{}^{\mathrm{id}}G^{\phi}} + \underbrace{x_i x_j \sum_{k=0}^{n} {}^{k}L(x_i - x_j)^k}_{{}^{\mathrm{E}}G^{\phi}} \tag{2.30}$$

${}^{\mathrm{ref}}G$ is the **reference** part corresponding to the energy amount of each i constituting element prior to mixing. ${}^{\mathrm{id}}G^{\phi}$ is the **ideal mixing** part, in that random mixing of atoms is assumed. ${}^{\mathrm{E}}G^{\phi}$ is the **excess term** part, that adjusts via its parameters the solution into the real case. For binary systems, the empirical Redlich-Kister equation[12] [45] is the most frequently used polynomial form to express it.

Redlich-Kister parameters ${}^{k}L$ are expressed with a formalism analogue to equation 2.29 but usually truncated to the first two terms:

$${}^{k}L = {}^{k}a + {}^{k}b \cdot T \tag{2.31}$$

where ${}^{k}a$ and ${}^{k}b$ are adjustable coefficients[13].

After modeling the phases follows a critical selection of available experimental data in the literature: phase diagram data (T – x, p – T, p – x) as well as thermodynamic properties data (a_i, C_p, $\Delta H^0_{298\ \mathrm{K}}$, $S^0_{298\ \mathrm{K}}$) are investigated to depict the multicomponent system.

□ Step 2: Optimization

These data are transposed into analytical expressions by an optimization program – in this study the BINGSS optimizer [32] will be used. The coefficients defining those expressions are then adjusted with the Gauss-Newton method.

In this method those coefficients, say c, are initially subjected to an approximate set of values: for each measured value $\dot{Z}_i$ is calculated a value $\tilde{Z}_i$. The difference weighted by a factor w_i is the error ε_i:

$$\varepsilon_i = w_i(\tilde{Z}_i - \dot{Z}_i) \tag{2.32}$$

This method is literally adjusting the m coefficients c_j to find the minimum value of $\sum_{i=1}^{n} \varepsilon_i^2$. In terms of derivatives it implies:

$$\frac{\partial \sum_{i=1}^{n} \varepsilon_i^2}{\partial c_j} = \sum_{i=1}^{n} \left(\varepsilon_i \frac{\partial \varepsilon_i}{\partial c_j} \right) = 0 \tag{2.33}$$

One can then expand the error ε_i into a Taylor series truncated after the linear term:

[11] Formed by random mixing of i components.

[12] Other descriptions can be applied, *e.g.* Margules [35] or van Laar [30] equations, albeit less commonly.

[13] Also referred as model parameters.

$$\varepsilon_i \approx \varepsilon_i^0 + \sum_{l=1}^{m} \left(\frac{\partial \varepsilon_i}{\partial c_l} \cdot \Delta c_l \right) \tag{2.34}$$

Inserting equation 2.34 in 2.33 leads to:

$$\sum_{l=1}^{m} \left(\sum_{i=1}^{n} \frac{\partial \varepsilon_i}{\partial c_j} \cdot \frac{\partial \varepsilon_i}{\partial c_l} \right) \Delta c_l = - \sum_{i=1}^{n} \varepsilon_i^0 \frac{\partial \varepsilon_i}{\partial c_j} \tag{2.35}$$

Equation 2.35 is a system of linear equations that can be solved for the m corrections Δc_l. The m coefficients are then adjusted into $c_j + \Delta c_l$.

This calculation is iterated until the corrections Δc_l reach a given low limit: model parameters thus take on their final shape and define the new optimized thermodynamic system.

2.2 Literature survey and data selection

The following articles already processed the optimization of the Si – P system. The phase diagrams they have modeled are available in Appendix A.

In 1985, **Olesinski et al.** [41] were the firsts to present an assessed Si – P phase diagram. The critical evaluation of the literature review is questionable, and the SiP_2 compound is not taken into account.

Tang et al. [55] then reviewed in 2009 a large number of Si – X systems in the framework of silicon purification for photovoltaic cells. **Safarian and Tangstad** [47] optimized this system after having processed to TG-DTA measurements[14]. For both of these studies, no precision is given on the optimization procedures, and only a phase diagram of the Si-rich region is shown.

Arutyunyan et al. [3] provided a partial phase diagram up to 70 at.% of phosphorus, but they did not specified the phase models used and did not considered SiP_2.

Jung and Zhang [25] as well as **Liang and Schmid-Fetzer** [31] all optimized with more details and accuracy this system, but the full potential of the literature review was not used, especially for the solubility of phosphorus in silicon $[P]_{(Si)}$.

One has therefore denoted shortcoming data and inaccuracies in these optimization articles, especially in the Si-rich region of the phase diagrams where $[P]_{(Si)}$ is intimately related to the liquid phase model, thus to the dephosphorization problematic. A comprehensive thermodynamic assessment of this system is then recommended.

In this study will only be presented the data considered necessary for the assessment. The reasons are explained all along.

[14] Not to be confused with the aforementioned article of the same authors [48].

2.2.1 Thermodynamic modeling of phases

In this first step, the objective is to choose the most accurate data for all the phases of the Si – P system and to model the parameters that describe their Gibbs free energies.

In their assessment, Liang and Schmid-Fetzer [31] relevantly selected the solid phases to be put in. In that extent the same ones are chosen; they are presented Table 2.3.

Table 2.3: Solid phases selected in the Si – P assessment

Phase	Pearson symbol	Space group	Prototype	Reference
Si_{dia}	cF8	Fd-3m	C (diamond)	[66]
P_{red}	mP84	P2/c		[57]
SiP	(orthorhombic)			[6]
	(orthorhombic)	Pnna		[70]
	oS48	$Cmc2_1$ (36)		[71]
SiP_2	oP24	Pbam	$GeAs_2$	[68]
	cP12	Pa-3	FeS_2 (pyrite)	[69]

Concerning the gas phase, Si, Si_2, Si_3, P, P_2 and P_4 are the known molecules considered according to the JANAF tables [11].

With this framework set out, Gibbs free energy of phases G^ϕ shall be modeled[15].

Pure elements and gas phases

The Gibbs free energy of pure elements are all extracted from the SGTE database [13]. Their formalism (given in equation 2.29) is used to describe on the one hand silicon in the diamond configuration, and on the other hand red phosphorus, its most stable allotropic form.

The gas phases are modeled by using data from JANAF tables [11]. They provide enthalpy of formation $\Delta_f H^0_{298\text{ K}}$, entropy $S^0_{298\text{ K}}$ as well as heat capacity C_p^0 for different given temperatures.

In the first place, C_p^0 is fitted in the form of equation 2.26. The Gibbs free energy of phase ϕ is then deduced from:

$$G^\phi = \Delta_f H^0_{298\text{ K}} + \int_{298\text{ K}}^{T} C_p dT - T\left(S^0_{298\text{ K}} + \int_{298\text{ K}}^{T} \frac{C_p}{T} dT\right) \tag{2.36}$$

The results respect the SGTE formalism, and are reported in Table 2.4.

[15] In the following parts G^ϕ is actually an abbreviation of $G^\phi(T) - {}^{\text{ref}}G(T)$.

Table 2.4: Phase models selected in the present work

Phase ϕ	G^ϕ [J.mol^{-1}]	T range [K]	Reference
Si_{dia}	$-8162.609 + 137.236859 \cdot T - 22.8317533 \cdot T \cdot \ln T - 1.912904 \cdot 10^{-3} \cdot T^2 - 0.003552 \cdot 10^{-6} \cdot T^3 + 176667 \cdot T^{-1}$	298.15 – 1687	[13]
	$-9457.642+167.281367 \cdot T-27.196 \cdot T \cdot \ln T-420.369 \cdot 10^{28} \cdot T^{-9}$	1687 – 3000	
$Si_{(l)}$	$42533.751+107.13742 \cdot T-22.8317533 \cdot T \cdot \ln T-1.912904 \cdot 10^{-3} \cdot T^2 - 0.003552 \cdot 10^{-6} \cdot T^3 + 176667 \cdot T^{-1} + 209.307 \cdot 10^{-23} \cdot T^7$	298.15 – 1687	[13]
	$40370.523 + 137.722298 \cdot T - 27.196 \cdot T \cdot \ln T$	1687 – 3000	
$Si_{(g)}$	$444502.7 - 33.3040 \cdot T - 20.2698 \cdot T \cdot \ln T - 2.30 \cdot 10^{-4} \cdot T^2 - 8.4647 \cdot 10^4 \cdot T^{-1} - 2.43845 \cdot 10^{-8} \cdot T^3$	200 – 3000	[11]
$Si_{2(g)}$	$575170.2 - 45.5463 \cdot T - 40.6715 \cdot T \cdot \ln T - 1.87 \cdot 10^{-3} \cdot T^2 + 3.65 \cdot 10^5 \cdot T^{-1} + 1.94 \cdot 10^{-7} \cdot T^3$	200 – 3000	[11]
$Si_{3(g)}$	$615338.3 + 152.968 \cdot T - 62.2584 \cdot T \cdot \ln T - 4.64 \cdot 10^{-4} \cdot T^2 + 3.18 \cdot 10^5 \cdot T^{-1} - 1.10 \cdot 10^{-7} \cdot T^3$	200 – 3000	[11]
P_{red}	$-25976.559 + 148.672002 \cdot T - 25.55 \cdot T \cdot \ln T + 3.4121 \cdot 10{-}3 \cdot T^2 - 2.418867 \cdot 10^{-6} \cdot T^3 + 160095 \cdot T^{-1}$	250 – 500	[13]
	$-21723.721 + 77.671737 \cdot T - 14.368 \cdot T \cdot \ln T - 9.57685 \cdot 10^{-3} \cdot T^2 + 0.393917 \cdot 10^{-6} \cdot T^3 - 141375 \cdot T^{-1}$	500 – 852.35	
	$-119408.413+1026.02962 \cdot T-149.4495562 \cdot T \cdot \ln T+67.272364 \cdot 10^{-3} \cdot T^2 - 6.651929 \cdot 10^{-6} \cdot T^3 + 12495943 \cdot T^{-1}$	852.35 – 1500	
	$-24524.119 + 153.839181 \cdot T - 26.326 \cdot T \cdot \ln T$	1500 – 3000	
$P_{(l)}$	$-26316.111 + 434.930931 \cdot T - 70.7440584 \cdot T \cdot \ln T - 2.898936 \cdot 10^{-3} \cdot T^2 + 39.049371 \cdot 10^{-6} \cdot T^3 + 1141147 \cdot T^{-1}$	250 – 317.3	[13]
	$-7232.449 + 133.291873 \cdot T - 26.326 \cdot T \cdot \ln T$	317.3 – 3000	
$P_{(g)}$	$309735.164 - 15.507 \cdot T - 21.907 \cdot T \cdot \ln T + 9.84 \cdot 10^{-4} \cdot T^2 + 3.03 \cdot 10^4 \cdot T^{-1} - 1.37 \cdot 10^{-7} \cdot T^3$	298.15 – 3000	[11]
$P_{2(g)}$	$131663.290 - 22.300 \cdot T - 35.657 \cdot T \cdot \ln T - 8.74 \cdot 10^{-4} \cdot T^2 + 1.91 \cdot 10^5 \cdot T^{-1} + 5.55 \cdot 10^{-8} \cdot T^3$	298.15 – 3000	[11]
$P_{4(g)}$	$30280.593 + 269.731 \cdot T - 81.068 \cdot T \cdot \ln T - 9.10 \cdot 10^{-4} \cdot T^2 + 6.52 \cdot 10^5 \cdot T^{-1} + 6.65 \cdot 10^{-8} \cdot T^3$	298.15 – 3000	[11]
$SiP_{(s)}$	$-76850.9 + 218.60 \cdot T - 37.80 \cdot T \cdot \ln T - 0.00510 \cdot T^2 + 2.67 \cdot 10^5 \cdot T^{-1} - 7.25 \cdot 10^{-7} \cdot T^3$	298.15 – 3000	[11, 44]
$SiP_{2(s)}$	$-108689+411.2 \cdot T-71 \cdot T \cdot \ln T+4.56 \cdot 10^5 \cdot T^{-1}-3.45 \cdot 10^{-6} \cdot T^3$	298.15 – 3000	[11, 44]

Solution phases

For the liquid phase, the regular model of equation 2.30 is initially adopted. In this case:

$$G^\phi = x_{Si} \cdot {}^0G^\phi_{Si} + x_P \cdot {}^0G^\phi_P + RT(x_{Si} \cdot \ln x_{Si} + x_P \cdot \ln x_P) + x_{Si}x_P \left[{}^0L^\phi + {}^1L^\phi(x_P - x_{Si})\right] \tag{2.37}$$

where G^ϕ represents the Gibbs free energy of liquid phase[16], ${}^0G^\phi_{Si}$, ${}^0G^\phi_P$ are the Gibbs free energies of the pure elements in their reference state, and ${}^0L^\phi$, ${}^1L^\phi$ are the

[16]The stable element reference (SER) is used as the reference state, so G^ϕ is an abbreviation of the difference $G^\phi(T) - \sum_{i=1}^{n} H_i^{\mathrm{SER}}(298\ \mathrm{K})$

Redlich-Kister parameters representing the interaction between those two elements.

Those parameters, fitted by the Gauss-Newton method, are:

$$\begin{aligned} {}^0L^{(l)} &= -20801.04 + 4.1172 \cdot T \\ {}^1L^{(l)} &= 13982.31 - 2.7877 \cdot T \\ \\ {}^0L^{(\mathrm{Si})} &= -40498.48 + 21.8079 \cdot T \end{aligned} \tag{2.38}$$

where ${}^0L^{(l)}$ and ${}^1L^{(l)}$ are the Redlich-Kister interaction coefficients describing the liquid phase and ${}^0L^{(\mathrm{Si})}$ the Si solid phase containing dissolved P.

Compounds

For the stoichiometric compounds SiP and SiP_2, $\Delta_f H^0_{298\ \mathrm{K}}$ and $S^0_{298\ \mathrm{K}}$ given by Philipp and Schmidt [44] are used to calculate G^ϕ. The indicated C^0_p are however not recommended: instead, the empirical additivity rule of Neumann-Kopp will be applied. This choice will be more thoroughly discussed in section 2.2.5.

All the phases are now correctly modeled for the Si – P system. The next step is then to review the experimental literature in that respect. Phase equilibrium data related to T, p and x will be discussed in the first place.

2.2.2 $T - x$ diagram data

This section includes the review of classic phase equilibrium data that encompasses the whole range of composition, but also a detailed study in the Si-rich region of the solubility of phosphorus in silicon which has remained unsolved by the previous works.

a. Phase equilibrium data

Three articles were found to have relevant experimental data concerning general $T - x$ values, briefly summarized in Table 2.5.

Table 2.5: Summary of the $T - x$ phase equilibrium data in the Si – P system

First author	Method	T range [K]	x_P range [at.%]
Giessen [1959]	Thermal analysis Metallography	1400 – 1823	0 – 60
Ugai [1987]	Static manometric	1398 – 1450	40 – 77
Safarian [2011]	TG-DTA	1235 – 1684	0 – 6

The first one is from **Giessen and Vogel** [17] who plotted the Si – P diagram by thermal analysis. The SiP compound was observed by microscopic characterization

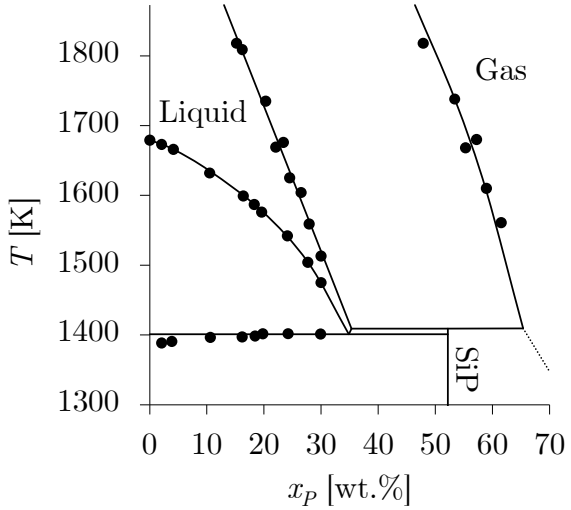

Figure 2.6: Reproduction of the experimental data observed by Giessen and Vogel [17]

and an eutectic is found to be at 1404 ± 2 K from 0 up to 35 ± 3% of phosphorus. A representation of their observed values is given Figure 2.6.

Their condensation line has been questioned by Jung, Zhang [25], Liang and Schmid-Fetzer [17]. The concerned experimental points have been assessed with a method relying on the lever rule. Its inaccuracy is due to the fact that for the atmospheric pressure, observing fumes relative to phosphorus with the naked eye is not systematically an evidence that evaporation line has been crossed. P can evaporate even below $p_P = 0.5$ bar.

Ugai et al. [64] are the next ones to assess $T - x$ equilibrium data[17] (Figure 2.7). By DTA analysis with control of the vapour pressure, they investigated the $T - x$ and

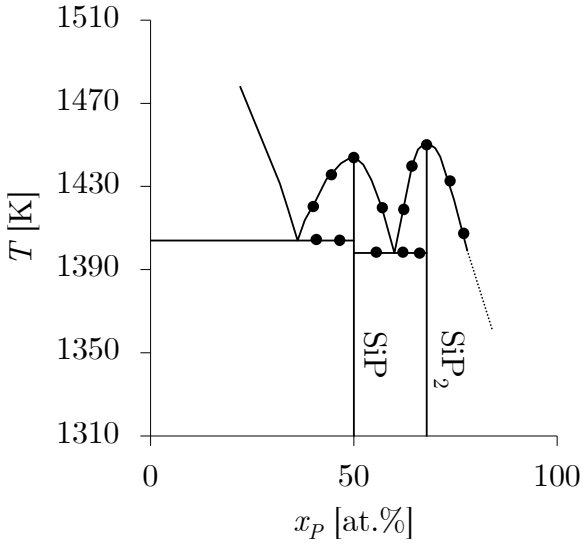

Figure 2.7: Reproduction of the experimental data observed by Ugai et al. [64]

[17] As a first author Ugai contributed in four other articles on Si – P [61–63, 65] not to be confused with.

$p - T$ diagrams of the Si – P system, and deduced the $p - x$ diagram. This special apparatus is described in a reference of his previous work [61]. The experiment is assumed to be operated beyond 10^{-4} bar (the so-called Knudsen limit) so that a mechanical equilibrium approach can be applied rather than a flow equilibrium approach.

The standard DTA study pertaining to the $T - x$ diagram is ranging from 50 to 75 at.% of phosphorus, and is performed by heating up to 1453 K a SiP sample with a high purity phosphorus, annealing it as so during 15 h and then cooling it down. Thereafter they only exploited the heating data because the melt considerably undercooled for the high phosphorus contents.

The thermal effects – eutectic, liquidus – are assumed to be measured without a phosphorus condensation, otherwise the composition of the sample would have evolved. They identified two eutectic lines: one between Si and SiP at 1404 K, and another between SiP and SiP_2 at 1398 K.

Concerning their measuring accuracy, no information is given about the exact position of the different thermocouples relative to the points they measure; in addition their calculation procedure is quite unclear. For all these reasons their interpretations are not considered here.

At last, **Safarian and Tangstad** [47] recently realized DTA and TGA experiments in open graphite crucibles with an atmospheric pressure of argon (1 bar, 20 mL.min^{-1}). Solidus and liquidus temperatures are fitted as so:

$$\begin{aligned} \forall x_P \in [0.35; 1 \text{ wt.\%}] \quad & T_S = -75.03 \cdot x_P + 1687 \\ \forall x_P < 6 \text{ wt.\%} \quad & T_L = -6.74 \cdot x_P + 1687 \end{aligned} \tag{2.39}$$

SiP dissociation (1304 ± 30 K) and melting temperature (1412 ± 2 K) are also provided. The latter corresponds to the decomposition under 1 atm at 1413 K of

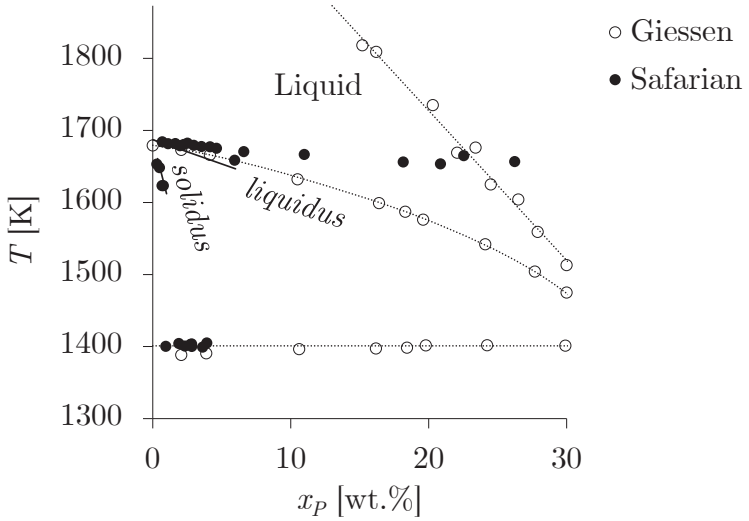

Figure 2.8: Reproduction of the experimental data observed by Safarian and Tangstad [47] (depicted in black). They compared it to those of Giessen and Vogel [17] in white dots and dashed lines.

Giessen and Vogel, while Ugai et al. observed 1440 K under pressure. They also indicate an eutectic temperature of 1402 ± 2 K, very close to the 1404 K of Giessen and Vogel. They diagram is reproduced in Figure 2.8 and is compared to the one of Giessen and Vogel [17].

b. Solubility data

In the Si-rich region of the phase diagram is identified a pending issue that is the solubility of phosphorus in silicon $[P]_{(Si)}$. The experimental data analyses made from the previous compilation works [3, 31, 41, 47, 55] were indeed either unspecified or questionable as it will be discussed in section 2.3.2.

A host of authors studied $[P]_{(Si)}$ via diffusion or implantation processes. An investigation has been done whereupon disparate interpretations of results emerged from those very authors.

In the profusion of articles analyzed (see Table 2.6), three main groups of studies were identified: (I) the Bell Laboratory (New Jersey) [14, 34, 56, 58, 59], (II) the Laboratorio Lamel (Bologna) [10, 15, 36, 39, 40, 42, 52] and (III) the Hitachi Central Research Laboratory (Tokyo) [23, 38, 53, 54, 67]. Apart from those groups naturally exist other unassociated studies [1, 8, 16, 24, 27, 47, 49, 50, 60, 73].

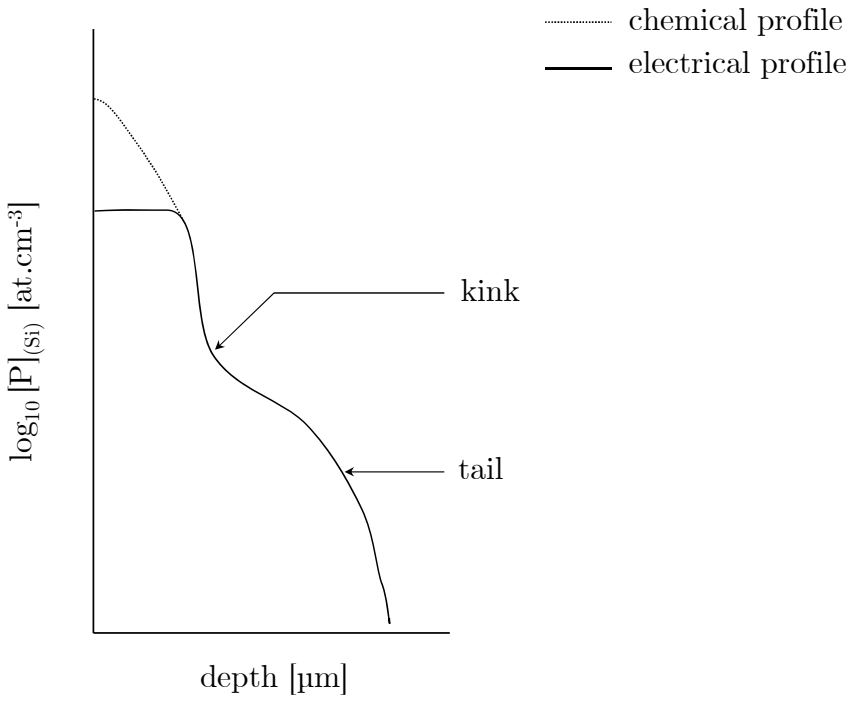

Figure 2.9: Schematic phosphorus diffusion profile observed in the literature.

From all these studies, a simplified diffusion profile of phosphorus can be represented (Figure 2.9). It has generally three particular characteristics: (1) a plateau region alongside the surface, (2) a kink located at concentrations increasing with

Table 2.6: Summary of the solubility data in the Si – P system. The abbreviated terms are explained in the nomenclature and all along the text.

First author		Preparation	Measurement	Characterization
Trumbore [1960]	(I)	Diffusion		
Tannenbaum [1961]	(I)	Diffusion	NAA SR	
Abrikosov [1962]		Isopiestic	MH	OM
Mackintosh [1962]	(I)	Diffusion	SR	
Kooi [1964]		Diffusion	NAA	
Schmidt [1964]		Diffusion	NAA SR	TEM XRD
Joshi [1966]		Diffusion	NAA SR	TEM
Tsai [1969]	(I)	Diffusion	SR	
Schwettmann [1971]		Diffusion	SR	
Yoshida [1974]		Diffusion	NAA SR	
Mousty [1974]	(II)	P^+ implantation	NAA SR HE	TEM XRT
Ostoja [1976]	(II)	Pulsed laser	SR	TEM
Fair [1977]	(I)	Diffusion	NAA SR	SIMS DC
Masetti [1977]	(II)	Diffusion	NAA SR HE	TEM XRT
Uda [1977]		P^+ implantation	SR	XRD EBSD
Tamura [1977]	(III)	Diffusion P^+ implantation	SR	TEM
Sunami [1978]	(III)	Diffusion P^+ implantation	SR	TEM
Wada [1978]	(III)	P^+ implantation	HE	TEM
Fogarassy [1980]		Diffusion Pulsed laser	SR HE	SIMS RBS
Miyao [1980]	(III)	P^+ implantation Pulsed laser	SR HE	TEM PL
Finetti [1981]	(II)	P^+ implantation Pulsed laser	SR HE	TEM RBS
Itoh [1982]	(III)	P^+ implantation Pulsed laser	SR HE	TEM
Nobili [1982]	(II)	P^+ implantation Pulsed laser	SR HE	TEM RBS
Borisenko [1987]		P^+ implantation Pulsed laser	HE	
Solmi [1996]	(II)	P^+ implantation	SR HE	TEM SNMS
Safarian [2011]				TG-DTA

predeposition temperature and (3) a tail in the distance. The dashed line is the chemical profile typically obtained by neutron activation analysis (NAA), evaluating by nature the total phosphorus amount. The solid line is the electrical profile obtained by sheet resistivity (SR) or Hall effect (HE) measurements: only the electrically active[18] phosphorus can be detected.

To determine the phosphorus profiles, some authors ([24, 50, 54, 56, 59, 73]) used the standard curves of Irvin [22] of resistivity (Ω.cm) versus impurity concentration (at.cm^{-3}). Based upon measurements in As, P and Sb doped silicon for n-type and Al, B and Ga for p-type, these curves help to convert differential conductivity measurements into the profiles. Two flaws of theirs are identified: the authors assign 10 % of inaccuracy regarding the various dopants included for a single curve; moreover beyond 10^{20} at.cm^{-3} (0.2 at.%) the resistivity data are overestimated. Mousty et al. [39] indeed noticed this difference can be up to 30 % for an impurity concentration of $1 \cdot 10^{20}$ at.cm^{-3}. They recreated the experiments only for P up to this latter concentration value. As a consequence, all the identified authors relying their procedures on Irvin work will have their values lowered in this study as later explained.

In the diffusion or implantation profiles, phosphorus concentration is commonly given in at.cm^{-3} (say X_P). The conversion into atomic percentage x_P is as follows:

$$x_P = X_P \frac{M_{Si} \cdot 10^6}{\mathcal{N}_A \rho_{Si}} \tag{2.40}$$

where M_{Si} is the atomic mass of silicon in kg.mol^{-1}, $\rho_{Si} = 2310$ kg.m^{-3} its density [20] and $\mathcal{N}_A$ the Avogadro number.

The main topic of experimenters disagreement is about the nature of electrically inactive phosphorus, and *a fortiori* if it still should be accounted as a silicon solute. Beyond a certain concentration limit, the excess phosphorus – until then active – turns inactive: some explain it precipitates into SiP, others assert it pairs with doubly charged vacancies.

To disentangle the reflexions from the various parties, the collected solubility limit literature is investigated chronologically.

In 1960, **Trumbore** [58] is the first author to mention $[P]_{(Si)}$. He actually compiled different impurities solubilities for silicon and germanium: the results come from a hitherto unpublished article from his colleague **Mackintosh** [34]. By their own admission, their high values may not be truly relevant as P_2O_5 and SiO_2 are involved in the thermal diffusions; a ternary Si – O – P would be a more appropriate system to depict their high values. This is the first evidence of the influence of oxygen on the Si – P system.

From the same laboratory, **Tannenbaum** [56] evaluated phosphorus diffusion experiments by NAA and SR measurements. The respectively resulting radio-tracer

[18] *i.e.* in terms of electrical conduction. Diluted phosphorus in silicon can either be active or inactive, while precipitated phosphorus is only inactive.

and resistivity profiles are significantly different for high concentrations. As a consequence she introduced the notion of electrically active and inactive phosphorus, and proposed two hypotheses: either SiP precipitates are responsible for the inactive P, or electron mobility decreases; however she favored the first one.

Abrikosov et al. [1] carried out an original procedure as they performed microhardness tests on bulk doped silicon and subsequently analyzed the samples structure under a microscope. They related the microhardness of the grains of solid solutions to the alloys composition for different temperatures. This technique seems reliable albeit poorly sensitive. A doubt is raised though on the two hottest points of their five values: phosphorus could possibly evaporate at those temperatures, considering that the chemical compositions are given before the microhardness tests, and the atmosphere – not described – could react with it. A greater uncertainty will thus be applied for those points.

Kooi [27] performed NAA on diffusion experiments, but as for Mackintosh the P_2O_5 source for predeposition skews the results, therefore those should be discarded.

Schmidt and Stickler [49] are the firsts to observe SiP precipitates on phosphorus diffused silicon. From their XRD and TEM examinations they found rod-shaped particles of about 1 µm and oriented along $< 110 >$ directions, but no diffusion profiles can be exploited.

NAA and SR measurements have also been done by **Joshi and Dash** [24] on phosphorus diffusion measurements, and analyzed the samples on TEM. No details are given on the experimental procedure, and the plateau obtained is depicted by only three measurements. A large uncertainty range will thus be applied.

In 1969, **Tsai** [59] used a $POCl_3$ source to realize diffusion profiles with SR measurements, and so did **Schwettmann and Kendall** [50] two years later for more temperatures set. The latter also studied concentration impact on the kinks and tails of the profiles [51], and suggested that the mechanism of kink formation was a diffusion of neutral and negatively charged E centers, *i.e.* phosphorus-vacancy pairs. One will not dwell further on this point defects theory: as it will be ulteriorly explained, it will be disproved [40, 52] as characterization methods are upgraded.

This very theory is nonetheless deepened by **Yoshida et al.** [73] who analyzed profiles of phosphorus concentration obtained by SR and NAA. However they did not compare their model in a quantitative way with experimental results. At 1173 K is given a concentration profile: the selected solubility is not the average surface value between the chemical and electrical profiles, but lower from the SR plateau.

From the Laboratorio Lamel, **Mousty et al.** [39] appear to be the firsts in a long list to use phosphorus ion implantation in silicon as a preparation method. The samples underwent SR and HE measurements, were analyzed by neutron activation and observed by TEM and X-ray topography (XRT).

Ostoja, who contributed to this previous work, was the first author of another study [42]. They did isochronal annealing by pulsed laser of n-type silicon samples up to 923 K and measured concentration profiles by SR. SiP precipitates of 0.2 µm were observed by TEM. They experimentally obtained an average of ten values at 923 K and extrapolated the result to 823 K, thus only the first raw data will be considered.

Fair and Tsai [14] used secondary ion mass spectrometry (SIMS) calibrated with NAA on diffused samples to determine total (active and inactive) phosphorus profiles. They also obtained active P^+ profiles from differential conductivity (DC) measurements. The surface phosphorus concentrations they indicate for different temperatures seem reliable, however the model of phosphorus diffusion in silicon they proposed joins the one of Schwettmann, Kendall, and Yoshida et al.

Masetti et al. [36] predeposited $POCl_3$ on silicon and carried out NAA, SR and HE measurements. The obtained values seem accurate as averaged for each by eight determinations. They could confirm by TEM and XRT the precipitation of SiP accompanying their predepositions. In their electrical profiles, they found that the plateau is defined by a concentration of charge carriers similar to the one in equilibrium with SiP, and that precipitation does not influence the kink.

Uda and Kamoshida [60] observed P^+ implanted silicon samples by XRD and electron backscatter diffraction (EBSD). No specific details are given on the annealing procedure of the only experiment at 1373 K; it will not therefore be retained.

From the Hitachi laboratory, **Tamura** [54] measured SR concomitantly on diffused (with $POCl_3$) and implanted samples, and observed the defects by TEM. One phosphorus solubility at 1373 K can be extracted from his work at dry N_2 atmosphere. Yet, the downward parabola shape of the corresponding implantation profile is problematic: it indicates in all likelihood that saturation has not been reached. Its range of uncertainty will be expanded in such an extent that it meets the maximum solubility limit observed.

The next year two articles from his colleagues were published: **Wada and Nishimatsu** [67] investigated the grain growth phenomena of P^+ implanted silicon with TEM and measured SR. They extracted from **Sunami** [53] $[P]_{(Si)}$ data and compared it with others, but these values cannot be taken into account as samples were heavily oxidized.

In 1980 **Fogarassy et al.** [16] submitted silicon doped by thermal diffusion to laser irradiation and used HE, SR measurements, SIMS and Rutherford backscattering spectrometry (RBS). The same profile shape as that of Tamura is observed, implying the same precaution on uncertainty.

Miyao et al. [38] saturated solutions by implanting P^+ in silicon, using pulse laser and furnace annealing. At 873 K two concentration profiles after annealing are given. One is slightly supersaturated, the other undersaturated: their mean value is decided to be used, and its uncertainty delimited by those raw points. They also confirmed by TEM the presence of SiP precipitated phase to be associated with the inactive phosphorus.

In the same vein, **Finetti et al.** [15] and **Itoh et al.** [23] both worked on supersaturated solutions with similar experimental designs, however no data seemed relevant to the $[P]_{(Si)}$ evaluation.

Up to now uncertainty remained concerning the interpretation of inactive P atoms. The publication of **Nobili et al.** [40] clarifies this problem in a detailed review of the past literature. For their samples doped by ion implantation and laser annealed, they asserted by means of TEM observations that $[P]_{(Si)}$ corresponds to the

electrically active P and that inactive P shall not be considered as dissolved in silicon, but rather as SiP precipitates[19]. Yet, this interpretation could not establish itself as the correct one so far. Firstly because the plateau of the profile commonly obtained was slightly sloping: they established that precipitation significantly enhance the phosphorus diffusivity. Secondly, the amount of SiP observed by characterization techniques seemed lesser than the inactive dopant. They succeeded in observing small but very dense coherent particles: those probably could not be detected by the previous and older TEM or RBS techniques.

Borisenko and Yudin [8] compiled $[P]_{(Si)}$ articles among other impurity elements. They also laser annealed ion implanted silicon and measured HE, but no carrier concentration profiles are provided; instead they simply assured those are similar to Nobili et al. profiles.

In 1996 **Solmi et al.** [52] heavily implanted phosphorus in silicon and investigated different anneals by TEM and secondary neutral mass spectrometry (SNMS). The focus in their work is on the thermal equilibration of their doped samples with SiP precipitates. The obtained phosphorus profiles consist of a high concentration region that corresponds to precipitates, and after a kink is a slight downward slope followed by a small tail. The previous thermodynamic optimizers have selected the saturated values from the kink (C_{sat} in the text), not the equilibrium carrier concentration (n_e) from the slope-tail limit. Actually the existence of the slope suggests that SiP residuals are present from one end to the other; therefore their n_e values are here retained.

Finally, the TG-DTA experiments of **Safarian and Tangstad** previously mentioned are partially used. The eutectic observed gives the value of the maximum solubility limit at 0.94 at.% of phosphorus, but the solidus values are not selected. It is noteworthy that the concentration value at 1474 K of Borisenko and Yudin on the solidus line contradicts their findings.

The retained data are used as such in the optimization program, except for the authors that worked with Irvin's curves for studying $[P]_{(Si)}$ ([24, 50, 54, 56, 59, 73]). Mousty et al. [39] found that overestimations of 30% can be achieved up to $1 \cdot 10^{20}$ at.cm^{-3} which is their observation limit. An extrapolation beyond this value is performed to address an uncertainty estimation: for instance, an experimental value composition with a difference of 45% between Mousty and Irvin's curves will induce a lowering of 30% and an uncertainty of $\pm$ 15%.

In Figure 2.10 are represented the final selected $[P]_{(Si)}$ data points. The already shortened range of composition (0 to 1.0 at.%) should be underlined. A decent correlation is evidenced along the solvus line. Regrettably, however, almost no data can sharpen the solidus modeling: the high temperatures complicate the experimental measurements.

[19]Formation of P_2 clusters around Si can be excluded: the Wagner interaction coefficient ε_P^P is positive as it is ulteriorly demonstrated (equation 3.49).

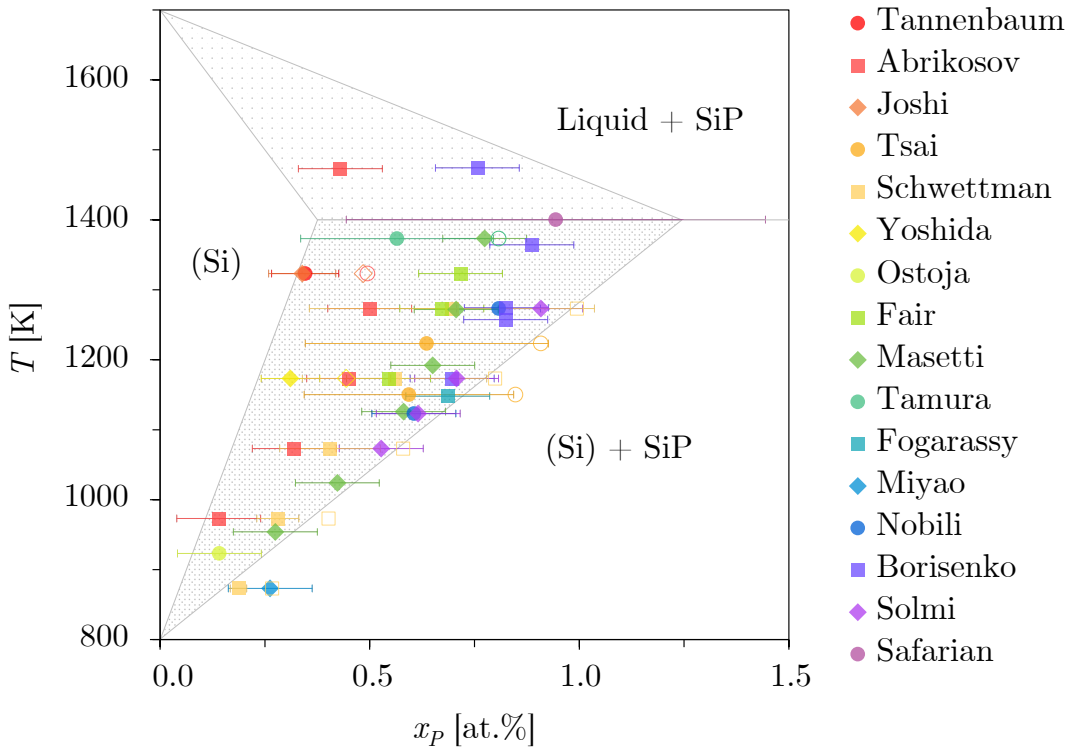

Figure 2.10: Experimental data of solubility limits observed by numerous authors. Contoured shape data points are original obsolete results based on Irvin resistivity curves [22]. Before any optimization, the dotted and the dashed areas are a guess of respectively the solidus and solvus lines locations.

2.2.3 $p - T$ diagram data

Although the pressure dependence is neglected for describing the system in Lukas programs, $p - T$ data (Table 2.7) are gathered to extract successively: partial pressures, activities, and ultimately chemical potential *i.e.* partial molar Gibbs free energies. This latter property is the one to be inserted in the assessment.

Table 2.7: Summary of the $p - T$ data in the Si – P system

First author	Method	T range [K]	p range [bar]
Biltz [1938]	Spiral manometer	1273 – 1413	0.08 – 1
Korb [1976]	Bourdon manometer	1173 – 1373	0.01 – 0.4
(1) Ugai [1981]	DTA under controlled p	1410 – 1439	0.4 – 3.5
(2) Ugai [1987]	Static manometric DTA under controlled p	1410 – 1450	0.4 – 43.3
(3) Ugai [1987]	Bourdon manometer	1345 – 1470	0.3 – 2.7

Biltz [7] wrote an article in 1938 that seems to be the oldest reliable thermodynamic study of this system. He designed the experiment similarly to the Faraday experiment for obtaining liquid chlorine. A vessel with a manometer is unevenly heated: the upper part is hotter and contains the crystallized sample of SiP, while the lower part can contain the resulting gas. The ratio of the two temperatures and the cooling time are adjusted so that the vapour pressure of the gaseous phase does not drop below the dissociation pressure of SiP. The formation of stoichiometric SiP is occurring by heating on one side of the quartz tube a ceramic crucible containing crystallized silicon at 1273 K and on the other side 99.7% purity P_{red} at 673 K. The thermal dissociation of SiP occurs at 1413 K for a total pressure of 1 atm.

The quartz spiral manometer operates in the same manner as a Bourdon manometer: when the vapour phase enters the spiral, its pressure unwinds the spiral connected via a gear mechanism to the pointer. The advantage of this apparatus is that the multiple turns allow a greater sensibility of the measure.

Table 2.8: Decomposition pressures of Biltz original work [7]. The bold values are the result of conversions into more relevant units for the study.

p		T		P/Si ratio	x_P
[mmHg]	**[bar]**	[°C]	**[K]**		**[at.%]**
64	**0.085**	1008	**1281**		
67	**0.089**	1010	**1283**		
162	**0.216**	1055	**1328**		
211	**0.281**	1068	**1341**	0.7	**0.412**
275	**0.367**	1084	**1357**		
289	**0.385**	1101	**1374**		
760	**1.014**	1140	**1413**		

The total pressure of the system is collected for seven temperatures given in Table 2.8. It shows a linear response as so:

$$\log_{10} p = -\frac{14672.4}{T} + 13.2601 \tag{2.41}$$

Other data from Biltz assimilated to a $p - x$ diagram will be discussed in the next section.

Korb and Hein [29] performed vapour pressure tests in the Zn – Si – P system. They present the results in three parts: the monophosphide SiP, the zinc phosphide Zn_3P_2 and the zinc silicon phosphide $ZnSiP_2$. The first part describes the dissociation pressure of SiP in the 1173 – 1373 K range. As a matter of fact, the monophosphide has a composition of $SiP_{0.8-0.9}$ so the data concerns the Si/SiP/gas three-phase equilibrium.

Their experimental apparatus consists of a Bourdon manometer connected through a pressure compensation system to a high vacuum pump working at $1.3 \cdot 10^{-2}$ mbar. Whenever the total pressure exceeds 0.96 bar, argon gas is injected in the system.

The equilibrium pressure of the sample is reached after an annealing time of 10 to 12 h. They measured the total pressure for seven different temperatures. No table of values is provided, only a graph reproduced Figure 2.11.

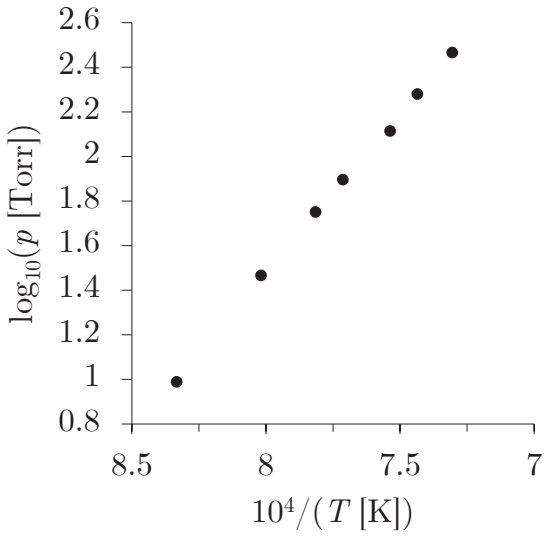

Figure 2.11: Reproduction of the dissociation pressure measurements from Korb and Hein work [29]. Equation 2.42 is applied for the fit.

The corresponding fit is as follows:

$$\log_{10} p = -\frac{13879.5}{T} + 12.5724 \tag{2.42}$$

For the dissociation reaction $\mathrm{SiP}_{(s)} \rightleftharpoons \mathrm{Si}_{(s)} + \frac{1}{4}\mathrm{P}_{4_{(g)}}$ the dissociation constant they calculate is:

$$\log_{10} K_d = -\frac{3714.75}{T} + 2.533 \tag{2.43}$$

Ugai published with different other co-authors a series of studies in the scope of the $p - T$ diagram [63–65].

In a first article from 1981 [65], they did DTA measurements under different neutral gas pressures to assess SiP decomposition. The maximum temperature corresponds to the congruent melting point of SiP and is observed at 1439 ± 5 K for 2.5 bar. The minimum temperature corresponds to the eutectic between Si and SiP and is guessed by extrapolation at about 1400 K for 0.944 bar according to their original graph. This latter is reproduced in Figure 2.12.

In the $p - T - x$ article already mentioned [64], Ugai et al. described their DTA measurements with control of the vapour pressure by heating presumably the same way a single-crystal silicon of semiconductor purity as for $T - x$ (Figure 2.13).

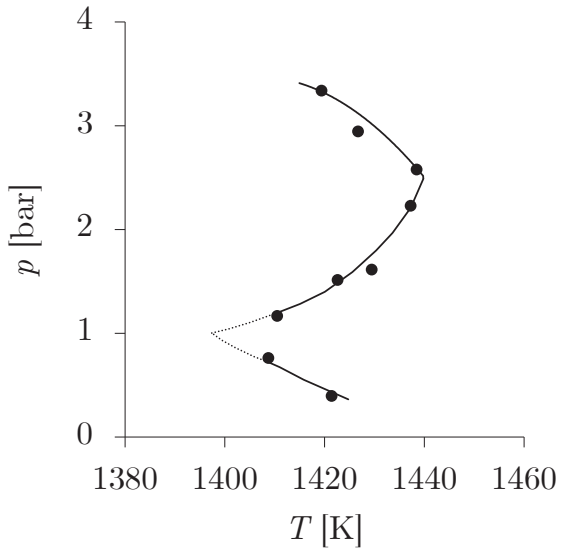

Figure 2.12: Reproduction of the three-phase equilibrium line of Ugai et al. [65] in the region of existence of SiP

The temperature at the top of the bulb decreases until the volatile phosphorus condensates, then from this cold spot it increases to evaporate.

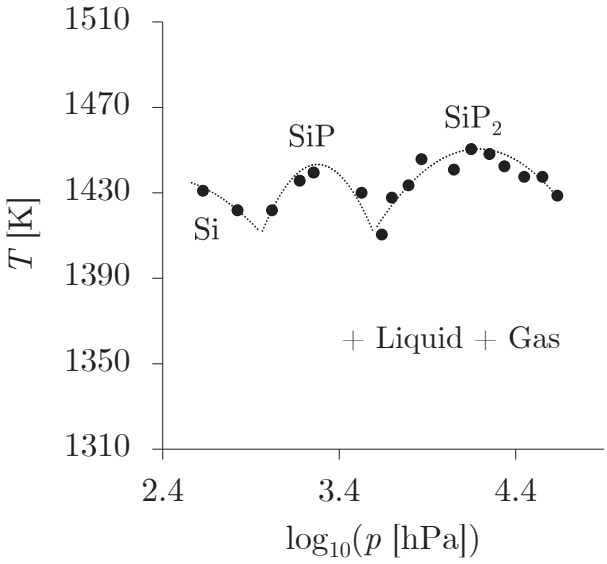

Figure 2.13: Reproduction of the experimental data observed by Ugai et al. [64].

In a third paper [63] Ugai et al. measured the static dissociation pressure of SiP by using a Bourdon manometer (Figure 2.14). The membrane has a sensibility of $\pm$ 1330 Pa per 1 mm, which means that the absolute precision of the results is 1330 Pa. The relative one is said to be $\pm$ 0.4%.

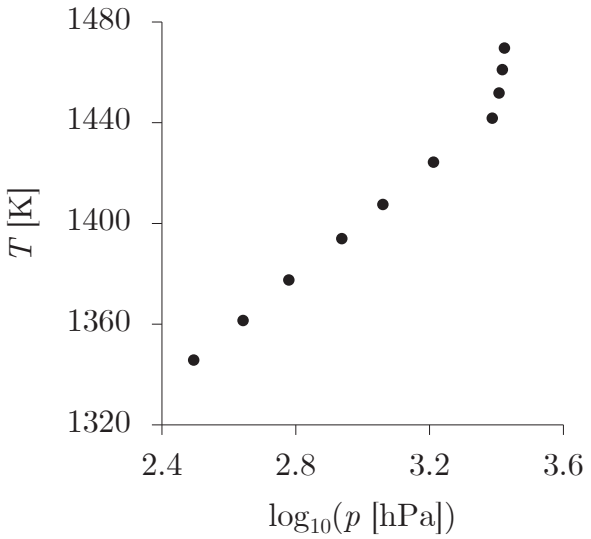

Figure 2.14: Reproduction of the temperature dependence of the vapour pressure of SiP from Ugai et al. work [63]

Single crystals ingots [61] of stoichiometric SiP are grounded into powder. Each experimental point is the result of a 4 – 6 h annealing period to reach equilibrium, and heating-cooling cycles are realized to find out if the pressures obtained are the same. They did not answer this question, nor have they specified if their experimental points are average results or a selection between the heating and the cooling step.

According to the authors, the major error is due to the relative precision of the pressure. In the present study, calculations include also the absolute precision of the pressure: this latter appears to be non negligible.

As their calculated table values seem to be wrong, they are discarded.

Exploitation of results

Partial pressures of gas species, phosphorus activity and ultimately partial Gibbs free energy of phosphorus will now be deduced from this set of articles, in order to store the latter values in the program. Here is approximated that the total phosphorus pressure p consists solely of $P_{2(g)}$ and $P_{4(g)}$:

$$p = p_{P_2} + p_{P_4} \tag{2.44}$$

Determining p_{P_2} and p_{P_4} from the total pressure is possible by considering the dissociation reaction $P_{4(g)} = 2P_{2(g)}$. The associated dissociation constant K_d is:

$$K_d = \frac{p_{P_2}^2}{p_{P_4}} \tag{2.45}$$

Depending only on the temperature, its value is fitted from the JANAF tables

including formation constants K_f of $P_{2(g)}$ and $P_{4(g)}$. By combining equation 2.44 and 2.45 arises the following second degree equation:

$$p_{P_2}^2 + K_d p_{P_2} - K_d p = 0 \tag{2.46}$$

Solving it gives the partial pressure of $P_{2(g)}$:

$$p_{P_2} = \frac{-K_d + \sqrt{K_d^2 + 4K_d p}}{2} \tag{2.47}$$

From equation 2.45 is then deduced p_{P_4}. Those partial pressures are fitted with linear functions, given in Table 2.9.

Table 2.9: Linear fitting values of dissociation pressures $\log_{10} p = A + B \times \frac{10000}{T}$

First authors	$\boldsymbol{T}$ **range [K]**	$\log_{10} p_{P_2}$		$\log_{10} p_{P_4}$	
		A	**B**	**A**	**B**
Biltz	1281 – 1413	8.95640	-1.32332	10.2581	-1.48903
Korb	1200 – 1369	9.02121	-1.33633	10.3842	-1.51458
Ugai	1345 – 1424	10.6537	-1.54956	0.80377	-0.08522
	1442 – 1470	4.21499	-0.61958	13.6811	-1.94518

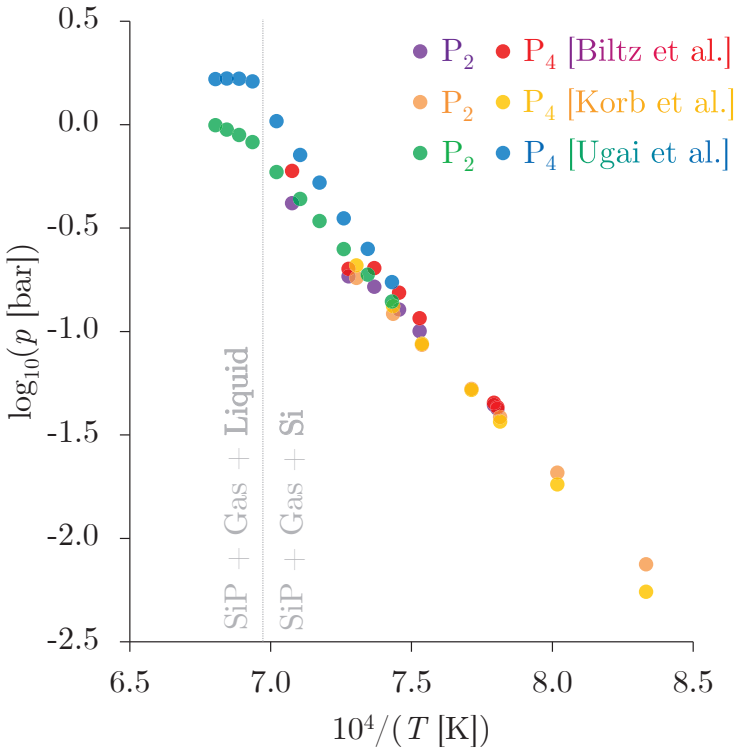

Figure 2.15: Dissociation pressures of SiP calculated from Biltz, Ugai et al. work, and dissociation pressure of $SiP_{0.8-0.9}$ calculated from Korb and Hein work

In Figure 2.15 is presented the dissociation pressures deduced from the different authors. They accurately correlate and point out the SiP melting at 1429 K.

With p_{P_2} and p_{P_4} known, it is possible to deduce activities. The equilibrium constant of the vaporization reaction $2P_{(l)} = P_{2(g)}$ is $K_{\text{eq}} = \dfrac{p_{P_2}}{a_P^2}$. In the case of pure elements the phosphorus activity is one; thus one can write[20]:

$$p^0_{P_2} = e^{\frac{-\Delta_{\text{vap}}G^0}{RT}} \tag{2.48}$$

To calculate the Gibbs free energy of vaporization $\Delta_{\text{vap}}G^0$, values of Gibbs free energies of formation in standard states $\Delta_f G^0$ of $P_{2(g)}$ and $P_{4(g)}$ are taken from JANAF tables. The phosphorus activity is then deducible from either partial pressure of $P_{2(g)}$ or $P_{4(g)}$ as so:

$$a_P = \sqrt{\frac{p_{P_2}}{p^0_{P_2}}} = \left(\frac{p_{P_4}}{p^0_{P_4}}\right)^{\frac{1}{4}} \tag{2.49}$$

In the end, the required chemical potential of phosphorus is obtained with:

$$\mu_P = RT \ln a_P \tag{2.50}$$

The μ_P calculated from the above articles (represented in Figure 2.16) are finally inserted in the optimization program.

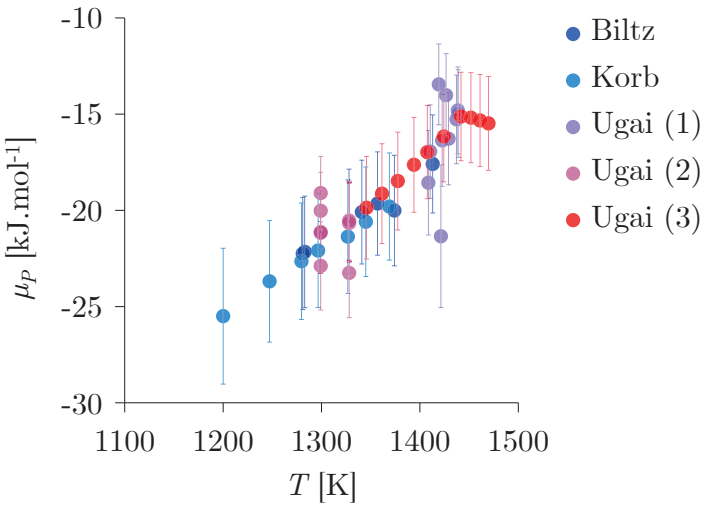

Figure 2.16: Partial Gibbs free energy calculated from the $p - T$ data of Biltz [7], Korb and Hein [29], and Ugai et al. [63–65] as a function of temperature

Its uncertainty $\delta\mu_P$ is deduced by estimating beforehand the pressures and activities uncertainties with the propagation of errors rules applied on their formulas.

2.2.4 $p - x$ diagram data

Using $p - x$ diagrams is another possibility to gather information about μ_P for optimizing the Si – P system (Table 2.10).

[20] The same goes for $p^0_{P_4}$.

Table 2.10: Summary of the $p - x$ data in the Si – P system

First author	Method	p range [bar]	x_P range [at.%]
Biltz [1938]	Spiral manometer	0.08 – 0.33	10 – 52
Ugai [1987]	Static manometric DTA under controlled p	0.4 – 43.3	40 – 75
Miki [1996]	Transpiration method	$8 \cdot 10^{-8}$ – $5 \cdot 10^{-6}$	0.013 – 0.10

Biltz carried in the same article [7] isothermal experiments enlightening phase disrupts. They are given in Table 2.11.

Table 2.11: Isothermal experiments of Biltz [7]

Phases	T [K]	x_P	p [bar]
SiP	917	0.517	0.3334
		0.512	0.2560
		0.510	0.1947
Si – SiP	1299	0.432	0.1414
		0.342	0.1400
Si – SiP /lim $Si_{(s,s)}$		0.145	0.1400
$Si_{(s,s)}$		0.107	0.0867
Si – SiP	1328	0.468	0.2214
		0.415	0.2160
		0.383	0.2160
		0.371	0.2187
		0.270	0.2160
Si – SiP /lim $Si_{(s,s)}$		0.213	0.2134
$Si_{(s,s)}$		0.153	0.1067

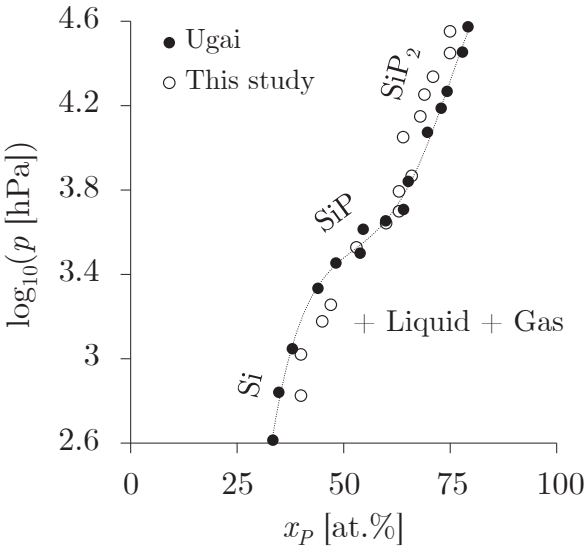

Figure 2.17: Reproduction of the $p - x$ diagram from Ugai et al. work [64]

The $p - x$ diagram of the previously mentioned **Ugai et al.** work [64] is constructed by combining the $T - x$ and $p - T$ diagrams but the calculations are unspecified. An attempt has been made to recreate Ugai et al.'s $p - x$ diagram, however the results are not matching as it can be seen Figure 2.17.

The present results will be favored in the assessment as their origin is known.

Miki et al. [37] measured the vapor pressure of phosphorus over Si-rich liquid for different isothermal experiments from 1723 to 1848 K by using a chemical equilibration technique (transpiration method).

Table 2.12: Experimental results from Miki et al. [37]

p [bar]	x_P [at.%]	T [K]
$8.59{\cdot}10^{-8}$	$1.37{\cdot}10^{-4}$	
$1.04{\cdot}10^{-7}$	$1.68{\cdot}10^{-4}$	
$3.31{\cdot}10^{-7}$	$2.88{\cdot}10^{-4}$	
$2.06{\cdot}10^{-6}$	$5.78{\cdot}10^{-4}$	1823
$3.57{\cdot}10^{-6}$	$8.10{\cdot}10^{-4}$	
$4.92{\cdot}10^{-6}$	$9.98{\cdot}10^{-4}$	
$2.12{\cdot}10^{-7}$	$3.40{\cdot}10^{-4}$	1723
$1.14{\cdot}10^{-7}$	$2.99{\cdot}10^{-4}$	
$2.09{\cdot}10^{-7}$	$2.72{\cdot}10^{-4}$	1748
$1.11{\cdot}10^{-7}$	$2.57{\cdot}10^{-4}$	
$2.06{\cdot}10^{-7}$	$2.49{\cdot}10^{-4}$	1773
$1.08{\cdot}10^{-7}$	$2.08{\cdot}10^{-4}$	
$1.07{\cdot}10^{-7}$	$1.99{\cdot}10^{-4}$	1798
$9.99{\cdot}10^{-8}$	$1.34{\cdot}10^{-4}$	

For a composition range of 0.02 – 0.10 at.% of P, they obtained the partial pressures of gaseous species P, P_2 and P_4. To determine the partial pressure of P_2 two methods were used: absorbing phosphorus gas into a bromine water at room temperature, and equilibrating phosphorus gas with molten silver at the same temperature altogether with that for silicon. No indication has been given whether a method was chosen over the other, or if the partial pressure values obtained are the same for both.

They provide their results in a table reproduced here with more relevant units (Table 2.12).

Exploitation of results

The same calculations as for $p - T$ are carried out here and are presented in Figure 2.18.

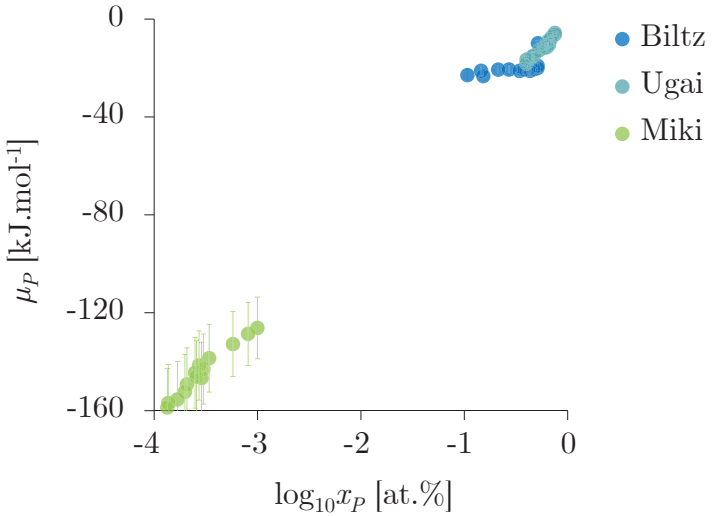

Figure 2.18: Partial Gibbs free energy calculated from the $p - x$ data of Biltz [7], Ugai et al. [64] and Miki et al. [37] as a function of the phosphorus content

All phase diagrams data of the Si – P system have been reviewed. A literature analysis of the thermodynamic functions is still left to be done.

2.2.5 Thermodynamic properties data

Articles about heat capacity C_p of stoichiometric compounds in the Si – P system as well as phosphorus activity in silicon a_P have been gathered (Table 2.2.5). The former can be used as such in the assessment, while the latter are converted into chemical potentials.

Table 2.13: Summary of the experimental activity and heat capacity data in the Si – P system

First author	Method	Type	T range [K]	x_P range [at.%]
Zaitsev [2001]	KCMS Static method	a_P	1507 – 1831	0.09 – 26.5
Ugai [1979]	Calorimetry	C_p	5 – 300	0.5 (SiP)
Barin [1991]	Unknown		298 – 1413	0.5 (SiP)
Jung [2012]	Revised Barin		298 – 1413	0.5 (SiP)
Philipp [2008]	DSC		–	0.66 (SiP_2)

a. Activity data

Zaitsev et al. [74] studied the composition of vapor and thermodynamic properties of Si-P melts by using Knudsen cell mass spectrometry (KCMS) and a static method. They give a hundred values of activity for phosphorus, and propose a liquid solution close to ideality.

Several experimental sources of uncertainty must be pointed out: (i) the temperature calibration of the doubled Knudsen cell thermocouple, (ii) the ionic current measurements, and (iii) the relative ionization cross section ratio between the phosphorus species and the reference component ($Fe_{(g)}$) used as a pressure reference.

They provided the activity of phosphorus in a table (reproduced Table 3.4 in Chapter 3), where experiment and calculation values are compared. The chemical potential to input is calculated with equation 2.50 and is presented in Figure 2.19.

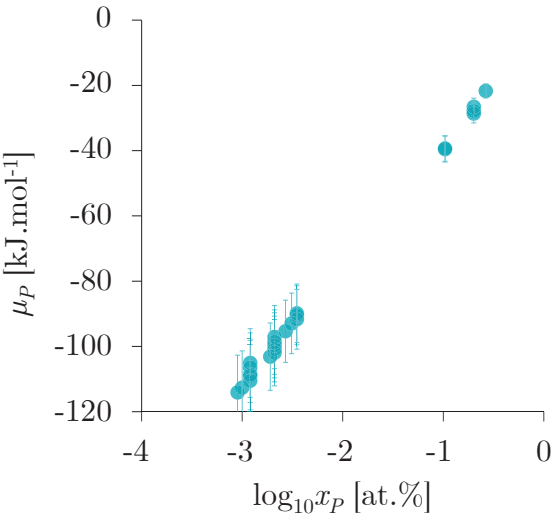

Figure 2.19: Partial Gibbs free energy calculated from the activity data of Zaitsev et al. [74] as a function of the phosphorus content

b. Heat capacity data

Ugai et al. [62] are presumably the only experimental investigators of C_p(SiP) below 298 K. Even if Lukas programs do not take into account heat capacity values for those low temperatures, it can be used to calibrate other higher values.

They used a calorimeter with germanium and platinum resistance thermometers to measure the specific heat of SiP. They smoothed their values every 5 K in a table, and precise their measurement accuracy. From an Al_2O_3 standard, they determined that within the range 5 – 40 K the mean error was 1.4%, from 40 to 100 K it was 0.54% and from 100 to 300 K the error was 0.3%.

A compilation handbook from **Barin et al.**[21] [5] gathered information about SiP. Heat capacity between 298 and 1413 K is given, however the source is missing and is an "educated guess" (sic). It might have been deduced from an article about GeP [75] as this reference is cited for another SiP quantity[22]. They give the following heat capacity, expressed in J.mol^{-1}.K^{-1}:

$$C_p(\mathrm{SiP}) = 42.886 + 10.878 \cdot 10^{-3} \cdot T - 5.65 \cdot 10^{5} \cdot T^{-2} \tag{2.51}$$

In their heat capacity assessment, **Jung and Zhang** [25] considered Ugai and Barin et al.'s work [5, 62], respectively evaluating below and above 298 K heat capacity. As they noticed a discrepancy between the two, they revised downward the first term of equation 2.51: from 42.886 to 38.343.

As regards $C_p(SiP_2)$ data, only one experimental work was denoted: **Philipp and Schmidt** [44] studied the crystal growth of $Si_{46-2x}P_{2x}Te_x$, and mentioned anecdotally a linear (sic) equation for this heat capacity obtained by DSC measurements, but without further details:

$$C_p(\mathrm{SiP_2}) = 67.02 + 17.14 \cdot 10^{-3} \cdot T \tag{2.52}$$

This description, expressed in J.mol^{-1}.K^{-1}, is evidently inaccurate, thus cannot be used for the assessment.

A clear discrepancy exists between C_p(SiP) data below and above 298 K. As Ugai et al. [62] experimental work is highly accurate, possible flaws should be investigated towards values above this room temperature. As the Barin et al. compilation handbook relies on a questionable reference for C_p(SiP), considering its formula seems unreasonable. Lowering its first term as Jung and Zhang did is even more so. Another solution shall be considered.

[21] The first author is different depending on the edition: it can also be referred as Knacke et al. [26].

[22] An analogy with GeP is conceivable: atomic weights and lattice vibrations frequencies contribute to the heat capacity value of a molecule; from the same group than silicon in the periodic table, germanium is the following heavier atom.

For a compound, Neumann-Kopp's rule of additivity can be applied [28]. They postulated that its heat capacity equals the sum of each constituting atom i:

$$C_p = \sum_i C_p(i) \tag{2.53}$$

Actually the first term of the C_p(SiP) obtained with this rule is lowered to match the accurate values of Ugai below 298 K.

Regarding the SiP_2 little and sparse information is given. The regular Neumann-Kopp's rule will then be applied by default with values from JANAF.

In Figure 2.20 are represented in bold lines the retained values of heat capacity. Ugai et al. work is considered valid and was used for calibration, but is not put in the optimization because their values are too low in temperature.

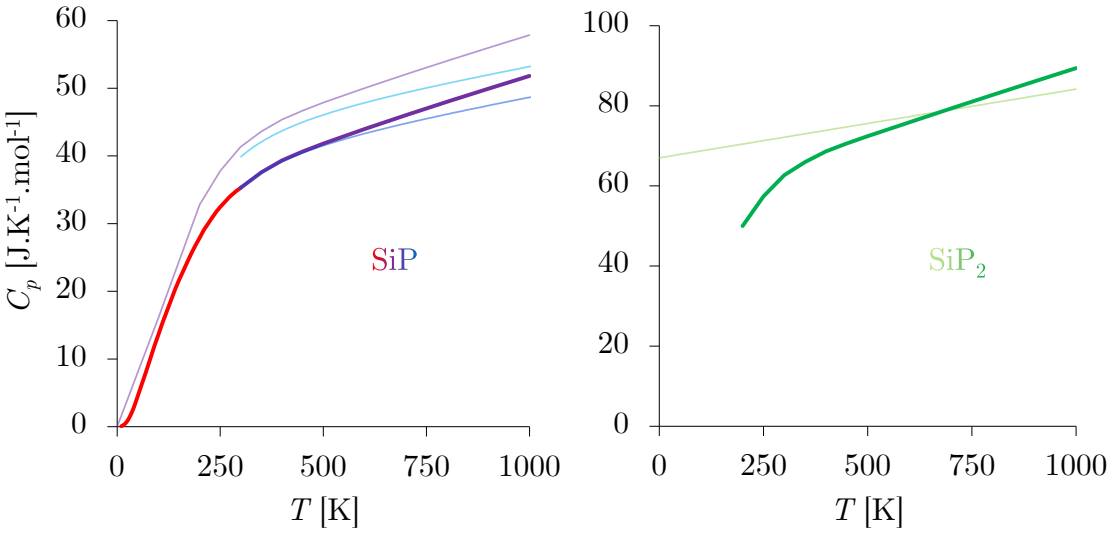

Figure 2.20: Different assessments of heat capacity of SiP and SiP_2. In bold lines are the retained values for the assessment: — Ugai et al. [62] and — the revised Neumann-Kopp's rule for SiP; — the regular Neumann-Kopp's rule for SiP_2. In thin lines are the discarded models: — the regular Neumann-Kopp's rule, — Barin et al. [5], and lowered — Jung and Zhang [25] values for SiP; — Philipp and Schmidt [44] for SiP_2.

c. Standard enthalpy change and entropy data

Some authors explicitly give those values at 298 K: $\Delta H^0_{298\ \mathrm{K}}$ and $S^0_{298\ \mathrm{K}}$ are either extracted from pressures, then equilibrium constants (Biltz [7], Korb and Hein [29]) or from calorimetry measurements (Ugai et al. [62], Philipp and Schmidt [44]).

Jung and Zhang [25] already optimized those thermodynamic properties: the results they suggested – reported in Table 2.14 – will then be used in the study.

Table 2.14: Summary of the experimental enthalpy and entropy data in the Si – P system. $\Delta H^0_{298\ \mathrm{K}}$ are expressed in kJ.mol^{-1} and $S^0_{298\ \mathrm{K}}$ in J.mol^{-1}.K^{-1}.

First author	Method	Type		Compound
Biltz [1938]	Spiral manometer	$\Delta H^0_{298\ \mathrm{K}}$	-79.03	SiP
Korb [1976]	Bourdon manometer		-75.2	SiP
Philipp [2008]	DSC		-84.3	SiP_2
Jung [2012]	Optimization		-63.3	SiP
			-79.3	SiP_2
Biltz [1938]	Spiral manometer	$S^0_{298\ \mathrm{K}}$	12.6	SiP
Korb [1976]	Bourdon manometer		15.9	SiP
Ugai [1979]	Calorimetry		34.78	SiP
Philipp [2008]	DSC		69.9	SiP_2
Jung [2012]	Optimization		34.74	SiP
			67.0	SiP_2

2.3 Optimization of the system

Every information needed for the calculation is now gathered. To optimize the Si – P system, one uses the following application programs developped by Lukas and Fries [32].

2.3.1 Special features of Lukas programs

The Lukas computer program that performs the least squares operation for binary systems is BINGSS[23]. The additional program BINFKT[24] calculates phase diagrams and produces plots of the thermodynamic properties for testing the results of BINGSS.

In BINGSS, three FORTRAN files are used with extensions .coe, .dat and .bgl. They are provided in Appendix B.

SiP.coe frames the assessment: it contains the phases described along with the adjustable coefficients. After running the program, this file is overwritten with those parameters adjusted. SiP.dat lists all the collected experimental data together with their estimated uncertainties. SiP.bgl contains the run conditions, *e.g.* the number of iteration steps.

The optimized file SiP.coe is read into BINFKT program to calculate phase diagrams and fit thermodynamic functions. The primary focus is to compare the result of BINGSS with the input data.

[23]For ternary systems the so-called TERGSS program is used.
[24]TERFKT is its equivalent for ternary systems.

To obtain the optimal accuracy, two conditions should be fulfilled: all the preliminarily selected experimental data should be taken into account, and all the thermodynamic properties of the different phases should be thermodynamically consistent with the phase diagram.

2.3.2 Calculation of the Si – P phase diagram

In Figure 2.21 is shown the optimized Si – P phase diagram in the case of a total pressure of 1 bar. The solubility data points are omitted to avoid overloading the graph, and are discussed afterwards.

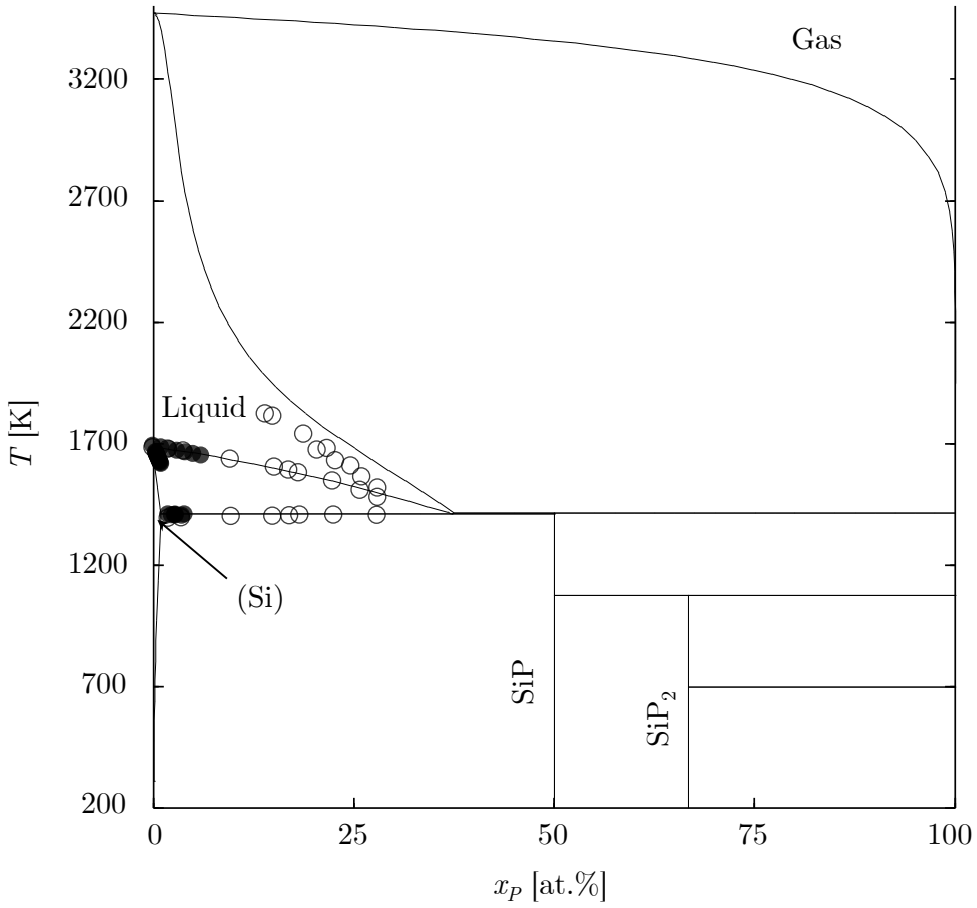

Figure 2.21: Calculated Si – P phase diagram at a total pressure of $p = 1$ bar. Experimental $T - x$ data from Giessen and Vogel [17] are represented in white, and Safarian and Tangstad [47] in black.

The results are in reasonably good agreement with the $T - x$ experimental data of Giessen and Vogel as well as Safarian and Tangstad. No major changes are

reportable compared to the lasts assessments [25, 31], which is explainable by the minor changes done on the corresponding data and phase models.

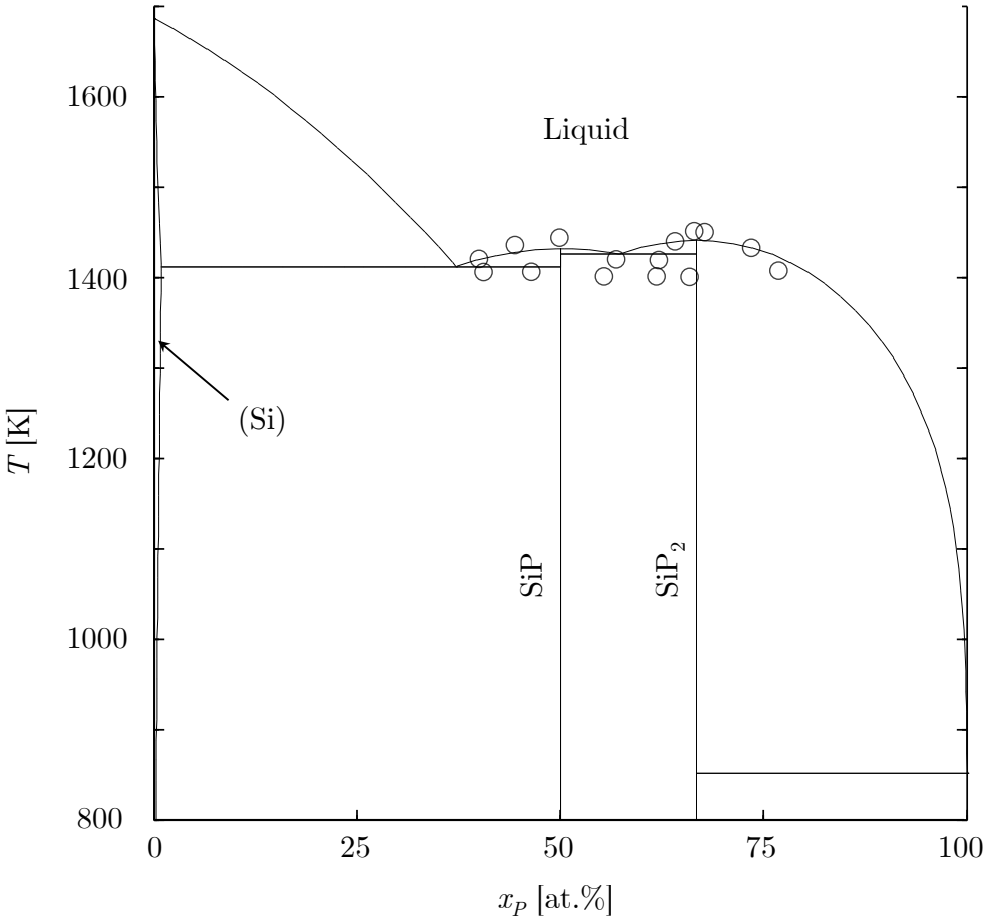

Figure 2.22: Calculated Si – P phase diagram at high pressures (figure valid for $p \geq 450$ bar). Experimental $T - x$ data from Ugai et al. [64] are represented in white.

The high pressure condition is imposed to reveal the liquidus that outlines the congruent melting of SiP and SiP_2. Above 155 bar this latter remains unchanged, however the evaporation line gradually fades in the P-rich region up to 450 bar.

The congruent melting of SiP is observed for pressures above 6.5 bar, and only 36.5 bar for SiP_2. Compared to Ugai et al. a small temperature difference respectively of 11 K and 9 K is denoted, which is a satisfactory agreement. As it can be seen in Table 2.15, those findings differ from Liang [31], Jung [25] et al. results. The reason is most likely that data of partial Gibbs free energy of P along the liquidus have been included in the current study, as well as more accurate C_p descriptions.

In the present work, the eutectic line between the two solid compounds is once more found to be higher in temperature than the one between dissolved silicon and SiP, which contradicts Ugai et al. [64] experiments. This may come from the description of the liquid phase as a regular solution. A model using an ideal associated

Table 2.15: Experimental and calculated high pressures invariant reactions of previous works compared to the present study

First author	T [K]	Reaction
Giessen	1404	Eutectic: Liquid = Si + SiP
Ugai	1404	
Jung	1400	
Safarian	1402	
Liang	1404	
	1407	
[This work]	**1413**	
Ugai	1398	Eutectic: Liquid = SiP + SiP_2
Jung	1407	
Liang	1430	
[This work]	**1427**	
Ugai	1443	Congruent melting: Liquid = SiP
Safarian	1412	
Jung	1410	
Liang	1434	
[This work]	**1432**	
Ugai	1451	Congruent melting: Liquid = SiP_2
Jung	1429	
Liang	1442	
[This work]	**1442**	

solution has be tested, *i.e.* describing the liquid with more species than only Si and P as in the present case. Zaitsev et al. [74] indeed proposed such a liquid description with additional Si_2P and SiP molecules, however no coherent optimization could be obtained here, regardless of the associate used. The regular solution is then kept, and the only remaining explanation to this problem seems that Ugai et al. work is not that consistent compared to the other kinds of data portraying this region.

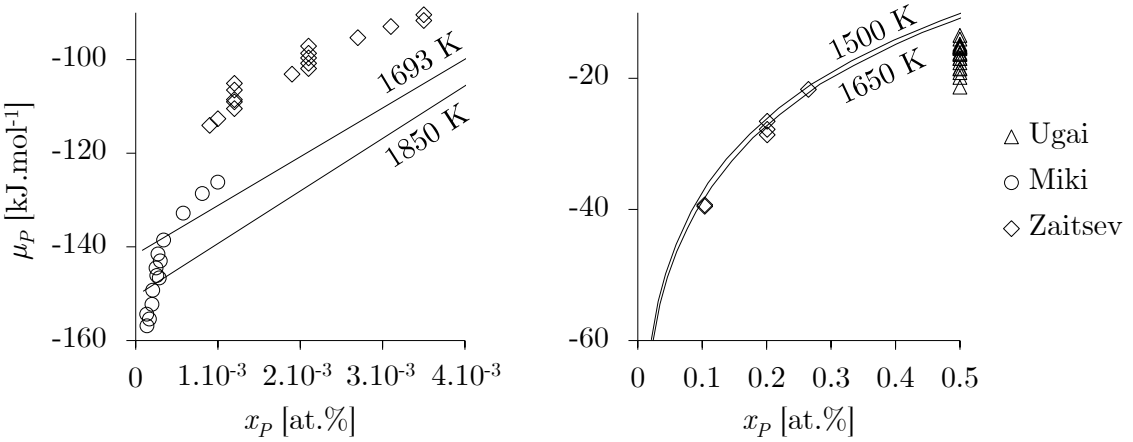

Figure 2.23: Optimized μ_P compared to the data from Ugai et al. [64], Miki et al. [37] and Zaitsev et al. [74]

This description of the liquid phase impacts the thermodynamic calculation of the partial Gibbs free energy of phosphorus as it can be seen in Figure 2.23. The present optimization is coherent with the phase diagram data [37, 64] and the activity [74] data from the liquid phase.

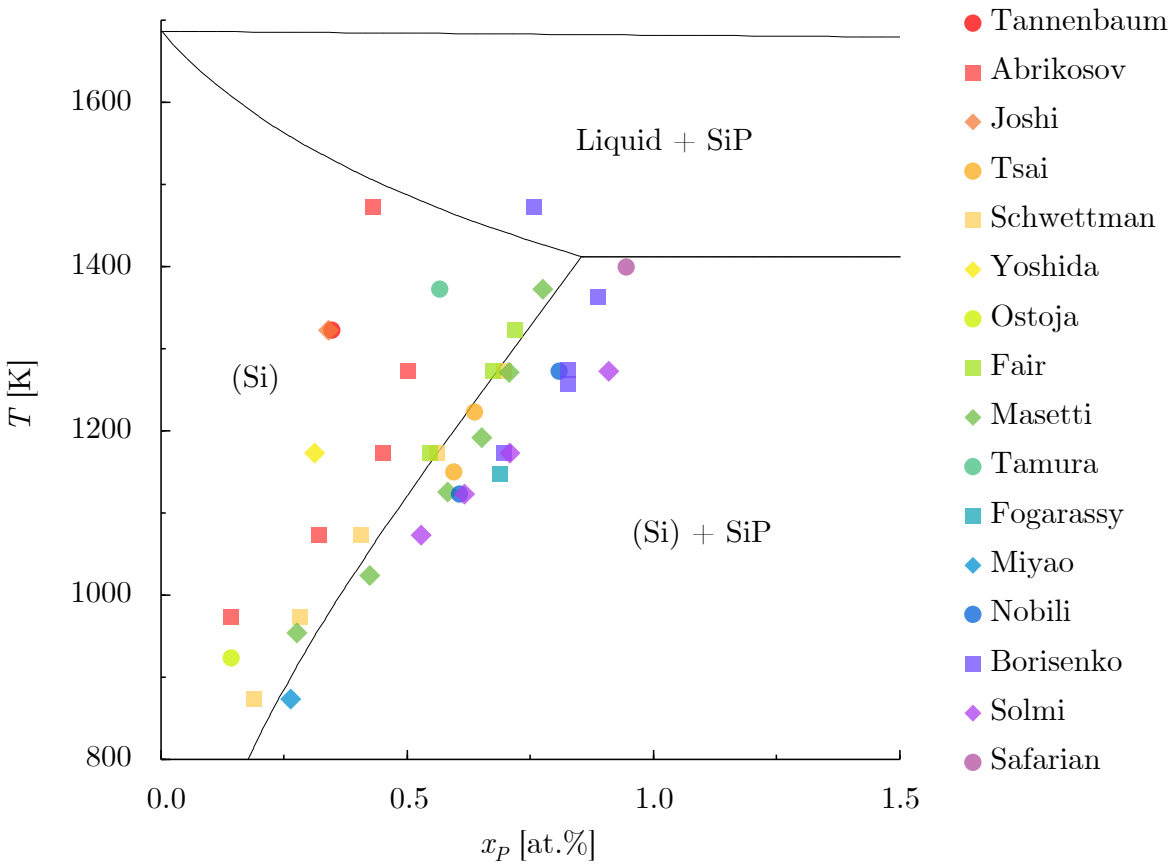

Figure 2.24: Calculated Si – P phase diagram in the Si-rich region at a total pressure of $p = 1$ bar.

The assessment of $[P]_{(Si)}$ is presented in Figure 2.24. These solubility data were the most problematic for the previous assessors (solubility diagrams in Appendix A): Tang et al. [55] gave a solubility limit at 2.3 at.% of P but without any precision on the optimization procedure. Even though Safarian and Tangstad [47] found it lower at 0.9 at.% of P, they proposed a hand-plotted solidus line outlining an unrealistic retrograde solubility to include their experimental results in. Arutyunyan et al. [3] assessed it at 2.3 at.%, while Jung and Zhang [25] determined it at 3.8 at.%: in both cases their literature reviews are not exhaustive. For Liang and Schmid-Fetzer [31], two models were suggested: one at 1.1 at.% and another at 3.6 at.% of maximum solubility. They favored the first one, but declared that they could not explain accurately this discrepancy.

The present study elucidated this issue in the $T - x$ data review section, and one can finally assert that $[P]^{max}_{(Si)} = 0.8$ at.%.

The optimized thermodynamic properties are also in accordance with the previous data (Table 2.14 of section 2.2.5). The absolute entropy value $S^0_{298\ \mathrm{K}}$ of SiP is estimated to be 34.74 J.mol^{-1}.K^{-1} while its enthalpy $\Delta H^0_{298\ \mathrm{K}}$ is -63.47 kJ.mol^{-1}. As for SiP_2, they are respectively 64.03 J.mol^{-1}.K^{-1} and -85.73 kJ.mol^{-1} .

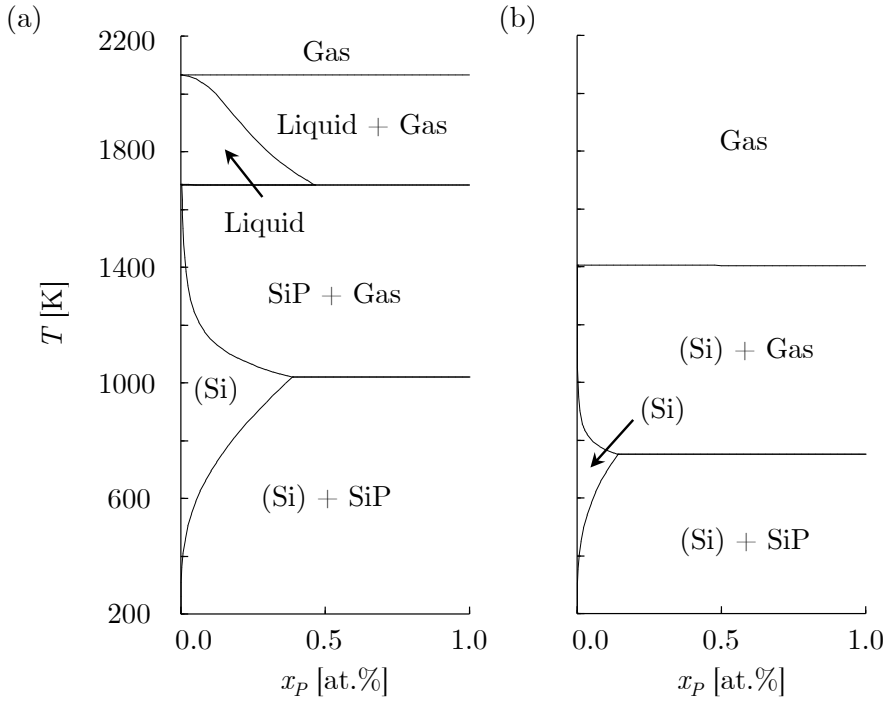

Figure 2.25: Calculated Si – P phase diagram in the Si-rich region for (a) $p = 10^{-4}$ bar and (b) $p = 10^{-9}$ bar

Phosphorus is removed from molten silicon at low pressures; regrettably no experimental data was found in these conditions. Extrapolating with Calphad the experimental data at atmospheric to high pressures provides however an estimation of phase equilibria as it can be seen in Figure 2.25. At $p = 10^{-4}$ bar the eutectic line is lowered to 1020 K, the gas phase starts from 2067 K for pure Si and liquid region has considerably diminished. At $p = 10^{-9}$ bar the eutectic line decreased to 752 K, the gas phase at 1406 K for pure Si and the liquid phase no longer exists.

2.3.3 Conclusions

After a thorough critical literature review of the available thermodynamic data, a Calphad assessment has been performed on the Si – P binary system. Although it has already been quite accurately investigated in the past, some gray areas needed to be clarified.

The main ensuing outcome is the resolution of the $[P]_{(Si)}$ issue. Up to now it has been left in abeyance because of the complex entanglement of the related diffusion

articles. Some authors misinterpretations has been noticed every so often: irrelevant adopted resistivity curves, disregarded SiP precipitates or else oxygen contamination biased the solubility results. After revising the concerned data points, its maximum limit at 1 bar is henceforth estimated to be 0.8 at.%.

With this solubility problematic solved, the present modeling of the liquid phase is more accurately described. The related Redlich-Kister interaction parameters are needed to calculate the activity coefficient at infinite dilution of phosphorus γ_P^{∞}. This variable is essential for simulating the dephosphorization of silicon.

Bibliography

[1] N. K. ABRIKOSOV, V. GLAZOV, AND L. CHEN-YUAN, *Individual and joint solubilities of aluminium and phosphorus in germanium and silicon*, Russian journal of inorganic chemistry, 7 (1962), pp. 429–431.

[2] J.-O. ANDERSSON, T. HELANDER, L. HOGLUND, P. SHI, AND B. SUNDMAN, *Thermo-calc and dictra, computational tools for materials science*, Calphad, 26 (2002), pp. 273–312.

[3] N. ARUTYUNYAN, A. ZAITSEV, AND N. SHAPOSHNIKOV, *Analysis of thermodynamic properties and phase equilibria in the si-p system*, Russian Journal of Physical Chemistry A, 85 (2011), pp. 911–915.

[4] C. BALE, E. BELISLE, P. CHARTRAND, S. DECTEROV, G. ERIKSSON, K. HACK, I.-H. JUNG, Y.-B. KANG, J. MELANCON, A. PELTON, ET AL., *Factsage thermochemical software and databases - recent developments*, Calphad, 33 (2009), pp. 295–311.

[5] I. BARIN, *O. knacke and o. kubaschewski*, Thermochemical Properties of Inorganic Substances, (1977), p. 825.

[6] C. BECK AND R. STICKLER, *Crystallography of sip and sias single crystals and of sip precipitates in si*, Journal of Applied Physics, 37 (1966), pp. 4683–4687.

[7] W. BILTZ AND A. KOCHER, *Beitrage zur systematischen verwandtschaftslehre. 82. uber das system tantal/schwefel*, Zeitschrift fur anorganische und allgemeine Chemie, 238 (1938), pp. 81–93.

[8] V. BORISENKO AND S. YUDIN, *Steady-state solubility of substitutional impurities in silicon*, physica status solidi (a), 101 (1987), pp. 123–127.

[9] W. CAO, S.-L. CHEN, F. ZHANG, K. WU, Y. YANG, Y. CHANG, R. SCHMID-FETZER, AND W. OATES, *Pandat software with panengine, panoptimizer and panprecipitation for multi-component phase diagram calculation and materials property simulation*, Calphad, 33 (2009), pp. 328–342.

[10] A. CARABELAS, D. NOBILI, AND S. SOLMI, *Grain boundary segregation in silicon heavily doped with phosphorus and arsenic*, Le Journal de Physique Colloques, 43 (1982), pp. C1–187.

[11] M. W. CHASE, *NIST-JANAF Thermochemical tables*, no. 4, american chemical society and the american institute of physics for the national institute of standards and technology ed.

[12] J. COX, D. D. WAGMAN, AND V. A. MEDVEDEV, *CODATA key values for thermodynamics*, Chem/Mats-Sci/E, 1989.

[13] A. DINSDALE, *Sgte data for pure elements*, Calphad, 15 (1991), pp. 317–425.

[14] R. B. Fair and J. Tsai, *A quantitative model for the diffusion of phosphorus in silicon and the emitter dip effect*, Journal of the Electrochemical Society, 124 (1977), pp. 1107–1118.

[15] M. Finetti, P. Negrini, S. Solmi, and D. Nobili, *Electrical properties and stability of supersaturated phosphorus-doped silicon layers*, Journal of the Electrochemical Society, 128 (1981), pp. 1313–1317.

[16] E. Fogarassy, R. Stuck, J. Muller, A. Grob, J. Grob, and P. Siffert, *Effects of laser irradiation on phosphorus diffused layers in silicon*, Journal of Electronic Materials, 9 (1980), pp. 197–209.

[17] B. Giessen and R. Vogel, *Uber das system silizium-phosphor*, Zeitschrift FuHhr Metallkunde, 50 (1959), pp. 274–277.

[18] V. Glushko, L. Gurvich, et al., *Thermodynamic properties of individual materials*, Handbook [in Russian], 2 (1978).

[19] L. V. Gurvich and I. Veyts, *Thermodynamic Properties of Individual Substances: Elements and Compounds*, vol. 2, CRC press, 1990.

[20] R. Hull, *Properties of crystalline silicon*, no. 20, IET, 1999.

[21] R. Hultgren, P. D. Desai, D. T. Hawkins, M. Gleiser, and K. K. Kelley, *Selected values of the thermodynamic properties of binary alloys*, tech. report, National Standard Reference Data System, 1973.

[22] J. C. Irvin, *Resistivity of bulk silicon and of diffused layers in silicon*, Bell Labs Technical Journal, 41 (1962), pp. 387–410.

[23] K. Itoh, Y. Sasaki, T. Mitsuishi, M. Miyao, and M. Tamura, *Thermal behavior of b, p and as atoms in supersaturated si produced by ion implantation and pulsed-laser annealing*, Japanese Journal of Applied Physics, 21 (1982), p. L245.

[24] M. Joshi and S. Dash, *Dislocation-induced deviation of phosphorus-diffusion profiles in silicon*, IBM Journal of Research and Development, 10 (1966), pp. 446–454.

[25] I.-H. Jung and Y. Zhang, *Thermodynamic calculations for the dephosphorization of silicon using molten slag*, JOM, 64 (2012), pp. 973–981.

[26] O. Knacke, O. Kubaschewski, K. Hesselmann, et al., *Thermochemical properties of inorganic substances*, vol. 1, Springer Berlin, 1991.

[27] E. Kooi, *Formation and composition of surface layers and solubility limits of phosphorus during diffusion in silicon*, Journal of the Electrochemical Society, 111 (1964), pp. 1383–1387.

[28] H. KOPP, *Investigations of the specific heat of solid bodies*, Philosophical Transactions of the Royal Society of London, 155 (1865), pp. 71–202.

[29] J. KORB AND K. HEIN, *Dampfdruckuntersuchungen im system zn-si-p*, 425 (1976), pp. 281–288.

[30] J. J. LAAR, *Sechs Vortrage uber das thermodynamische Potential und seine Anwendungen auf chemische und physikalische Gleichgewichtsprobleme*, F. Vieweg und sohn, 1906.

[31] S.-M. LIANG AND R. SCHMID-FETZER, *Modeling of thermodynamic properties and phase equilibria of the si-p system*, Journal of Phase Equilibria and Diffusion, 35 (2014), pp. 24–35.

[32] H. LUKAS, E. T. HENIG, AND B. ZIMMERMANN, *Optimization of phase diagrams by a least squares method using simultaneously different types of data*, Calphad, 1 (1977), pp. 225–236.

[33] H. L. LUKAS, S. G. FRIES, B. SUNDMAN, ET AL., *Computational thermodynamics: the Calphad method*, vol. 131, Cambridge university press Cambridge, 2007.

[34] I. MACKINTOSH, *The diffusion of phosphorus in silicon*, Journal of The Electrochemical Society, 109 (1962), pp. 392–401.

[35] M. MARGULES, *Uber die zusammensetzung der gesattigten dampfe von mischungen*, Sitzungsber. Akad. Wiss. Wien, math.-naturwiss. Klasse, 104 (1895), pp. 1243–1278.

[36] G. MASETTI, D. NOBILI, AND S. SOLMI, *Profiles of phosphorus predeposited in silicon and carrier concentration in equilibrium with sip precipitates'*, Semiconductor silicon 1977, (1977), pp. 648–657.

[37] T. MIKI, K. MORITA, AND N. SANO, *Thermodynamics of phosphorus in molten silicon*, Metallurgical and Materials Transactions B, 27 (1996), pp. 937–941.

[38] M. MIYAO, K. ITOH, M. TAMURA, H. TAMURA, AND T. TOKUYAMA, *Furnace annealing behavior of phosphorus implanted, laser annealed silicon*, Journal of Applied Physics, 51 (1980), pp. 4139–4144.

[39] F. MOUSTY, P. OSTOJA, AND L. PASSARI, *Relationship between resistivity and phosphorus concentration in silicon*, Journal of Applied Physics, 45 (1974), pp. 4576–4580.

[40] D. NOBILI, A. ARMIGLIATO, M. FINNETTI, AND S. SOLMI, *Precipitation as the phenomenon responsible for the electrically inactive phosphorus in silicon*, Journal of Applied Physics, 53 (1982), pp. 1484–1491.

[41] R. Olesinski, N. Kanani, and G. Abbaschian, *The p- si (phosphorus-silicon) system*, Journal of Phase Equilibria, 6 (1985), pp. 130–133.

[42] P. Ostoja, D. Nobili, A. Armigliato, and R. Angelucci, *Isochronal annealing of silicon-phosphorus solid solutions*, Journal of The Electrochemical Society, 123 (1976), pp. 124–129.

[43] L. Pankratz, J. Stuve, and N. Gokcen, *Thermodynamic data for mineral technology*, (1984).

[44] F. Philipp and P. Schmidt, *The cationic clathrate si 46- 2 xp 2 xtex crystal growth by chemical vapour transport*, Journal of Crystal Growth, 310 (2008), pp. 5402–5408.

[45] O. Redlich and A. Kister, *Algebraic representation of thermodynamic properties and the classification of solutions*, Industrial and Engineering Chemistry, 40 (1948), pp. 345–348.

[46] R. A. Robie and B. S. Hemingway, *Thermodynamic properties of minerals and related substances at 298.15 k and 1 bar (10ˆ 5 pascals) pressure and at higher temperatures*, US Geol. Survey Bull., vol. 2131, p. 461-461 (1995)., 2131 (1995), pp. 461–461.

[47] J. Safarian and M. Tangstad, *Phase diagram study of the si–p system in si-rich region*, Journal of Materials Research, 26 (2011), pp. 1494–1503.

[48] ——, *Kinetics and mechanism of phosphorus removal from silicon in vacuum induction refining*, High Temperature Materials and Processes, 31 (2012), pp. 73–81.

[49] P. Schmidt and R. Stickler, *Silicon phosphide precipitates in diffused silicon*, Journal of the Electrochemical Society, 111 (1964), pp. 1188–1189.

[50] F. Schwettmann and D. Kendall, *Carrier profile change for phosphorus-diffused layers on low-temperature heat treatment*, Applied Physics Letters, 19 (1971), pp. 218–220.

[51] ——, *On the nature of the kink in the carrier profile for phosphorus-diffused layers in silicon*, Applied Physics Letters, 21 (1972), pp. 2–4.

[52] S. Solmi, A. Parisini, R. Angelucci, A. Armigliato, D. Nobili, and L. Moro, *Dopant and carrier concentration in si in equilibrium with monoclinic sip precipitates*, Physical Review B, 53 (1996), p. 7836.

[53] H. Sunami, *Thermal oxidation of phosphorus-doped polycrystalline silicon in wet oxygen*, Journal of The Electrochemical Society, 125 (1978), pp. 892–897.

[54] M. Tamura, *Dislocation networks in phosphorus-implanted silicon*, Philosophical Magazine, 35 (1977), pp. 663–691.

[55] K. TANG, E. J. OVRELID, G. TRANELL, AND M. TANGSTAD, *Thermochemical and kinetic databases for the solar cell silicon materials*, in Crystal growth of Si for solar cells, Springer, 2009, pp. 219–251.

[56] E. TANNENBAUM, *Detailed analysis of thin phosphorus-diffused layers in p-type silicon*, Solid-State Electronics, 2 (1961), pp. 123–132.

[57] H. THURN AND H. KREBS, *Uber struktur und eigenschaften der halbmetalle. xxii. die kristallstruktur des hittorfschen phosphors*, Acta Crystallographica Section B: Structural Crystallography and Crystal Chemistry, 25 (1969), pp. 125–135.

[58] F. A. TRUMBORE, *Solid solubilities of impurity elements in germanium and silicon*, Bell System Technical Journal, 39 (1960), pp. 205–233.

[59] J. C. TSAI, *Shallow phosphorus diffusion profiles in silicon*, Proceedings of the IEEE, 57 (1969), pp. 1499–1506.

[60] K. UDA AND M. KAMOSHIDA, *Annealing characteristics of highly p+-ion-implanted silicon crystal-two-step anneal*, Journal of Applied Physics, 48 (1977), pp. 18–21.

[61] Y. A. UGAI, *Vvedenie v Khimiyu Poluprovodnikov - Introduction to Semiconductor Chemistry*, no. 2, vysshaya shkola ed.

[62] Y. A. UGAI, A. DEMIDENKO, V. KOSHCHENKO, V. YACHMENEV, L. SOKOLOV, AND E. GONCHAROV, *Thermodynamic properties of silicon and germanium monophosphides*, Inorganic Materials, 15 (1979), pp. 578–581.

[63] Y. A. UGAI, G. SEMENOVA, AND L. SOKOLOV, *Thermal dissociation of silicon monophosphide*, Zhurnal Neorganicheskoi Khimii, 32 (1987), pp. 1459–62.

[64] Y. A. UGAI, L. SOKOLOV, AND E. GONCHAROV, *P-t-x state diagram and thermodynamics of phase equilibria in the silicon - phosphorus system*, Zhurnal Neorganicheskoi Khimii, 32 (1987), pp. 1198–1200.

[65] Y. A. UGAI, L. I. SOKOLOV, E. G. GONCHAROV, AND A. N. LUKIN, *Preparation of single-crystal silicon phosphide*, 17, pp. 851–852.

[66] P. VILLARS, L. CALVERT, AND W. PEARSON, *Pearson's handbook of crystallographic data for intermetallic phases. volumes 1, 2, 3*, American Society for Metals, 1985,, (1985), p. 3258.

[67] Y. WADA AND S. NISHIMATSU, *Grain growth mechanism of heavily phosphorus-implanted polycrystalline silicon*, Journal of The Electrochemical Society, 125 (1978), pp. 1499–1504.

[68] T. WADSTEN, *Crystal structures of sip2 sias2 and gep*, 1967.

[69] T. Wadsten, *Synthesis of a pyrite-type modification of sip2*, Acta Chem. Scand, 21 (1967), pp. 1374–1376.

[70] T. Wadsten, *Synthesis and structural data of sip*, 1969.

[71] T. Wadsten, *Preparative and crystal-structure studies on orthorhombic silicon monophosphide*, Chemica Scripta, 8 (1975), pp. 63–69.

[72] D. Wagman, W. Evans, V. Parker, R. Schumm, I. Halow, S. Bailey, K. Churney, and R. Nuttall, *The nbs tables of chemical thermodynamics*, J. Phys. Chem. Ref. Data, 11 (1982).

[73] M. Yoshida, E. Arai, H. Nakamura, and Y. Terunuma, *Excess vacancy generation mechanism at phosphorus diffusion into silicon*, Journal of Applied Physics, 45 (1974), pp. 1498–1506.

[74] A. I. Zaitsev, A. D. Litvina, and N. E. Shelkova, *Thermodynamic properties of si–p melts*, High Temperature, 39 (2001), pp. 227–232.

[75] M. Zumbusch, M. Heimbrecht, and W. Biltz, *Beitrage zur systematischen verwandtschaftslehre. 90. germaniumphosphid*, Zeitschrift fur anorganische und allgemeine Chemie, 242 (1939), pp. 237–248.

3

Thermodynamic simulation of the silicon dephosphorization

THE dephosphorization problematic intrinsically involves a time factor that previous thermodynamic tools do not provide. Abecedarian kinetic gas theory will thenceforth be discussed to fill that need.

Under vacuum[1], this distillation process physically implies particles flows that should be quantified. Expressing those entails the use of indispensable tools that are the ideal gas law and the Maxwell-Boltzmann distribution of speeds. In the following section is described their origin.

3.1 Kinetic gas theory concepts

Several assumptions are made in kinetic gas theory. The studied system contains a large number N of particles of identical mass m, which have a negligible volume. They randomly collide by obeying Newton's laws, and their collisions are considered elastic so that no energy is lost afterward.

First of all the equipartition of energy needs to be clarified for later purposes. Its general formula is applied in classical statistical physics, but for facilitation reasons the following section will introduce it in the case of ideal monatomic gas.

[1] The term vacuum actually refers to a rarefied atmosphere.

3.1.1 Equipartition theorem

The law of equipartition predicts that when a system is at thermodynamic equilibrium, its total kinetic energy is shared equally among its different components. Its theorem relates the temperature T of a macroscopic system with the average energies of its microscopic components. For a monatomic ideal gas:

$$\langle E^{\text{kin}} \rangle = \frac{3}{2} k_b T \tag{3.1}$$

with $\langle E^{\text{kin}} \rangle$ the mean kinetic energy of the system of particles with three degrees of freedom[2].

3.1.2 Ideal gas law

Let i be a unidirectionally moving particle in a cube of side L. Its momentum in the direction of a wall mc_x is only the opposite of its momentum after its collision $-mc_x$, giving the change in momentum $2mc_x$. According to Newton's second law, its force is equal to the change in momentum for the corresponding interval of time $\Delta t = \dfrac{2L}{c_x}$. The resulting pressure is this very force over the surface of the wall L^2:

$$p_i = \frac{mc_x^2}{V} \tag{3.2}$$

with $V = L^3$ the volume of the cube. Now considering N particles, the total pressure of the system is:

$$p = \frac{m\langle c_x^2 \rangle}{V} N \tag{3.3}$$

Since the velocity c of a particle is the sum of its components c_x, c_y and c_z, and that the mean value of each are the same, one can write $\langle c^2 \rangle = 3\langle c_x^2 \rangle$. Therefore the total pressure can be reformulated as so:

$$p = \frac{N}{3V} m\langle c^2 \rangle \tag{3.4}$$

According to classical mechanics, the kinetic energy of the system is $\left\langle E^{\text{kin}} \right\rangle = \dfrac{1}{2} m\langle c^2 \rangle$. For a monatomic gas, the energy of its atoms is only kinetic from translational movements, therefore by using the equipartition theorem one deduces that:

$$pV = Nk_B T \tag{3.5}$$

This relation, known as the ideal gas law, is most commonly written under the form:

$$pV = nRT \tag{3.6}$$

[2]Hence the three halves in equation 3.1.

It was first stated in 1834 by Émile Clapeyron as the combination of the following empirical gas laws listed in chronological order:

$$\begin{array}{ll} \text{Boyle-Mariotte law:} & p \propto \frac{1}{V} \\ \text{Charles' law:} & V \propto T \\ \text{Gay-Lussac's law:} & p \propto T \\ \text{Avogadro's law:} & V \propto n \end{array} \tag{3.7}$$

3.1.3 Maxwell-Boltzmann distribution

In a system of idealized gas particles at thermodynamic equilibrium, the Maxwell-Boltzmann distribution has been introduced to describe the speed distribution, depending on the temperature T and the mass of the particle m. This is the centerpiece of the kinetic gas theory, that will help thereafter to express gas flows relevant to the dephosphorization problematic.

For a given time, a monatomic molecule can be described by its position vector $\vec{r}$ and its velocity vector $\vec{c}$. In a Cartesian coordinate system:

$$\vec{r} = (x, y, z) \text{ and } \vec{c} = (c_x, c_y, c_z) \tag{3.8}$$

To understand the statistical behaviour of a system of molecules, one needs to introduce the notion of **distribution function** $f(\vec{c}, \vec{r}, t)$. It provides information on the probability of finding molecules in the system with such position and velocity. Thereby at time t, the average number of molecules with position in the range of $\{\vec{r}; \vec{r} + d\vec{r}\}$ and at velocity $\{\vec{c}; \vec{c} + d\vec{c}\}$ is:

$$dN_{d\vec{c},d\vec{r},t} = f(\vec{c}, \vec{r}, t) d\vec{c} d\vec{r} \tag{3.9}$$

Considering a monatomic ideal gas system, the energy E of its constituting atoms is solely kinetic due to their translational movement:

$$E = \frac{1}{2} m (c_x^2 + c_y^2 + c_z^2) \tag{3.10}$$

Boltzmann formulated the probability of finding atoms with energy E at temperature T in equilibrium with the **probability density function** (PDF) $f(E)$:

$$f(E) = \alpha \, \mathrm{e}^{-\frac{E}{k_B T}} \tag{3.11}$$

In order to find the value of the coefficient α, it is necessary to use the normalization of $f(E)$: one is sure to find a particle with an energy in the range of $\{0;\infty\}$. This results in:

$$\int_{-\infty}^{+\infty}\int\int f(c_x, c_y, c_z) dc_x dc_y dc_z = 1 \tag{3.12}$$

The employment of spherical coordinates simplifies the problem as:

$$\int_0^{+\infty} \underbrace{4\pi c^2}_{\theta,\varphi} f(c)dc = \int_0^{+\infty} 4\pi c^2 \alpha \, \mathrm{e}^{-\frac{mc^2}{2k_B T}} \, dc = 1 \tag{3.13}$$

with θ the polar angle and φ the azimutal angle. Since $\int_0^{+\infty} x^n \, \mathrm{e}^{-ax^2} \, dx = \frac{\Gamma\left(\frac{n+1}{2}\right)}{2a^{\frac{n+1}{2}}}$ with the gamma function $\Gamma(t) = \int_0^{+\infty} x^{t-1} \, \mathrm{e}^{-x} \, dx$, one deduces that:

$$4\pi\alpha \frac{\Gamma\left(\frac{3}{2}\right)}{2\left(\frac{m}{2k_B T}\right)^{\frac{3}{2}}} = 1 \tag{3.14}$$

As $\Gamma\left(\frac{3}{2}\right) = \frac{\sqrt{\pi}}{2}$ the coefficient α is found to be $\left(\frac{m}{2\pi k_B T}\right)^{\frac{3}{2}}$. Ultimately the **Maxwell-Boltzmann distribution of speeds** can be written as follows:

$$f(\vec{c}) = 4\pi c^2 \left(\frac{m}{2\pi k_B T}\right)^{\frac{3}{2}} \mathrm{e}^{-\frac{mc^2}{2k_B T}} \tag{3.15}$$

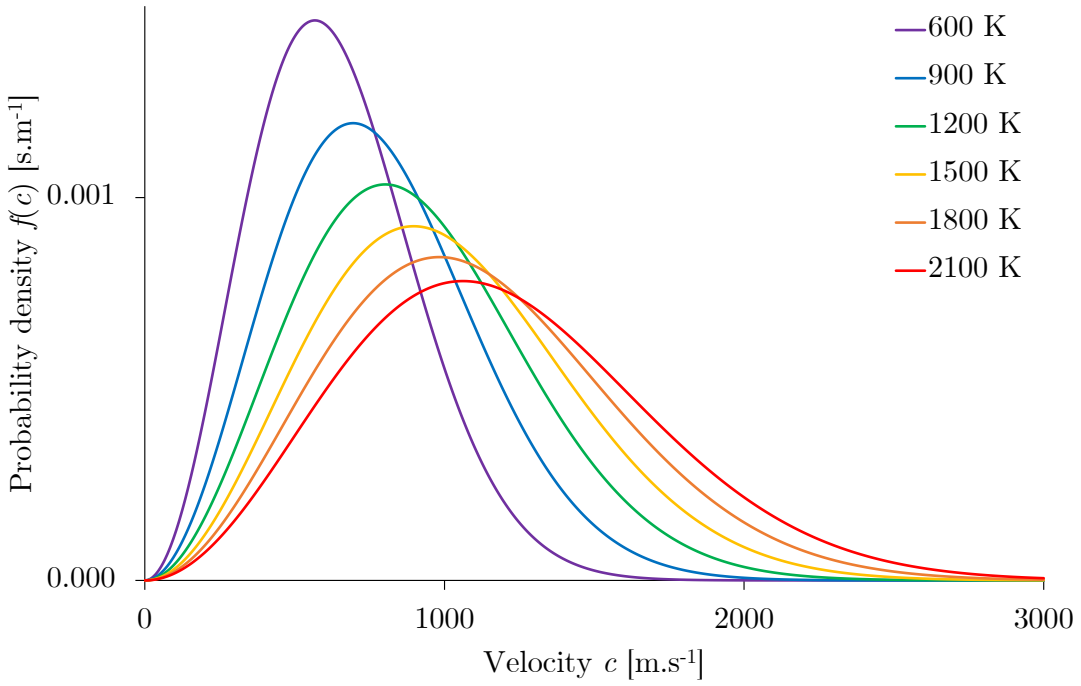

Figure 3.1: Maxwell-Boltzmann distribution of phosphorus for different temperatures

3.1.4 Impingement rate

As mentioned previously, the time factor shall be considered for calculating evaporation flows. The principle of the impingement rate of molecules on a surface is thus introduced in this section.

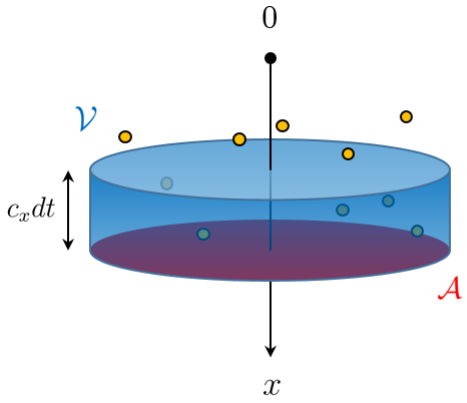

Figure 3.2: Schema of the system used to calculate the impingement rate $\phi_{\mathcal{A},dt}$ during an interval dt. On a wall of area $\mathcal{A}$ are colliding molecules with x-component of velocity c_x represented in yellow. $\mathcal{V}$ is the volume in which impinging molecules during dt are located.

This notion refers to the number of molecules colliding with a surface per unit time and per unit area. The Figure 3.2 represents the different parameters required to calculate it. The molecules of velocity c_x impinge the wall in dt only if they lie within a distance $c_x dt$ from it. The volume $\mathcal{V}$ in which they are located is nothing else than $\mathcal{A}c_x dt$. It therefore contains $N_\mathcal{V}$ molecules :

$$N_\mathcal{V} = \frac{N}{V}\mathcal{A}c_x dt \tag{3.16}$$

Where the fraction of N molecules over a certain volume V is the gas density. To consider the number $N_{\mathcal{V},c_x}$ of those molecules having the velocity c_x one shall introduce the notion of Maxwell-Boltzmann distribution discussed above:

$$N_{\mathcal{V},c_x} = N_\mathcal{V} f(c_x) dc_x \tag{3.17}$$

Those molecules necessarily impinge the wall $\mathcal{A}$ during dt. The total number of collisions during this interval *i.e.* the impingement rate is then obtained by integrating $N_{\mathcal{V},c_x}$ over all positive c_x:

$$\phi_{\mathcal{A},dt} = \frac{N}{V}\mathcal{A}dt \int_0^\infty c_x f(c_x) dc_x \tag{3.18}$$

The PDF of equation 3.15 considers the three dimensions of space $\{x,y,z\}$. In this particular case of only one dimension its formula shall be revised. In equilibrium at temperature T:

$$f(c_x) = \alpha \, \mathrm{e}^{\frac{-mc_x^2}{2k_BT}} \tag{3.19}$$

Since $\int_{-\infty}^{+\infty} f(c_x)dc_x = 1$, one can use the known definite integral $\int_{-\infty}^{+\infty} \mathrm{e}^{-x^2} = \sqrt{\pi}$ with $x = \sqrt{\frac{m}{2k_BT}}c_x$. In that case:

$$\int_{-\infty}^{+\infty} \mathrm{e}^{-\frac{mc_x^2}{2k_BT}} \, d\left(\sqrt{\frac{m}{2k_BT}}c_x\right) = \sqrt{\pi} \tag{3.20}$$

Put it differently:

$$\sqrt{\frac{m}{2k_BT}} \int_{-\infty}^{+\infty} \frac{f(c_x)}{\alpha} d(c_x) = \sqrt{\pi} \tag{3.21}$$

It follows that the coefficient α is in that specific case $\sqrt{\frac{m}{2\pi k_BT}}$. The impingement rate of equation 3.18 can then be rewritten as:

$$\phi_{\mathcal{A},dt} = \frac{N}{V}\mathcal{A}dt\sqrt{\frac{m}{2\pi k_BT}} \int_0^{\infty} c_x \, \mathrm{e}^{-\frac{mc_x^2}{2k_BT}} \, dc_x \tag{3.22}$$

Since $\int_0^{+\infty} x^n \, \mathrm{e}^{-ax^2} = \frac{\Gamma\left(\frac{n+1}{2}\right)}{2a^{\frac{n+1}{2}}}$, with $n = 1$ and $a = \frac{m}{2k_BT}$ one should write:

$$\phi_{\mathcal{A},dt} = \frac{N}{V}\mathcal{A}dt\sqrt{\frac{k_BT}{2\pi m}} \tag{3.23}$$

The mean value of the velocity is $\langle c \rangle = \sqrt{\frac{8k_BT}{\pi m}}$ so the impingement rate can be reformulated as a function of it:

$$\phi_{\mathcal{A},dt} = \frac{\mathcal{A}dt}{4}\frac{N}{V}\langle c \rangle \tag{3.24}$$

This formula stands for a wall of area $\mathcal{A}$ during an interval dt. The impingement rate per unit of time and area is then:

$$\phi = \frac{1}{4}\frac{N}{V}\langle c \rangle \tag{3.25}$$

Using N and V for obtaining this rate is experimentally inconvenient; according to the ideal gas law, the gas density is also $\frac{p}{k_BT}$. The following formula of the impingement rate per unit of time and area is thus more widely use:

$$\phi = \frac{p}{\sqrt{2\pi m k_BT}} \tag{3.26}$$

This molecular flow has its molar equivalent:

$$\Phi = \frac{p}{\sqrt{2\pi MRT}} \tag{3.27}$$

3.1.5 Hertz-Knudsen flow

Heinrich Hertz experimentally observed with mercury that hydrostatic pressure p_h exerted at the liquid surface should be taken off from the equilibrium vapour pressure p^* [4]. In addition to this, Martin Knudsen pointed out another hindering phenomenon: the molar flow Φ is rarely achieved as only a fraction of particles transits from the liquid to the vapour phase [6]. He then suggested to implement the empirical evaporation coefficient α_e to the formula; the net molecular evaporation rate is thereby expressed as the Hertz-Knudsen flow:

$$\Phi_{HK} = \frac{\alpha_e(p^* - p_h)}{\sqrt{2\pi MRT}} \tag{3.28}$$

Now that kinetic gas theory concepts are properly introduced, it is possible to enter the heart of the matter that is assessing the dephosphorization process of molten silicon.

3.2 Evaluation of phosphorus removal in molten silicon

An algorithm is written to simulate the dephosphorization rate of a silicon ball that can take into account the presence of oxygen. After investigating thermodynamic literature, relevant data values are extracted to implement the calculation of the distillation time of the sample. Moreover its weight loss shall be considered: a dephosphorization process is ineffective if the sample is overly evaporated, even though the distillation is rapid.

3.2.1 Selected literature

Determining the dephosphorization rate of silicon is possible by means of Hertz-Knudsen flows calculations, involving partial pressures of the different species. Those pressures are obtained by stating gaseous equilibria linking the latter to activities and constant equilibria.

In the available literature dealing with binary Si – P system, several articles have been retained to the appropriate data therein contained. The previously introduced works from **Miki et al.** [7] and **Zaitsev et al.** [10] are considered, as well as the thermodynamic assessment presented in the previous chapter. As it is explained in the following part, activity coefficients are conveniently extractable from their results. This latter calculation also requires interaction parameters linked to oxygen.

An article from **Narushima et al.** [8] fulfilled this demand. They determined oxygen solubility in liquid Si-P alloys equilibrated with solid silica in the temperature range between 1693 and 1823 K. Switching from solubility values to those interaction coefficients will next be discussed.

3.2.2 Extracted thermodynamic data

Preliminary thermodynamic properties for distillation

From a thermodynamic point of view, in the distillation process phosphorus is the solute and silicon is the solvent. At a given temperature the liquid phase remains in equilibrium with the vaporizing gaseous phase even if there is no vapor back flow, because the vaporization reactions are rapid at the surface of a liquid. Silicon follows the Raoult's law in the liquid phase:

$$a_{Si} = \gamma_{Si} x_{Si} \tag{3.29}$$

relation in which a_{Si} is the silicon activity, γ_{Si} the silicon activity coefficient and x_{Si} the silicon molar fraction. In the gas phase:

$$a_{Si} = \frac{p_{Si}}{p^0_{Si}} \tag{3.30}$$

where p_{Si} is the equilibrium partial pressure and the p^0_{Si} is the standard pressure. Phosphorus is the dilute solution and follows Henry's law in liquid phase:

$$a_P = \gamma^\infty_P x_P \tag{3.31}$$

where a_P is the phosphorus activity, γ^∞_P the phosphorus activity coefficient at infinite dilution and x_P the phosphorus molar fraction. In the gas phase:

$$a_P = \frac{p_P}{\gamma^\infty_P p^0_P} \tag{3.32}$$

In order to characterize the distillation efficiency, a **partition coefficient** k_0 shall be used. It is defined as the ratio between the phosphorus and silicon contents in the gas phase related to the one in the liquid phase:

$$k_0 = \frac{\left(\frac{x_P}{x_{Si}}\right)_{(g)}}{\left(\frac{x_P}{x_{Si}}\right)_{(l)}} = \gamma^\infty_P \frac{p^0_P}{p^0_{Si}} \tag{3.33}$$

Distillation then occurs when this coefficient is more than 1. The value of this coefficient k_0 is directly determined from the activity coefficient at infinite dilution of phosphorus, and this for known standard pressures of both elements when the gas phase is monatomic for each component.

In vacuum devices there is a background vacuum which consists of molecules such as $CO_{(g)}$, $H_2O_{(g)}$, or $O_{2(g)}$. The possible role of the oxygen in the distillation

process shall then be taken into account. In Table 3.1 are listed the known molecules in the vapor phase of the Si – O – P system.

Table 3.1: List of the molecules concerned by the study

System considered	Molecules in the vapor phase [3]
Si	Si, Si_2, Si_3
P	P, P_2, P_3, P_4
O	O, O_2, O_3
Si – P	SiP, Si_2P, Si_2P_2
Si – O	SiO, SiO_2, Si_2O_2
P – O	PO, PO_2, P_2O_3, P_2O_4, P_2O_5, P_3O_6, P_4O_6, P_4O_7, P_4O_8, P_4O_9, P_4O_{10}

All partial pressures can be determined by choosing any gaseous partial vaporization equilibria. The corresponding equilibrium constants, presented in Table 3.2, are calculated from the Gurvich thermodynamic tables [3], making the link between partial pressures and activities.

Infinite dilution in Si – P and Si – O

The activity coefficient at infinite dilution characterizes the behavior of the solute component (phosphorus or oxygen) when it is only surrounded by solvent silicon (for binary Si – P and Si – O systems). Knowing the activity coefficient at infinite dilution is essential in order to calculate all the partial pressures of the solute component in the system under distillation.

From the Miki and Zaitsev et al. [7, 10] studies, this coefficient is calculated using Henry's law equation, whereas from the thermodynamic assessment presented in Chapter 2 the coefficient is calculated with the help of Redlich-Kister interaction parameters describing the liquid solution.

In Miki et al. [7] work, the experimental partial pressure measurements of $P_{2(g)}$ is extracted. For the activity (equal to unity) reference the pressure $p^0_{P_2}$ over pure phosphorus (liquid) is calculated from the vaporization equilibrium n°5 stated in Table 3.2 that becomes the equilibrium constant formula:

$$K_p(5) = p^0_{P_2} \tag{3.34}$$

The equilibrium constant depends only on the temperature. Thus, using the vaporization equilibrium n°5, the relation between the phosphorus activity in the liquid and the pressure of $P_{2(g)}$ is:

$$a_P = \sqrt{\frac{p_{P_2}}{p^0_{P_2}}} \tag{3.35}$$

According to Henry's law equation 3.31, the activity coefficient at infinite dilution of phosphorus is then:

Table 3.2: Equilibrium constants of the vaporization reactions according to $\log K_p = \frac{A}{T} + B$

	Vaporization reaction	**Equilibrium constant**	**A**	**B**	***T* range [K]**
1	$Si_{(l)} = Si_{(g)}$	$K_p(1) = \frac{p_{Si}}{a_{Si}}$	-20436	5.8549	
2	$2Si_{(l)} = Si_{2(g)}$	$K_p(2) = \frac{p_{Si_2}}{a_{Si}^2}$	-23923	5.3439	
3	$3Si_{(l)} = Si_{3(g)}$	$K_p(3) = \frac{p_{Si_3}}{a_{Si}^3}$	-23194	4.3462	
4	$P_{(l)} = P_{(g)}$	$K_p(4) = \frac{p_P}{a_P}$	-16908	5.7147	1700 – 2500
5	$2P_{(l)} = P_{2(g)}$	$K_p(5) = \frac{p_{P_2}}{a_P^2}$	-5998.2	5.1931	
6	$3P_{(l)} = P_{3(g)}$	$K_p(6) = \frac{p_{P_3}}{a_P^3}$	-6941.8	-4.5460	
7	$4P_{(l)} = P_{4(g)}$	$K_p(7) = \frac{p_{P_4}}{a_P^4}$	-678.93	2.9330	
8	$Si_{(l)} + P_{(l)} = SiP_{(g)}$	$K_p(8) = \frac{p_{SiP}}{a_{Si}a_P}$	-17789	5.7825	
9	$2Si_{(l)} + P_{(l)} = Si_2P_{(g)}$	$K_p(9) = \frac{p_{Si_2P}}{a_{Si}^2 a_P}$	-15784	4.9735	
10	$2Si_{(l)} + 2P_{(l)} = Si_2P_{2(g)}$	$K_p(10) = \frac{p_{Si_2P_2}}{a_{Si}^2 a_P^2}$	-16962	5.1454	
11	$P_{(l)} + \frac{1}{2}O_{2(g)} = PO_{(g)}$	$K_p(11) = \frac{p_{PO}}{a_P a_O}$	2217.6	3.1949	
12	$P_{(l)} + O_{2(g)} = PO_{2(g)}$	$K_p(12) = \frac{p_{PO_2}}{a_P a_O^2}$	15500	-0.6823	
13	$2P_{(l)} + \frac{3}{2}O_{2(g)} = P_2O_{3(g)}$	$K_p(13) = \frac{p_{P_2O_3}}{a_P^2 a_O^3}$	36370	-5.0949	
14	$2P_{(l)} + 2O_{2(g)} = P_2O_{4(g)}$	$K_p(14) = \frac{p_{P_2O_4}}{a_P^2 a_O^4}$	48977	-10.104	900 – 1500
15	$2P_{(l)} + \frac{5}{2}O_{2(g)} = P_2O_{5(g)}$	$K_p(15) = \frac{p_{P_2O_5}}{a_P^2 a_O^5}$	58367	-12.016	
16	$3P_{(l)} + 3O_{2(g)} = P_3O_{6(g)}$	$K_p(16) = \frac{p_{P_3O_6}}{a_P^3 a_O^6}$	80744	-18.090	
17	$4P_{(l)} + 3O_{2(g)} = P_4O_{6(g)}$	$K_p(17) = \frac{p_{P_4O_6}}{a_P^4 a_O^6}$	83459	-22.538	
18	$4P_{(l)} + \frac{7}{2}O_{2(g)} = P_4O_{7(g)}$	$K_p(18) = \frac{p_{P_4O_7}}{a_P^4 a_O^7}$	102909	-26.452	
19	$4P_{(l)} + 4O_{2(g)} = P_4O_{8(g)}$	$K_p(19) = \frac{p_{P_4O_8}}{a_P^4 a_O^8}$	119188	-30.802	
20	$4P_{(l)} + \frac{9}{2}O_{2(g)} = P_4O_{9(g)}$	$K_p(20) = \frac{p_{P_4O_9}}{a_P^4 a_O^9}$	135154	-35.545	
21	$4P_{(l)} + 5O_{2(g)} = P_4O_{10(g)}$	$K_p(21) = \frac{p_{P_4O_{10}}}{a_P^4 a_O^{10}}$	150100	-40.704	
22	$Si_{(l)} + \frac{1}{2}O_{2(g)} = SiO_{(g)}$	$K_p(22) = \frac{p_{SiO}}{a_{Si}a_O}$	8539.0	2.3934	
23	$Si_{(l)} + O_{2(g)} = SiO_{2(g)}$	$K_p(23) = \frac{p_{SiO_2}}{a_{Si}a_O^2}$	19759	-1.6466	1700 – 2500
24	$2Si_{(l)} + O_{2(g)} = Si_2O_{2(g)}$	$K_p(24) = \frac{p_{Si_2O_2}}{a_{Si}^2 a_O^2}$	27326	-2.1191	
25	$O_{2(g)} = 2O_{2(g)}$	$K_p(25) = \frac{p_{O^2}}{p_{O_2}}$	-26678	6.9848	1700 – 2500
26	$O_{2(g)} = \frac{2}{3}O_{3(g)}$	$K_p(26) = \frac{p_{O_3}}{p_{O_2}^{3/2}}$	-5212.2	-2.2065	

$$\gamma_P^{\infty} = \frac{1}{x_P}\sqrt{\frac{p_{P_2}}{p^0_{P_2}}} \tag{3.36}$$

The resulting values are listed in Table 3.3 which contains the authors experimental results.

Table 3.3: Activity coefficient at infinite dilution of phosphorus in relation with Miki et al. [7] experimental results

T [K]	p_{P_2} [Pa]	wt.% P	**Molar fraction x_P**	**$\ln\gamma_P^{\infty}$**
1823	0.00859	0.0151	**0.000136**	**-1.44830**
	0.0104	0.0185	**0.000167**	**-1.55578**
	0.0331	0.0317	**0.000286**	**-1.51547**
	0.206	0.0637	**0.000575**	**-1.29920**
	0.357	0.0893	**0.000807**	**-1.36211**
	0.492	0.11	**0.000994**	**-1.41024**
1723	0.0212	0.0375	**0.000339**	**-1.68158**
	0.0114	0.033	**0.000298**	**-1.86394**
1748	0.0209	0.03	**0.000271**	**-1.52414**
	0.0111	0.0283	**0.000256**	**-1.78220**
1773	0.0206	0.0274	**0.000247**	**-1.49764**
	0.0108	0.0229	**0.000207**	**-1.64110**
1798	0.0107	0.0219	**0.000198**	**-1.65645**
1848	0.00999	0.0148	**0.000134**	**-1.40511**

In order to get the activity coefficients of Zaitsev et al. [10], one determines it from their experimental results of phosphorus activity as a function of phosphorus composition:

$$\gamma_P^{\infty} = \frac{a_P}{x_P} \tag{3.37}$$

This coefficient is compared to the previous results in Table 3.4.

The presented thermodynamic assessment of the Si – P enables one to calculate the activity coefficient from the Gibbs free energy formula of the Si – P liquid:

$$G^{(l)} = RT(x_P \ln x_P + x_{Si} \ln x_{Si}) + x_P x_{Si}[{}^0L + {}^1L(x_P - x_{Si})] \tag{3.38}$$

relation in which ${}^0L$ and ${}^1L$ are the so-called Redlich-Kister interaction parameters.

The phosphorus chemical potential is the derivative of this energy with respect to the phosphorus number of moles:

$$\mu_P = RT \ln x_P + {}^0L(1 - x_P)^2 + {}^1L(1 - x_P)(-4x_P^2 + 5x_P - 1) \tag{3.39}$$

and with the basic definition:

Table 3.4: Activity coefficient at infinite dilution of phosphorus in relation with Zaitsev et al. [10] experimental results

T [K]	x_P	a_P		$\ln\gamma_P^\infty$	
		experiment	calculation	**experiment**	**calculation**
1693	0.0035	0.00169	0.00161	**-0.72803**	**-0.77653**
1712	0.0035	0.00174	0.00168	**-0.69888**	**-0.73397**
1743	0.0035	0.00179	0.00181	**-0.67055**	**-0.65944**
1743	0.0031	0.00164	0.0016	**-0.63671**	**-0.66140**
1743	0.0027	0.00139	0.00139	**-0.66395**	**-0.66395**
1691	0.0021	0.001	0.00096	**-0.74194**	**-0.78276**
1730	0.0021	0.00105	0.00105	**-0.69315**	**-0.69315**
1771	0.0021	0.00115	0.00115	**-0.60218**	**-0.60218**
1809	0.0021	0.00123	0.00123	**-0.53492**	**-0.53492**
1827	0.0021	0.00122	0.00127	**-0.54309**	**-0.50292**
1823	0.0019	0.00111	0.00114	**-0.53749**	**-0.51083**
1697	0.0012	0.00058	0.00055	**-0.72705**	**-0.78016**
1734	0.0012	0.00062	0.0006	**-0.66036**	**-0.69315**
1782	0.0012	0.00066	0.00067	**-0.59784**	**-0.58280**
1803	0.0012	0.00069	0.00069	**-0.55339**	**-0.55339**
1831	0.0012	0.00071	0.00073	**-0.52481**	**-0.49703**
1819	0.001	0.00058	0.00059	**-0.54473**	**-0.52763**
1819	0.0009	0.00053	0.00053	**-0.52952**	**-0.52952**
1507	0.265	0.177	0.167	**-0.40358**	**-0.46174**
1572	0.201	0.131	0.116	**-0.42811**	**-0.54971**
1618	0.201	0.119	0.127	**-0.52418**	**-0.45912**
1657	0.201	0.133	0.135	**-0.41296**	**-0.39803**
1638	0.104	0.055	0.053	**-0.63706**	**-0.67410**
1653	0.104	0.057	0.053	**-0.60134**	**-0.67410**

$$\mu_P = RT\ln a_P = RT\ln x_P + RT\ln\gamma_P \tag{3.40}$$

Therefore, the activity coefficient at any content of phosphorus is:

$$\ln\gamma_P = \frac{1}{RT}[{}^0L(1-x_P)^2 + {}^1L(1-x_P)(-4x_P^2+5x_P-1)] \tag{3.41}$$

The Redlich-Kister interaction parameters are ${}^0L = -29844.22 + 8.5679\cdot T$ and ${}^1L = 3535.19 - 1.1732\cdot T$. The activity coefficient at infinite dilution is the one deduced at $x_P = 0$ and the relation is:

$$\ln\gamma_P^\infty = \frac{1}{RT}[{}^0L - {}^1L] = -\frac{4014.5}{T} + 1.1715 \tag{3.42}$$

As it can be seen in Figure 3.3, the experimental data are disparate. The data from the thermodynamic optimization offers a compromise and will be therefore

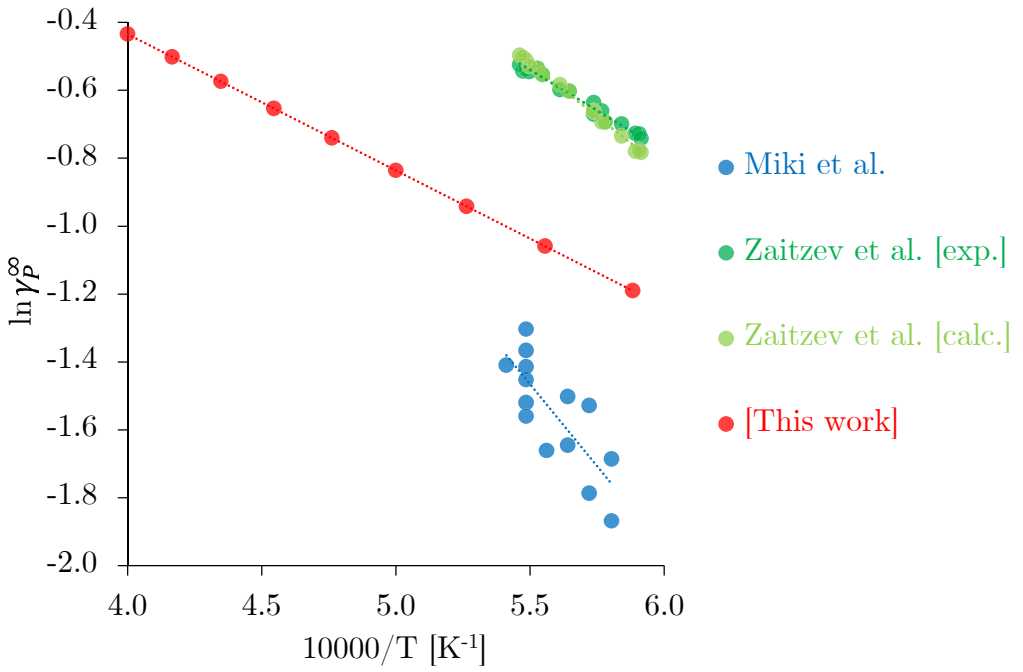

Figure 3.3: Activity coefficients at infinite dilution as a function of the temperature, calculated from Miki et al. [7], Zaitsev et al. [10] and the thermodynamic assessment data

retained.

For upcoming calculations in the ternary Si – O – P system, one first needs to know the activity coefficient at infinite dilution of oxygen in the Si – O system. Henry's law is then used, valid for any diluted element. From the optimized data published in Thermodata [2] the Table 3.5 is recalculated in the 1700 – 2300 K range.

From this table one deduces the following relations for the activity and solubility of O along the liquidus in equilibrium with SiO_2 and the activity of oxygen in silicon:

$$\ln a_O = -\frac{56576}{T} + 11.720 \tag{3.43}$$

$$\ln x_{(O,lim)} = -\frac{15025}{T} - 0.7583 \tag{3.44}$$

$$\ln \gamma_O = -\frac{41551}{T} + 12.478 \tag{3.45}$$

Considering the very low value of the solubility limit, the above activity coefficient is considered as the activity coefficient at infinite dilution.

The oxygen activity values correspond to those who can be deduced from the JANAF thermodynamic tables [1].

Table 3.5: Oxygen solubility and activity calculations in the Si – O system based on the Thermodata [2] optimization

T [K]	$\ln x_{(O,lim)}$	$\ln a_O$	$\ln \gamma_O$
1700	-9.61	-21.5744	-11.96473
1730	-9.45	-20.993	-11.53958
1760	-9.30	-20.4317	-11.12919
1790	-9.16	-19.8896	-10.73287
1820	-9.02	-19.3655	-10.35003
1850	-8.88	-18.8586	-9.980002
1880	-8.75	-18.368	-9.622211
1910	-8.62	-17.8929	-9.276053
1940	-8.49	-17.4327	-8.940967
1970	-8.37	-16.9867	-8.616523
2000	-8.25	-16.5547	-8.301604
2030	-8.15	-16.1392	-7.992874
2060	-8.04	-15.736	-7.693414
2090	-7.94	-15.3446	-7.402787
2120	-7.84	-14.9645	-7.120628
2150	-7.75	-14.5952	-6.84659
2180	-7.66	-14.2363	-6.580346
2210	-7.57	-13.8874	-6.321565
2240	-7.48	-13.5481	-6.069967
2300	-7.31	-12.8965	-5.587095

Narushima et al. [8] recently redetermined the oxygen content in pure silicon in equilibrium with SiO_2 and the deduced activity coefficient at infinite dilution is consistent with the above optimization.

Infinite dilution in Si – O – P

The Wagner interaction coefficients ε are used to describe the diluted solution beyond the range of composition stated by Henry's law. The binary interaction coefficients are expressed as follows:

$$\ln \gamma_{[P]_{(Si)}} = \ln \gamma_P^{\infty} + x_P \varepsilon_P^P \tag{3.46}$$

$$\ln \gamma_{[O]_{(Si)}} = \ln \gamma_O^{\infty} + x_O \varepsilon_O^O \tag{3.47}$$

Binary interaction coefficients ε_P^P and ε_O^O are assessed in the Si – P and Si – O binary system. In the Si – O – P system, the cross coefficient $\varepsilon_O^P = \varepsilon_P^O$ describes the behavior of the ternary system. Concerning the Si – O – P ternary system, the crossing coefficient ε_O^P is obtained from the following equation:

$$\ln \gamma_{[O]_{(Si-O-P)}} = \ln \gamma_O^{\infty} + x_O \varepsilon_O^O + x_P \varepsilon_P^O \tag{3.48}$$

Once they are determined, calculating the partial pressures of every compound, including gaseous oxides will be conceivable.

The binary Si – P Wagner interaction coefficient ε_P^P is firstly determined. Starting from equation 3.41, the value of $\ln \gamma_{[P]_{(Si)}}$ is calculated beyond the Henry's law domain for different temperatures. ε_P^P corresponds to the slopes of the curves presented in Figure 3.4.

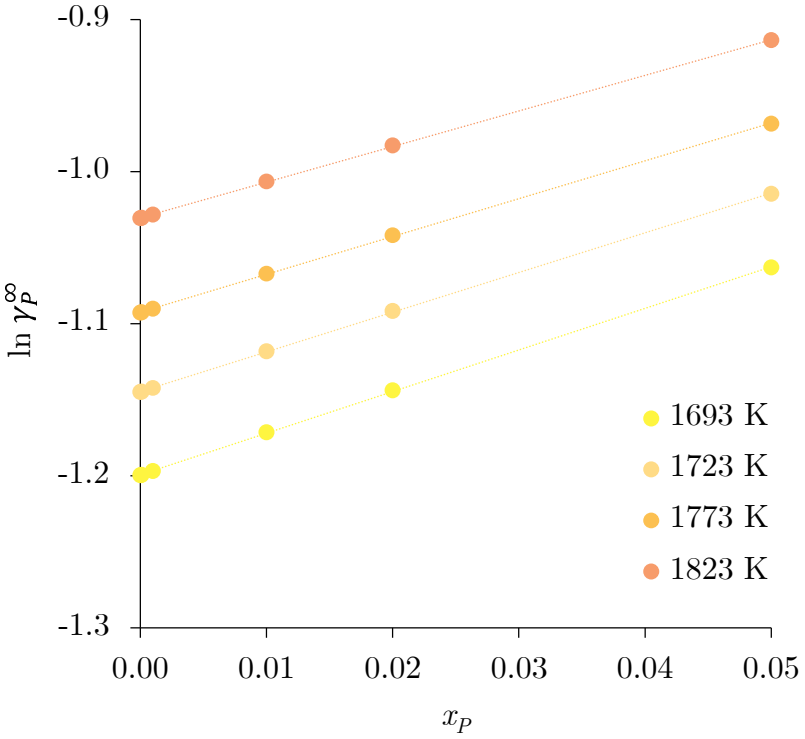

Figure 3.4: Representation in the Si – P system of the activity coefficient of phosphorus diluted in silicon as a function of the phosphorus molar fraction. Values are derived from the thermodynamic assessment presented in the previous chapter.

With the four slope values obtained, the interaction coefficient can be represented as follows:

$$\varepsilon_P^P = \frac{9370.7}{T} - 2.7964 \tag{3.49}$$

Concerning the Si – O system, the binary interaction coefficient ε_O^O is not calculated since the $x_O \varepsilon_O^O$ product is close to zero due to solutions always too diluted ($x_O < 10^{-4}$ according to equation 3.44).

The cross coefficient ε_O^P from the equation 3.48 is determined from the data of Narushima et al. [8] (Table 3.6). The authors give solubility values of phosphorus and oxygen in silicon melts equilibrated with silica at 1693, 1733, 1773 and 1823 K. The activity coefficient of oxygen in the ternary system $\gamma_{[O]_{(Si-O-P)}}$ is calculated from the oxygen activity in the Si – SiO_2 binary system ($a_{Si} = 1$ since the impurities

contents are $< 10^{-3}$) and the oxygen solubility limit x_O is determined by Narushima et al. [8].

The Wagner cross coefficient values obtained are sometimes very different from the mean value for each temperature. These unreasonable values are discarded and the total arithmetic mean value is retained, since no clear evolution with temperature was observed: $\varepsilon_O^P = -37.05$.

Gaseous phase description

Partial pressures over the Si doped P are determined applying Henry's law and for the vaporization of the different phosphorus species $P_{(g)}$, $P_{2(g)}$ and $P_{4(g)}$:

From equation 3.32:

$$\log p_P = \log p_P^0 + \log x_P + \log \gamma_P^\infty \tag{3.50}$$

From equation 3.36:

$$\log p_{P_2} = \log p_{P_2}^0 + 2\log x_P + 2\log \gamma_P^\infty \tag{3.51}$$

From the vaporization reaction n°7 (Table 3.2):

$$\log p_{P_4} = \log p_{P_4}^0 + 4\log x_P + 4\log \gamma_P^\infty \tag{3.52}$$

The standard partial pressures are calculated from Table 3.2, by stating that the phosphorus activity is unity (for pure liquid phosphorus). Indeed, the equilibrium constant only depends on the temperature.

Silicon is the solvent in this study, hence an activity coefficient being unity (Raoult's law), and $a_{Si} = 1 - x_P$. Partial pressures are:

$$\log p_{Si} = \log p_{Si}^0 + \log(1 - x_P) \tag{3.53}$$

$$\log p_{Si_2} = \log p_{Si_2}^0 + 2\log(1 - x_P) \tag{3.54}$$

$$\log p_{Si_3} = \log p_{Si_3}^0 + 3\log(1 - x_P) \tag{3.55}$$

3.2.3 Hertz-Knudsen flows calculation

Distillation in Si – P system

In an enclosure under vacuum, the composition above the melt evolves following evaporation flow of every components. According to vaporization laws, the evaporation flow of any molecule per second and per unit surface into the gas phase is evolving as follows:

$$\Phi_i = \frac{dn}{dt} = \frac{\nu_i p_i}{\sqrt{2\pi M_i RT}} \tag{3.56}$$

where ν_i is a stoichiometric coefficient, p_i a partial pressure, and M_i a molar mass.

Table 3.6: Assessment of the mean ε_P^O value. The bold data are taken from Narushima et al. [8]. The ε_P^O values are calculated from the equation 3.48. Unreasonable values are indicated in italic.

T [K]	P [wt.%]	O [ppm]	$\ln x_P$	$\ln x_O$	$\ln a_O$	$\ln \gamma_O^t$	$\ln \gamma_O$	ε_P^O
	0.361	**39.6**	-5.72161	-9.57365		-12.1087		3.58758
	0.353	**43.2**	-5.74403	-9.48665		-12.1957		-23.5034
	0.0029	**33.4**	-10.5461	-9.74426		-11.9381		*6934.602*
1693	**0.388**	**47.7**	-5.64946	-9.38753	-21.6824	-12.2948	-12.1205	-49.5465
	0.505	**48.0**	-5.38580	-9.38115		-12.3012		-39.4556
	0.932	**49.3**	-4.77263	-9.35403		-12.3283		-24.5768
	0.361	**51.1**	-5.72162	-9.31871		-12.3637		-74.2729
	0.786	**58.9**	-4.94315	-9.17626		-11.7292		-33.737
	0.369	**65.2**	-5.69970	-9.07504		-11.8305		-102.135
	0.0059	**55.5**	-9.83588	-9.23644		-11.6690		*-3372.73*
1733	**0.0248**	**41.5**	-8.39996	-9.52711	-20.9055	-11.3784	-11.4886	*490.1779*
	0.16	**54.8**	-6.53551	-9.24899		-11.6565		-115.703
	0.661	**53.3**	-5.11647	-9.27628		-11.6292		-23.444
	0.797	**79.1**	-4.92926	-8.88139		-12.0241		-74.0447
	0.408	**67.0**	-5.59920	-9.04777		-11.8577		-99.7366
	0.0496	**60.6**	-7.70680	-9.14850		-11.0152		*-288.808*
	0.0036	**48.9**	-10.3299	-9.36305		-10.8006		*2593.495*
	0.312	**60.4**	-5.86755	-9.15156		-11.0121		-44.8202
1773	**0.701**	**63.2**	-5.05768	-9.10588	-20.1637	-11.0578	-10.8853	-27.1227
	0.137	**56.4**	-6.69073	-9.22024		-10.9434		-46.8074
	0.023	**49.5**	-8.47532	-9.35083		-10.8128		*347.371*
	0.313	**57.8**	-5.86434	-9.19555		-10.9681		-29.1787
	0.819	**59.1**	-4.90199	-9.17284		-10.1093		7.940902
	0.406	**60.0**	-5.60411	-9.15811		-10.1240		12.02574
	0.14	**63.5**	-6.66907	-9.10167		-10.1805		-9.576
1823	**0.35**	**70.0**	-5.75259	-9.00402	-19.2821	-10.2781	-10.1683	-34.5887
	0.0316	**60.6**	-8.15766	-9.14851		-10.1336		*121.0554*
	0.052	**65.2**	-7.65955	-9.07533		-10.2068		*-81.6378*
	0.725	**77.5**	-5.02401	-8.90190		-10.3802		-32.2175
	0.0951	**60.3**	-7.05582	-9.15342		-10.1287		45.908
								mean value of ε_P^O -37.0457

This relation is the Hertz-Knudsen molar flow, where the square root of the molar mass plays a role. The Hertz-Knudsen molar flow assumes all molecules that hit back the melt condense and all molecules that evaporate go in the vapor: equilibrium conditions are established when the two flows are equal. In case of the only vaporization process the Hertz-Knudsen equation is correct if the vaporization rate is rapid and there is no activation enthalpy barrier in excess of the vaporization enthalpy, as it is the case generally for liquids due to surface disorder as stated by Pound [9] in a compilation of these coefficients. The only physical limitation to the vaporization flows would come from surface depletion associated with bulk diffusion when equilibrium vaporization flows become too important.

As the escaping gas composition is the composition of the Knudsen flow under vacuum, the partition coefficient can be redefined as follows:

$$k_0 = \frac{\left(\frac{\Phi_P}{\Phi_{Si}}\right)_{(g)}}{\left(\frac{x_P}{x_{Si}}\right)_{(l)}} \tag{3.57}$$

relation in which the flows are atomic flows for each component as calculated from each molecular flow. Using the Hertz-Knudsen relation for each molecular flow, the atomic evaporation flows of silicon and phosphorus are expressed as:

$$\Phi_{Si} = \frac{Sdt}{\sqrt{2\pi RT}}\left(\frac{p_{Si}}{\sqrt{M_{Si}}} + \frac{2p_{Si_2}}{\sqrt{M_{Si_2}}} + \frac{3p_{Si_3}}{\sqrt{M_{Si_3}}} + \frac{p_{SiP}}{\sqrt{M_{SiP}}} + \frac{2p_{Si_2P}}{\sqrt{M_{Si_2P}}} + \frac{2p_{Si_2P_2}}{\sqrt{M_{Si_2P_2}}}\right) \tag{3.58}$$

$$\Phi_P = \frac{Sdt}{\sqrt{2\pi RT}}\left(\frac{p_P}{\sqrt{M_P}} + \frac{2p_{P_2}}{\sqrt{M_{P_2}}} + \frac{3p_{P_3}}{\sqrt{M_{P_3}}} + \frac{4p_{P_4}}{\sqrt{M_{P_4}}} + \frac{p_{SiP}}{\sqrt{M_{SiP}}} + \frac{p_{Si_2P}}{\sqrt{M_{Si_2P}}} + \frac{2p_{Si_2P_2}}{\sqrt{M_{Si_2P_2}}}\right) \tag{3.59}$$

where S is the melted silicon surface, dt is a timestep. The summation takes into account every species presented in Table 3.1. Those atomic flows will be used to calculate the partition coefficient under vacuum.

Distillation in Si – O – P

In an enclosure, due to the vacuum pumping process, the surface of the silicon receives a gas background flow: at the silicon surface, there may be adsorption, reaction with silicon and re-vaporization of these molecules under different species. At 300 K, all the oxygen containing molecules such as $CO_{(g)}$, $H_2O_{(g)}$, $CO_{2(g)}$ are assimilated to a dioxygen incident flow. The total atomic oxygen flow $\Phi_O^{\searrow}$ from the

walls (pumping system at oxygen pressure $p^0_{O_2}$) *incident* to the surface of the melted silicon is:

$$\Phi_O^{\searrow} = \frac{2p^0_{O_2} Sdt}{\sqrt{2\pi M_{O_2} RT_0}} \tag{3.60}$$

whereas another oxygen flow $\Phi_O^{\nearrow}$ *evaporates* from the silicon surface to the walls, taking into account of the formation of all the possible gaseous species existing in the Si – O – P system (Table 3.1):

$$\Phi_O^{\nearrow} = \frac{Sdt}{\sqrt{2\pi RT}}\left(\frac{p_O}{\sqrt{M_O}} + \frac{2p_{O_2}}{\sqrt{M_{O_2}}} + \frac{p_{SiO}}{\sqrt{M_{SiO}}} + \frac{2p_{SiO_2}}{\sqrt{M_{SiO_2}}} + \frac{2p_{Si_2O_2}}{\sqrt{M_{Si_2O_2}}} + \frac{p_{PO}}{\sqrt{M_{PO}}} + \frac{2p_{PO_2}}{\sqrt{M_{PO_2}}} + \frac{3p_{P_2O_3}}{\sqrt{M_{P_2O_3}}} + \frac{4p_{P_2O_4}}{\sqrt{M_{P_2O_4}}} + \frac{5p_{P_2O_5}}{\sqrt{M_{P_2O_5}}} + \frac{6p_{P_3O_6}}{\sqrt{M_{P_3O_6}}} + \frac{6p_{P_4O_6}}{\sqrt{M_{P_4O_6}}} + \frac{7p_{P_4O_7}}{\sqrt{M_{P_4O_7}}} + \frac{8p_{P_4O_8}}{\sqrt{M_{P_4O_8}}} + \frac{9p_{P_4O_9}}{\sqrt{M_{P_4O_9}}} + \frac{10p_{P_4O_{10}}}{\sqrt{M_{P_4O_{10}}}}\right) \tag{3.61}$$

S is the melted silicon surface, T_0 the wall temperature (300 K). When the dynamic pumping reaches its equilibrium, the flow of oxygen that reaches the surface from the housings will be balanced by the flow of oxygen and oxides that goes to the walls, when there is no silica created at the surface (the so-called active oxidation range, for instance described in Honstein et al. [5]). In order to solve this balance, one needs to fix the phosphorus content and the oxygen pressure of the furnace $p^0_{O_2}$ to be considered in the steady state. A surface pressure of O_2 matching an equivalent oxygen vaporization flow is sought.

Every gaseous oxide pressure at the surface is determined from the surface oxygen pressure taking into account the following equilibria:

$$\alpha \mathrm{Si}_{(l)} + \frac{\beta}{2}\mathrm{O}_{2(\mathrm{surface})} = \mathrm{Si}_\alpha \mathrm{O}_{\beta(g)} \tag{3.62}$$

$$\gamma \mathrm{P}_{(l)} + \frac{\delta}{2}\mathrm{O}_{2(\mathrm{surface})} = \mathrm{P}_\gamma \mathrm{O}_{\delta(g)} \tag{3.63}$$

$$\mathrm{O}_{2(\mathrm{surface})} = 2\mathrm{O}_{(g)} \tag{3.64}$$

The upper limit of the surface pressure $p^{lim}_{O_2}$ is the pressure for which SiO_2 is formed at the silicon alloy surface. This pressure is deduced from the equation 3.43 according to:

$$\ln p_{O_2} = 2 \ln a_O \tag{3.65}$$

From this value the oxygen pressure is decreased stepwise until $\Phi_O^{\searrow}$ and $\Phi_O^{\nearrow}$ are equal.

Algorithm 1 Dephosphorization process of a silicon sample

Input: Equilibrium constants $K_p\{\text{Si, P, O, Si – P, P – O, Si – O}\}$ ▷ calc. based upon JANAF
Activity coefficients at infinite dilution γ_P^∞, γ_O^∞ ▷ calc. based upon the optimization
Wagner coefficients ε_P^P, ε_O^O, ε_O^P ▷ calc. based upon Narushima et al.
Partial pressures $p\{\text{Si, P, O, Si – P, P – O, Si – O}\}$
Temperature of the sample T
Initial weight of the sample $m_{Si}(0)$
Initial fraction of phosphorus in sample $x_P(0)$
Output: Weight of the sample m_{Si}
Dephosphorization time t

procedure
for all $p_{O_2} \in \{10^{-10}\text{ bar}; \ldots; 10^{-5}\text{ bar}\}$, $T \in \{1723\text{ K}; \ldots; 2123\text{ K}\}$ **do**
$z = 0$
$m_{Si}(0) = 1.83$ g
$m_P(0) = \dfrac{n_{Si}(0)x_P(0)}{1 - x_P(0)} M_P$ ▷ with $x_P(0) = 50$ ppm
$S(z) = 4\pi r(z)^2$ ▷ with $r(z) = \left(\dfrac{3m_{Si}(z)}{4\pi d_{Si}}\right)^{\frac{1}{3}}$
$\Phi_O^{\searrow} = \dfrac{2p_{O_2}S(z)}{\sqrt{2\pi M_{O_2} R T_0}}$ ▷ with T_0 the temperature of the enclosure walls
for all $i \in \{\log_{10} x_P(0); \ldots; \log_{10} x_P(0) - \alpha\}$ with step_i **do** ▷ with α an arbitrary limit to reach
$dx_P = 10^i - 10^{i+\text{step}_i}$
$a_{Si} = 1 - x_P(i)$
$a_P = \gamma_{[P]_{(\text{Si – O – P})}} x_P(i)$ ▷ with $\ln \gamma_{[P]_{(\text{Si – O – P})}} = \ln \gamma_P^\infty + x_P \varepsilon_P^P + x_O(z)\varepsilon_O^P$
❶ **for all** $j \in \{\log_{10} p_{O_2}^{lim}; \ldots; \log_{10} p_{O_2}^{lim} - \beta\}$ with step_j **do** ▷ with β an arbitrary limit to reach
$a_O = 10^{\frac{j}{2}}$
$a_{Si} = 1 - x_P - x_O$
$\Phi_{Si}^{\nearrow} = \dfrac{S(z)}{\sqrt{2\pi RT}} \left(\sum_\circ \dfrac{\nu_\circ p_{Si_\circ}}{\sqrt{M_{Si_\circ}}} + \sum_\diamond \dfrac{\nu_\diamond p_{Si_\diamond P_\diamond}}{\sqrt{M_{Si_\diamond P_\diamond}}} + \sum_\triangle \dfrac{\nu_\triangle p_{Si_\triangle O_\triangle}}{\sqrt{M_{Si_\triangle O_\triangle}}} \right)$
$\Phi_P^{\nearrow} = \dfrac{S(z)}{\sqrt{2\pi RT}} \left(\sum_\bullet \dfrac{\nu_\bullet p_{P_\bullet}}{\sqrt{M_{P_\bullet}}} + \sum_\diamond \dfrac{\nu_\diamond p_{Si_\diamond P_\diamond}}{\sqrt{M_{Si_\diamond P_\diamond}}} + \sum_\star \dfrac{\nu_\star p_{P_\star O_\star}}{\sqrt{M_{P_\star O_\star}}} \right)$
$\Phi_O^{\nearrow} = \dfrac{S(z)}{\sqrt{2\pi RT}} \left(\sum_\blacktriangle \dfrac{\nu_\blacktriangle p_{O_\blacktriangle}}{\sqrt{M_{O_\blacktriangle}}} + \sum_\triangle \dfrac{\nu_\triangle p_{Si_\triangle O_\triangle}}{\sqrt{M_{Si_\triangle O_\triangle}}} + \sum_\star \dfrac{\nu_\star p_{P_\star O_\star}}{\sqrt{M_{P_\star O_\star}}} \right)$
if $\Phi_O^{\nearrow} < \Phi_O^{\searrow}$ **then**
$\left[\{\log_{10} p_{O_2}^{lim}; \ldots; \log_{10} p_{O_2}^{lim} - \beta\} \textbf{ with step}_j\right] \leftarrow \left[\{j - \textbf{step}_j; \ldots; j\} \textbf{ with } \dfrac{\text{step}_j}{10}\right]$
if $\text{step}_j < \xi$ **then** ▷ with ξ a limit value
go to ❷
end if
end if
go to ❶
end for
❷ $x_O(z) = \dfrac{a_O}{\gamma_{[O]_{(\text{Si – O – P})}}}$ ▷ with $\ln \gamma_{[O]_{(\text{Si – O – P})}} = \ln \gamma_O^\infty + x_O \varepsilon_O^O + x_P(z)\varepsilon_O^P$
$dm_{Si}(z) = \dfrac{m_{Si}(z)dx_P}{[1 - x_P(z) - x_O(z)]\left[\dfrac{\Phi_P}{\Phi_{Si}}(1 - x_P(z)) - x_P(z)\right]}$
$dt(z) = \dfrac{dm_{Si}(z)}{\Phi_{Si} M_{Si}}$
$z = z + 1$
end for
end for
end procedure

3.2.4 Description of the algorithm

Different thermodynamic variables are input. Equilibrium constants K_p of vaporization reactions between molecules in the Si – O – P system are calculated according to JANAF data [1]. Activity coefficients at infinite dilution γ_P^∞, γ_O^∞ as well as Wagner coefficients ε_P^P, ε_O^O, ε_O^P are taken respectively from previous the thermodynamic assessment of Si – P and Narushima et al. [8] to determine activity values and ultimately partial pressures of every gaseous species of this system. In addition to this, characteristics of the sample are introduced such as its temperature, initial weight, and initial fraction of phosphorus $x_P(0)$.

The procedure scans the temperature of the sample and the oxygen pressure of the enclosure. For an iteration z, evaporating Hertz-Knudsen flows of silicon $\Phi_{Si}^{\nearrow}$, phosphorus $\Phi_P^{\nearrow}$ and oxygen $\Phi_O^{\nearrow}$ are evaluated, and the latter is compared to the condensing Hertz-Knudsen flow of oxygen $\Phi_O^{\searrow}$. In Algorithm 1, S is the melted silicon surface, ν the stoichiometric coefficient of the species, T_0 is the wall temperature (300 K) and M their molar mass. Geometric shapes $(\circ, \diamond, \triangle, \bullet, \star)$ are used to describe the different species of Table 3.1 for convenience reasons.

The calculation procedure starts from the pressure $p_{O_2}^{lim}$ at which silica is formed at the sample surface, then decreases in pressure. If the condensing flow $\Phi_O^{\searrow}$ is greater than the evaporating flow $\Phi_O^{\nearrow}$, the iteration step value decreases its order of magnitude to improve the assessment accuracy until a limit value ξ. At this point the weight variation of the sample dm_{Si} and the time variation dt are determined by means of the following equation hereinafter demonstrated:

$$dm_{Si}(z) = \frac{m_{Si}(z)dx_P}{[1 - x_P(z) - x_O(z)]\left[\dfrac{\Phi_P}{\Phi_{Si}}(1 - x_P(z)) - x_P(z)\right]} \tag{3.66}$$

$$dt(z) = \frac{dm_{Si}(z)}{\Phi_{Si} M_{Si}} \tag{3.67}$$

The procedure then continues from the beginning for an iteration $z + 1$. The relative written VBA programs are available in Appendix C.

3.2.5 Results and discussion

Distillation of Si – P diluted alloys

Gaseous phase description In order to evaluate the transport of phosphorus via gaseous phase and, consequently, calculate the total weight loss of silicon during the distillation process, the partial pressures as a function of the composition of phosphorus in the pure binary Si – P diluted in phosphorus are evaluated. They are calculated with equations 3.50, 3.51 and 3.52 using the activity coefficient of the optimization (Figure 3.5). $Si_{(g)}$ is practically constant due to its high purity (Raoult's law). At molar fractions higher than 10^{-4} the main gaseous phosphorus species is $P_{2(g)}$, whereas at low P content ($< 10^{-5}$) the main based phosphorus species remains the only $P_{(g)}$ species.

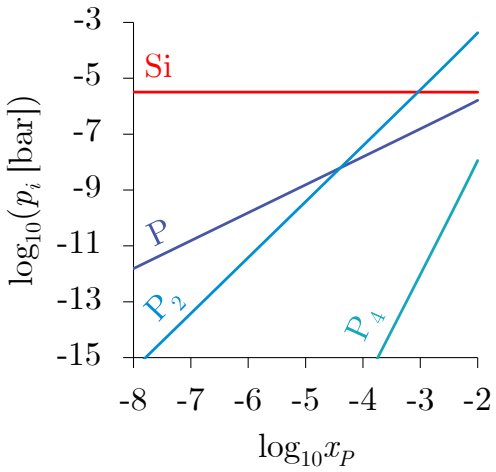

Figure 3.5: Partial pressures of $Si_{(g)}$, $P_{(g)}$, $P_{2(g)}$ and $P_{4(g)}$ as a function of the composition of phosphorus at 1800 K

Partial pressures are presented as a function of the temperature in Figure 3.6 from the optimization. At low temperatures, $P_{2(g)}$ is the predominant species, however it increases less than $P_{(g)}$ with temperature. At high temperatures, the pressures of $P_{(g)}$ and $P_{2(g)}$ meet, whereas $Si_{(g)}$ increases rapidly and finally prevails above 1800 K.

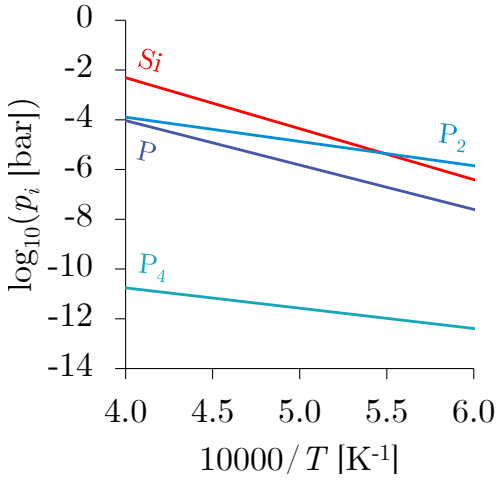

Figure 3.6: Partial pressures of $Si_{(g)}$, $P_{(g)}$, $P_{2(g)}$ and $P_{4(g)}$ as a function of the temperature for a composition of phosphorus of $x_P = 10^{-3}$ at.%

Distillation yield under vacuum In order to evaluate the distillation yield in the binary system Si – P, the partition coefficient is calculated according to the equation 3.57.

In this equation, the distillation process is possible if the ratio is more than one. The present partition coefficient is always so (Figure 3.7), even for low amounts of

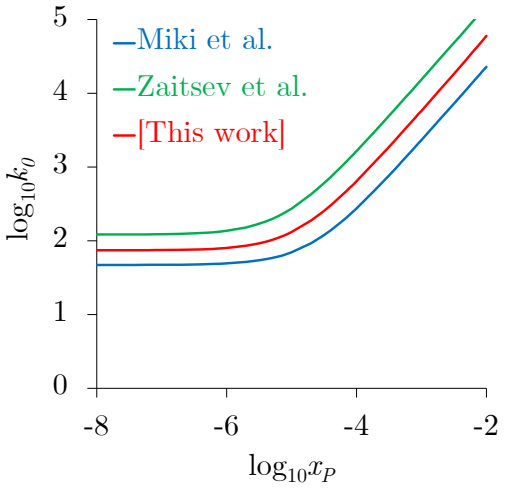

Figure 3.7: Partition coefficient calculated from the presented optimization data as a function of the phosphorus content at 1800 K, and compared to those calculated from Miki et al. [7] and Zaitsev et al. [10]

phosphorus where it lies between 50 and 100, which means that the distillation can occur till pure silicon.

Distillation time and silicon ball weight loss The phosphorus content is expressed in molar fraction:

$$x_P(z) = \frac{n_P(z)}{n_{Si}(z) + n_P(z)} \tag{3.68}$$

A composition step dx_P is fixed that corresponds to a certain dt range. Since the vaporization phenomenon concerns both simultaneously silicon and phosphorus, one writes the Si or P weight losses for the same time dt, according to the following relations:

$$\Phi_{Si} = \frac{dn_{Si}}{dt} = \frac{S}{\sqrt{2\pi RT}} \left(\sum_i \frac{\nu_i p_i}{\sqrt{M_i}} \right) \tag{3.69}$$

$$\Phi_P = \frac{dn_P}{dt} = \frac{S}{\sqrt{2\pi RT}} \left(\sum_j \frac{\nu_j p_j}{\sqrt{M_j}} \right) \tag{3.70}$$

Then from equations 3.69 and 3.70 one gets:

$$\frac{dn_{Si}}{\Phi_{Si}} = \frac{dn_P}{\Phi_P} \tag{3.71}$$

This relation relates Si and P weight losses. For a fixed dx_P, one needs to find the Si (or P) weight loss at the final composition $x_P(z) + dx_P$. By deriving the phosphorus content (equation 3.68), a relation between silicon and phosphorus weight losses can be obtained:

$$dx_P = \frac{dn_P}{n_{Si} + n_P} - n_P \frac{dn_{Si} + dn_P}{(n_{Si} + n_P)^2} \tag{3.72}$$

Using equation 3.71, dn_P is eliminated:

$$(n_{Si} + n_P)dx_P = dn_{Si}\frac{\Phi_P}{\Phi_{Si}}(1 - x_P) - x_P dn_{Si} \tag{3.73}$$

$$(n_{Si} + n_P)M_{Si}dx_P = dm_{Si}\left[\frac{\Phi_P}{\Phi_{Si}}(1 - x_P) - x_P\right] \tag{3.74}$$

Using equation 3.68:

$$M_{Si}\frac{n_P}{x_P}dx_P = dm_{Si}\left[\frac{\Phi_P}{\Phi_{Si}}(1 - x_P) - x_P\right] \tag{3.75}$$

$$M_{Si}\frac{n_{Si}}{1 - x_P}dx_P = dm_{Si}\left[\frac{\Phi_P}{\Phi_{Si}}(1 - x_P) - x_P\right] \tag{3.76}$$

Thus:

$$dm_{Si} = \frac{m_{Si}dx_P}{\frac{\Phi_P}{\Phi_{Si}}(1 - x_P)^2 - x_P(1 - x_P)} \tag{3.77}$$

From this relation, the weight loss of silicon leads to a decrease of the silicon ball surface, which is taken into account in the flow reactions. As the phosphorus content is very low, one only considers the silicon density ρ_{Si}:

$$S = 4\pi\left(\frac{3m_{Si}}{4\pi\rho_{Si}}\right)^{\frac{2}{3}} \tag{3.78}$$

In the electromagnetic levitation pilot development presented in the next chapter, calibrated silicon samples of 1.83 g and containing 50 ppm of phosphorus are operated. For such a silicon ball, the dephosphorization time (down to 0.5 ppm) and the ball weight loss as a function of the temperature are presented in Figure 3.8.

On the one hand, the dephosphorizing process requires less time when the temperature increases. The time necessary to obtain a ball with 0.5 ppm of phosphorus is eight time less important between 1700 and 2000 K. On the other hand, the ball loses more weight for high temperatures, but is generally rather low (up to only 1.70% for 2000 K).

Distillation of Si – O – P diluted alloys

Gaseous phase evolution To find out the influence of the residual oxygen present in the vacuum, the gaseous species formed above the melt are shown when the 0.069 m^3 chamber used in the levitation experiment has a high vacuum associated with sufficient pumping capacities (i.e., $p_{O_2} = 10^{-9}$ bar, Figure 3.9) and when it reaches

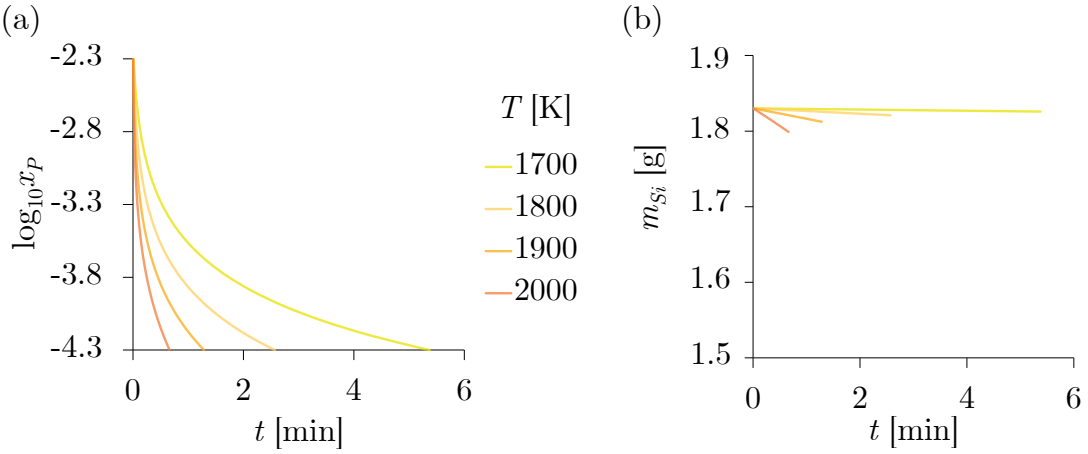

Figure 3.8: Silicon (a) dephosphorization time and (b) weight loss as a function of the temperature for a 1.83 g ball initially containing 50 ppm and dephosphorizing down to 0.5 ppm

the Knudsen limit $p_{O_2} = 10^{-4}$ bar, Figure 3.10). Figure 3.9 and 3.10 do not consider molecules such as $O_{2(g)}$, $O_{3(g)}$, $P_{3(g)}$, $PO_{2(g)}$, $P_2O_{3(g)}$ and the other phosphorus oxides because their partial pressures are too low. Compared to Figure 3.5, the behavior of the partial pressures of $Si_{(g)}$, $P_{(g)}$, $P_{2(g)}$ and $P_{4(g)}$ as a function of the composition of phosphorus is the same as in the Si – O – P system regardless of the dioxygen pressure of the pumps. This p_{O_2} does not affect either $Si_{2(g)}$, $Si_{3(g)}$, $O_{(g)}$, $Si_2P_{(g)}$, $SiP_{(g)}$ or $Si_2P_{2(g)}$.

$Si_{(g)}$, $Si_{2(g)}$, $SiO_{(g)}$, $Si_{3(g)}$, and $O_{(g)}$ are practically constant owing to Raoult's law, and they prevail in that order. Concerning the phosphorus species, $P_{2(g)}$ is the most important one for high amounts of phosphorus ($> 10^{-5}$). Beneath this value is $P_{(g)}$ immediately followed by $Si_2P_{(g)}$ and $SiP_{(g)}$.

At the Knudsen limit, several silicon oxides emerge: $SiO_{(g)}$ predominates at almost 10^{-3} bar regardless the phosphorus composition. Following $Si_{(g)}$ and right above $Si_{2(g)}$ is the $Si_2O_{2(g)}$, also practically constant. Finally, $SiO_{2(g)}$ lies above the $O_{(g)}$ at less than 10^{-11} bar. The most important phosphorus oxide is $PO_{(g)}$, varying roughly between 10^{-15} and 10^{-9} bar from 10^{-8} to 10^{-2} in phosphorus content. Thus, when there is an important amount of oxygen in the enclosure, the oxygen leaves the silicon mostly in the form of silicon oxides.

Distillation yield under vacuum Figure 3.11 (a) presents the partition coefficient for the Si – O – P system.

At low temperatures near the melting point of the silicon, the more p_{O_2} is sent from the enclosure the less important is this coefficient. In that case, $O_{2(g)}$ is clearly a hindrance to the distillation. For higher temperatures, however, the dioxygen seems to have no particular effect on the partition coefficient: for different p_{O_2} sent from the vessel, its values converge to a single point.

Figure 3.11 (b) represents the partition coefficient for the temperature of 1800 K but at different enclosure oxygen pressures. The introduction of $O_{2(g)}$ hampers the

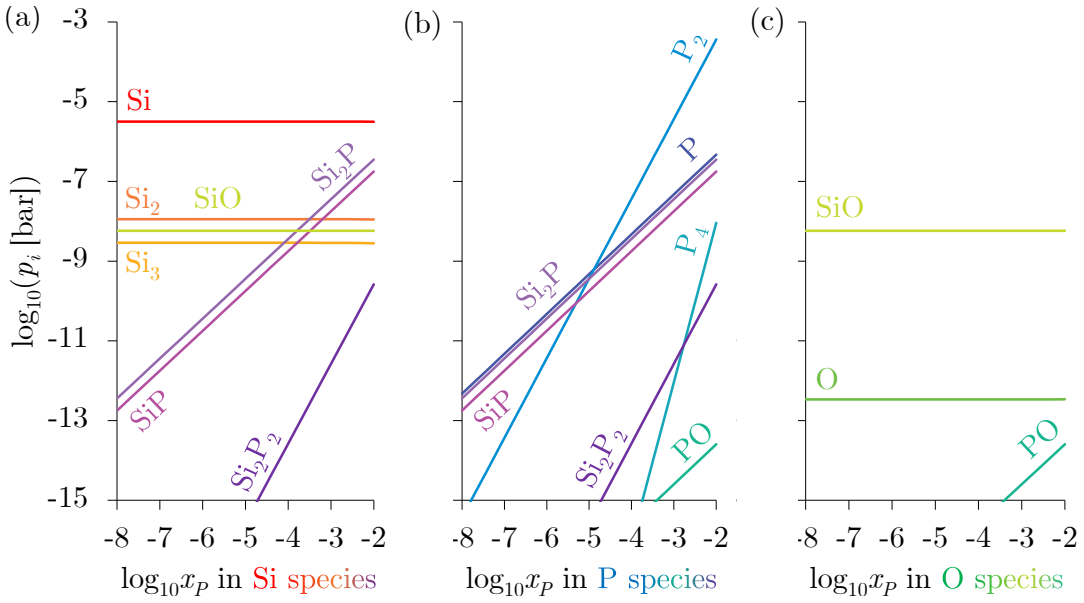

Figure 3.9: Partial pressures of (a) Si species (b) P species and (c) O species under $p_{O_2} = 10^{-9}$ bar as a function of the composition of phosphorus at 1800 K

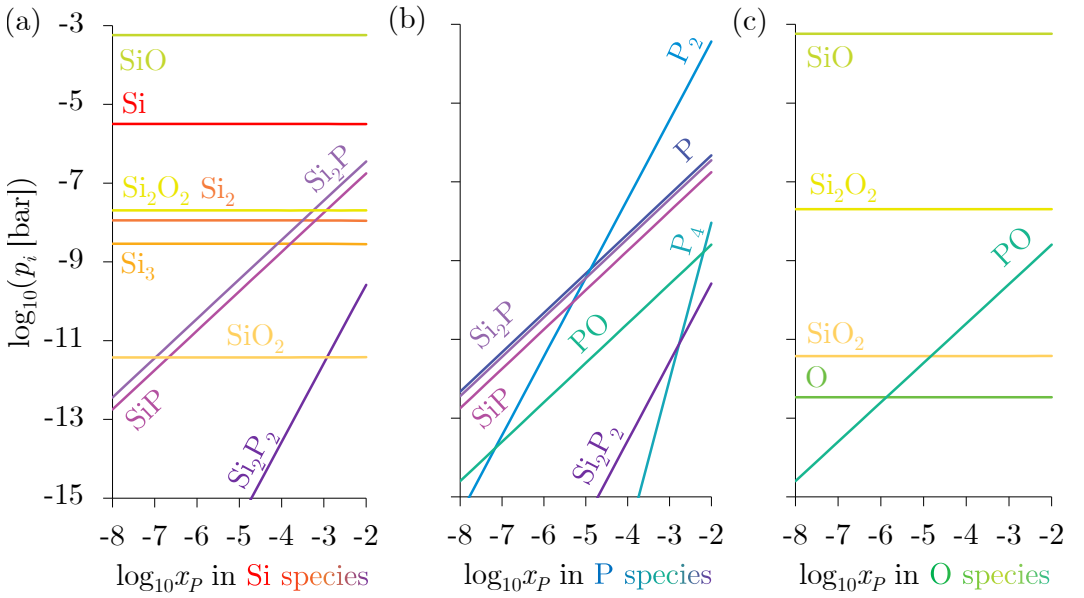

Figure 3.10: Partial pressures of (a) Si species (b) P species and (c) O species pressures under $p_{O_2} = 10^{-4}$ bar as a function of the composition of phosphorus at 1800 K

distillation starting from 10^{-7} bar of p_{O_2}. For low amounts of phosphorus ($< 10^{-5}$), the value of the partition coefficient falls to 10 for 10^{-6} bar, 2 for 10^{-5} bar and the distillation is not possible for $p_{O_2} = 10^{-4}$ bar under a phosphorus content of 10^{-4}.

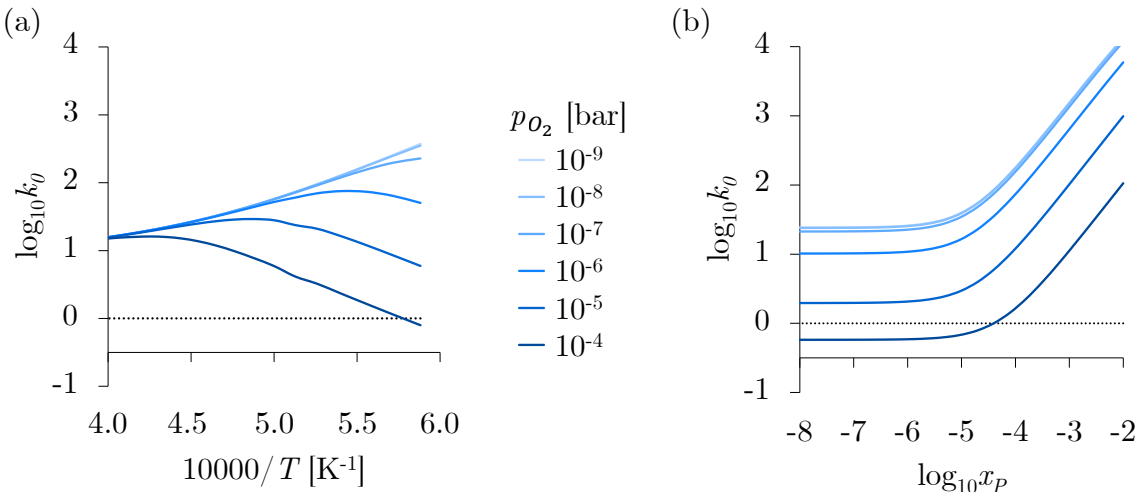

Figure 3.11: Partition coefficient as a function of (a) the temperature for a phosphorus content of $x_P = 10^{-4}$ and (b) the phosphorus content, for a temperature of 1800 K and different enclosure oxygen pressures

Distillation time and silicon ball weight loss In that case the phosphorus content is expressed by considering also the oxygen molar fraction:

$$x_P(z) = \frac{n_P(z)}{n_{Si}(z) + n_P(z) + n_O(z)} \tag{3.79}$$

The oxygen content of the silicon ball does not vary since the incident flow equals the evaporating flow: $dn_O = 0$. Finding the Si weight loss at the final composition $x_P(z) + dx_P$ is feasible the same way as previously, by deriving the phosphorus content:

$$dx_P = \frac{dn_P}{n_{Si} + n_P + n_O} - n_P \frac{dn_{Si} + dn_P}{(n_{Si} + n_P + n_O)^2} \tag{3.80}$$

Using equation 3.71, dn_P is eliminated:

$$(n_{Si} + n_P + n_O)dx_P = dn_{Si}\frac{\Phi_P}{\Phi_{Si}}(1 - x_P) - x_P dn_{Si} \tag{3.81}$$

$$(n_{Si} + n_P + n_O)M_{Si}dx_P = dm_{Si}\left[\frac{\Phi_P}{\Phi_{Si}}(1 - x_P) - x_P\right] \tag{3.82}$$

Using equation 3.79:

$$M_{Si}\frac{n_P}{x_P}dx_P = dm_{Si}\left[\frac{\Phi_P}{\Phi_{Si}}(1 - x_P) - x_P\right] \tag{3.83}$$

$$M_{Si}\frac{n_{Si}}{1 - x_P - x_O}dx_P = dm_{Si}\left[\frac{\Phi_P}{\Phi_{Si}}(1 - x_P) - x_P\right] \tag{3.84}$$

Thus:

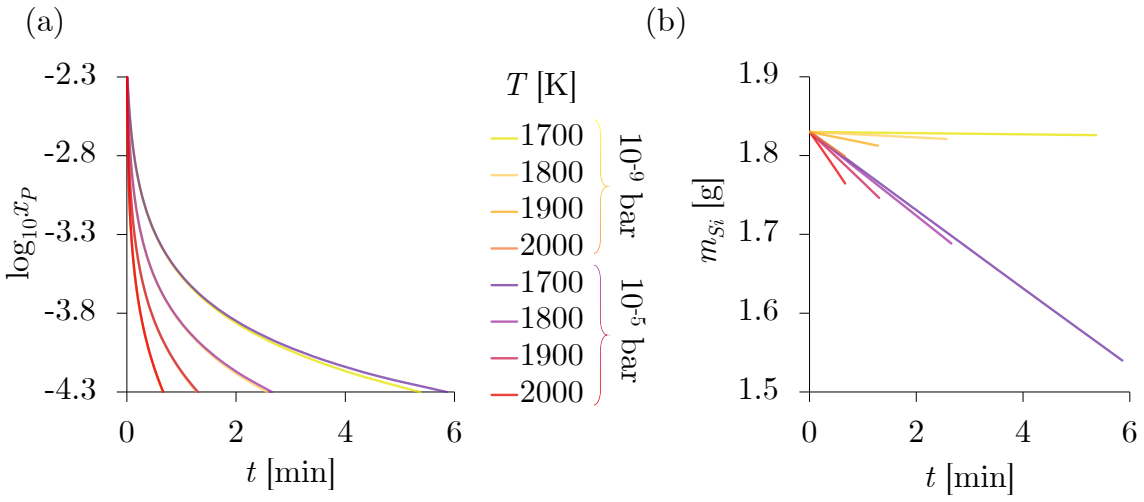

Figure 3.12: Silicon (a) dephosphorization time and (b) weight loss as a function of the temperature for a 1.83 g ball initially containing 50 ppm and dephosphorizing down to 0.5 ppm for different enclosure oxygen pressures

$$dm_{Si} = \frac{m_{Si} dx_P}{(1 - x_P - x_O)\dfrac{\Phi_P}{\Phi_{Si}}(1 - x_P) - x_P} \tag{3.85}$$

Figure 3.12 shows the distillation time for a 1.83 g silicon ball containing 50 ppm of phosphorus exposed at each end of the oxygen pressure range in the vessel, as a function of the temperature. According to Figure 3.11 (a), the distillation cannot occur for $p_{O_2} = 10^{-4}$ bar for few amounts of phosphorus.

For $p_{O_2} = 10^{-9}$ bar, the dephosphorizing time and the silicon weight loss are logically very similar to the ones without the oxygen in Figure 3.8. However for $p_{O_2} = 10^{-5}$ bar, those two parameters increase: significantly for low temperatures, and slightly for the high ones.

A wider visualization of the phenomenon may be desired to deepen its understanding. In Figure 3.13 the distillation time is given for $p_{O_2} \in \{10^{-10}; ...; 10^{-5}\}$ bar and $T \in \{1723; ...; 2123\}$ K. It exponentially increases from 18 seconds at 2123 K to approximately 271 seconds at 1723 K from 10^{-10} to 10^{-6} bar: the impact of p_{O_2} in the enclosure is extremely minor. Above and up to 10^{-5} bar – the order of magnitude below the Knudsen limit – the distillation time is mildly affected for the lowest temperatures: at 1723 K it increases to 290 seconds.

The corresponding final weight loss of the sample is given in Figure 3.14. For $p_{O_2} < 10^{-7}$ bar the results are identical: the sample loses from 0.3% to 3.0% of its weight from 1723 to 2123 K. Above this pressure, the loss increases exponentially when the sample cools down to the melting point. At 1723 K the sample loses 13.2% of its weight for $p_{O_2} = 10^{-5}$ bar.

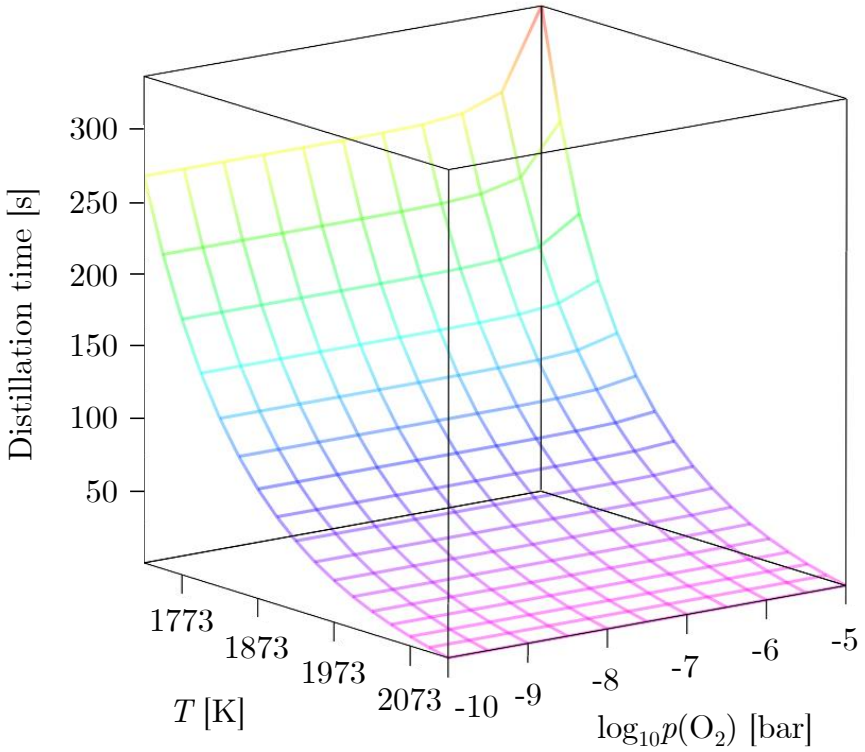

Figure 3.13: Distillation time of a silicon sample initially of 1.83 g dephosphorized from 50 to 0.5 ppm. The temperature step is 25 K and the $\log_{10} p_{O_2}$ step is 0.5.

3.2.6 Conclusions

Using available thermodynamic data and the optimization of the Si – P system presented in the previous chapter, one confirms that removing the phosphorus from the molten silicon is feasible.

From the thermodynamic calculations, if one considers the binary Si – P, a 1.83 g silicon ball at 1800 K containing 50 ppm phosphorus, it is found out that phosphorus is thermodynamically carried away from the melt as $P_{2(g)}$, until the phosphorus ratio reaches 10^{-3} when $Si_{(g)}$ becomes the major gaseous species. In this case, the distillation yield, which is given by the composition ratio of phosphorus and silicon in the liquid phase and in the gas phase, was found to be above 50%.

It takes 154 seconds to distill to 0.5 ppm P, and loses 0.49% of its mass. If $p_{O_2} = 10^{-9}$ bar, those parameters remain unchanged.

However, at the Knudsen limit ($p_{O_2} = 10^{-4}$ bar), the oxygen evaporates in the form of silicon oxides rather than phosphorus oxides: $SiO_{(g)}$ is the main species in that case.

The distillation yield is also affected: for low phosphorus contents ($< 10^{-5}$) the phenomenon is not conceivable. For $p_{O_2} = 10^{-5}$ bar, the dephosphorizing time is 160 seconds, which is not an inconvenient, yet the ball loses 7.74% of its weight.

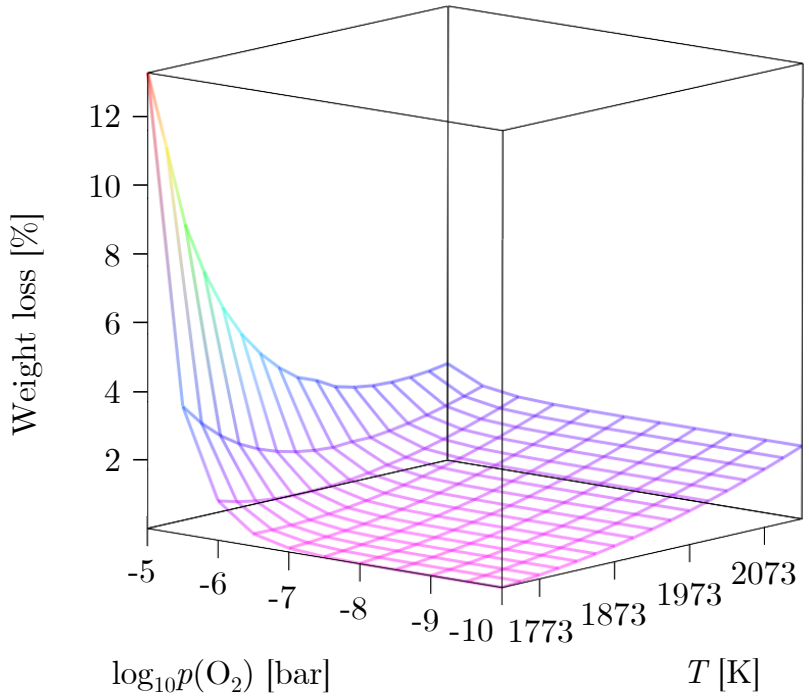

Figure 3.14: Weight loss of a silicon sample initially of 1.83 g dephosphorized from 50 to 0.5 ppm. The temperature step is 25 K and the $\log_{10} p_{O_2}$ step is 0.5.

The effect of the parameters discussed on the dephosphorization process shall now be examined experimentally. For this purpose an electromagnetic levitation device will be used.

Bibliography

[1] M. W. Chase, *NIST-JANAF Thermochemical tables*, no. 4, american chemical society and the american institute of physics for the national institute of standards and technology ed.

[2] B. Cheynet, P. Chaud, P.-Y. Chevalier, E. Fischer, P. Mason, and M. Mignanelli, *Nuclea "proprietes thermodynamiques et equilibres de phases dans les systemes d'interet nucleaire"*, in Journal de Physique IV (Proceedings), vol. 113, EDP sciences, 2004, pp. 61–64.

[3] L. V. Gurvich and I. Veyts, *Thermodynamic Properties of Individual Substances: Elements and Compounds*, vol. 2, CRC press, 1990.

[4] H. Hertz, *Uber die beruhrung fester elastischer korper.*, Journal fur die reine und angewandte Mathematik, 92 (1882), pp. 156–171.

[5] G. Honstein, C. Chatillon, and F. Baillet, *Thermodynamic approach to the vaporization and growth phenomena of sic ceramics. ii. the sic surface under oxidative conditions*, Journal of the European Ceramic Society, 32 (2012), pp. 1137–1147.

[6] M. Knudsen, *Die maximale verdampfungsgeschwindigkeit des quecksilbers*, Annalen der Physik, 352 (1915), pp. 697–708.

[7] T. Miki, K. Morita, and N. Sano, *Thermodynamics of phosphorus in molten silicon*, Metallurgical and Materials Transactions B, 27 (1996), pp. 937–941.

[8] T. Narushima, K. Matsuzawa, Y. Mukai, and Y. Iguchi, *Oxygen solubility in liquid silicon*, Materials Transactions, JIM, 35 (1994), pp. 522–528.

[9] G. Pound, *Selected values of evaporation and condensation coefficients for simple substances*, Journal of Physical and Chemical Reference Data, 1 (1972), pp. 135–146.

[10] A. I. Zaitsev, A. D. Litvina, and N. E. Shelkova, *Thermodynamic properties of si–p melts*, High Temperature, 39 (2001), pp. 227–232.

4

Experimental development with electromagnetic levitation

WITHIN the SIMaP laboratory, Beaudhuin [3] developed an **electromagnetic levitation** (EML) setup called SPYCE[1] initially to determine the undercooling of a pure element versus impurity concentration.

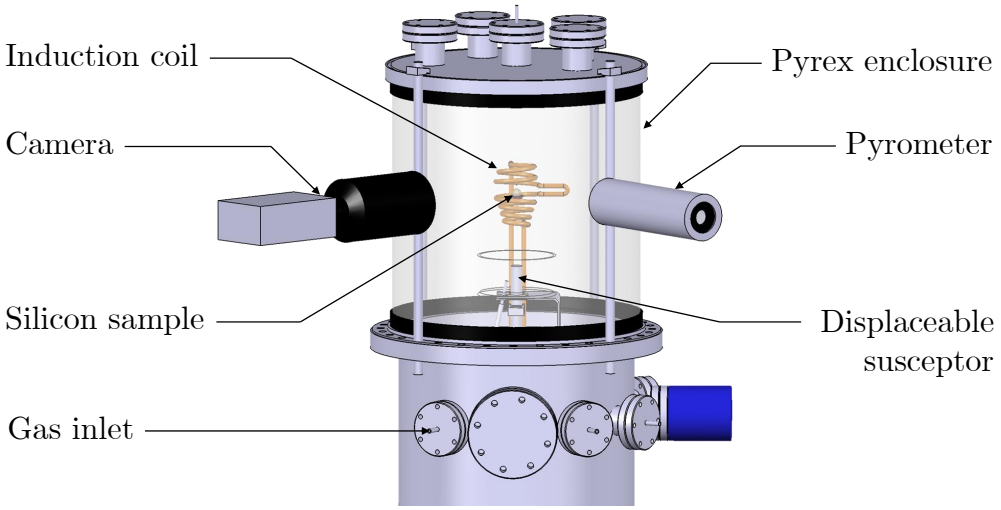

Figure 4.1: Original design of the core of SPYCE

Involved in the same photovoltaic framework, he investigated a problem present in the solidification step: the silicon degree of purity affects to an unknown extent the structure and properties of casted ingots. Si_3N_4 and SiC are two of the major

[1] **S**ilicon **P**urit**Y** **C**ontrolled under **E**lectromagnetic levitation

impurities that precipitate at the solid/liquid interface and alter the grain growth. He succeeded in predicting experimentally the amount of precipitates in the silicon droplets by controlling p_{CH_4} and p_{N_2} inlet partial pressures [4].

One foresees the diversion of its initial use to remove phosphorus from molten silicon without any crucible.

4.1 Specific features of the device

Sundry characteristics of the EML setup legitimize its use in this study. The core of this levitation apparatus is condensed Figure 4.1.

First and foremost its employment is justified by the need of having a clean and controlled environment to validate the simulation presented in the previous chapter. Si, P and residual O included inside are indeed the only elements considered. The most essential feature of this device is firstly introduced.

4.1.1 Electromagnetic levitation

From the will of getting rid of the contamination inherent to crucibles arises the idea of levitating metals. A patent deposited by Muck pioneered this technology in 1923 [11], albeit it fell into oblivion for decades. It regained interest only in the beginning of the 1950s as reliable devices emerged at the laboratory scale for generating the required electromagnetic field strengths. It did insomuch that it is presently featured in the set of experimental devices of the International Space Station[2] (Figure 4.2).

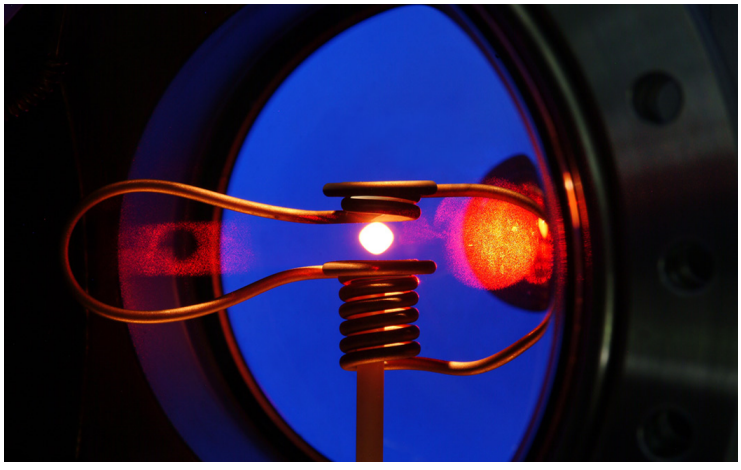

Figure 4.2: Picture of the ISS Electromagnetic Levitator, from [2]

In order to develop a clear understanding of this process, a few reminders are given beforehand.

[2]The microgravity conditions remove the stirring phenomenon of the sample.

Faraday's law of induction describes the interaction between an external magnetic field $\vec{B}$ and an electrical circuit in a resulting electromotive force $\mathcal{E}$, *i.e.* an electrical field $\vec{E}$ circulation $\oint_{\partial\Sigma} \vec{E} \cdot d\vec{l}$.

Faraday experimentally noticed in 1831 that $\mathcal{E}$ is induced by a *variation* in magnetic flux[3] Φ_B, that is:

$$\mathcal{E} = -\frac{d\Phi_B}{dt} \tag{4.1}$$

Considering the formulas which define of $\mathcal{E}$ and Φ_B, it is nothing more than the integral version of the Maxwell – Faraday's equation ulteriorly established:

$$\vec{\nabla} \wedge \vec{E} = -\frac{\partial \vec{B}}{\partial t} \tag{4.2}$$

The negative sign of equation 4.1 indicates a meaningful statement: the magnetic field resulting from this induced current will be in the opposite direction of the variation of Φ_B. This is a direct consequence of the conservation of energy.

This feature has been independently discovered by Heinrich Lenz, hence this formula also being referred as **Lenz's law**.

The heart of the EML stands in Lenz's law applied on a material with conductive properties, *e.g.* liquid silicon. A visual description accompanies the following explanation in Figure 4.3.

A high frequency (HF) alternative electrical current is applied in an induction coil, generating a magnetic field $\vec{B}$ around its windings. This induces currents – called eddy currents – in the conductive sample. The simultaneous presence of the magnetic field and an induced current density $\vec{j}$ results in an electromagnetic force $\vec{F}_L = \vec{j} \wedge \vec{B}$ called **Lorentz force** that governs the interaction between the sample and the coil. When $\vec{F}_L$ exceeds the gravitational force $\vec{F}_G = m\vec{g}_n$, the conductive sample levitates.

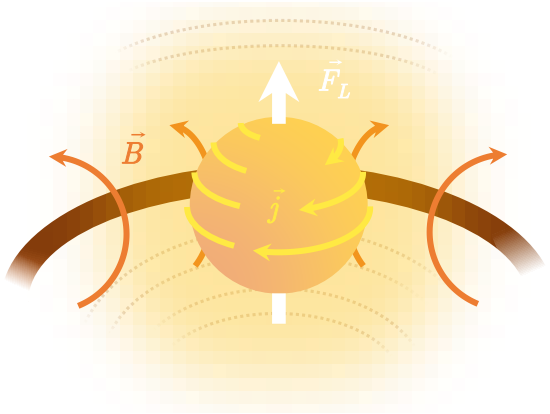

Figure 4.3: Illustration of the EML principle

[3]Related to $\vec{B}$ by $\Phi_B = \iint_\Sigma \vec{B} \cdot \vec{n} dS$

A convenient byproduct of the induced currents is the important **Joule effect** that can heat the sample up to its melting temperature. The power absorbed by this latter will be discussed in section 4.1.3. To avoid the same fate for the coil, water flows through the copper tubing to cool it.

Another great advantage of this levitation technique is that the melt is thoroughly stirred electromagnetically.

In the molten droplet, the internal flow consists of two counter-rotating vortices at the top and bottom part. In gravity conditions, these are dissymmetrical as shown in Figure 4.4:

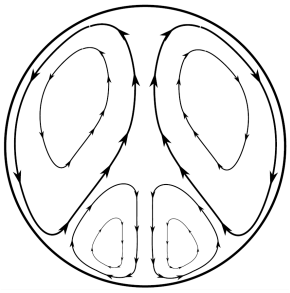

Figure 4.4: Illustration of the electromagnetic stirring in the droplet [14]

The Alfvén speed characterizes the maximum rotational speed it can achieve when submitted to a magnetic field:

$$v_{\mathrm{A}} = \sqrt{\frac{B^2}{\rho \mu_0}} \tag{4.3}$$

where ρ is the density of the sample in kg.m^{-3} and $\mu_0 = 4\pi \cdot 10^{-7}$ H.m^{-1} is the permeability constant.

Alfvén speed in the range of 0.5 – 2 m.s^{-1} is expected [3]. It can be considered thermally and chemically homogeneous in the experiment timescale as the average speed of the silicon droplet resulting is 0.2 – 0.3 m.s^{-1} [3, 9].

EML has been proved to be an interesting technique for operating without any contaminant crucible an homogeneous liquid silicon. It can moreover protect it by a suitable atmosphere or a vacuum.

4.1.2 Surrounding environment

Constitution choice

Operating in a clean environment is a central item in the specifications of the experimental investigation. In the initial setup, the experiment takes place in a 69 L vessel consisting of a cylindrical wall made of borosilicate glass (Figure 4.1). To clean its content, manipulating under vacuum is preferred over using an inert gas. This choice is more deeply explained in Appendix D.

Vacuum technology

For a vacuum line of characteristic length L, different flow regimes can be defined depending on the mean free path ℓ of the remaining particles – more precisely the remaining gas pressure, its nature, speed and viscosity. The adimensionnal Knudsen number Kn is used to characterize it:

$$\mathrm{Kn} = \frac{\ell}{L} \tag{4.4}$$

For dry air at 300 K, a flow is said viscous if the mean free path is negligible compared to L, thus for $\mathrm{Kn} < 0.01$. When the Kn value is between 0.01 and 1, the flow is transitory. Above one, it is referred as a molecular flow. In Figure 4.5 is illustrated these regimes for the present case.

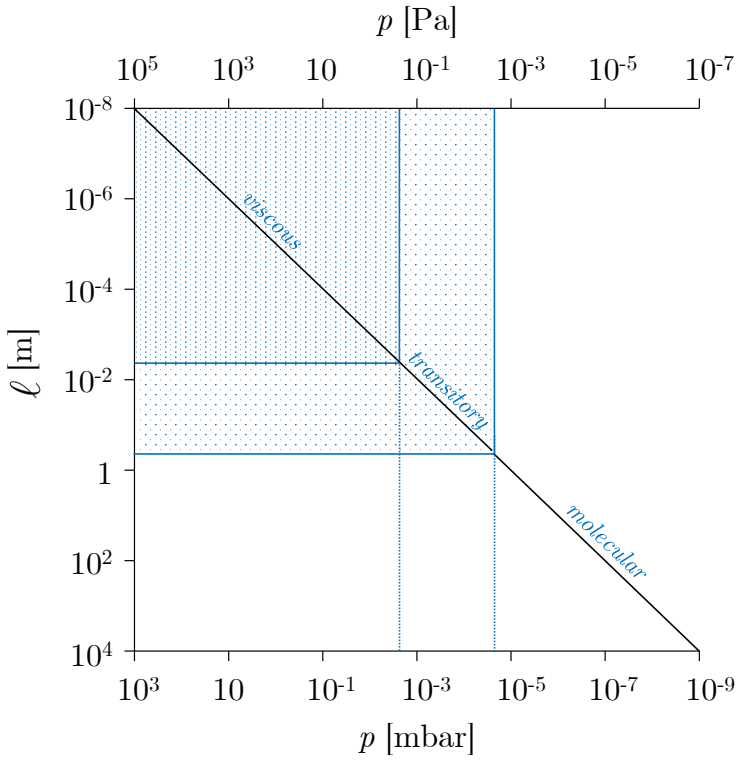

Figure 4.5: Different categories of flows for the present enclosure of 69 L at 300 K

Several kinds of pumping systems can be employed to reach a proper molecular flow regime. The initial setup required a series of three different pumps to reach a dynamic vacuum of $1 \cdot 10^{-8}$ mbar and a static one of $1 \cdot 10^{-6}$ mbar. These pumps are not oil or water filled but dry, which prevents from any backscattering of matter into the enclosure. Their functioning is here introduced.

Firstly, a **diaphragm pump**[4] is used: a vibrating elastomer diaphragm alternatively drags from each of its sides the air of the enclosure out to a valve. It acts as a

[4] Also known as membrane pump.

primary pump, which means that it can evacuate the gas at atmospheric pressure, but here only down to 10^{-2} mbar.

A **turbomolecular pump** is activated thereafter as a secondary pump. It comprises a bladed rotor inserted in a stator with opposite angled fins. The important rotation speed drags the gas molecules towards the outlet pipe which is connected to the primary pump. With the initial model used – a Leybold Turbovac TW 70 H with a N_2 pumping speed of 65 L.s^{-1} –, a dynamic vacuum of about 10^{-7} mbar is theoretically achievable. In practice, 10^{-5} mbar is rather the order of magnitude obtained, mostly due to the large size of the vessel in comparison.

An **ion pump** from the Riber manufacturer is finally used as a complementary device on the initial setup, once the turbomolecular reaches its limit. An assembly of stainless steel tubes constitutes the anodic part and is surrounded by two titanium based cathodes. The overall is submitted to an axial magnetic field. The gas is ionized at low pressure and is chimisorbed to the titanium surfaces. A vacuum of 10^{-7} mbar could be obtained with such a device.

When an apparatus is connected to a pump, the resulting vacuum may vary according to several factors : leaks from the seals, walls degassing, or else a differential vacuum induced by various canalization diameters.

4.1.3 Temperature control

Silicon needs to be molten to process dephosphorization. To that end, a radio frequency (RF) generator is used: indeed its power and frequency – up to 50 kW and 135 kHz – do not only affect levitation, but also the heating of the sample by Joule effect. The intertwining of these two factors is briefly exposed.

Consider a spherical sample of a given material of radius r, electrical conductivity σ and magnetic permeability[5] μ surrounded by a vacuum in which there exists an uniform unidirectional sinusoidally alternating magnetic field of angular frequency $\omega = 2\pi f$.

Eddy currents are induced in the sphere and depend on those parameters. For estimating the impact of the alternating magnetic field on the sphere, defining the skin depth δ of the sample is necessary. It is a certain surface depth of the sphere that is the most conductive, and is settled by:

$$\delta = \sqrt{\frac{2}{\omega\sigma\mu_0}} \tag{4.5}$$

In the appendix of Rony [13] the lifting Lorentz force acting on the sample has been demonstrated to be related to all those parameters by:

$$\vec{F_L} = -\frac{2\pi r^3}{\mu_0} G(q) \nabla \vec{B}^2 \qquad \text{with } G(q) = 1 - \frac{3}{2q}\frac{\sinh 2q - \sin 2q}{\cosh 2q - \cos 2q} \tag{4.6}$$

[5]For non magnetic materials like silicon, the permeability constant is used.

$G(q)$ being the dimensionless force function of the radius-to-skin-depth ratio $q = \frac{r}{\delta}$.

Regarding the power of heating absorbed by the sample, he found that:

$$P = \frac{3\pi r}{\sigma\mu_0^2} H(q) B^2 \qquad \text{with } H(q) = \frac{q(\sinh 2q + \sin 2q)}{\cosh 2q - \cos 2q} - 1 \tag{4.7}$$

$H(q)$ is the dimensionless heat function.

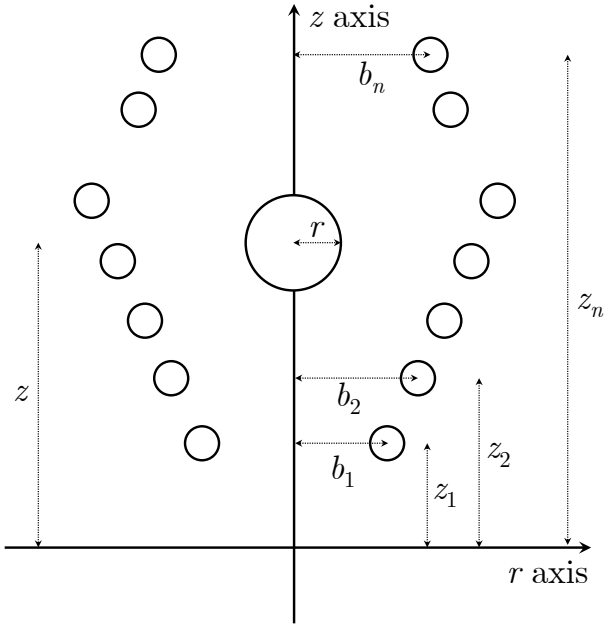

Figure 4.6: Coil geometry used in the calculation of the lifting force F_z

With the geometry of the coil taken into account (illustrated in Figure 4.6), the final equation of the lifting force on the z-axis is approximated by Fromm and Jehn as follows [7]:

$$F_z = \frac{3}{2}\pi\mu_0 I^2 r^3 G(q) \sum_i \frac{b_i^2}{\left[b_i^2 + (z - z_i)^2\right]^{3/2}} \sum_i \frac{b_i^2 (z - z_i)}{\left[b_i^2 + (z - z_i)^2\right]^{5/2}} \tag{4.8}$$

where z is the height of the sample, z_i the height of the i-th spire and b_i is the distance between the i-th spire and the z-axis.

From the same authors, the power absorbed by the sample can also be estimated:

$$P = \frac{3}{4}\pi \sqrt{\frac{\mu_0 \omega}{2\sigma}} I^2 r^2 \left(\sum_i \frac{b_i^2}{\left[b_i^2 + (z - z_i)^2\right]^{3/2}} \right)^2 \tag{4.9}$$

In the specific case of a sample of n-type silicon, its resistivity is significant: about 10^{-4} Ω.m at room temperature. For the frequency of 130 kHz applied in the seven spires induction coil, the induced force calculated is negligible compared to the gravitational force exerted on the sample:

$$F_z = 9.680 \cdot 10^{-6} \text{ N} \quad \ll \quad F_g = 1.795 \cdot 10^{-2} \text{ N} \tag{4.10}$$

In these conditions, the sample can neither levitate nor melt as such.

In the current experimental configuration, the only lever one has to increase this lifting force is to preheat the sample.

This energy input is conceivable by using an intermediate material with a lower resistivity: a graphite pellet is then used, encapsulated in a quartz cap that holds the sample. The overall is disposed on the top of a quartz rod.

As its resistivity is lower – in the order of 10^{-6} Ω.m [12] – it will heat itself up, then heat silicon via radiation. Thereby the silicon temperature-dependent resistivity will decrease: in the liquid state ρ_{Si} is about $6.5 \cdot 10^{-7}$ Ω.m [8].

The resulting force increases to $F_z = 1.892 \cdot 10^{-2}$ N and thus outweighs F_g: the sample can be lifted.

Once the distillation experiment is over, the sample has to solidify before dropping in order to be analyzed in its entirety. Varying the power of the induction coil happened to be an ineffective option as the droplet suddenly falls after one temperature fluctuation too many. Instead, an inert gas such as helium is injected for a cooling by convection.

4.1.4 Measurements techniques

To compare the earlier presented simulation results with the experiment, several parameters must be measured. Investigations focus on the silicon sample temperature, its weight loss and dephosphorization – for convenience reasons, only the difference between the initial and final x_P is considered – but also the surrounding p_{O_2}.

Before the experiment

The initial sample shall be precisely weighted. It will be compared to its weight after the experiment: indeed a considerable dephosphorization of the silicon sample is pointless if it loses too much weight. This parameter is theoretically discussed in the previous chapter, and an experimental comparison is intended.

Samples weight m_{Si} is calibrated from the supplier to 1.83 g in order to fit the dimensional needs – 10 mm of both diameter and height –, and so is its initial fraction of phosphorus $x_P = 50$ ppm. The n-type silicon used is Czochralski grown and presents a resistivity of $1.2 \cdot 10^{-4}$ – $1.6 \cdot 10^{-4}$ Ω.m.

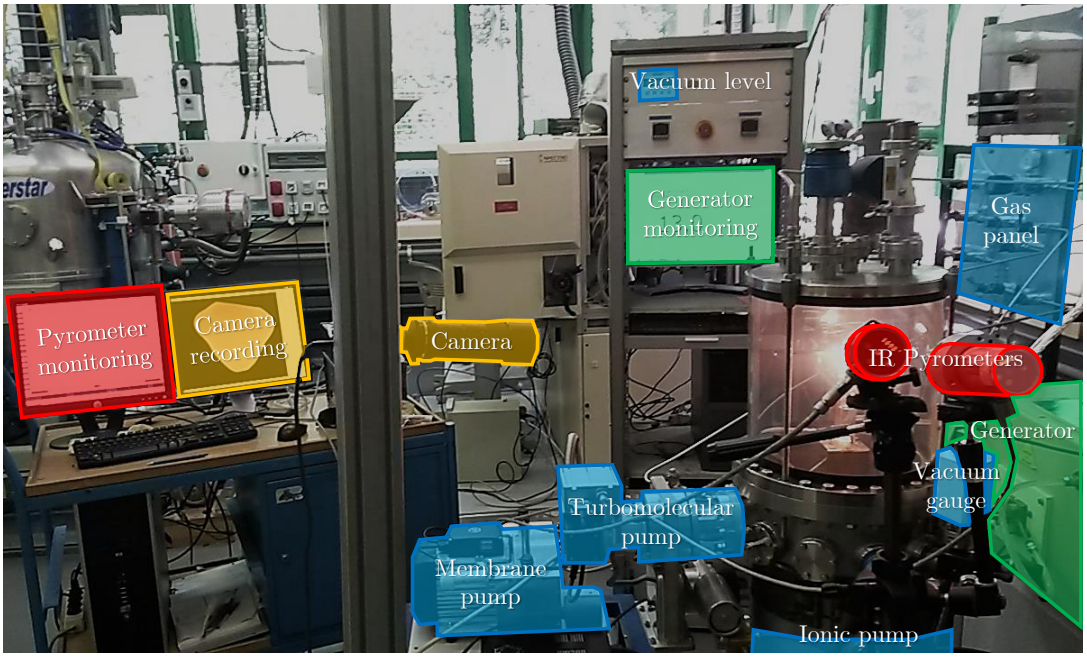

Figure 4.7: Picture of the initial setup

During the experiment

The initial experimental equipment is described Figure 4.7:
The following parameters are all synchronized over time:

- temperature T with a bichromatic IR pyrometer (Ircon 5R1810) monitored with the NetDAQ software. It measures the infrared thermal radiation emitted by the silicon droplet in the 0.75 – 1.05 µm and 1.0 – 1.1 µm spectral range with a short response time (10 ms).

  According to Planck's law, the spectral radiance $B_\lambda(\lambda, T)$ of a body of wavelength λ and temperature T is given in W.m^{-3}.sr^{-1} by:

$$B_\lambda(\lambda, T) = \varepsilon(\lambda) \cdot \underbrace{\frac{2hc^2}{\lambda^5} \frac{1}{e^{\frac{hc}{\lambda k_B T}} - 1}}_{\text{Black body}} \tag{4.11}$$

  where $\varepsilon(\lambda)$ is its emissivity, h the Planck constant and c the speed of light in vacuum.

  The bichromatic pyrometer determines precisely T with (i) the emissivity slope between two spectral bands and (ii) the ratio of their intensities between them.

  Its measurements are here calibrated on the silicon fusion at 1687 K. Two pyrometers are positioned on different samples spots in Figure 4.7. It ensures that the measurement is correctly done even if a local inhomogeneity is targeted by one of them;

- phase changes with a high speed camera of 100 Hz (PixeLINK PL-A780). It is of great use especially for post-mortem observations;
- the vacuum level with a combined Penning/Pirani gauge (Inficon MPG400). This association allows to encompass a large pressure range, from 5.10^{-9} to 1.10^{3} mbar.

  The Penning gauge ionizes the gas, and are collected by an anode. The resulting measured electrical current depend on the pressure. The Pirani part also measures indirectly the pressure by means of a fine heated electrical wire: the cooling effect of the surrounding gas decreases with a pressure decrease which modifies its voltage. Both gauges are presented in Appendix E;
- the electromagnetic power in the coil with a LabVIEW program connected to the RF generator (CELES). With a maximum capacity of 50 kW, it works at 135 kHz and 500 A. Its alternating current is also measured with a Rogowski coil wrapped around. A voltage is induced within and is directly proportional to the copper coil current.

The synchronization of inlet p_{O_2} will be discussed in section 4.3 dealing with the modified setup.

After the experiment

The final weight of m_{Si} will be measured to obtain the weight loss, whereas the final x_P will be determined by glow discharge mass spectrometry, also known as GDMS. This characterization method is used to detect trace elements in solids, in this case phosphorus in silicon, with a great sensitivity in the order of the ppb. Its operating principle is exposed in Appendix E.

No GDMS analytical services are accessible within the laboratory reach, therefore these measurements will be delegated to an external one.

4.2 Operating the initial setup

4.2.1 Procedural stages

In the present configuration, dephosphorizing the silicon sample is possible by fulfilling the following several steps.

- **Lifting stage:** the graphite pellet enclosed in the rod is heated by the coil sufficiently to heat in turn the solid sample. Its resistivity will decrease until it can levitate;
- **Melting of the sample:** the distance between silicon and the translatable rod is adjusted by the operator to enable the heat induction to continue until the sample is completely liquid. The rod will then be pulled down;

- **Holding the sample temperature:** the droplet levitation is the crucial point of the experiment as the dephosphorization takes place during this phase;
- **Solidification of the levitating sample:** convective cooling is operated by an inert gas, namely helium;
- **Dropping stage:** the solidified silicon falls in the brass basket and is retrievable.

4.2.2 Trials under argon atmosphere

The entire setup was moved to another room and has not been used for a long period. The first objective is then to recreate the prevailing conditions of Beaudhuin's previous work [4].

No particular precaution is taken for the sample preparation as it will not be analyzed thereafter. In fact, the lifted samples were silicon lumps contaminated with more elements than just phosphorus.

A lump of about 10 mm diameter is disposed upon the quartz susceptor, the pyrex enclosure is sealed and the three-pump system is launched. A high vacuum of $2 \cdot 10^{-5}$ mbar is obtained. Argon of 6N purity is afterward injected in the vessel for a pressure of 1 bar. A power of 15 kW is progressively applied in the coils to lift the lump off the quartz rod. As this latter contains a hot graphite, the operator can bring it closer to the sample to enhance its heat radiation. In this way, silicon can melt without any additional power increase in the induction coil.

The reproduction of Beaudhuin's conditions has been carried out a couple times. The sample temperature could be maintained for a long time: more than a dozen minutes. Helium is the inert gas blown toward its surface for cooling it down to its solidification point. A typical example is reported in Figure 4.8 by the camera.

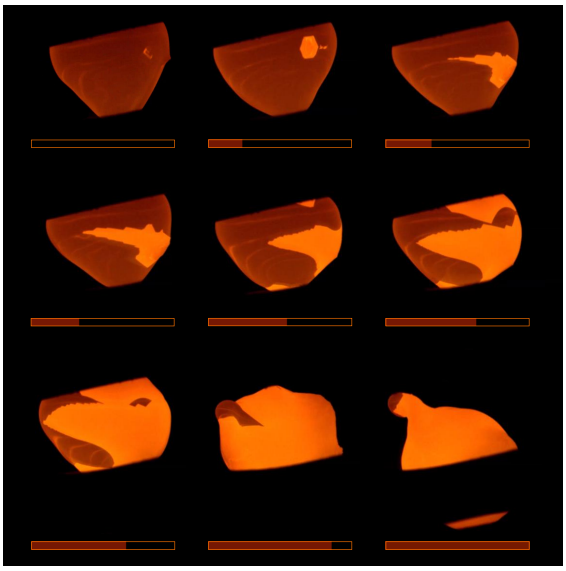

Figure 4.8: Silicon droplet solidifying under argon atmosphere with the initial setup. The time scale below each picture is given for a total length of 52 s.

Screenshots have been selected from the recording to have a clear idea of the solidification front, however the silicon growth is not analyzable as the droplet constantly rotates.

Every levitation stage has been successfully recreated under argon. The next logical step is to operate under high vacuum, which is the desired condition to validate the presented dephosphorization simulation.

4.2.3 Trials under vacuum

Due to their initial high purity, it is enough to preclean the samples by means of a piranha etch followed by a steep in diluted hydrofluoric acid [3].

It consists of immersing the sample for 15 minutes in a 1:1 mixture of sulphuric acid H_2SO_4 and hydrogen peroxide H_2O_2 in a first step, then transferring it in a 10:1 mixture of H_2O:HF for 20 seconds.

A vacuum of $2 \cdot 10^{-5}$ mbar is also here obtained: in these conditions a power input of about 7 kW is enough to levitate the sample off the rod. It could be melted by adjusting the silicon-rod distance the same way as previously.

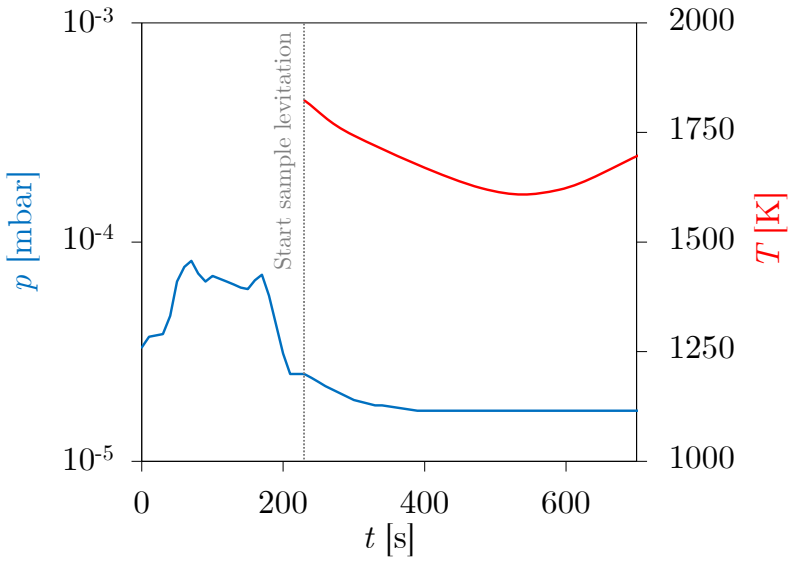

Figure 4.9: Evolution in time of the vessel inner pressure and the droplet temperature during the sample levitation

A rise in pressure is observed at the beginning of the experiment (Figure 4.9) when increasing the power generated in the coils. The enclosure walls are indeed degassing due to the thermal radiation, and the desorbed molecules are detected by the vacuum gauge.

When the coil power increases to 7 kW, the sample levitates shortly thereafter. Figure 4.9 highlights the difficulty of stabilizing the temperature: in this trial it oscillates between 1618 and 1823 K.

The cause of such a decrease is the sample sputtering during this high distillation rate process. The viewport is sprayed with sample particles and it consequently affects the pyrometers measurement. The installation of a vaporization shield is necessary to avoid this phenomenon. The increase observed at the end of this experiment is due to the rod brought near the sample in an attempt to mitigate the sudden convective cooling process.

The levitation experiments could not be carried out to the end. The encountered problem concerns the dropping phase: it occurs while the sample is still liquid. It drips onto the quartz rod and crystallizes, generally in several pieces. Weighting or analyzing by GDMS the splattered sample is not possible.

The blown gas actually makes the sample fall before it reaches its solidification temperature: when helium is added in this rarefied atmosphere, it induces the formation of a corona discharge – a cloud of plasma around a high current carrier – from the induction coils. It is not desirable as it interrupts the levitation currents.

Different solutions have been envisaged to overcome this problem. Firstly, nitrogen has been used to replace helium. Its higher molar mass and lower heat capacity [5] was expected to moderate its convective cooling potential. Even with an extremely reduced flow, the liquid drop was inevitable.

A thin graphite rod has then been conceived with the objective of acting like a crystal seed for the silicon. The operator can transfer it vertically above the droplet to dip into it at the end of the levitation stage. Its main drawback is obviously the carbon contamination of the sample. As it can be seen on Figure 4.10, silicon is too heavy to hang on it as it solidifies.

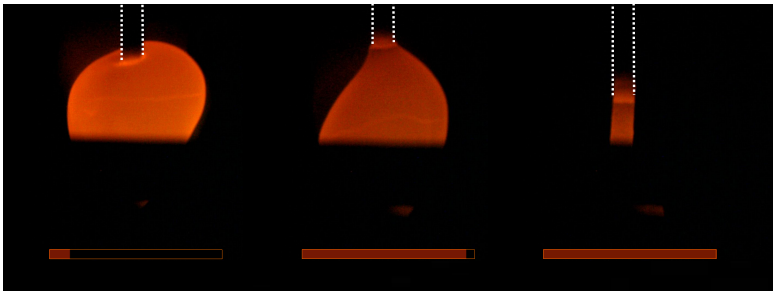

Figure 4.10: Silicon droplet of about 10 mm diameter attempting to solidify under vacuum around a thin graphite rod (highlighted in dotted white lines). The time scale below each picture is given for a total length of 28 s.

Withdrawing the susceptor from the coil axis, and replace it with a container is an alternative solution. The need of incorporating in the setup a rotary plate then arose. Its implementation is described in the next section.

4.3 Development of the setup

In order to be more adapted to the study problematic, several improvements on the initial EML device have been achieved. Reaching a greater vacuum level, retrieving the levitating liquid sample and controlling the oxygen partial pressure inside the vessel are three requirements broached here.

4.3.1 Modified parts

Stainless steel enclosure

A recurrent issue was the vacuum limited by the poor airtightness of the L-shaped toric FKM[6] joints at the top and bottom of the pyrex vessel. A new custom water-cooled double wall stainless steel enclosure has then been conceived to replace this chamber (Figure 4.11). It features three viewports to maintain temperature measurements, video recording and a sight for the operator as well as a vaporization shield.

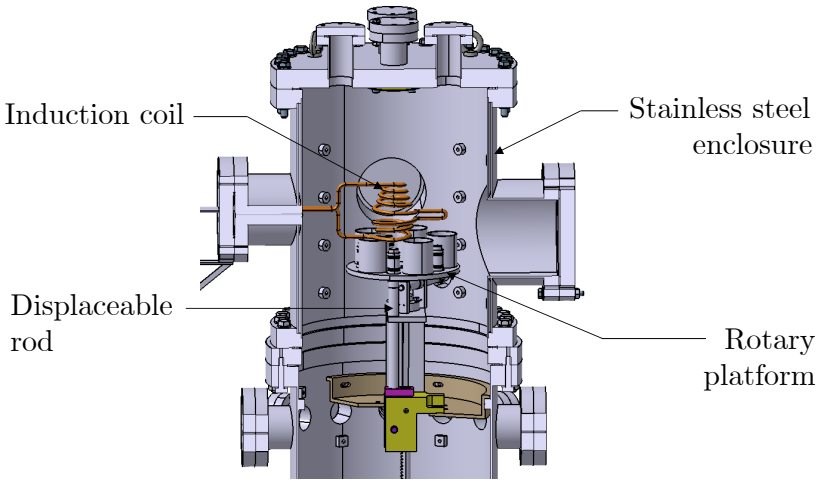

Figure 4.11: New design of the core of the EML device

This change provides a better sealing efficiency, a possibility of heating for degassing and the water-cooling ensures a better compatibility at high temperature and condensation upon the walls.

One encountered several times technical problems with the ion pump, most likely due to its old age. It has been the opportunity to replace both the ion and turbomolecular pumps by another turbomolecular with bigger capacity: an Alcatel ATP 400 with a N_2 pumping speed of 400 $L.s^{-1}$. It is better placed with the new enclosure at the level of the levitating sample.

[6] A fluoropolymer elastomer also called Viton, its main trade name.

Rotary platform

Inside the enclosure is added a rotary platform to maximize each new trial by performing several experiments in a row (Figure 4.12). Not only it enables the operator to withdraw the quartz rod from the coil axis and replace it with one container, but this can be done for five samples and five corresponding reception baskets disposed along the plate.

To collect the liquid droplet, vacuum pump oil in a quartz container is firstly envisaged. At the bottom graphite moss was disposed to mitigate the fall. Even with a slightly filled container, the quench boiled the content and spilled both the oil and the droplet.

Copper ladle instead confers a better heat absorption. It contaminates the still liquid sample, but provided that copper has a high degree of purity, this element will not unduly downgrade the GDMS analysis.

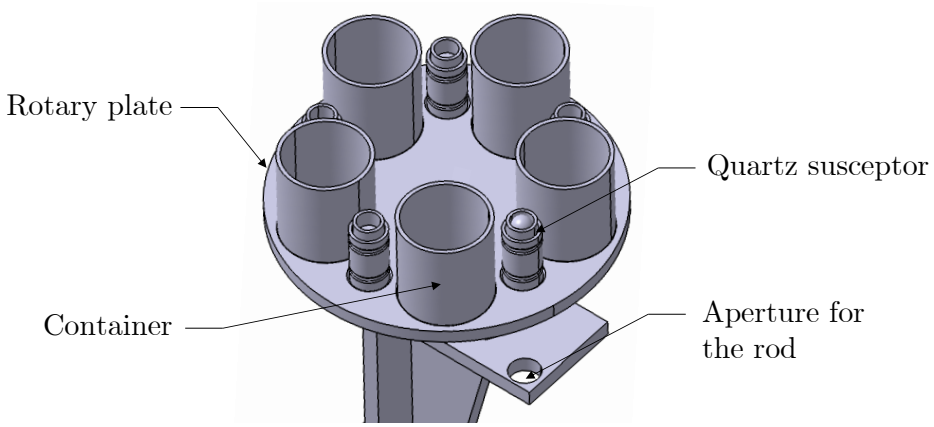

Figure 4.12: Rotary plate design included in the new setup

4.3.2 Surrounding environment control

The oxygen content inside the enclosure should be directly adjustable to provide a great accuracy. An oxygen regulation system is installed to control the total pressure as well as p_{O_2}. As it is separated from the enclosure, the gas chemical composition can easily be affected: to that extent a particular attention will be brought to the connection between those two parts. A residual gas analyzer is moreover required to precisely estimate p_{O_2}, and more generally the gas composition.

Inlet p_{O_2} with an oxygen pump-gauge

By the residual nature of present p_{O_2}, its range is limited: it is necessary to develop a system that introduce a tunable oxygen amount. An oxygen pump-gauge is then connected upstream – a SETNAG Gen'Air MEX030 – and controls the atmosphere by both generating and measuring this partial pressure.

☐ The oxygen pump part is made of an YSZ[7] tube in which a voltage is applied on each side (Figure 4.13): O^{2-} ions migrate through it. Depending on the current direction, it enriches or depletes in oxygen the gas within. The resulting variation between outlet $p_{O_2}^{\text{out}}$ and inlet $p_{O_2}^{\text{in}}$ of the tube is provided by the manufacturer:

$$p_{O_2}^{\text{out}} = p_{O_2}^{\text{in}} \pm 0.2095 \cdot \frac{I}{D} \tag{4.12}$$

where I is the current circulating through the oxygen pump tube walls expressed in A, and D is the flow of the carried gas in L.min^{-1}.

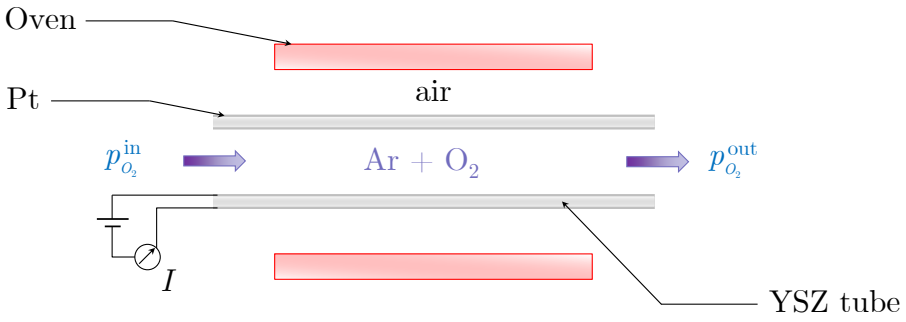

Figure 4.13: Illustration of the oxygen pump principle

☐ The oxygen gauge part consists of an electrochemical zirconia probe named MicroPoas that provides a relative measurement accuracy of 2% and is based on the Nernst's law [6]:

$$E = \frac{RT}{4F} \ln\left(\frac{p_{O_2}}{p^{\text{ref}}}\right) \tag{4.13}$$

where E is the potential obtained between the two sides of the zirconia electrolyte expressed in V, and F the Faraday constant in C.mol^{-1}.

In this case one side of the electrolyte has an internal metallic reference for p^{ref}, and thus does not use any other gas reference. With p^{ref} fixed, measuring the potential E at a given T enables to estimate p_{O_2} on the other side.

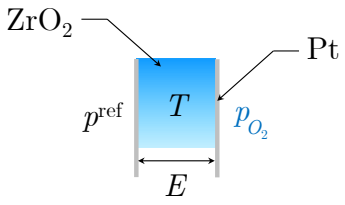

Figure 4.14: Illustration of the oxygen gauge principle

[7] Yttria-stabilized zirconia, *i.e.* ZrO_2 stabilized at room temperature by an addition of Y_2O_3.

6N argon is used as a carrier gas with oxygen to ensure a better control of overall contaminants and an improved repeatability. A mass flow controller is installed to regulate its rate. To avoid overrunning the turbomolecular pump capacity with the injected gas, a dedicated dry pump is added to the setup: it has a variable valve to adjust the total pressure. It also provides a high reactivity when p_{O_2} is regulated: the small volume in the piping set is indeed rapidly renewed by the important gas flow.

Adjusting p_{O_2} with a needle valve

During the experiments only p_{O_2} should be regulated and therefore separated from the total pressure regulation system. A needle valve is used to act as a tunable leak.

According to conservation law, the leakage flow through this needle valve at p^{up} is equal to the flow pumped in the enclosure at p. For an inlet at 1 bar and for a turbomolecular pumping speed of 400 L.s^{-1}, the leakage flow is $4 \cdot 10^{-6}$ L.s^{-1}. Applying such a low leak is difficult for the operator as it corresponds to a very small degree of openness.

An Ar/O_2 mixture is used in the experiment: due to their different viscosities, it may cause a gas selectivity problem.

One can derive the valve conductance C of the pipe from the Hagen – Poiseuille law for laminar flows:

$$\Delta p = \frac{8\eta L \dot{V}}{\pi r^4} \tag{4.14}$$

where Δp is the difference of pressure at the ends of the pipe, η the gas dynamic viscosity expressed in Pa.s, L the length of pipe, $\dot{V}$ the volumetric flow rate in L.s^{-1} and r the pipe radius.

An analogy with electrical circuits allows one to write $\dot{V} = C\Delta p$. It gives:

$$C = \frac{\pi r^4}{8L\eta} \tag{4.15}$$

With the valve conductance C expressed in L.Pa^{-1}.s^{-1}. In the present case $L \approx 3 \cdot 10^{-2}$ m.

At $p^{\text{up}} = 1$ bar, argon and dioxygen dynamic viscosities are $\eta_{Ar} = 2.27 \cdot 10^{-5}$ Pa.s [10] and $\eta_{O_2} = 2.06 \cdot 10^{-5}$ Pa.s [10]. The calculated valve conductance is in the same order of magnitude than the leakage conductance, which confirms the possibility of a deviation in composition.

However for a reduced pressure – at 5 mbar – the leakage flow is increased to $8 \cdot 10^{-4}$ L.s^{-1} so the viscosity influence is negligible compared to the valve conductance. The composition is thus not affected by the reduced section of the valve.

As long as the condition of $p^{\text{up}} \leq 5$ mbar is fulfilled, one concludes that the tunable leakage flow of Ar and O_2 enables to drive independently the inlet oxygen pressure and the total pressure p in the vessel.

Measuring p_{O_2} with a residual gas analyzer

The total pressure value given by the enclosure vacuum gauge does not reflect the composition deviation due to pumping. Indeed, the compression ratio K_0 defined between the discharge pressure and the intake pressure is different for argon and dioxygen. It is then essential to measure in-situ p_{O_2} to obtain more accurate data.

Based on a mass spectrometer, the SRS[8] residual gas analyzer RGA300 determines with a mass range of 1 to 300 amu[9] the composition of the residual gaseous species, particularly O_2. It must operate under high vacuum – less than 10^{-4} mbar. The probe depicted in Figure 4.15 comprises three parts: an ion **(1)** source, **(2)** filter and **(3)** detector.

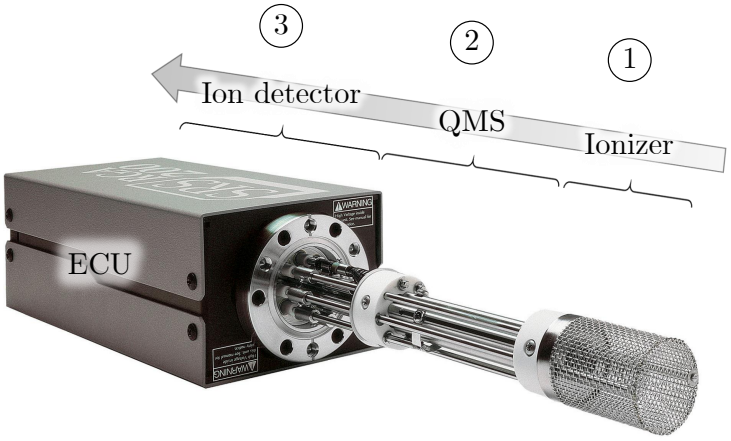

Figure 4.15: SRS residual gas analyzer components. Picture adapted from [1]

In the ionizer **(1)**, cations are produced by bombarding the residual gas molecules with electrons originating from a heated oxidation resistant ThO_2/Ir filament.

They are directed towards the ion filter **(2)** – a quadrupole mass spectrometer (QMS) – where they are refined based on their mass-to-charge ratio. This QMS is an electrodynamic device that combines variable voltages – two alternative RF and two direct – between its four cylindrical electrodes. The resulting forces select ions of specific mass, and by varying the voltages amplitude the entire mass spectrum is examined. The ultimate resolution is established from the number of cycles through the quadrupole the ions made before they reach the detector: for the RGA300 model it is estimated at 0.3 amu.

The ion detector **(3)** assembly includes a Faraday cup (FC) part that can directly measure ion currents corresponding to pressures above 10^{-9} mbar, and an optional electron multiplier part to investigate pressures below. In the present study, the FC part will merely detect residual p_{O_2} as it is within its detection range. The

[8] **S**tanford **R**esearch **S**ystem

[9] **a**tomic **m**ass **u**nit: 1 amu $\approx 1.661 \cdot 10^{-27}$ kg

cations arriving in the cup strike a metal wall and are neutralized by wall electron transfer. It establishes an electrical current with the same intensity than the ion current. The signal is carried into the electronic control unit (ECU) that ensures the numeric communication with the computer for extracting data.

The final developed system is illustrated Figure 4.16.

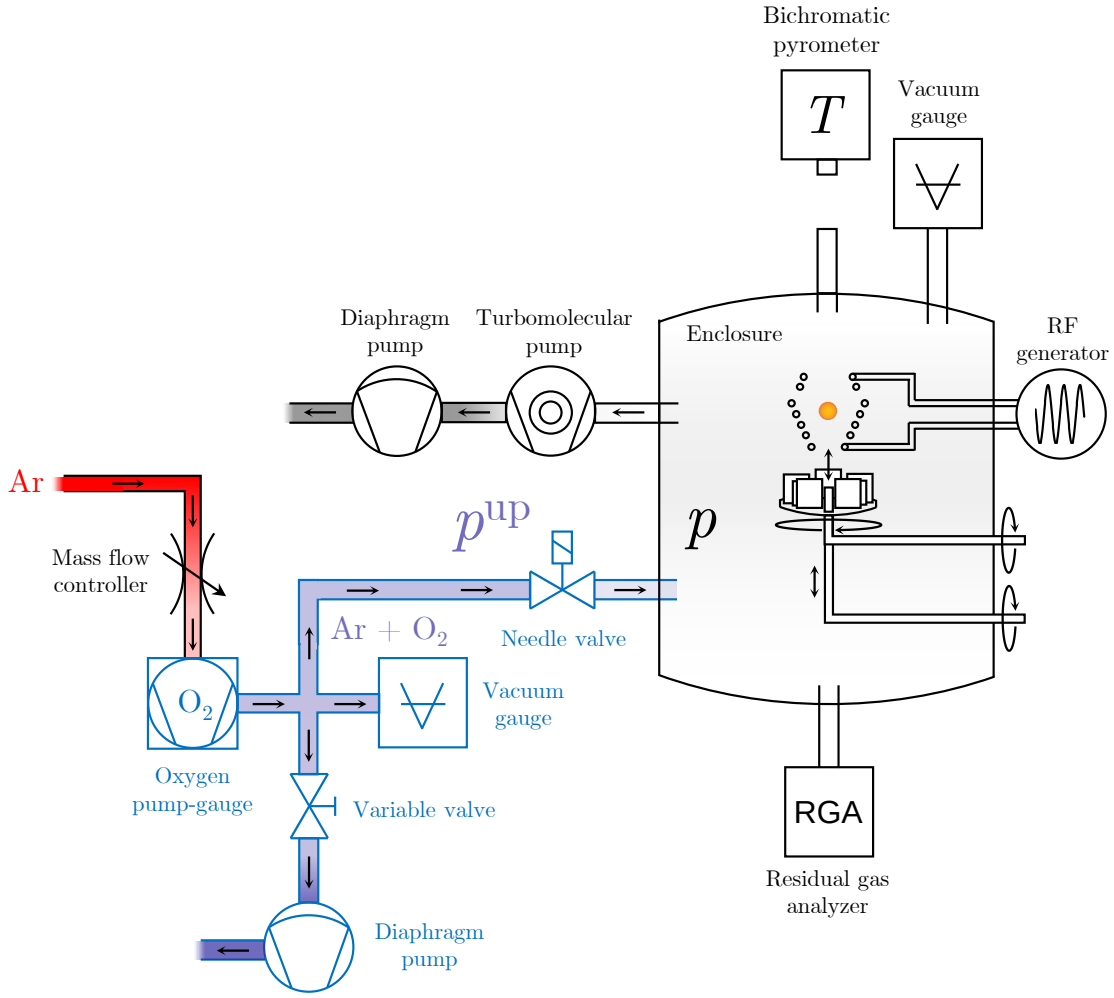

Figure 4.16: Schematic view of the experimental EML pilot

4.4 Operating the modified setup

4.4.1 Vacuum level

After sealing and evacuating the new stainless steel vessel, a vacuum level of 10 mbar is only reached. Extensive leak detection campaign revealed that new custom made flanges where poorly machined as the copper seals did not fit the seal groove.

This limitation could be overcome by machining copper seals in a lower diameter, but flange changes should be considered as a better solution for the future. Vacuum was then pushed downward dramatically and a limit of $1.5 \cdot 10^{-8}$ mbar was obtained after pumping for 40 hours.

This satisfactory result makes the targeted 10^{-8} – 10^{-1} mbar range reachable. The needle valve is also slowly opened in order to visualize its impact on the total pressure. As anticipated once p^{up} is set to 1 bar, a small valve openness provides enough gas flow to increase the pressure up to 10^{-4} mbar inside the enclosure. Switching on the diaphragm pump to reduce p^{up} gives more comfortable conditions to manipulate the needle valve – a wider opening relatively to its capacity.

4.4.2 Limits encountered

A first series of qualifications is then realized to test the new installations. Argon is flown through the oxygen pump-gauge at 7 L.min^{-1} and the oxygen voltage is set to stabilize $p^{\text{up}}_{O_2} = 2.8$ mbar, which leads to $p^{\text{up}} = 20$ mbar. Before the experiment the needle valve is slowly opened to stabilize in the vessel $p = 6.7 \cdot 10^{-6}$ mbar.

Figure 4.17 shows the evolution of p_{Ar}, p_{N_2} from residual air and p_{O_2} over time obtained from the RGA[10].

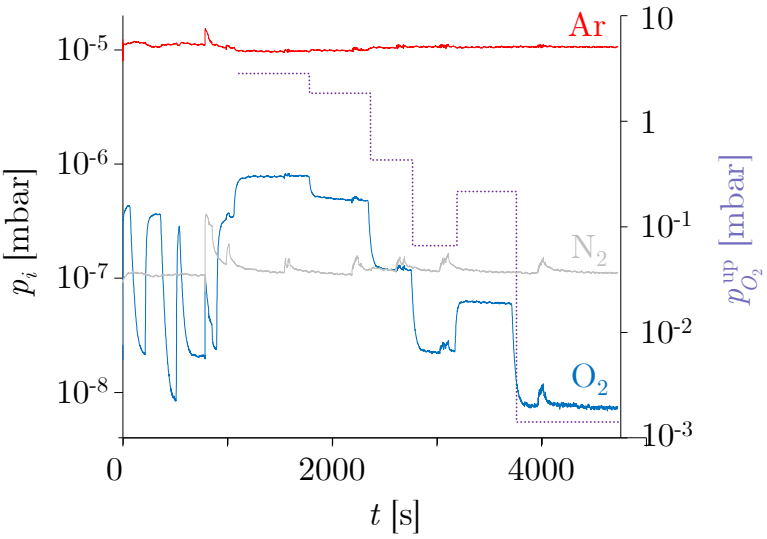

Figure 4.17: RGA measurements from the first series of experiments

From 0 to 1000 s voltage in the oxygen cell is changed to make $p^{\text{up}}_{O_2}$ evolve. As it can be seen only p_{O_2} is affected. Given these first satisfactory conditions $p^{\text{up}}_{O_2}$ is progressively decreased after 1000 s without modifying other parameters.

The impact of the generator power is investigated by turning it on at its maximum value before every plateau ending. Argon signal is poorly influenced, but N_2 is perturbed with a constant noise amplitude every time. Concerning O_2, the

[10]Even if p_O is skipped due to recording error, interpretation is still valid.

signal noise is enhanced when its partial pressure is decreased: the electromagnetic perturbation is not filtered efficiently by the RGA front grid, and will have to be avoided by a more efficient shielding. A better protection is obtained when moving the RGA to another flange, under a mass connected metal plate.

Even if this first experiment appears to be convincing concerning p_{O_2} adjustment, thorough investigations lead to a less affirmative claim. A linear dependence has been observed between p_{O_2} and $p_{O_2}^{\text{up}}$, but not for the lowest pressures (Figure 4.18).

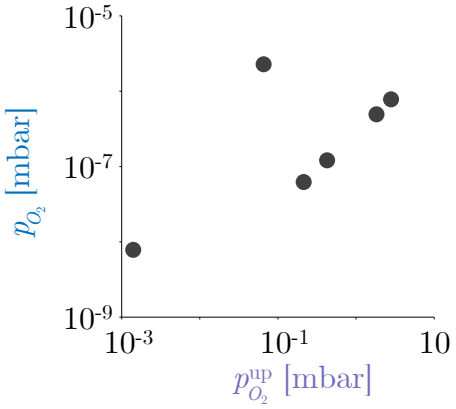

Figure 4.18: Evolution of p_{O_2} as a function of $p_{O_2}^{\text{up}}$

Valve selectivity may be responsible for this phenomenon as p_{Ar} is not affected during the experiment. To further investigate this possibility another experiment is designed according to Figure 4.19.

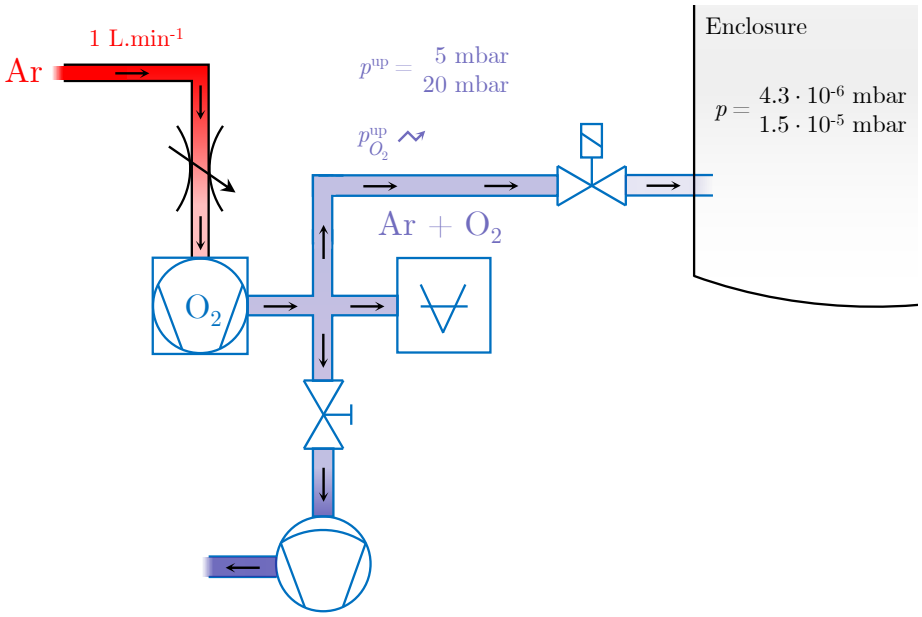

Figure 4.19: Operating conditions to investigate the influence of the leak valve conductance on the gas selectivity

Total pressure upstream is interchanged between 5 or 20 mbar. After changing the leak valve position, $4.3 \cdot 10^{-6}$ and $1.5 \cdot 10^{-5}$ mbar are respectively obtained. This valve setting is maintained to work with a fixed conductance. Argon is then flown through the oxygen regulation system and $p^{\text{up}}_{O_2}$ is slowly increased from about 10^{-5} mbar to 1 mbar.

RGA measurements showed that Ar signal is fairly neat, evolving accordingly to p^{up} variations (Figure 4.20). On the contrary both O_2 and O signals are poorly changed, while $p^{\text{up}}_{O_2}$ is actually increased by orders of magnitude. O_2 signal seems to become influenced by upstream changes only at already high $p^{\text{up}}_{O_2}$ values.

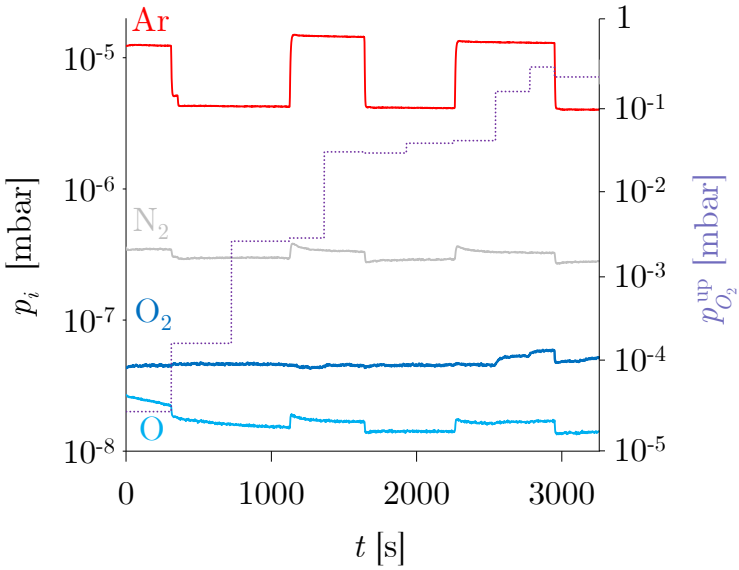

Figure 4.20: RGA measurements obtained to investigate the influence of the leak valve conductance over gas selectivity

To avoid this gas selectivity, it is necessary to further decrease p^{up} to increase leak valve conductance.

4.4.3 Revised conditions

In this last experiment, conductance will be fixed as high as possible. Variable valve from Figure 4.19 is then set to obtain a constant upstream total pressure of 3.35 mbar, with argon still flowing at 1.0 L.min^{-1}. Leak valve is also operated here to fix $p \approx 10^{-5}$ mbar. $p^{\text{up}}_{O_2}$ is firstly decreased from 1.1 mbar to $1.4 \cdot 10^{-1}$ mbar and then increased back.

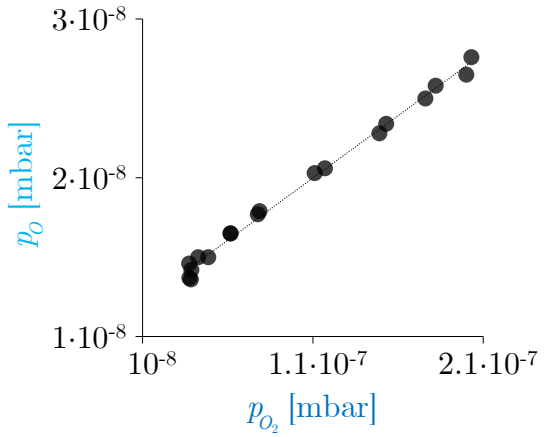

Figure 4.21: Evolution of the p_{O_2}/p_O ratio during the descending and ascending ramps of $p_{O_2}^{\text{up}}$

A first new outcome is the evolution of the p_{O_2}/p_O ratio plotted in Figure 4.21 during the $p_{O_2}^{\text{up}}$ descending and ascending ramps. A satisfactory linearity is observed with no hysteresis effect, which means that no memory has to be taken into consideration – for instance condensation or desorption from the walls.

Compared to previous results of Figure 4.18, a decent linearity is obtained even for low values (Figure 4.22). This result shows that the new operating limits are reachable.

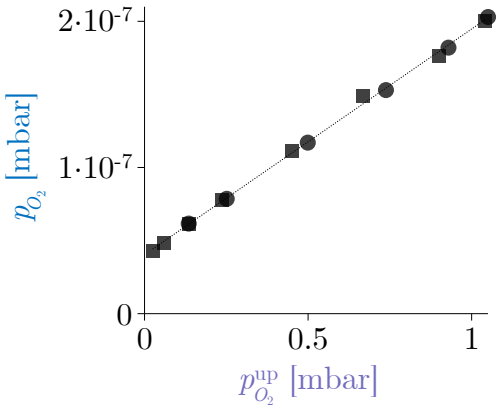

Figure 4.22: Evolution of p_{O_2} as a function of $p_{O_2}^{\text{up}}$. Round and square data points concern respectively the ascending and the descending ramp.

To illustrate the present operating conditions, most important partial pressures of N_2, Ar, O_2 and O monitored by RGA are presented on Figure 4.23.

Both p_{Ar} and p_{N_2} remain constant in the enclosure when $p_{O_2}^{\text{up}}$ varies. Meanwhile both p_{O_2} and p_O evolve linearly in good agreement with it.

The objective to improve the EML device by reaching high vacuum while controlling total pressure is achieved. Furthermore managing an accurate and meaningful value of p_{O_2} within the enclosure, while the others remain constant, is also obtained.

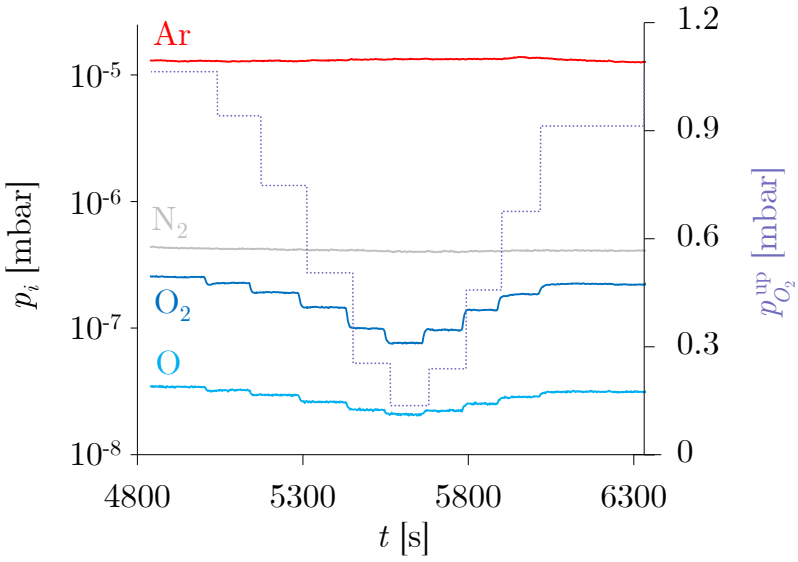

Figure 4.23: RGA measurements in optimized conditions

4.4.4 Conclusions

The EML technique is totally adapted for the dephosphorization study of silicon at a laboratory scale, and this chapter explained the different reasons.

The sample is operated without any polluting crucible or container during the experiment. It can be protected in the vessel by a vacuum system that can distill it. Finally, it is electromagnetically mixed once melted.

However, modifying drastically the existing device was required to validate the thermodynamic simulation. Improvements on an enclosure under higher vacuum, total pressure control as well as p_{O_2} control and measurements have been achieved in that sense.

Further developments regarding sample retrieval under high vacuum are still needed to realize the full demonstration of levitation under accurate gas control. Dephosphorization experiments will then be possible and compared to theoretical results, which is the main perspective of this chapter.

Bibliography

[1] *Stanford Research Systems RGA100/200/300 datasheet.*

[2] E. S. Agency, *Electromagnetic levitator*, 2014.

[3] M. Beaudhuin, *Etude expérimentale et numérique de la précipitation d'impuretés et de la formation des grains dans le silicium photovoltaïque*, PhD thesis, Institut National Polytechnique de Grenoble-INPG, 2009.

[4] M. Beaudhuin, K. Zaidat, T. Duffar, and M. Lemiti, *Silicon purity controlled under electromagnetic levitation (spyce): influences on undercooling*, Journal of materials science, 45 (2010), pp. 2218–2222.

[5] M. W. Chase, *NIST-JANAF Thermochemical tables*, no. 4, american chemical society and the american institute of physics for the national institute of standards and technology ed.

[6] J. Fouletier, G. Vitter, and M. Kleitz, *Measurement and regulation of oxygen content in gases using solid electrolyte cells. iii. oxygen pump-gauge*, Journal of Applied Electrochemistry, 5 (1975), pp. 111–120.

[7] E. Fromm and H. Jehn, *Electromagnetic forces and power absorption in levitation melting*, British Journal of Applied Physics, 16 (1965), p. 653.

[8] R. Hull, *Properties of crystalline silicon*, no. 20, IET, 1999.

[9] R. W. Hyers, *Fluid flow effects in levitated droplets*, Measurement science and Technology, 16 (2005), p. 394.

[10] E. W. Lemmon and R. Jacobsen, *Viscosity and thermal conductivity equations for nitrogen, oxygen, argon, and air*, International journal of thermophysics, 25 (2004), pp. 21–69.

[11] O. Muck, *Verfahren und vorrichtung zum schmelzen, insbesondere von leitern u. dgl. durch elektrische induktionsstrohme (process and device for melting, especially of conductors and so on by means of electrical induction currents)*, 1923. DE Patent 422,004.

[12] H. O. Pierson, *Handbook of carbon, graphite, diamond, and fullerenes, processing, properties and applications*, 1993.

[13] P. R. Rony, *The electromagnetic levitation of metals*, tech. report, California. Univ., Berkeley. Lawrence Radiation Lab. and California. Univ., Berkeley, 1964.

[14] P. Schetelat, *Modélisation et simulation de la calorimétrie modulée inductive*, PhD thesis, Institut National Polytechnique de Grenoble-INPG, 2009.

Conclusion and outlook

THE intricate thermodynamic relation between silicon and phosphorus has been investigated in the framework of the photovoltaic area. The already diluted phosphorus shall have its amount more reduced to fulfill the purity requirement needed for this industry. In the metallurgical route, induction vacuum refining furnaces are used for this purpose. Up to now this dephosphorization problematic has not been broached by taking into account the influence of oxygen that is contained in the crucible and the residual atmosphere of the furnaces.

The available literature on the Si – P system proved to be sparse, particularly in the Si-rich region of interest that depicts the solubility of phosphorus in silicon $[P]_{(Si)}$.

To that extent, a better insight has been first given into this binary system. A Calphad modeling has then been performed by using selected phase equilibria and thermodynamic properties data and optimizing it with BINGSS/BINFKT Lukas programs.

With a critical review of relevant diffusion and ion implantation articles, $[P]_{(Si)}$ has been accurately estimated. Previous assessments gave disparate shapes for the solubility curve, with indicatively a maximum ranging from 1.0 to 3.8 at.%. In the current study, $[P]^{max}_{(Si)}$ has been evaluated at 1 bar to 0.8 at.%. This lower amount is explainable by the exclusion of experimental articles that contained either a non-negligible oxygen quantity, undetected SiP precipitates, or else improvable resistivity-to-impurity calculations. This solubility is intimately related to the activity coefficient at infinite dilution of phosphorus γ^{∞}_{P}, a key element in the ensuing thermodynamic description of phosphorus removal.

Based on those outcomes, the P removal process of molten Si in presence of O could be modeled. Its efficiency can be evaluated by comparing its dephosphorization time to its weight loss.

An algorithm has been developed that integrates γ^{∞}_{P} along with other thermodynamic variables from the literature.

At 1800 K and for a low amount of surrounding oxygen ($p_{O_2} = 10^{-9}$ bar), among all the gaseous species, $P_{2(g)}$ evaporates predominantly from the melt, then it becomes $Si_{(g)}$. For higher amounts it increasingly oxidizes Si and P. At the Knudsen limit ($p_{O_2} = 10^{-4}$ bar), oxygen evaporates mostly in the form of $SiO_{(g)}$.

Time factor has been incorporated with the use of condensing and evaporating Hertz-Knudsen flows that depend on the partial pressures and nature of constituting

species, but also temperature. To distill from 50 to 0.5 ppm at $p_{O_2} = 10^{-9}$ bar and 1800 K, it has been demonstrated that the given sample takes 154 seconds and loses 0.5% of its weight. Below the Knudsen limit at $p_{O_2} = 10^{-5}$ bar it only takes six more seconds, however it loses 7.7% of its mass.

Therefore from those statements the residual oxygen present in the vacuum has been theoretically proved to be a hindrance to the dephosphorization process.

An electromagnetic levitation device present in the laboratory has been improved to become a strong candidate to corroborate this thermodynamic simulation.

This technique fulfills all the specifications required to remove phosphorus from molten silicon in a cleaned and controlled environment. However, it was originally designed to operate under argon atmosphere.

After several trials with the initial setup, modifications were processed. A stainless steel enclosure with viewports replaces the pyrex to reach a higher vacuum of 10^{-8} mbar, and a rotary platform including five containers maximizes the number of levitated samples in a single experiment. In addition, an oxygen partial pressure regulation system involving an oxygen pump-gauge and a tunable leak valve is installed to control separately the total and oxygen partial pressures. Finally, a residual gas analyzer based on a quadrupole mass spectrometer accurately estimates the different partial pressures inside the vessel over time.

When an inert gas is injected to cool the droplet by convection, it drops before solidifying. Retrieving it as a whole and uncontaminated is the main perspective to compare its weight loss and distillation time with the conjectured theory.

In a nutshell, it has been proved that even if the oxygen has a minor impact on the dephosphorization time, it reduces the process efficiency as it carries silicon away through silicon oxides. A high vacuum is then necessary at the industry scale to avoid pure silicon to evaporate from the melt. If this vacuum condition cannot be satisfied, a high temperature will compensate the oxygen contamination.

Apart from the experimental validation of the thermodynamic simulation, the logical outlook of this study would be to consider other contaminant elements in the Si – P system than oxygen only. During the silicon purification step, residual nitrogen, carbon or else boron are also present in the melt, thus their impact on the dephosphorization process should be determined with the thermodynamic tools provided herein, as well as with the modified electromagnetic levitation device.

Appendices

A

Phase diagrams of previous thermodynamic assessments

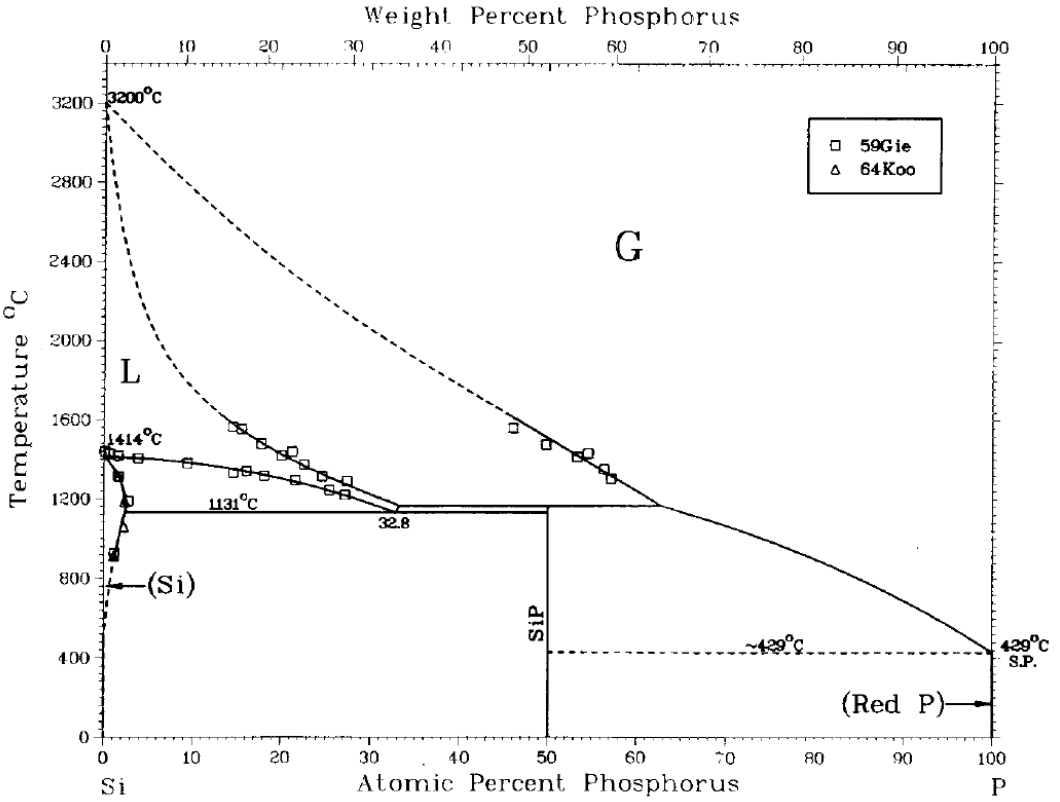

Figure A.1: Optimized phase diagram from Olesinski et al. [36]

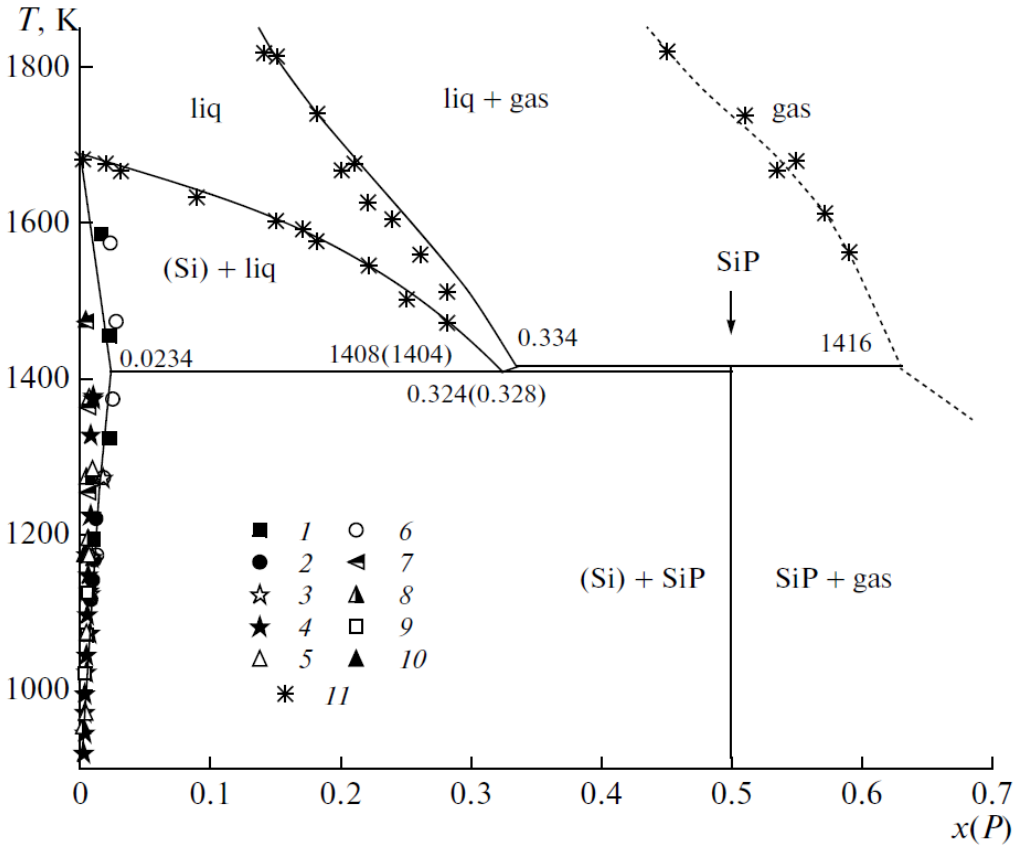

Figure A.2: Optimized phase diagram from Arutyunyan et al. [2]. The dash lines are the data from Giessen and Vogel [17], and the points are experimental data of (1) Kooi [27], (2) Bentzen et al. [7], (3) and (4) Solmi et al. [43] (5) Schwettmann and Kendall [41], (6) Trumbore [49], (7) Borisenko and Yudin [8], (8) Masetti et al. [31], (9) Carabelas et al. [10], (10) Abrikosov et al. [1] and (11) Giessen and Vogel [17].

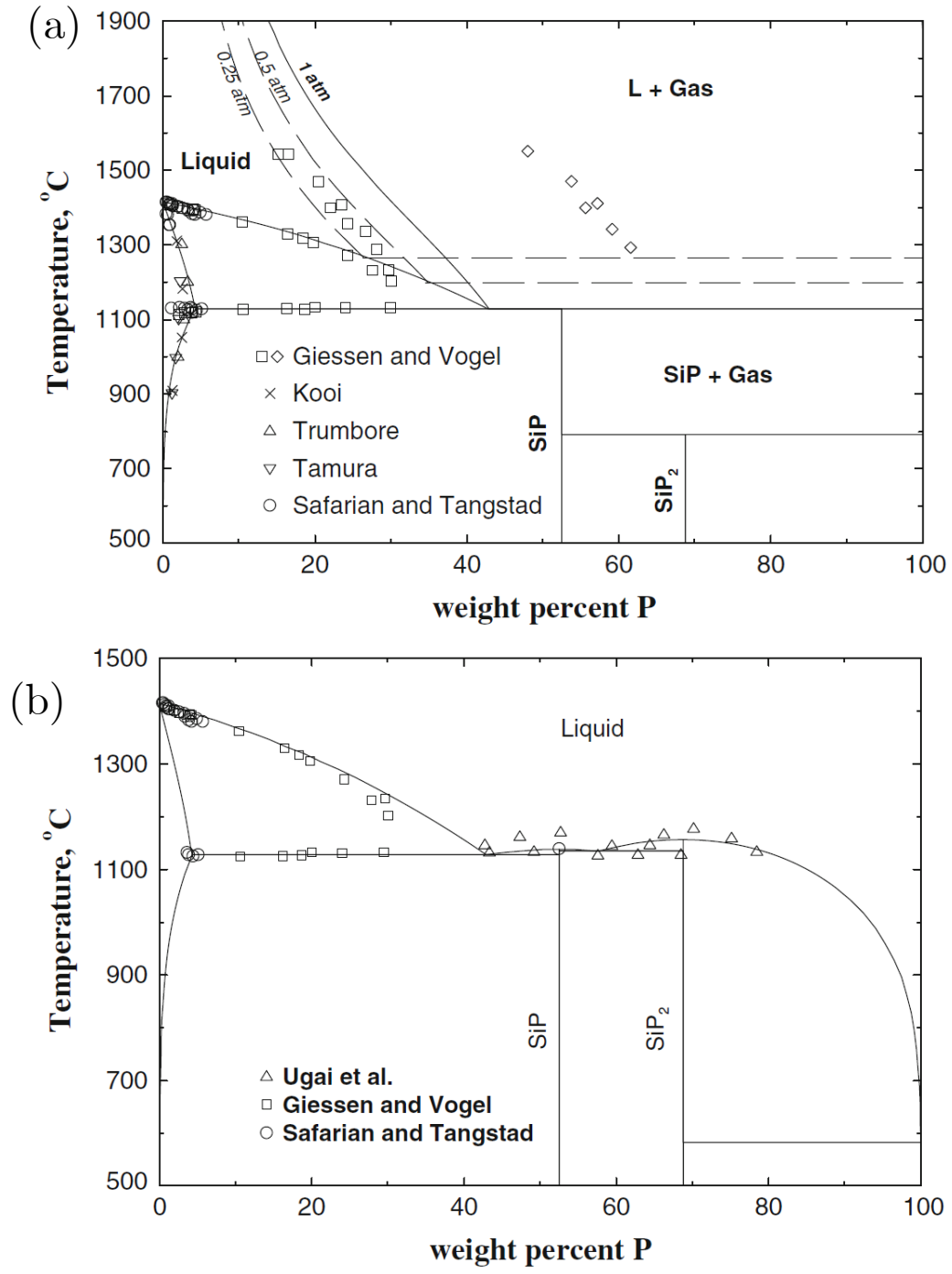

Figure A.3: Optimized phase diagrams from Jung and Zhang [26] (a) for 0.25, 0.5, 1 atm and (b) without gas phase

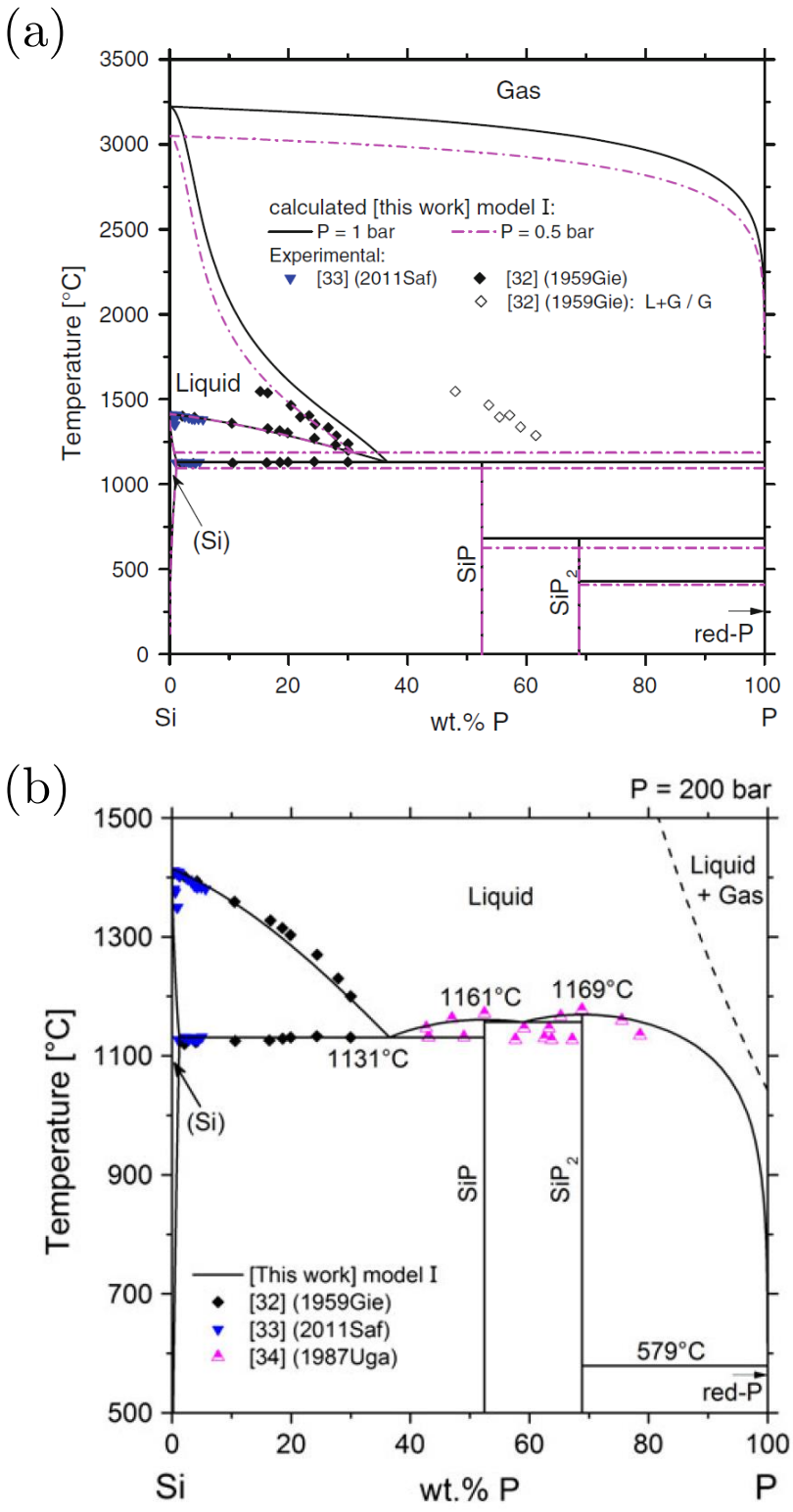

Figure A.4: Optimized phase diagrams from Liang and Schmid-Fetzer [28] (a) for 0.5, 1 bar and (b) 200 bar

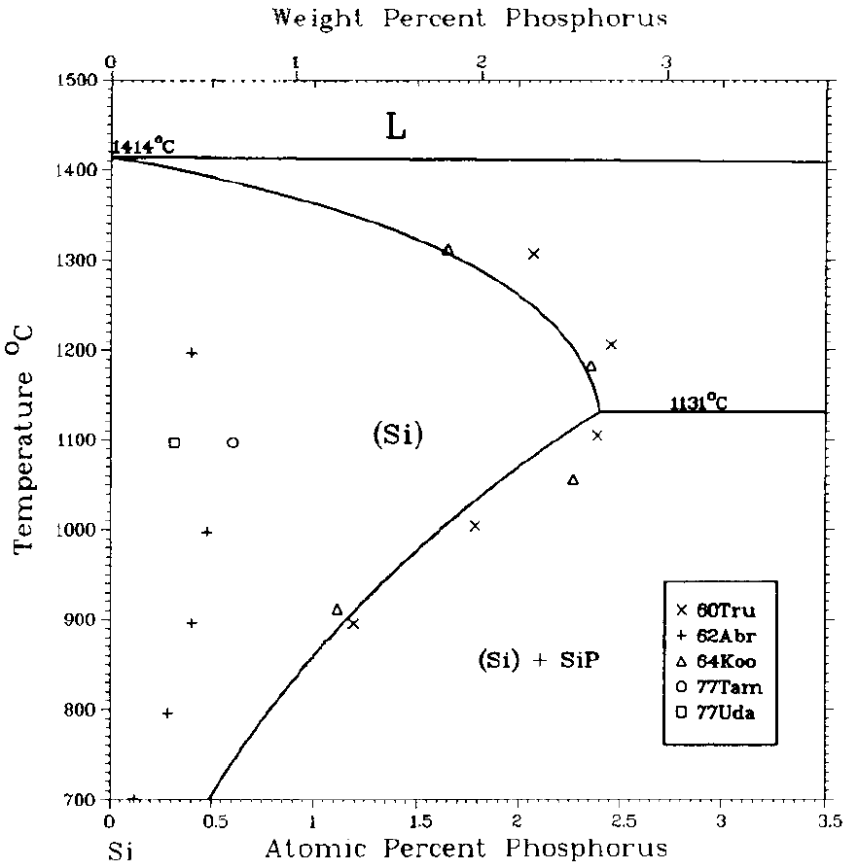

Figure A.5: Optimized phase diagram of the Si-rich region from Olesinski et al. [36]

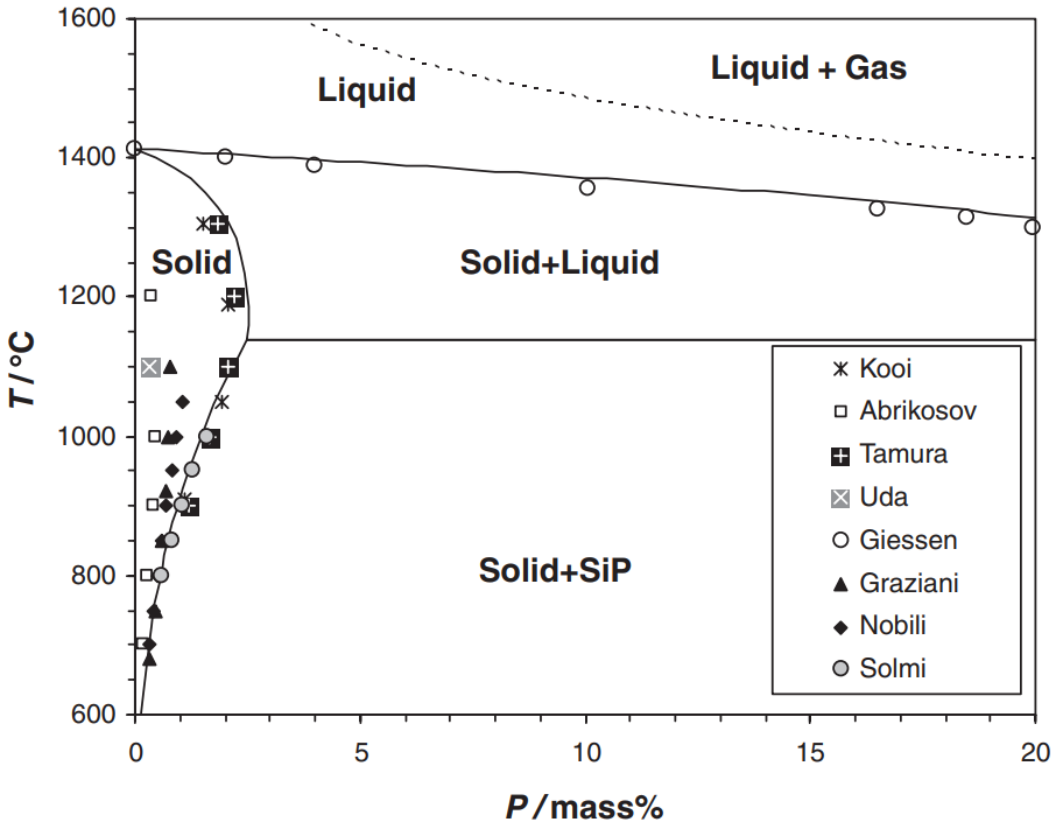

Figure A.6: Optimized phase diagrams of the Si-rich region from Tang et al. [47]

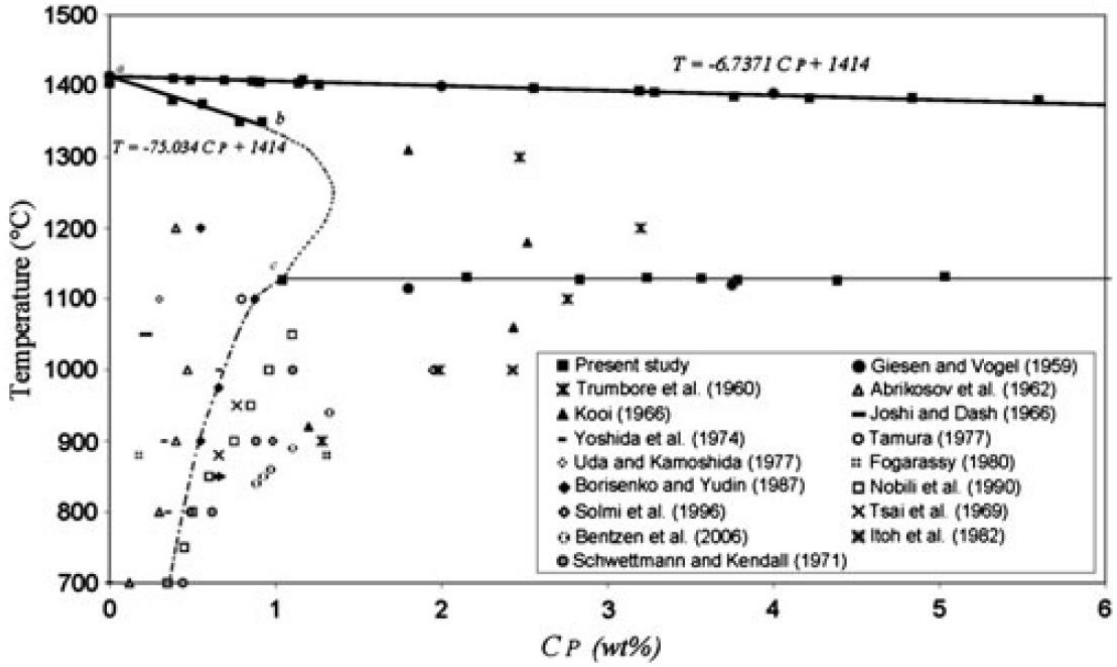

Figure A.7: Optimized phase diagrams of the Si-rich region from Safarian and Tangstad [39]

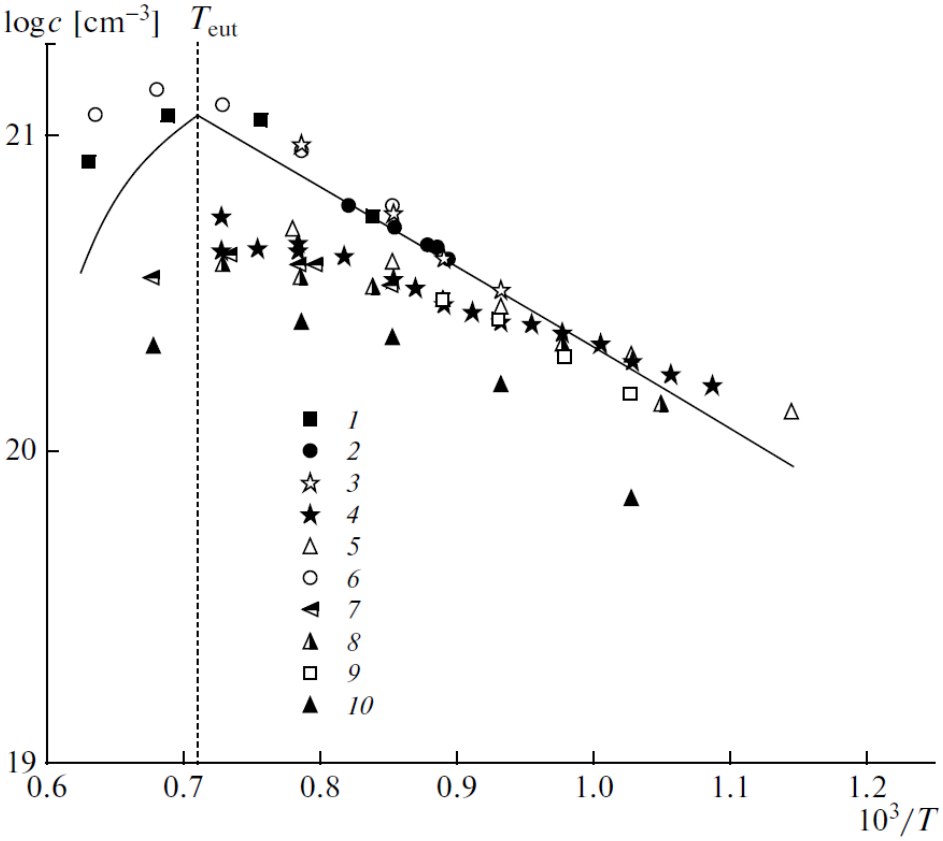

Figure A.8: Optimized phase diagrams of the Si-rich region from Arutyunyan [2]. For denotations, see Figure A.2.

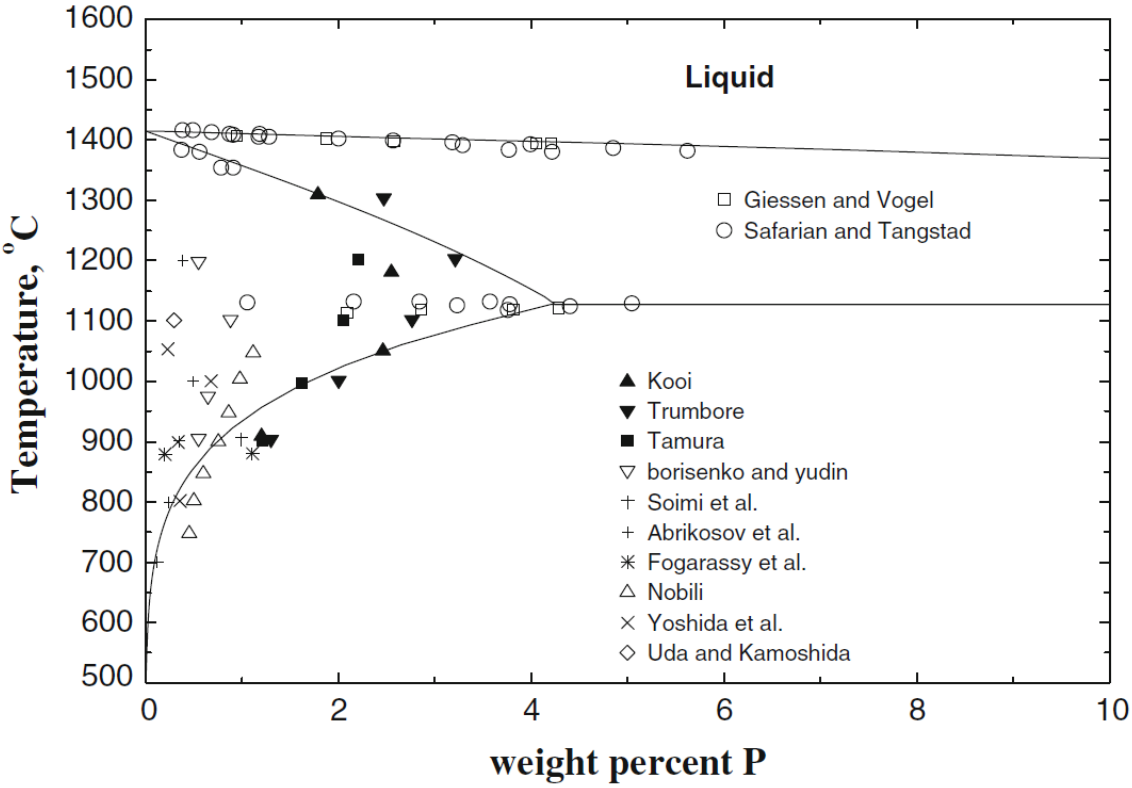

Figure A.9: Optimized phase diagrams of the Si-rich region from Jung and Zhang [26]

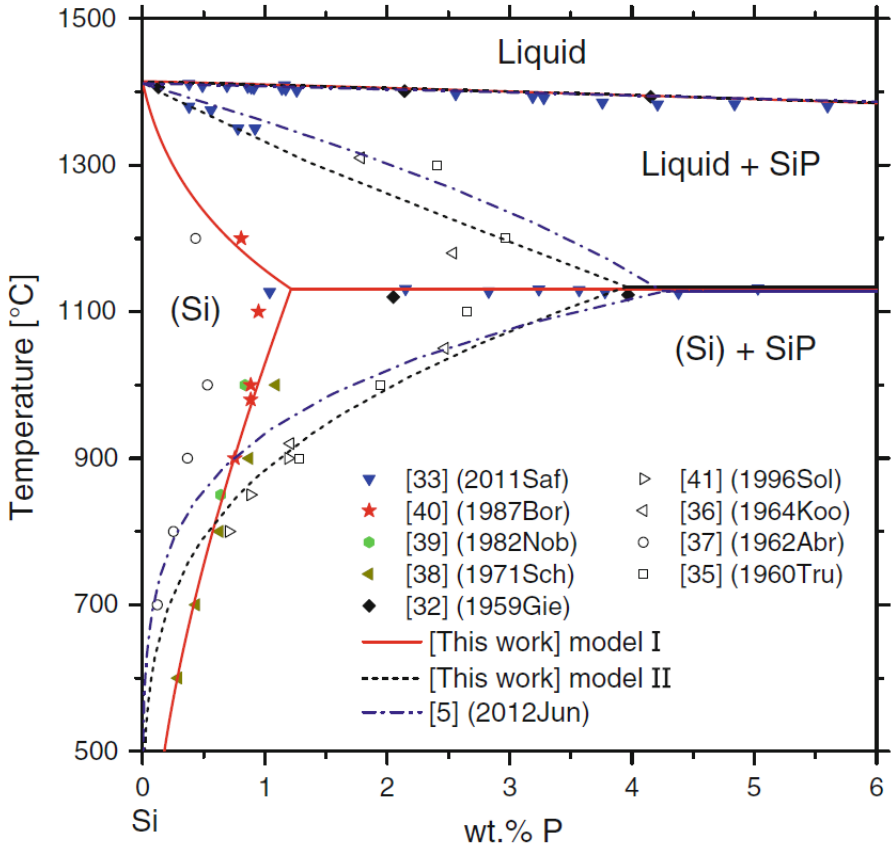

Figure A.10: Optimized phase diagrams of the Si-rich region from Liang and Schmid-Fetzer [28]

B

Files used in the Lukas programs for the thermodynamic assessment of Si – P

.coe file

```
10 6 SIP 3 5 9 1 6100.00
2 SI1(DIA_A4)
150.00 -8.16260867D+03 1.37236859D+02 -2.28317533D+01 -1.91290388D-03
1.7666710D+05 -3.5517837D-09 0.000000D+00 0.000000D+00 0.000000D+00
1687.00 -9.45764198D+03 1.67281367D+02 -2.71960000D+01 0.00000000D+00
0.0000000D+00 0.0000000D+00 0.000000D+00 0.000000D+00 -4.203692D+30
2 SI1(L)
150.00 4.25337509D+04 1.07137420D+02 -2.28317533D+01 -1.91290388D-03
1.7666710D+05 -3.5517837D-09 0.000000D+00 2.093066D-21 0.000000D+00
1687.00 4.03705228D+04 1.37722298D+02 -2.71960000D+01 0.00000000D+00
0.0000000D+00 0.0000000D+00 0.000000D+00 0.000000D+00 0.000000D+00
1 SER
150.00 0.00000000D+00 0.00000000D+00 0.00000000D+00 0.00000000D+00
0.0000000D+00 0.0000000D+00 0.000000D+00 0.000000D+00 0.000000D+00
4 P1(RED)
250.00 -2.59765590D+04 1.48672002D+02 -2.55500000D+01 3.41210000D-03
1.6009500D+05 -2.4188667D-06 0.000000D+00 0.000000D+00 0.000000D+00
500.00 -2.17237207D+04 7.76717365D+01 -1.43680000D+01 -9.57685000D-03
-1.4137500D+05 3.9391667D-07 0.000000D+00 0.000000D+00 0.000000D+00
852.35 -1.19408413D+05 1.02602962D+03 -1.49449556D+02 6.72723639D-02
1.2495943D+07 -6.6519289D-06 0.000000D+00 0.000000D+00 0.000000D+00
1500.00 -2.45241188D+04 1.53839181D+02 -2.63260000D+01 0.00000000D+00
0.0000000D+00 0.0000000D+00 0.000000D+00 0.000000D+00 0.000000D+00
2 P1(L)
250.00 -2.63161114D+04 4.34930931D+02 -7.07440584D+01 -2.89893611D-03
```

```
1.1411467D+06 3.9049371D-05 0.000000D+00 0.000000D+00 0.000000D+00
317.30 -7.23244867D+03 1.33291873D+02 -2.63260000D+01 0.00000000D+00
0.0000000D+00 0.0000000D+00 0.000000D+00 0.000000D+00 0.000000D+00
1 SER
150.00 0.00000000D+00 0.00000000D+00 0.00000000D+00 0.00000000D+00
0.0000000D+00 0.0000000D+00 0.000000D+00 0.000000D+00 0.000000D+00
2 P1(G)
298.00 3.09735164D+05 -1.55073551D+01 -2.19072138D+01 9.84632977D-04
3.0328168D+04 -1.3743367D-07 0.000000D+00 0.000000D+00 0.000000D+00
2 0.5*P2(G)
298.00 6.58316450D+04 1.11500506D+01 -1.78286646D+01 -4.37085745D-04
9.54610719D+04 2.77586310D-08 0.000000D+00 0.000000D+00 0.000000D+00
2 0.25*P4(G)
298.00 7.57014834D+03 6.74326790D+01 -2.02669509D+01 -2.27398629D-04
1.6292819D+05 1.6633036D-08 0.000000D+00 0.000000D+00 0.000000D+00
2 SI1(G)
298.00 4.44502664D+05 -3.33039842D+01 -2.02697724D+01 -2.29778507D-04
-8.4647067D+04 -2.4384488D-08 0.000000D+00 0.000000D+00 0.000000D+00
2 0.5*SI2(G)
298.00 2.87585083D+05 2.27731402D+01 -2.03357672D+01 -9.37153150D-04
1.8241442D+05 9.6972615D-08 0.000000D+00 0.000000D+00 0.000000D+00
2 0.3*SI3(G)
298.00 2.05112752D+05 5.09893641D+01 -2.07527931D+01 1.54830227D-04
1.0608398D+05 -3.68092819D-08 0.000000D+00 0.000000D+00 0.000000D+00
7Liquid 12 0 0 0 0 0 0 2 2
000000 .00 .00000 .000000 .000000 0.  .00000
000000 .00 .00000 .000000 .000000 0.  .00000
110000 -20801.04 4.11720 .000000 .000000 0.  .00000
110000 -13982.31 2.78770 .000000 .000000 0.  .00000
000000 .00 .00000 .000000 .000000 0.  .00000
000000 .00 .00000 .000000 .000000 0.  .00000
000000 .00 .00000 .000000 .000000 0.  .00000
3DIA(SI) 12 0 0 0 0 0 0 1 3
000000 .00 .00000 .000000 .000000 0.  .00000
000000 .00 30.00000 .000000 .000000 0.  .00000
000000 -40498.48 21.80790 .000000 .000000 0.  .00000
1<Pred> 3 0 1 0 0 0 0 1 1
000000 .00 .00000 .000000 .000000 0.  .00000
1<SiP> 4 1 1 0 0 0 0 3 4
010000 -38425.47 109.30143 -18.901300 -2.55D-03 133294.  -3.62675D-07
1<SiP2> 5 1 2 0 0 0 0 3 4
010000 -36229.62 137.07888 -23.644767 .000000 151893.  -1.15144D-06
1(0.5P2(G)) 6 0 1 0 0 0 0 3 5
000000 .00 .00000 .000000 .000000 0.  .00000
1P1(L) 7 0 1 0 0 0 0 2 2
000000 .00 .00000 .000000 .000000 0.  .00000
1SI1SER 8 1 0 0 0 0 0 3 4
000000 .00 .00000 .000000 .000000 0.  .00000
```

```
1P1SER 9 0 1 0 0 0 0 3 4
000000 .00 .00000 .000000 .000000 0.  .00000
1DIA(SI) 0 1 0 0 0 0 0 1 1
000000 .00 .00000 .000000 .000000 0.  .00000
00000000000000000000000000000000000000000000000000000000000000000000000000000000
```

.dat file

```
'ef' 1 4 6 0 6 3 0 0 1404.15 10 0 0 0.340000 0.0200 0.50000 0.0000 1.000 0
'ef' 1 5 3 0 6 3 0 0 852.15 10 0 0 0.999000 0.0050 0.66660 0.0000 1.000 0
'be' 2 4 0 0 6 2 0 0 1119.89 5 0 0 0.007326 0.0100 0.500000 0.0000 0.00 0
'be' 2 4 0 0 6 2 0 0 1130.44 5 0 0 0.008090 0.0100 0.500000 0.0000 0.00 0
'be' 2 4 0 0 6 2 0 0 1140.61 5 0 0 0.008259 0.0100 0.500000 0.0000 0.00 0
'be' 2 4 0 0 6 2 0 0 1171.90 5 0 0 0.009358 0.0100 0.500000 0.0000 0.00 0
'be' 2 4 0 0 6 2 0 0 1220.40 5 0 0 0.010994 0.0100 0.500000 0.0000 0.00 0
'ta' 2 4 0 0 6 2 0 0 1323.15 5 0 0 0.004500 0.0010 0.500000 0.0000 0.00 0
'ab' 2 4 0 0 6 2 0 0 973.15 5 0 0 0.001400 0.0010 0.500000 0.0000 0.00 0
'ab' 2 4 0 0 6 2 0 0 1073.15 5 0 0 0.003200 0.0010 0.500000 0.0000 0.00 0
'ab' 2 4 0 0 6 2 0 0 1173.15 5 0 0 0.004500 0.0010 0.500000 0.0000 0.00 0
'ab' 2 4 0 0 6 2 0 0 1273.15 5 0 0 0.005000 0.0010 0.500000 0.0000 0.00 0
'ab' 2 4 0 0 6 2 0 0 1473.15 5 0 0 0.004300 0.0010 0.500000 0.0000 0.00 0
'jo' 2 4 0 0 6 2 0 0 1323.15 5 0 0 0.004396 0.0010 0.500000 0.0000 0.00 0
'ts' 2 4 0 0 6 2 0 0 1150.15 5 0 0 0.007695 0.0010 0.500000 0.0000 0.00 0
'ts' 2 4 0 0 6 2 0 0 1223.15 5 0 0 0.008245 0.0010 0.500000 0.0000 0.00 0
'sc' 2 4 0 0 6 2 0 0 873.15 5 0 0 0.002423 0.0010 0.500000 0.0000 0.00 0
'sc' 2 4 0 0 6 2 0 0 973.15 5 0 0 0.003643 0.0010 0.500000 0.0000 0.00 0
'sc' 2 4 0 0 6 2 0 0 1073.15 5 0 0 0.005258 0.0010 0.500000 0.0000 0.00 0
'sc' 2 4 0 0 6 2 0 0 1173.15 5 0 0 0.007251 0.0010 0.500000 0.0000 0.00 0
'sc' 2 4 0 0 6 2 0 0 1273.15 5 0 0 0.009022 0.0010 0.500000 0.0000 0.00 0
'yo' 2 4 0 0 6 2 0 0 1173.15 5 0 0 0.007328 0.0010 0.500000 0.0000 0.00 0
'fa' 2 4 0 0 6 2 0 0 1173.15 5 0 0 0.004945 0.0010 0.500000 0.0000 0.00 0
'fa' 2 4 0 0 6 2 0 0 1273.15 5 0 0 0.006100 0.0010 0.500000 0.0000 0.00 0
'fa' 2 4 0 0 6 2 0 0 1323.15 5 0 0 0.006503 0.0010 0.500000 0.0000 0.00 0
'ma' 2 4 0 0 6 2 0 0 1373.28 5 0 0 0.007028 0.0010 0.500000 0.0000 0.00 0
'ma' 2 4 0 0 6 2 0 0 1271.77 5 0 0 0.006408 0.0010 0.500000 0.0000 0.00 0
'ma' 2 4 0 0 6 2 0 0 1192.10 5 0 0 0.005902 0.0010 0.500000 0.0000 0.00 0
'ma' 2 4 0 0 6 2 0 0 1125.85 5 0 0 0.005272 0.0010 0.500000 0.0000 0.00 0
'ma' 2 4 0 0 6 2 0 0 1023.97 5 0 0 0.003836 0.0010 0.500000 0.0000 0.00 0
'ma' 2 4 0 0 6 2 0 0 953.97 5 0 0 0.002493 0.0010 0.500000 0.0000 0.00 0
'ta' 2 4 0 0 6 2 0 0 1373.15 5 0 0 0.007328 0.0010 0.500000 0.0000 0.00 0
'ud' 2 4 0 0 6 2 0 0 1373.15 5 0 0 0.002380 0.0010 0.500000 0.0000 0.00 0
'fo' 2 4 0 0 6 2 0 0 1148.15 5 0 0 0.003296 0.0010 0.500000 0.0000 0.00 0
'mi' 2 4 0 0 6 2 0 0 873.15 5 0 0 0.003040 0.0010 0.500000 0.0000 0.00 0
'no' 2 4 0 0 6 2 0 0 1123.15 5 0 0 0.005495 0.0010 0.500000 0.0000 0.00 0
'no' 2 4 0 0 6 2 0 0 1273.15 5 0 0 0.007328 0.0010 0.500000 0.0000 0.00 0
'bo' 2 4 0 0 6 2 0 0 1474.22 5 0 0 0.006867 0.0010 0.500000 0.0000 0.00 0
'bo' 2 4 0 0 6 2 0 0 1364.18 5 0 0 0.008050 0.0010 0.500000 0.0000 0.00 0
'bo' 2 4 0 0 6 2 0 0 1274.40 5 0 0 0.007495 0.0010 0.500000 0.0000 0.00 0
'bo' 2 4 0 0 6 2 0 0 1257.28 5 0 0 0.007483 0.0010 0.500000 0.0000 0.00 0
'bo' 2 4 0 0 6 2 0 0 1173.33 5 0 0 0.006319 0.0010 0.500000 0.0000 0.00 0
'so' 2 4 0 0 6 2 0 0 1073.15 5 0 0 0.005862 0.0010 0.500000 0.0000 0.00 0
'so' 2 4 0 0 6 2 0 0 1123.15 5 0 0 0.007328 0.0010 0.500000 0.0000 0.00 0
'so' 2 4 0 0 6 2 0 0 1173.15 5 0 0 0.009896 0.0010 0.500000 0.0000 0.00 0
'gi' 1 6 0 0 6 2 0 0 1818.15 20 0 0 0.139810 0.0050 1.00000 0.0000 0.00 0
```

```
'gi' 1 6 0 0 6 2 0 0 1809.15 20 0 0 0.149150 0.0050 1.00000 0.0000 0.00 0
'gi' 1 6 0 0 6 2 0 0 1735.15 5 0 0 0.187620 0.0050 1.00000 0.0000 0.00 0
'gi' 1 6 0 0 6 2 0 0 1676.15 5 0 0 0.216920 0.0050 1.00000 0.0000 0.00 0
'gi' 1 6 0 0 6 2 0 0 1669.15 5 0 0 0.204330 0.0050 1.00000 0.0000 0.00 0
'gi' 1 6 0 0 6 2 0 0 1625.15 5 0 0 0.227350 0.0050 1.00000 0.0000 0.00 0
'gi' 1 6 0 0 6 2 0 0 1604.15 5 0 0 0.246380 0.0050 1.00000 0.0000 0.00 0
'gi' 1 6 0 0 6 2 0 0 1559.15 5 0 0 0.259740 0.0050 1.00000 0.0000 0.00 0
'gi' 1 6 0 0 6 2 0 0 1513.15 5 0 0 0.279860 0.0050 1.00000 0.0000 0.00 0
'gi' 1 2 0 0 6 2 0 0 1673.15 5 0 0 0.018810 0.0100 0.000600 0.0050 0.00 0
'gi' 1 2 0 0 6 2 0 0 1666.15 5 0 0 0.037690 0.0100 0.000600 0.0050 0.00 0
'gi' 1 2 0 0 6 2 0 0 1632.15 5 0 0 0.096150 0.0100 0.000900 0.0050 0.00 0
'gi' 1 2 0 0 6 2 0 0 1599.15 5 0 0 0.151020 0.0100 0.001600 0.0050 0.00 0
'gi' 1 2 0 0 6 2 0 0 1587.15 5 0 0 0.168820 0.0100 0.002000 0.0050 0.00 0
'gi' 1 2 0 0 6 2 0 0 1576.15 5 0 0 0.181030 0.0100 0.002400 0.0050 0.00 0
'gi' 1 2 0 0 6 2 0 0 1542.15 5 0 0 0.223550 0.0100 0.003000 0.0050 0.00 0
'gi' 1 2 0 0 6 2 0 0 1504.15 5 0 0 0.257830 0.0100 0.005000 0.0050 0.00 0
'gi' 1 2 0 0 6 2 0 0 1475.15 5 0 0 0.279860 0.0100 0.006700 0.0050 0.00 0
'gi' 1 2 0 0 6 2 0 0 1404.15 5 0 0 0.350000 0.0100 0.009000 0.0020 0.00 0
'gi' 1 2 4 0 6 3 0 0 1404.15 5 0 0 0.350000 0.0100 0.009000 0.0020 0.50 0
'gi' 1 4 0 0 6 2 0 0 1404.15 5 0 0 0.350000 0.0100 0.500000 0.0000 0.00 0
'ug' 1 2 0 0 6 2 0 0 1404.00 5 0 0 0.370000 0.0200 0.010800 0.0100 0.00 0
'ug' 1 2 4 0 6 3 0 0 1404.00 5 0 0 0.370000 0.0200 0.010800 0.0100 0.50 0
'ug' 1 4 0 0 6 2 0 0 1404.00 5 0 0 0.370000 0.0200 0.500000 0.0000 0.00 0
'ug' 1 4 0 0 6 2 0 0 1398.00 5 0 0 0.560000 0.0200 0.500000 0.0000 0.00 0
'ug' 1 4 5 0 6 3 0 0 1398.00 5 0 0 0.560000 0.0200 0.500000 0.0000 0.6666 0
'ug' 1 5 0 0 6 2 0 0 1398.00 5 0 0 0.560000 0.0200 0.666000 0.0000 0.00 0
'ug' 1 4 0 0 6 2 0 0 1420.00 5 0 0 0.400690 0.0100 0.500000 0.0000 0.00 0
'ug' 1 4 0 0 6 2 0 0 1436.00 5 0 0 0.445120 0.0100 0.500000 0.0000 0.00 0
'ug' 1 4 0 0 6 2 0 0 1443.00 5 0 0 0.500000 0.0100 0.500000 0.0000 0.00 0
'ug' 1 4 0 0 6 2 0 0 1420.00 5 0 0 0.570100 0.0100 0.500000 0.0000 0.00 0
'ug' 1 5 0 0 6 2 0 0 1419.00 5 0 0 0.623180 0.0100 0.666000 0.0000 0.00 0
'ug' 1 5 0 0 6 2 0 0 1440.00 5 0 0 0.642950 0.0100 0.666000 0.0000 0.00 0
'ug' 1 5 0 0 6 2 0 0 1450.00 5 0 0 0.679380 0.0100 0.666000 0.0000 0.00 0
'ug' 1 5 0 0 6 2 0 0 1451.00 5 0 0 0.666660 0.0100 0.666000 0.0000 0.00 0
'ug' 1 5 0 0 6 2 0 0 1433.00 5 0 0 0.737050 0.0100 0.666000 0.0000 0.00 0
'ug' 1 5 0 0 6 2 0 0 1407.00 20 0 0 0.770480 0.0300 0.666000 0.0000 0.00 0
'sa' 1 2 0 0 6 2 0 0 1680.00 5 0 0 0.010000 0.0050 0.000960 0.0100 0.00 0
'sa' 1 2 0 0 6 2 0 0 1674.00 5 0 0 0.020000 0.0050 0.001759 0.0100 0.00 0
'sa' 1 2 0 0 6 2 0 0 1667.00 5 0 0 0.030000 0.0050 0.002692 0.0100 0.00 0
'sa' 1 2 0 0 6 2 0 0 1660.00 5 0 0 0.040000 0.0050 0.003625 0.0100 0.00 0
'sa' 1 2 0 0 6 2 0 0 1653.00 5 0 0 0.050000 0.0050 0.004558 0.0100 0.00 0
'sa' 1 2 0 0 6 2 0 0 1647.00 5 0 0 0.060000 0.0050 0.005358 0.0100 0.00 0
'sa' 2 1 0 0 6 2 0 0 1402.00 2 0 0 0.011300 0.0100 0.350000 0.0100 0.00 0
'sa' 1 2 0 0 6 2 0 0 1402.00 2 0 0 0.350000 0.0100 0.011300 0.0050 0.00 0
'sa' 1 2 4 0 6 3 0 0 1402.00 2 0 0 0.350000 0.0100 0.011300 0.0050 0.50 0
'sa' 1 4 0 0 6 2 0 0 1402.00 2 0 0 0.350000 0.0100 0.500000 0.0000 0.00 0
'sa' 1 4 0 0 6 2 0 0 1412.00 2 0 0 0.500000 0.0010 0.500000 0.0000 0.00 0
'JU' 4 2 3 0 3 1 -31650 1500 298.15 0 0 0 0.500 0.000 0.000 0.0000 1.00 0
```

```
'JU' 4 8 9 0 9 3 17.37 1.7 298.15 0 0 0 0.500 0.000 0.000 0.0000 1.00 0
'PH' 5 2 3 0 3 1 -28100 1500 298.15 0 0 0 0.660 0.000 0.000 0.0000 1.00 0
'PH' 5 8 9 0 9 3 23.3 2.3 298.15 0 0 0 0.660 0.000 0.000 0.0000 1.00 0
'ZA' 1 7 0 0 2 1 -89850 8985 1693.00 0 0.00 0 0.0035 0.00 1.00 0.00 0.00 0
'ZA' 1 7 0 0 2 1 -90444 9044 1712.00 0 0.00 0 0.0035 0.00 1.00 0.00 0.00 0
'ZA' 1 7 0 0 2 1 -91671 9167 1743.00 0 0.00 0 0.0035 0.00 1.00 0.00 0.00 0
'ZA' 1 7 0 0 2 1 -92939 9294 1743.00 0 0.00 0 0.0031 0.00 1.00 0.00 0.00 0
'ZA' 1 7 0 0 2 1 -95336 9534 1743.00 0 0.00 0 0.0027 0.00 1.00 0.00 0.00 0
'ZA' 1 7 0 0 2 1 -97122 9712 1691.00 0 0.00 0 0.0021 0.00 1.00 0.00 0.00 0
'ZA' 1 7 0 0 2 1 -98660 9866 1730.00 0 0.00 0 0.0021 0.00 1.00 0.00 0.00 0
'ZA' 1 7 0 0 2 1 -99659 9966 1771.00 0 0.00 0 0.0021 0.00 1.00 0.00 0.00 0
'ZA' 1 7 0 0 2 1 -100785 10079 1809.00 0 0.00 0 0.0021 0.00 1.00 0.00 0.00 0
'ZA' 1 7 0 0 2 1 -101912 10191 1827.00 0 0.00 0 0.0021 0.00 1.00 0.00 0.00 0
'ZA' 1 7 0 0 2 1 -103121 10312 1823.00 0 0.00 0 0.0019 0.00 1.00 0.00 0.00 0
'ZA' 1 7 0 0 2 1 -105152 10515 1697.00 0 0.00 0 0.0012 0.00 1.00 0.00 0.00 0
'ZA' 1 7 0 0 2 1 -106483 10648 1734.00 0 0.00 0 0.0012 0.00 1.00 0.00 0.00 0
'ZA' 1 7 0 0 2 1 -108505 10852 1782.00 0 0.00 0 0.0012 0.00 1.00 0.00 0.00 0
'ZA' 1 7 0 0 2 1 -109117 10912 1803.00 0 0.00 0 0.0012 0.00 1.00 0.00 0.00 0
'ZA' 1 7 0 0 2 1 -110377 11038 1831.00 0 0.00 0 0.0012 0.00 1.00 0.00 0.00 0
'ZA' 1 7 0 0 2 1 -112712 11271 1819.00 0 0.00 0 0.0010 0.00 1.00 0.00 0.00 0
'ZA' 1 7 0 0 2 1 -114075 11408 1819.00 0 0.00 0 0.0009 0.00 1.00 0.00 0.00 0
'Z1' 1 7 0 0 2 1 -21697 2170 1507.00 0 0.00 0 0.2650 0.0050 1.00 0.00 0.00 0
'Z1' 1 7 0 0 2 1 -26566 2657 1572.00 0 0.00 0 0.2010 0.0050 1.00 0.00 0.00 0
'Z1' 1 7 0 0 2 1 -28636 2864 1618.00 0 0.00 0 0.2010 0.0050 1.00 0.00 0.00 0
'Z1' 1 7 0 0 2 1 -27794 2779 1657.00 0 0.00 0 0.2010 0.0050 1.00 0.00 0.00 0
'Z1' 1 7 0 0 2 1 -39526 3953 1638.00 0 0.00 0 0.1040 0.0050 1.00 0.00 0.00 0
'Z1' 1 7 0 0 2 1 -39324 3932 1653.00 0 0.00 0 0.1040 0.0050 1.00 0.00 0.00 0
'MI' 1 7 0 0 2 1 -156853 5000 1823.00 0 0.00 0 0.000136 0.00001 1.0 0.0 0.0 0
'MI' 1 7 0 0 2 1 -155404 5000 1823.00 0 0.00 0 0.000167 0.00001 1.0 0.0 0.0 0
'MI' 1 7 0 0 2 1 -146629 5000 1823.00 0 0.00 0 0.000286 0.00001 1.0 0.0 0.0 0
'MI' 1 7 0 0 2 1 -132773 5000 1823.00 0 0.00 0 0.000575 0.00001 1.0 0.0 0.0 0
'MI' 1 7 0 0 2 1 -128606 5000 1823.00 0 0.00 0 0.000807 0.00001 1.0 0.0 0.0 0
'MI' 1 7 0 0 2 1 -126175 5000 1823.00 0 0.00 0 0.000994 0.00001 1.0 0.0 0.0 0
'MI' 1 7 0 0 2 1 -138559 5000 1723.00 0 0.00 0 0.000339 0.00001 1.0 0.0 0.0 0
'MI' 1 7 0 0 2 1 -143002 5000 1723.00 0 0.00 0 0.000298 0.00001 1.0 0.0 0.0 0
'MI' 1 7 0 0 2 1 -141524 5000 1748.00 0 0.00 0 0.000271 0.00001 1.0 0.0 0.0 0
'MI' 1 7 0 0 2 1 -146123 5000 1748.00 0 0.00 0 0.000256 0.00001 1.0 0.0 0.0 0
'MI' 1 7 0 0 2 1 -144494 5000 1773.00 0 0.00 0 0.000247 0.00001 1.0 0.0 0.0 0
'MI' 1 7 0 0 2 1 -149254 5000 1773.00 0 0.00 0 0.000207 0.00001 1.0 0.0 0.0 0
'MI' 1 7 0 0 2 1 -152255 5000 1798.00 0 0.00 0 0.000198 0.00001 1.0 0.0 0.0 0
'MI' 1 7 0 0 2 1 -158648 5000 1848.00 0 0.00 0 0.000134 0.00001 1.0 0.0 0.0 0
'UG' 1 1 0 0 2 1 -15287 1529 1439.00 0 0 0 0.50 0.0050 1.00 0.0000 0.00 0
'U1' 1 1 0 0 2 1 -14367 1437 1427.00 0 0 0 0.50 0.0050 1.00 0.0000 0.00 0
'U1' 1 1 0 0 2 1 -15125 1512 1439.00 0 0 0 0.50 0.0050 1.000 0.0000 0.00 0
'U1' 1 1 0 0 2 1 -15596 1560 1437.00 0 0 0 0.50 0.0050 1.000 0.0000 0.00 0
'U1' 1 1 0 0 2 1 -15084 1508 1441.79 0 0 0 0.50 0.0050 1.000 0.0000 0.00 0
'U1' 1 1 0 0 2 1 -15147 1515 1451.79 0 0 0 0.50 0.0050 1.000 0.0000 0.00 0
'U1' 1 1 0 0 2 1 -15283 1528 1461.07 0 0 0 0.50 0.0050 1.000 0.0000 0.00 0
```

```
'U1' 1 1 0 0 2 1 -15434 1543 1469.64 0 0 0 0.50 0.0050 1.000 0.0000 0.00 0
'U2' 1 4 7 0 2 2 -13827 1383 1419.00 0 0 0 0.449 0.0200 0.50 0.0000 1.00 0
'U2' 1 4 7 0 2 2 -16618 1662 1429.00 0 0 0 0.490 0.0200 0.50 0.0000 1.00 0
'U2' 1 4 7 0 2 2 -16724 1672 1423.00 0 0 0 0.450 0.0200 0.50 0.0000 1.00 0
'U2' 1 4 7 0 2 2 -17338 1734 1410.00 0 0 0 0.396 0.0200 0.50 0.0000 1.00 0
'U2' 1 4 7 0 2 2 -18965 1896 1409.00 0 0 0 0.396 0.0200 0.50 0.0000 1.00 0
'U2' 1 4 7 0 2 2 -21707 2171 1421.00 0 0 0 0.450 0.0200 0.50 0.0000 1.00 0
'U2' 1 4 7 0 2 2 -16123 1612 1424.29 0 0 0 0.450 0.0200 0.50 0.0000 1.00 0
'B2' 2 4 7 0 2 2 -22252 2225 1281.00 0 0.00 0 0.009675 0.001 0.50 0.00 1.00 0
'B2' 2 4 7 0 2 2 -22164 2216 1283.00 0 0.00 0 0.009719 0.001 0.50 0.00 1.00 0
'B2' 2 4 7 0 2 2 -20612 2061 1328.00 0 0.00 0 0.010728 0.001 0.50 0.00 1.00 0
'B2' 2 4 7 0 2 2 -20092 2009 1341.00 0 0.00 0 0.011028 0.001 0.50 0.00 1.00 0
'B2' 2 4 7 0 2 2 -19649 1965 1357.00 0 0.00 0 0.011403 0.001 0.50 0.00 1.00 0
'B2' 2 4 7 0 2 2 -20014 2001 1374.00 0 0.00 0 0.011809 0.001 0.50 0.00 1.00 0
'B2' 2 4 7 0 2 2 -17593 1759 1413.00 0 0.00 0 0.012764 0.001 0.50 0.00 1.00 0
'K2' 2 4 7 0 2 2 -19802 1980 1368.90 0 0.00 0 0.011687 0.001 0.50 0.00 1.00 0
'K2' 2 4 7 0 2 2 -20592 2059 1345.00 0 0.00 0 0.011121 0.001 0.50 0.00 1.00 0
'K2' 2 4 7 0 2 2 -21365 2136 1326.80 0 0.00 0 0.010700 0.001 0.50 0.00 1.00 0
'K2' 2 4 7 0 2 2 -22088 2209 1296.50 0 0.00 0 0.010017 0.001 0.50 0.00 1.00 0
'K2' 2 4 7 0 2 2 -22646 2265 1279.60 0 0.00 0 0.009644 0.001 0.50 0.00 1.00 0
'K2' 2 4 7 0 2 2 -23690 2369 1247.20 0 0.00 0 0.008950 0.001 0.50 0.00 1.00 0
'K2' 2 4 7 0 2 2 -25498 2550 1200.00 0 0.00 0 0.007984 0.001 0.50 0.00 1.00 0
'E1' 1 0 0 0 1 1 -114869 9572 6000.00 0 0 0 0.90000 0.000 0.00000 0.000 0 0
'E1' 1 0 0 0 1 1 -80291 9572 6000.00 0 0 0 0.80000 0.000 0.00000 0.000 0 0
'E1' 1 0 0 0 1 1 -60062 6691 6000.00 0 0 0 0.70000 0.000 0.00000 0.000 0 0
'E1' 1 0 0 0 1 1 -45711 5005 6000.00 0 0 0 0.60000 0.000 0.00000 0.000 0 0
'E1' 1 0 0 0 1 1 -34579 3809 6000.00 0 0 0 0.50000 0.000 0.00000 0.000 0 0
'E1' 1 0 0 0 1 1 -25484 2882 6000.00 0 0 0 0.40000 0.000 0.00000 0.000 0 0
'E1' 1 0 0 0 1 1 -17793 2124 6000.00 0 0 0 0.30000 0.000 0.00000 0.000 0 0
'E1' 1 0 0 0 1 1 -11132 2124 6000.00 0 0 0 0.20000 0.000 0.00000 0.000 0 0
'E1' 1 0 0 0 1 1 -5256 1483 6000.00 0 0 0 0.10000 0.000 0.00000 0.000 0 0
'E1' 1 0 0 0 2 1 -114869 9572 6000.00 0 0 0 0.10000 0.000 0.00000 0.000 0 0
'E1' 1 0 0 0 2 1 -80291 9572 6000.00 0 0 0 0.20000 0.000 0.00000 0.000 0 0
'E1' 1 0 0 0 2 1 -60062 6691 6000.00 0 0 0 0.30000 0.000 0.00000 0.000 0 0
'E1' 1 0 0 0 2 1 -45711 5005 6000.00 0 0 0 0.40000 0.000 0.00000 0.000 0 0
'E1' 1 0 0 0 2 1 -34579 3809 6000.00 0 0 0 0.50000 0.000 0.00000 0.000 0 0
'E1' 1 0 0 0 2 1 -25484 2882 6000.00 0 0 0 0.60000 0.000 0.00000 0.000 0 0
'E1' 1 0 0 0 2 1 -17793 2124 6000.00 0 0 0 0.70000 0.000 0.00000 0.000 0 0
'E1' 1 0 0 0 2 1 -11132 1483 6000.00 0 0 0 0.80000 0.000 0.00000 0.000 0 0
'E1' 1 0 0 0 2 1 -5256 1483 6000.00 0 0 0 0.90000 0.000 0.00000 0.000 0 0
```

.bfl file

```
6 0 1
1 1 1 1 1 1 1
10
1409.30 0.03600 0.50000 0.34900 2 4 1 1 1 1 1
10
1418.40 0.56600 0.50000 0.66666 1 4 5 1 1 1 1
10
852.00 0.66666 0.99000 1.00000 5 1 3 1 1 1 1
8
1409.30 300.00 80 80 2 2 4 0.03600 0.50000 1 1
1 2 1 0 1 3 1 0
8
1409.30 1425.00 80 80 2 1 4 0.34900 0.50000 1 1
1 2 1 0 1 3 1 0
8
1418.40 1425.00 80 80 2 1 4 0.56600 0.50000 1 1
1 2 1 0 1 3 1 0
8
1409.30 1687.00 80 80 2 1 2 0.34900 0.03600 1 1
1 2 1 0 1 3 1 0
8
1418.40 1440.00 80 80 2 1 5 0.56600 0.66666 1 1
1 2 1 0 1 3 1 0
8
1440.00 852.00 80 80 2 1 5 0.68000 0.66666 1 1
1 2 1 0 1 3 1 0
8
852.35 1440.00 80 80 2 1 5 0.99990 0.66666 1 1
1 2 1 0 1 3 1 0
8
300.00 1404.05 10 10 2 4 5 0.50000 0.66666 1 1
1 2 1 0 1 3 1 0
8
1409.30 2800.05 50 50 2 1 6 0.37000 1.00000 1 1
1 2 1 0 1 3 1 0
19
1 6 2 4 2 0 5 0.0000000 0.0000000
-1gi 1 -2ug 1 -3sa 1 -4vo 1 -5gs 1
19
1 6 2 4 2 0 5 0.0000000 0.0000000
-1ta 1 -2ab 1 -3jo 1 -4ts 1 -5sc 1
19
1 6 2 4 2 0 5 0.0000000 0.0000000
-6yo 1 -7fa 1 -8ma 1 -9ta 1 -1ud 2
19
1 6 2 4 2 0 5 0.0000000 0.0000000
```

```
-2fo 2 -3mi 2 -4no 2 -5bo 2 -6so 2
19
1 6 2 4 2 0 5 0.0000000 0.0000000
-8be 6 -8gi 2 -9gl 2 -1ug 3 -2sa 3
19
1 6 2 4 2 0 4 0.0000000 0.0000000
-3bi 3 -4ko 3 -5ug 3 -6u1 3 -2sx 3
19
1 6 2 4 2 0 4 0.0000000 0.0000000
-7u2 3 -8za 3 -9ju 3 -1ph 4
19
1 6 2 4 2 0 2 0.0000000 0.0000000
-2ju 4 -3ef 4
4
1200.00000 0.00010 0.55000 90 90 2 1 1 7
2 1 8 2
4
1413.00000 0.00010 0.55000 90 90 2 1 1 7
2 1 8 3
19
2 2 1 4 1 0 2 0.0000000 0.0000000
-1BI 1 -2KO 1
19
2 2 2 4 1 0 2 0.0000000 0.0000000
-1B2 4 -2K2 4
4
1400.00000 0.00500 0.55000 90 90 1 1 1 7
4 1 8 2
4
1500.00000 0.00500 0.55000 90 90 1 1 1 7
4 1 8 3
4
1650.00000 0.00500 0.55000 90 90 1 1 1 7
4 1 8 4
19
4 2 1 4 1 0 3 0.0000000 0.0000000
-1U1 4 -2UG 4 -3Z1 4
19
4 2 2 4 1 0 1 0.0000000 0.0000000
-4U2 4
10
1409.30 0.03600 0.50000 0.34900 2 4 1 1 1 1 1
10
1409.30 0.03600 0.50000 0.34900 2 4 1 2 1 1 1 1
10
1418.40 0.56600 0.50000 0.66666 1 4 5 2 1 1 1 1
10
852.00 0.66666 0.99000 1.00000 5 1 3 2 1 1 1 1
```

```
8
1409.30 300.00 80 80 2 2 4 0.03600 0.50000 1 1
5 2 1 0 1 3 1 0
8
1409.30 1434.00 80 80 2 1 4 0.34900 0.50000 1 1
5 2 1 0 1 3 1 0
8
1418.40 1434.00 80 80 2 1 4 0.56600 0.50000 1 1
5 2 1 0 1 3 1 0
8
1687.00 1407.00 95 95 2 1 2 0.00000 0.00000 1 1
5 2 1 0 1 3 1 0
8
1409.30 1687.00 80 80 2 1 2 0.34900 0.03600 1 1
5 2 1 0 1 3 1 0
19
5 6 2 4 2 0 5 0.0000000 0.0000000
-1ta 1 -2ab 1 -3jo 1 -4ts 1 -5sc 1
19
5 6 2 4 2 0 5 0.0000000 0.0000000
-1yo 1 -2fa 1 -3ma 1 -4t1 1 -5ud 1
19
5 6 2 4 2 0 5 0.0000000 0.0000000
-6fo 1 -7mi 1 -8no 1 -9bo 1 -1so 2
19
5 6 2 4 2 0 5 0.0000000 0.0000000
-2gi 2 -3ug 2 -4sa 2
19
5 6 2 4 2 0 5 0.0000000 0.0000000
-8be 6 -8gi 2 -9gl 2 -1ug 3 -2sa 3
19
5 6 2 4 2 0 4 0.0000000 0.0000000
-3bi 3 -4ko 3 -5ug 3 -6u1 3 -2sx 3
19
5 6 2 4 2 0 4 0.0000000 0.0000000
-7u2 3 -8za 3 -9ju 3 -1ph 4
19
5 6 2 4 2 0 2 0.0000000 0.0000000
-2ju 4 -3ef 4
4
1850.00000 0.00010 0.55000 90 90 1 1 1 7
6 1 8 3
4
1693.00000 0.00010 0.55000 90 90 1 1 1 7
6 1 8 2
19
6 2 1 4 1 0 2 0.0000000 0.0000000
-1MI 2 -2ZA 2
```

```
16
15
10
1493.00 0.30000 0.00800 1.00000 1 2 6 1 1 1 1
10
1419.30 0.50000 0.00580 1.00000 4 2 6 1 1 1 1
```

C

VBA programs written to simulate the silicon dephosphorization

```
Public T, Pi, xP, xO, xSi(400), xPP(400), aSi, aP, aO, Seff, X(400), Tps(400),
minitSi(400), minitP(400), minitO(400), xO1(400)
Public KSi, KSi2, KSi3, KP, KP2, KP3, KP4, KPSi, KPSi2, KP2Si2
Public KSiO, KSiO2, KSi2O2, KO3, KPO, KPO2, KP2O3, KP2O4, KP2O5, KP3O6, KP4O6,
KP4O7, KP4O8, KP4O9
Public KP4O10, KO, KO2, KSiSiO2
Public GammaInfiniP, EpsilonPP, GammaInfiniO, EpsilonOO, GammaP, GammaO, GammaPter,
GammaOter, EpsilonOP
Public pSi, pSi2, pSi3, pP, pP2, pP3, pP4, pPSi, pPSi2, pP2Si2, pSiO, pSiO2,
pSi2O2
Public pO2lim, pO, pO2, pO3
Public pPO, pPO2, pP2O3, pP2O4, pP2O5, pP3O6, pP4O6, pP4O7, pP4O8, pP4O9, pP4O10
Public R, MSi, MP, MO, Pst, dSi, dPred, Sbille(400), rayon(400)
```

```
Sub constantes_standard()
Pi = 4 * Atn(1)
Pst = 100000 'standard pressure in Pa
R = 8.31441
MSi = 0.028096 'Si weight (kg)
MP = 0.030974
MO = 0.015999
Reff = 0.001 'rayon de l'orifice de la cellule d'effusion en m
Clausing = 1
Seff = Clausing * Pi * Reff ^2 ' surface d'effusion
dSi = 2330 'kg.m-3
dPred = 2160 'kg.m-3
```

```
End Sub
```

```
Sub constantes_equilibre()
'Si(liq,1700K) - P(liq,1700K): Equilibres de re-vaporisation Log Si(g)=A/T+B
dans l'equilibre (à 1000 bar)

KSi = 10^(-20435.6988 / T + 5.854934969) ' Si(l) = Si(g)
KSi2 = 10^(-23923.49907 / T + 5.343919088) ' 2 Si(l) = Si2(g)
KSi3 = 10^(-23194.24067 / T + 4.346158998) ' 3Si(l) = Si3(g) du Si-P

KP = 10^(-16908.08151 / T + 5.714720003) ' P(l) = P(g) du Si-P
KP2 = 10^(-5998.240469 / T + 5.193059582) ' 2P(l) =P2(g) du Si-P
KP3 = 10^(-6941.766924 / T - 4.546006219) ' 3P(l) =P3(g) du Si-P
KP4 = 10^(-678.9268003 / T + 2.933013326) ' 4P(l) =P4(g) du Si-P

KPSi = 10^(-17789.47578 / T + 5.782509987) ' Si(l) + P(l) = SiP(g) du Si-P
KPSi2 = 10^(-15783.92085 / T + 4.973463429) ' 2Si(l) + P(l) = Si2P(g) du Si-P
KP2Si2 = 10^(-16961.8208 / T + 5.14536849) ' 2Si(l) + 2P(l) = Si2P2(g) du Si-P

'P-P2O5:  Equilibres de re-vaporisation Log Si(g)=A/T+B dans l'equilibre à 1000
bar
KPO = 10^(2217.61449 / T + 3.194944019) 'KPO= PO(g)-1/2O2(g)-P(liq) du P(liq)+1/2
O2(g)=PO(g)
KPO2 = 10^(15500.4427 / T - 0.682322528) ' P(liq)+O2(g)=PO2(g)
KP2O3 = 10^(36369.76596 / T - 5.094858024) ' 2P(liq)+3/2O2(g)=P2O3(g)
KP2O4 = 10^(48976.91171 / T - 10.1040177) ' 2P(liq)+2O2(g)=P2O4(g)
KP2O5 = 10^(58366.88894 / T - 12.01629232) ' 2P(liq)+5/2O2(g)=P2O5(g)
KP3O6 = 10^(80744.27446 / T - 18.08969753) ' 3P(liq)+3O2(g)=P3O6(g)
KP4O6 = 10^(83458.73128 / T - 22.53780507) ' 4P(liq)+6O2(g)=P4O6(g)
KP4O7 = 10^(102909.1795 / T - 26.45224205) ' 4P(liq)+7/2O2(g)=P4O7(g)
KP4O8 = 10^(119188.1544 / T - 30.80213323) ' 4P(liq)+4O2(g)=P4O8(g)
KP4O9 = 10^(135153.9469 / T - 35.54532763) ' 4P(liq)+9/2O2(g)=P4O9(g)
KP4O10 = 10^(150100.3106 / T - 40.70424683) ' 4P(liq)+5O2(g)=P4O10(g)
'Si-SiO2:  Equilibres de re-vaporisation Log Si(g)=A/T+B dans l'equilibre à 1000
bar
KSiO = 10^(8538.953912 / T + 2.393445894) ' Si(liq)+1/2 O2(g)=SiO(g)
KSiO2 = 10^(19759.25066 / T - 1.646585674) ' Si(liq)+O2(g)=SiO2(g)
KSi2O2 = 10^(27326.31807 / T - 2.119098244) ' 2Si(liq)+O2(g)=Si2O2(g)

' O2=2O(g)
KO = 10^(-26678.04125 / T + 6.984811558) ' O2=2O(g) valeurs prises dans Si-SiO2

'O2=O2(g)limite de phase

KSiSiO2 = 10^(48805.96887 / T - 10.01148494) ' Si(lig)+O2(g)=SiO2(liq) (log(a)-O2(g)
du Si-SiO2)
```

```
KO3 = 10^(-5212.246237 / T - 2.206485392) ' O2=2/3O3(g)du Si-SiO2 valeurs prises
dans Si-SiO2
End Sub
```

```
Sub coefficients_activite()

'Si-P
GammaInfiniP = Exp(-4181.3 / T + 0.8302) ' gamma infini du P dans Si utilisant
l'opimisation
EpsilonPP = Exp(-14245 / T - 2.8332) ' coeff Wagner :  ln gamma_P( P dilue dans
Si)=ln gamma_P(infini)+ xP*epsilonPP utilisant l'opimisation
GammaP = Exp(Math.Log(GammaInfiniP) + xP * EpsilonPP)
'Si-O
GammaInfiniO = Exp(-20128 / T + 6.6251) ' gamma infini du P dans Si utilisant
l'opimisation
EpsilonOO = 0 ' coeff Wagner :  ln gamma_P( P dilue dans Si)=ln gamma_P(infini)+
xP*epsilonPP utilisant l'opimisation
GammaO = Exp(Math.Log(GammaInfiniO) + xO * EpsilonOO)
'Si-P-O
EpsilonOP = -37.05
'GammaPter = Exp(Math.Log(GammaInfiniP) + (xP * EpsilonPP) + (xO * EpsilonOP))
'GammaOter = Exp(Math.Log(GammaInfiniO) + (xO * EpsilonOO) + (xP * EpsilonOP))
End Sub
```

```
Sub definition_pression()
constantes_equilibre

pSi = aSi * KSi
pSi2 = (aSi)^2 * KSi2
pSi3 = (aSi)^3 * KSi3

pP = aP * KP
pP2 = (aP)^2 * KP2
pP3 = (aP)^3 * KP3
pP4 = (aP)^4 * KP4
pPSi = aSi * aP * KPSi
pPSi2 = (aSi)^2 * aP * KPSi2
pP2Si2 = (aSi)^2 * (aP)^2 * KP2Si2

pSiO = aSi * aO * KSiO
pSiO2 = aSi * aO^2 * KSiO2

pSi2O2 = aSi^2 * aO^2 * KSi2O2

pO2 = 1 / (aSi * KSiSiO2)
pO = (pO2 * KO)^(1 / 2)

pO3 = (KO3 * pO2)^(3 / 2)
```

```
pPO = aP * aO * KPO
pPO2 = aP * aO^2 * KPO2
pP2O3 = aP^2 * aO^3 * KP2O3
pP2O4 = aP^2 * aO^4 * KP2O4
pP2O5 = aP^2 * aO^5 * KP2O5
pP3O6 = aP^3 * aO^6 * KP3O6
pP4O6 = aP^4 * aO^6 * KP4O6
pP4O7 = aP^4 * aO^7 * KP4O7
pP4O8 = aP^4 * aO^8 * KP4O8
pP4O9 = aP^4 * aO^9 * KP4O9
pP4O10 = aP^4 * aO^10 * KP4O10

End Sub
```

```
Sub calcul_SiOP_sous_vide2() ' calcul avec une PO2 four fixee avec SGTE-SGPS(Gurvitch)
constantes_standard

J = 0

Worksheets("calc_four2").Cells(1 + J, 1).Value = "xP"
Worksheets("calc_four2").Cells(1 + J, 2).Value = "log xP"
Worksheets("calc_four2").Cells(1 + J, 3).Value = "T(K)"
Worksheets("calc_four2").Cells(1 + J, 4).Value = "1/T(K)"
Worksheets("calc_four2").Cells(1 + J, 5).Value = "a(Si)"
Worksheets("calc_four2").Cells(1 + J, 6).Value = "log a(P)"
Worksheets("calc_four2").Cells(1 + J, 7).Value = "log pSi(bar)"
Worksheets("calc_four2").Cells(1 + J, 8).Value = "log pSi2(bar)"
Worksheets("calc_four2").Cells(1 + J, 9).Value = "log pSi3(bar)"
Worksheets("calc_four2").Cells(1 + J, 10).Value = "log pP3(bar)"
Worksheets("calc_four2").Cells(1 + J, 11).Value = "log pO(bar)"
Worksheets("calc_four2").Cells(1 + J, 12).Value = "log pO2(bar)"
Worksheets("calc_four2").Cells(1 + J, 13).Value = "log pO3(bar)"
Worksheets("calc_four2").Cells(1 + J, 14).Value = "log pP(bar)"
Worksheets("calc_four2").Cells(1 + J, 15).Value = "log pP2(bar)"
Worksheets("calc_four2").Cells(1 + J, 16).Value = "log pP4(bar)"
Worksheets("calc_four2").Cells(1 + J, 17).Value = "log pPSi(bar)"
Worksheets("calc_four2").Cells(1 + J, 18).Value = "log pPSi2(bar)"
Worksheets("calc_four2").Cells(1 + J, 19).Value = "log pP2Si2(bar)"
Worksheets("calc_four2").Cells(1 + J, 20).Value = "log pSiO(bar)"
Worksheets("calc_four2").Cells(1 + J, 21).Value = "log pSiO2(bar)"
Worksheets("calc_four2").Cells(1 + J, 22).Value = "log pSi2O2(bar)"
Worksheets("calc_four2").Cells(1 + J, 23).Value = "log pPO(bar)"
Worksheets("calc_four2").Cells(1 + J, 24).Value = "log pPO2bar)"
Worksheets("calc_four2").Cells(1 + J, 25).Value = "log pP2O3(bar)"
Worksheets("calc_four2").Cells(1 + J, 26).Value = "log pP2O4(bar)"
Worksheets("calc_four2").Cells(1 + J, 27).Value = "log pP2O5(bar)"
Worksheets("calc_four2").Cells(1 + J, 28).Value = "log pP4O6(bar)"
Worksheets("calc_four2").Cells(1 + J, 29).Value = "log pP4O7(bar)"
```

```
Worksheets("calc_four2").Cells(1 + J, 30).Value = "log pP4O8(bar)"
Worksheets("calc_four2").Cells(1 + J, 31).Value = "log pP4O9(bar)"
Worksheets("calc_four2").Cells(1 + J, 32).Value = "log pP4O10(bar)"
Worksheets("calc_four2").Cells(1 + J, 33).Value = "log(NP_SiOP)"
Worksheets("calc_four2").Cells(1 + J, 34).Value = "log(NSi_SiOP)"
Worksheets("calc_four2").Cells(1 + J, 35).Value = "log(NO_SiOP)"
Worksheets("calc_four2").Cells(1 + J, 36).Value = "log NP_SiOP / NSi_SiOP(bar)"
Worksheets("calc_four2").Cells(1 + J, 37).Value = "log Flux P evap"
Worksheets("calc_four2").Cells(1 + J, 38).Value = "log Flux Si evap"
Worksheets("calc_four2").Cells(1 + J, 39).Value = "log Flux O evap"
Worksheets("calc_four2").Cells(1 + J, 40).Value = "log Flux P/Flux Si evap"
Worksheets("calc_four2").Cells(1 + J, 41).Value = "log Flux O inc"
Worksheets("calc_four2").Cells(1 + J, 42).Value = "log Flux O evap/inc"
Worksheets("calc_four2").Cells(1 + J, 43).Value = "log x(O)"
Worksheets("calc_four2").Cells(1 + J, 44).Value = "M"

pO2four = 10^-4 ' pression en bar du four

fluxO_inc = 2 * pO2four * Pst * Seff * ((2 * Pi * 2 * MO * R * 300)^(-1 / 2))
' flux incident depuis les parois à 300K

For L = -2 To -8.1 Step -0.3
xP = 10^(L) 'fraction molaire de phosphore
'xP = 0.0001

'For T = 1700 To 2500 Step 50
T = 1800 '1700 à l'origine
constantes_equilibre
coefficients_activite

Line0:
xSi = 1 - xP 'activite de de silicium
aSi = xSi
If M = 0 Then
aP = GammaInfiniP * xP

Else
xSi = 1 - xP - xO 'activite de de silicium
aSi = xSi
coefficients_activite
aP = GammaPter * xP
End If
pO2lim = 1 / KSiSiO2
Imax = Log(pO2lim) / Log(10)
Imin = Imax - 60
Pas = -1
```

```
Line1:
For I = Imax To Imin Step Pas
pO2 = 10^I
aO = pO2^(1 / 2) 'equilibre avec la SiO2

definition_pression

NSi_SiOP = pSi + 2 * pSi2 + 3 * pSi3 + pPSi + 2 * pPSi2 + 2 * pP2Si2 + pSiO +
pSiO2 + 2 * pSi2O2
NP_SiOP = pP + 2 * pP2 + 3 * pP3 + 4 * pP4 + pPSi + pPSi2 + 2 * pP2Si2 + pPO
+ pPO2 + 2 * pP2O3 + 2 * pP2O4 + 2 * pP2O5 + 3 * pP3O6 + 4 * pP4O6 + 4 * pP4O7
+ 4 * pP4O8 + 4 * pP4O9 + 4 * pP4O10
NO_SiOP = pSiO + 2 * pSiO2 + 2 * pSi2O2 + pPO + 2 * pPO2 + 3 * pP2O3 + 4 * pP2O4
+ 5 * pP2O5 + 6 * pP3O6 + 6 * pP4O6 + 7 * pP4O7 + 8 * pP4O8 + 9 * pP4O9 + 10
* pP4O10
fluxSi = (Seff * Pst / ((2 * Pi * R * T)^(1 / 2))) * (pSi / ((MSi)^(1 / 2)) +
2 * pSi2 / ((2 * MSi)^(1 / 2)) + 3 * pSi3 / ((3 * MSi)^(1 / 2)) + pPSi / ((MSi
+ MP)^(1 / 2)) + 2 * pPSi2 / ((2 * MSi + MP)^(1 / 2)) + pSiO / ((MSi + MO)^(1
/ 2)) + pSiO2 / ((MSi + 2 * MO)^(1 / 2)) + 2 * pSi2O2 / ((2 * MSi + 2 * MO)^(1
/ 2)) + 2 * pP2Si2 / ((2 * MSi + 2 * MP)^(1 / 2)))
fluxP = (Seff * Pst / ((2 * Pi * R * T)^(1 / 2))) * (pP / ((MP)^(1 / 2)) + 2
* pP2 / ((2 * MP)^(1 / 2)) + 3 * pP3 / ((3 * MP)^(1 / 2)) + 4 * pP4 / ((4 * MP)^(1
/ 2)) + pPSi / ((MSi + MP)^(1 / 2)) + pPSi2 / ((2 * MSi + MP)^(1 / 2)) + 2 *
pP2Si2 / ((2 * MSi + 2 * MP)^(1 / 2))) + pPO / ((MP + MO)^(1 / 2)) + pPO2 / ((MP
+ 2 * MO)^(1 / 2)) + 2 * pP2O3 / ((2 * MP + 3 * MO)^(1 / 2)) + 2 * pP2O4 / ((2
* MP + 4 * MO)^(1 / 2)) + 2 * pP2O5 / ((2 * MP + 5 * MO)^(1 / 2)) + 3 * pP3O6
/ ((3 * MP + 6 * MO)^(1 / 2)) + 4 * pP4O6 / ((4 * MP + 6 * MO)^(1 / 2)) + 4 *
pP4O7 / ((4 * MP + 7 * MO)^(1 / 2)) + 4 * pP4O8 / ((4 * MP + 8 * MO)^(1 / 2))
+ 4 * pP4O9 / ((4 * MP + 9 * MO)^(1 / 2)) + 4 * pP4O10 / ((4 * MP + 10 * MO)^(1
/ 2))
fluxO = (Seff * Pst / ((2 * Pi * R * T)^(1 / 2))) * (pSiO / ((MSi + MO)^(1 /
2)) + 2 * pSiO2 / ((MSi + 2 * MO)^(1 / 2)) + 2 * pSi2O2 / ((2 * MSi + 2 * MO)^(1
/ 2)) + pPO / ((MP + MO)^(1 / 2)) + 2 * pPO2 / ((MP + 2 * MO)^(1 / 2)) + 3 *
pP2O3 / ((2 * MP + 3 * MO)^(1 / 2)) + 4 * pP2O4 / ((2 * MP + 4 * MO)^(1 / 2))
+ 5 * pP2O5 / ((2 * MP + 5 * MO)^(1 / 2)) + 6 * pP3O6 / ((3 * MP + 6 * MO)^(1
/ 2)) + 6 * pP4O6 / ((4 * MP + 6 * MO)^(1 / 2)) + 7 * pP4O7 / ((4 * MP + 7 *
MO)^(1 / 2)) + 8 * pP4O8 / ((4 * MP + 8 * MO)^(1 / 2)) + 9 * pP4O9 / ((4 * MP
+ 9 * MO)^(1 / 2)) + 10 * pP4O10 / ((4 * MP + 10 * MO)^(1 / 2)))

If fluxO / fluxO_inc < 1 Then
Imin = I
Imax = I - Pas
Pas = Pas / 10
If Pas > -0.001 Then
GoTo Line2:
End If
GoTo Line1:
End If
Next I
```

```
Line2:

If M = 0 Then
xO = aO / GammaOter
xO1(M) = xO
M = M + 1

J = J + 1

Worksheets("calc_four2").Cells(1 + J, 1).Value = xP
Worksheets("calc_four2").Cells(1 + J, 2).Value = Log(xP) / Log(10)
Worksheets("calc_four2").Cells(1 + J, 3).Value = T
Worksheets("calc_four2").Cells(1 + J, 4).Value = 1 / T
Worksheets("calc_four2").Cells(1 + J, 5).Value = aSi
Worksheets("calc_four2").Cells(1 + J, 6).Value = Log(aP) / Log(10)
Worksheets("calc_four2").Cells(1 + J, 7).Value = Log(pSi) / Log(10)
Worksheets("calc_four2").Cells(1 + J, 8).Value = Log(pSi2) / Log(10)
Worksheets("calc_four2").Cells(1 + J, 9).Value = Log(pSi3) / Log(10)
Worksheets("calc_four2").Cells(1 + J, 10).Value = Log(pP3) / Log(10)
Worksheets("calc_four2").Cells(1 + J, 11).Value = Log(pO) / Log(10)
Worksheets("calc_four2").Cells(1 + J, 12).Value = Log(pO2) / Log(10)
Worksheets("calc_four2").Cells(1 + J, 13).Value = Log(pO3) / Log(10)
Worksheets("calc_four2").Cells(1 + J, 14).Value = Log(pP) / Log(10)
Worksheets("calc_four2").Cells(1 + J, 15).Value = Log(pP2) / Log(10)
Worksheets("calc_four2").Cells(1 + J, 16).Value = Log(pP4) / Log(10)
Worksheets("calc_four2").Cells(1 + J, 17).Value = Log(pPSi) / Log(10)
Worksheets("calc_four2").Cells(1 + J, 18).Value = Log(pPSi2) / Log(10)
Worksheets("calc_four2").Cells(1 + J, 19).Value = Log(pP2Si2) / Log(10)
Worksheets("calc_four2").Cells(1 + J, 20).Value = Log(pSiO) / Log(10)
Worksheets("calc_four2").Cells(1 + J, 21).Value = Log(pSiO2) / Log(10)
Worksheets("calc_four2").Cells(1 + J, 22).Value = Log(pSi2O2) / Log(10)
Worksheets("calc_four2").Cells(1 + J, 23).Value = Log(pPO) / Log(10)
Worksheets("calc_four2").Cells(1 + J, 24).Value = Log(pPO2) / Log(10)
Worksheets("calc_four2").Cells(1 + J, 25).Value = Log(pP2O3) / Log(10)
Worksheets("calc_four2").Cells(1 + J, 26).Value = Log(pP2O4) / Log(10)
Worksheets("calc_four2").Cells(1 + J, 27).Value = Log(pP2O5) / Log(10)
Worksheets("calc_four2").Cells(1 + J, 28).Value = Log(pP4O6) / Log(10)
Worksheets("calc_four2").Cells(1 + J, 29).Value = Log(pP4O7) / Log(10)
Worksheets("calc_four2").Cells(1 + J, 30).Value = Log(pP4O8) / Log(10)
Worksheets("calc_four2").Cells(1 + J, 31).Value = Log(pP4O9) / Log(10)
Worksheets("calc_four2").Cells(1 + J, 32).Value = Log(pP4O10) / Log(10)
Worksheets("calc_four2").Cells(1 + J, 33).Value = Log(NP_SiOP) / Log(10)
Worksheets("calc_four2").Cells(1 + J, 34).Value = Log(NSi_SiOP) / Log(10)
Worksheets("calc_four2").Cells(1 + J, 35).Value = Log(NO_SiOP) / Log(10)
Worksheets("calc_four2").Cells(1 + J, 36).Value = Log(NP_SiOP / NSi_SiOP) / Log(10)
Worksheets("calc_four2").Cells(1 + J, 37).Value = Log(fluxP) / Log(10)
Worksheets("calc_four2").Cells(1 + J, 38).Value = Log(fluxSi) / Log(10)
Worksheets("calc_four2").Cells(1 + J, 39).Value = Log(fluxO) / Log(10)
```

```
Worksheets("calc_four2").Cells(1 + J, 40).Value = Log(fluxP / fluxSi) / Log(10)
Worksheets("calc_four2").Cells(1 + J, 41).Value = Log(fluxO_inc) / Log(10)
Worksheets("calc_four2").Cells(1 + J, 42).Value = Log(fluxO / fluxO_inc) / Log(10)
Worksheets("calc_four2").Cells(1 + J, 43).Value = Log(xO) / Log(10)
Worksheets("calc_four2").Cells(1 + J, 44).Value = M

GoTo Line0:

Else
coefficients_activite
xO = aO / GammaOter
xO1(M) = xO
If (xO1(M) - xO1(M - 1)) / xO1(M) < 0.01 Then
GoTo Line3:
End If
M = M + 1

GoTo Line0:

End If

Line3:

J = J + 1

Worksheets("calc_four2").Cells(1 + J, 1).Value = xP
Worksheets("calc_four2").Cells(1 + J, 2).Value = Log(xP) / Log(10)
Worksheets("calc_four2").Cells(1 + J, 3).Value = T
Worksheets("calc_four2").Cells(1 + J, 4).Value = 1 / T
Worksheets("calc_four2").Cells(1 + J, 5).Value = aSi
Worksheets("calc_four2").Cells(1 + J, 6).Value = Log(aP) / Log(10)
Worksheets("calc_four2").Cells(1 + J, 7).Value = Log(pSi) / Log(10)
Worksheets("calc_four2").Cells(1 + J, 8).Value = Log(pSi2) / Log(10)
Worksheets("calc_four2").Cells(1 + J, 9).Value = Log(pSi3) / Log(10)
Worksheets("calc_four2").Cells(1 + J, 10).Value = Log(pP3) / Log(10)
Worksheets("calc_four2").Cells(1 + J, 11).Value = Log(pO) / Log(10)
Worksheets("calc_four2").Cells(1 + J, 12).Value = Log(pO2) / Log(10)
Worksheets("calc_four2").Cells(1 + J, 13).Value = Log(pO3) / Log(10)
Worksheets("calc_four2").Cells(1 + J, 14).Value = Log(pP) / Log(10)
Worksheets("calc_four2").Cells(1 + J, 15).Value = Log(pP2) / Log(10)
Worksheets("calc_four2").Cells(1 + J, 16).Value = Log(pP4) / Log(10)
Worksheets("calc_four2").Cells(1 + J, 17).Value = Log(pPSi) / Log(10)
Worksheets("calc_four2").Cells(1 + J, 18).Value = Log(pPSi2) / Log(10)
Worksheets("calc_four2").Cells(1 + J, 19).Value = Log(pP2Si2) / Log(10)
Worksheets("calc_four2").Cells(1 + J, 20).Value = Log(pSiO) / Log(10)
Worksheets("calc_four2").Cells(1 + J, 21).Value = Log(pSiO2) / Log(10)
Worksheets("calc_four2").Cells(1 + J, 22).Value = Log(pSi2O2) / Log(10)
Worksheets("calc_four2").Cells(1 + J, 23).Value = Log(pPO) / Log(10)
Worksheets("calc_four2").Cells(1 + J, 24).Value = Log(pPO2) / Log(10)
```

```
Worksheets("calc_four2").Cells(1 + J, 25).Value = Log(pP2O3) / Log(10)
Worksheets("calc_four2").Cells(1 + J, 26).Value = Log(pP2O4) / Log(10)
Worksheets("calc_four2").Cells(1 + J, 27).Value = Log(pP2O5) / Log(10)
Worksheets("calc_four2").Cells(1 + J, 28).Value = Log(pP4O6) / Log(10)
Worksheets("calc_four2").Cells(1 + J, 29).Value = Log(pP4O7) / Log(10)
Worksheets("calc_four2").Cells(1 + J, 30).Value = Log(pP4O8) / Log(10)
Worksheets("calc_four2").Cells(1 + J, 31).Value = Log(pP4O9) / Log(10)
Worksheets("calc_four2").Cells(1 + J, 32).Value = Log(pP4O10) / Log(10)
Worksheets("calc_four2").Cells(1 + J, 33).Value = Log(NP_SiOP) / Log(10)
Worksheets("calc_four2").Cells(1 + J, 34).Value = Log(NSi_SiOP) / Log(10)
Worksheets("calc_four2").Cells(1 + J, 35).Value = Log(NO_SiOP) / Log(10)
Worksheets("calc_four2").Cells(1 + J, 36).Value = Log(NP_SiOP / NSi_SiOP) / Log(10)
Worksheets("calc_four2").Cells(1 + J, 37).Value = Log(fluxP) / Log(10)
Worksheets("calc_four2").Cells(1 + J, 38).Value = Log(fluxSi) / Log(10)
Worksheets("calc_four2").Cells(1 + J, 39).Value = Log(fluxO) / Log(10)
Worksheets("calc_four2").Cells(1 + J, 40).Value = Log(fluxP / fluxSi) / Log(10)
Worksheets("calc_four2").Cells(1 + J, 41).Value = Log(fluxO_inc) / Log(10)
Worksheets("calc_four2").Cells(1 + J, 42).Value = Log(fluxO / fluxO_inc) / Log(10)
Worksheets("calc_four2").Cells(1 + J, 43).Value = Log(xO) / Log(10)
Worksheets("calc_four2").Cells(1 + J, 44).Value = M

Next L

J = 0

End Sub
```

```
Sub Bille()
constantes_standard

J = 0
Worksheets("bille").Cells(1 + J, 1).Value = "T(K)"
Worksheets("bille").Cells(1 + J, 2).Value = "mOSi(kg)"
Worksheets("bille").Cells(1 + J, 3).Value = "mOP(kg)"
Worksheets("bille").Cells(1 + J, 4).Value = "xOP(fraction molaire)"
Worksheets("bille").Cells(1 + J, 5).Value = "dxP (pas)"
Worksheets("bille").Cells(1 + J, 6).Value = "masse Si"
Worksheets("bille").Cells(1 + J, 7).Value = "Delta mSi"
Worksheets("bille").Cells(1 + J, 8).Value = "Delta t(h)"
Worksheets("bille").Cells(1 + J, 9).Value = "XP (frac molaire à tout instant)"
Worksheets("bille").Cells(1 + J, 10).Value = "K"
Worksheets("bille").Cells(1 + J, 11).Value = "Temps(h)"
Worksheets("bille").Cells(1 + J, 12).Value = "log XP(K)"
Worksheets("bille").Cells(1 + J, 13).Value = "rayon(K)"
Worksheets("bille").Cells(1 + J, 14).Value = "Sbille(K)"

For T = 1800 To 2000 Step 100
```

```
constantes_equilibre
coefficients_activité

m0bille = 0.00183 'kg
m0Si = m0bille ' masse initiale de Si en kg
n0Si = m0Si / MSi 'nb mols initiale de Si
x0P = 0.005
n0P = n0Si * x0P / (1 - x0P) 'nb mols initiale de P
m0P = n0P * MP ' masse initiale de P en kg
rayon(0) = (3 * m0Si / (4 * Pi * dSi)) ^(1 / 3)
Sbille(0) = 4 * Pi * rayon(0) ^2

Pas = -0.1 '-0.1
Imin = Log(x0P) / Log(10)
Imax = Imin - 6
K = 0
For I = Imin To Imax Step Pas
xP = 10 ^(I + Pas / 2)
dxP = 10 ^I - 10 ^(I + Pas)
X(K) = 10 ^I
aSi = 1 - xP
aP = GammaP * xP
definition_pression
NSi_GAS = pSi + 2 * pSi2 + 3 * pSi3 + pPSi + 2 * pPSi2 + 2 * pP2Si2 + pSiO +
pSiO2 + 2 * pSi2O2
NP_GAS = pP + 2 * pP2 + 3 * pP3 + 4 * pP4 + pPSi + pPSi2 + 2 * pP2Si2 + pPO +
pPO2 + 2 * pP2O3 + 2 * pP2O4 + 2 * pP2O5 + 3 * pP3O6 + 4 * pP4O6 + 4 * pP4O7
+ 4 * pP4O8 + 4 * pP4O9 + 4 * pP4O10
fluxSi = (Sbille(K) * Pst / ((2 * Pi * R * T) ^(1 / 2))) * (pSi / ((MSi) ^(1
/ 2)) + 2 * pSi2 / ((2 * MSi) ^(1 / 2)) + 3 * pSi3 / ((3 * MSi) ^(1 / 2)) + pPSi
/ ((MSi + MP) ^(1 / 2)) + 2 * pPSi2 / ((2 * MSi + MP) ^(1 / 2)) + 2 * pP2Si2
/ ((2 * MSi + 2 * MP) ^(1 / 2)))
fluxP = (Sbille(K) * Pst / ((2 * Pi * R * T) ^(1 / 2))) * (pP / ((MP) ^(1 / 2))
+ 2 * pP2 / ((2 * MP) ^(1 / 2)) + 3 * pP3 / ((3 * MP) ^(1 / 2)) + 4 * pP4 / ((4
* MP) ^(1 / 2)) + pPSi / ((MSi + MP) ^(1 / 2)) + pPSi2 / ((2 * MSi + MP) ^(1
/ 2)) + 2 * pP2Si2 / ((2 * MSi + 2 * MP) ^(1 / 2))) + pPO / ((MP + MO) ^(1 /
2)) + pPO2 / ((MP + 2 * MO) ^(1 / 2)) + 2 * pP2O3 / ((2 * MP + 3 * MO) ^(1 /
2)) + 2 * pP2O4 / ((2 * MP + 4 * MO) ^(1 / 2)) + 2 * pP2O5 / ((2 * MP + 5 * MO)
^(1 / 2)) + 3 * pP3O6 / ((3 * MP + 6 * MO) ^(1 / 2)) + 4 * pP4O6 / ((4 * MP +
6 * MO) ^(1 / 2)) + 4 * pP4O7 / ((4 * MP + 7 * MO) ^(1 / 2)) + 4 * pP4O8 / ((4
* MP + 8 * MO) ^(1 / 2)) + 4 * pP4O9 / ((4 * MP + 9 * MO) ^(1 / 2)) + 4 * pP4O10
/ ((4 * MP + 10 * MO) ^(1 / 2))
F0Si = fluxSi
F0P = fluxP
If K = 0 Then
m1si = m0Si
minitSi(K) = m0Si
Else
```

```
m1si = minitSi(K)
End If
dmSi = (m1si * dxP / ((F0P / F0Si) * (1 - X(K)) ^2 - X(K) * (1 - X(K))))
dt = dmSi / (F0Si * MSi) / 3600

If K = 0 Then
Tps(K) = dt
minitSi(K + 1) = m0Si - dmSi
rayon(K + 1) = (3 * minitSi(K + 1) / (4 * Pi * dSi)) ^(1 / 3)
Sbille(K + 1) = 4 * Pi * rayon(K + 1) ^2
Else
Tps(K) = dt + Tps(K - 1)
minitSi(K + 1) = minitSi(K) - dmSi
rayon(K + 1) = (3 * minitSi(K + 1) / (4 * Pi * dSi)) ^(1 / 3)
Sbille(K + 1) = 4 * Pi * rayon(K + 1) ^2
End If

J = J + 1

Worksheets("bille").Cells(1 + J, 1).Value = T
Worksheets("bille").Cells(1 + J, 2).Value = m0Si
Worksheets("bille").Cells(1 + J, 3).Value = m0P
Worksheets("bille").Cells(1 + J, 4).Value = x0P
Worksheets("bille").Cells(1 + J, 5).Value = dxP
Worksheets("bille").Cells(1 + J, 6).Value = minitSi(K)
Worksheets("bille").Cells(1 + J, 7).Value = dmSi
Worksheets("bille").Cells(1 + J, 8).Value = dt
Worksheets("bille").Cells(1 + J, 9).Value = X(K)
Worksheets("bille").Cells(1 + J, 10).Value = K
Worksheets("bille").Cells(1 + J, 11).Value = Tps(K)
Worksheets("bille").Cells(1 + J, 12).Value = Log(X(K)) / Log(10)
Worksheets("bille").Cells(1 + J, 13).Value = rayon(K)
Worksheets("bille").Cells(1 + J, 14).Value = Sbille(K)

K = K + 1
Next I

'Stop

J = J + 1

Next T

End Sub
```

```
Sub Bille02()
constantes_standard
```

```
J = 0
Worksheets("billeO2").Cells(1 + J, 1).Value = "T(K)"
Worksheets("billeO2").Cells(1 + J, 2).Value = "m0Si(kg)"
Worksheets("billeO2").Cells(1 + J, 3).Value = "m0P(kg)"
Worksheets("billeO2").Cells(1 + J, 4).Value = "x0P(fraction molaire)"
Worksheets("billeO2").Cells(1 + J, 5).Value = "dxP (pas)"
Worksheets("billeO2").Cells(1 + J, 6).Value = "masse Si"
Worksheets("billeO2").Cells(1 + J, 7).Value = "Delta mSi"
Worksheets("billeO2").Cells(1 + J, 8).Value = "Delta t(h)"
Worksheets("billeO2").Cells(1 + J, 9).Value = "XP (frac molaire à tout instant)"
Worksheets("billeO2").Cells(1 + J, 10).Value = "K"
Worksheets("billeO2").Cells(1 + J, 11).Value = "Temps(h)"
Worksheets("billeO2").Cells(1 + J, 12).Value = "log XPP(K)"
Worksheets("billeO2").Cells(1 + J, 13).Value = "rayon(K)"
Worksheets("billeO2").Cells(1 + J, 14).Value = "Sbille(K)"
Worksheets("billeO2").Cells(1 + J, 15).Value = "log pSi(bar)"
Worksheets("billeO2").Cells(1 + J, 16).Value = "log pSi2(bar)"
Worksheets("billeO2").Cells(1 + J, 17).Value = "log pSi3(bar)"
Worksheets("billeO2").Cells(1 + J, 18).Value = "log pP3(bar)"
Worksheets("billeO2").Cells(1 + J, 19).Value = "log pO(bar)"
Worksheets("billeO2").Cells(1 + J, 20).Value = "log pO2(bar)"
Worksheets("billeO2").Cells(1 + J, 21).Value = "log pO3(bar)"
Worksheets("billeO2").Cells(1 + J, 22).Value = "log pP(bar)"
Worksheets("billeO2").Cells(1 + J, 23).Value = "log pP2(bar)"
Worksheets("billeO2").Cells(1 + J, 24).Value = "log pP4(bar)"
Worksheets("billeO2").Cells(1 + J, 25).Value = "log pPSi(bar)"
Worksheets("billeO2").Cells(1 + J, 26).Value = "log pPSi2(bar)"
Worksheets("billeO2").Cells(1 + J, 27).Value = "log pP2Si2(bar)"
Worksheets("billeO2").Cells(1 + J, 28).Value = "log pSiO(bar)"
Worksheets("billeO2").Cells(1 + J, 29).Value = "log pSiO2(bar)"
Worksheets("billeO2").Cells(1 + J, 30).Value = "log pSi2O2(bar)"
Worksheets("billeO2").Cells(1 + J, 31).Value = "log pPO(bar)"
Worksheets("billeO2").Cells(1 + J, 32).Value = "log pPO2bar)"
Worksheets("billeO2").Cells(1 + J, 33).Value = "log pP2O3(bar)"
Worksheets("billeO2").Cells(1 + J, 34).Value = "log pP2O4(bar)"
Worksheets("billeO2").Cells(1 + J, 35).Value = "log pP2O5(bar)"
Worksheets("billeO2").Cells(1 + J, 36).Value = "log pP4O6(bar)"
Worksheets("billeO2").Cells(1 + J, 37).Value = "log pP4O7(bar)"
Worksheets("billeO2").Cells(1 + J, 38).Value = "log pP4O8(bar)"
Worksheets("billeO2").Cells(1 + J, 39).Value = "log pP4O9(bar)"
Worksheets("billeO2").Cells(1 + J, 40).Value = "log pP4O10(bar)"
Worksheets("billeO2").Cells(1 + J, 41).Value = "coeff partage"
Worksheets("billeO2").Cells(1 + J, 42).Value = "xO1(K)"
Worksheets("billeO2").Cells(1 + J, 43).Value = "xP"
Worksheets("billeO2").Cells(1 + J, 44).Value = "EpsilonOP"
Worksheets("billeO2").Cells(1 + J, 45).Value = "EpsilonPP"
Worksheets("billeO2").Cells(1 + J, 46).Value = "GammaInfiniP"
Worksheets("billeO2").Cells(1 + J, 47).Value = "GammaInfiniO"
```

```
Worksheets("billeO2").Cells(1 + J, 48).Value = "GammaPter"
Worksheets("billeO2").Cells(1 + J, 49).Value = "GammaOter"
Worksheets("billeO2").Cells(1 + J, 50).Value = "aO"
Worksheets("billeO2").Cells(1 + J, 51).Value = "Lmax"
Worksheets("billeO2").Cells(1 + J, 52).Value = "pO2lim"

T = 1800

constantes_equilibre
coefficients_activité

For N = -9 To -4 Step 8

K = 0
mObille = 0.00183 'kg
mOSi = mObille ' masse initiale de Si en kg
nOSi = mOSi / MSi 'nb mols initiale de Si
xOP = 0.005
xPP(K) = xOP
nOP = nOSi * xOP / (1 - xOP) 'nb mols initiale de P
mOP = nOP * MP ' masse initiale de P en kg
rayon(K) = (3 * mOSi / (4 * Pi * dSi)) ^(1 / 3) 'K=0
Sbille(K) = 4 * Pi * rayon(0) ^2 'K=0
pO2four = 10 ^N ' pression en bar du four

fluxO_inc = 2 * pO2four * Pst * Sbille(K) * ((2 * Pi * 2 * MO * R * 300) ^(-1
/ 2)) ' flux incident depuis les parois à 300K
Pas = -0.1 '-0.1
Imin = Log(xOP) / Log(10)
Imax = Imin - 11

For I = Imin To Imax Step Pas
xPP(K) = 10 ^I
xP = 10 ^(I + Pas / 2)
dxP = 10 ^I - 10 ^(I + Pas)
X(K) = xP
aSi = 1 - xP
'aP = GammaP * xP
''aP = GammaPter * xPP(K)

GammaPter = Exp(Math.Log(GammaInfiniP) + (xP * EpsilonPP) + (xO1(K) * EpsilonOP))
GammaOter = Exp(Math.Log(GammaInfiniO) + (xO1(K) * EpsilonOO) + (xP * EpsilonOP))

aP = GammaPter * xP

pO2lim = 1 / KSiSiO2
Lmax = Log(pO2lim) / Log(10)
Lmin = Lmax - 60
Pas2 = -1
```

```
Line1:
For L = Lmax To Lmin Step Pas2
pO2 = 10 ^L
aO = pO2 ^(1 / 2)
aSi = 1 - xP - xO

definition_pression

'NSi_SiOP = pSi + 2 * pSi2 + 3 * pSi3 + pPSi + 2 * pPSi2 + 2 * pP2Si2 + pSiO
+ pSiO2 + 2 * pSi2O2
'NP_SiOP = pP + 2 * pP2 + 3 * pP3 + 4 * pP4 + pPSi + pPSi2 + 2 * pP2Si2 + pPO
+ pPO2 + 2 * pP2O3 + 2 * pP2O4 + 2 * pP2O5 + 3 * pP3O6 + 4 * pP4O6 + 4 * pP4O7
+ 4 * pP4O8 + 4 * pP4O9 + 4 * pP4O10
'NO_SiOP = pSiO + 2 * pSiO2 + 2 * pSi2O2 + pPO + 2 * pPO2 + 3 * pP2O3 + 4 * pP2O4
+ 5 * pP2O5 + 6 * pP3O6 + 6 * pP4O6 + 7 * pP4O7 + 8 * pP4O8 + 9 * pP4O9 + 10
* pP4O10
' attention ici c'est Sbille(K) et non Seff
''flux avec O
fluxSi = (Sbille(K) * Pst / ((2 * Pi * R * T) ^(1 / 2))) * (pSi / ((MSi) ^(1
/ 2)) + 2 * pSi2 / ((2 * MSi) ^(1 / 2)) + 3 * pSi3 / ((3 * MSi) ^(1 / 2)) + pPSi
/ ((MSi + MP) ^(1 / 2)) + 2 * pPSi2 / ((2 * MSi + MP) ^(1 / 2)) + pSiO / ((MSi
+ MO) ^(1 / 2)) + pSiO2 / ((MSi + 2 * MO) ^(1 / 2)) + 2 * pSi2O2 / ((2 * MSi
+ 2 * MO) ^(1 / 2)) + 2 * pP2Si2 / ((2 * MSi + 2 * MP) ^(1 / 2)))
fluxP = (Sbille(K) * Pst / ((2 * Pi * R * T) ^(1 / 2))) * (pP / ((MP) ^(1 / 2))
+ 2 * pP2 / ((2 * MP) ^(1 / 2)) + 3 * pP3 / ((3 * MP) ^(1 / 2)) + 4 * pP4 / ((4
* MP) ^(1 / 2)) + pPSi / ((MSi + MP) ^(1 / 2)) + pPSi2 / ((2 * MSi + MP) ^(1
/ 2)) + 2 * pP2Si2 / ((2 * MSi + 2 * MP) ^(1 / 2))) + pPO / ((MP + MO) ^(1 /
2)) + pPO2 / ((MP + 2 * MO) ^(1 / 2)) + 2 * pP2O3 / ((2 * MP + 3 * MO) ^(1 /
2)) + 2 * pP2O4 / ((2 * MP + 4 * MO) ^(1 / 2)) + 2 * pP2O5 / ((2 * MP + 5 * MO)
^(1 / 2)) + 3 * pP3O6 / ((3 * MP + 6 * MO) ^(1 / 2)) + 4 * pP4O6 / ((4 * MP +
6 * MO) ^(1 / 2)) + 4 * pP4O7 / ((4 * MP + 7 * MO) ^(1 / 2)) + 4 * pP4O8 / ((4
* MP + 8 * MO) ^(1 / 2)) + 4 * pP4O9 / ((4 * MP + 9 * MO) ^(1 / 2)) + 4 * pP4O10
/ ((4 * MP + 10 * MO) ^(1 / 2))
''flux sans O
'fluxSi = (Sbille(K) * Pst / ((2 * Pi * R * T) ^(1 / 2))) * (pSi / ((MSi) ^(1
/ 2)) + 2 * pSi2 / ((2 * MSi) ^(1 / 2)) + 3 * pSi3 / ((3 * MSi) ^(1 / 2)) + pPSi
/ ((MSi + MP) ^(1 / 2)) + 2 * pPSi2 / ((2 * MSi + MP) ^(1 / 2)) + 2 * pP2Si2
/ ((2 * MSi + 2 * MP) ^(1 / 2)))
'fluxP = (Sbille(K) * Pst / ((2 * Pi * R * T) ^(1 / 2))) * (pP / ((MP) ^(1 /
2)) + 2 * pP2 / ((2 * MP) ^(1 / 2)) + 3 * pP3 / ((3 * MP) ^(1 / 2)) + 4 * pP4
/ ((4 * MP) ^(1 / 2)) + pPSi / ((MSi + MP) ^(1 / 2)) + pPSi2 / ((2 * MSi + MP)
^(1 / 2)) + 2 * pP2Si2 / ((2 * MSi + 2 * MP) ^(1 / 2))) + pPO / ((MP + MO) ^(1
/ 2)) + pPO2 / ((MP + 2 * MO) ^(1 / 2)) + 2 * pP2O3 / ((2 * MP + 3 * MO) ^(1
/ 2)) + 2 * pP2O4 / ((2 * MP + 4 * MO) ^(1 / 2)) + 2 * pP2O5 / ((2 * MP + 5 *
MO) ^(1 / 2)) + 3 * pP3O6 / ((3 * MP + 6 * MO) ^(1 / 2)) + 4 * pP4O6 / ((4 *
MP + 6 * MO) ^(1 / 2)) + 4 * pP4O7 / ((4 * MP + 7 * MO) ^(1 / 2)) + 4 * pP4O8
/ ((4 * MP + 8 * MO) ^(1 / 2)) + 4 * pP4O9 / ((4 * MP + 9 * MO) ^(1 / 2)) + 4
* pP4O10 / ((4 * MP + 10 * MO) ^(1 / 2))
```

```
fluxO = (Sbille(K) * Pst / ((2 * Pi * R * T) ^(1 / 2))) * (pSiO / ((MSi + MO)
^(1 / 2)) + 2 * pSiO2 / ((MSi + 2 * MO) ^(1 / 2)) + 2 * pSi2O2 / ((2 * MSi +
2 * MO) ^(1 / 2)) + pPO / ((MP + MO) ^(1 / 2)) + 2 * pPO2 / ((MP + 2 * MO) ^(1
/ 2)) + 3 * pP2O3 / ((2 * MP + 3 * MO) ^(1 / 2)) + 4 * pP2O4 / ((2 * MP + 4 *
MO) ^(1 / 2)) + 5 * pP2O5 / ((2 * MP + 5 * MO) ^(1 / 2)) + 6 * pP3O6 / ((3 *
MP + 6 * MO) ^(1 / 2)) + 6 * pP4O6 / ((4 * MP + 6 * MO) ^(1 / 2)) + 7 * pP4O7
/ ((4 * MP + 7 * MO) ^(1 / 2)) + 8 * pP4O8 / ((4 * MP + 8 * MO) ^(1 / 2)) + 9
* pP4O9 / ((4 * MP + 9 * MO) ^(1 / 2)) + 10 * pP4O10 / ((4 * MP + 10 * MO) ^(1
/ 2)))
FOSi = fluxSi
FOP = fluxP
FOO = fluxO

If fluxO / fluxO_inc < 1 Then
Lmin = L
Lmax = L - Pas2
Pas2 = Pas2 / 10
If Pas2 > -0.001 Then
GoTo Line2:
End If
GoTo Line1:
End If
Next L

Line2:
'If M = 0 Then
xO = aO / GammaOter
xO1(K) = xO
' M = M + 1
'End If

Rapp = (FOP / FOSi) / (xP / aSi)
If Rapp < 1 Then
GoTo Line3:
End If

If K = 0 Then
m1si = m0Si
minitSi(K) = m0Si
Else
m1si = minitSi(K)
End If
''dmSi = (m1si * dxP / ((1 - xPP(K) - xO1(K)) * ((FOP / FOSi) * (1 - xPP(K)) -
X(P))))
dmSi = (m1si * dxP / ((1 - xPP(K) - xO) * ((FOP / FOSi) * (1 - xPP(K)) - xPP(K))))
'dmSi = (m1si * dxP / ((1 - xP) * ((FOP / FOSi) * (1 - xP) - xP)))
dt = dmSi / (FOSi * MSi) / 3600
```

```
If K = 0 Then
Tps(K) = dt
minitSi(K + 1) = m0Si - dmSi
rayon(K + 1) = (3 * minitSi(K + 1) / (4 * Pi * dSi)) ^(1 / 3)
Sbille(K + 1) = 4 * Pi * rayon(K + 1) ^2
Else
Tps(K) = dt + Tps(K - 1)
minitSi(K + 1) = minitSi(K) - dmSi
rayon(K + 1) = (3 * minitSi(K + 1) / (4 * Pi * dSi)) ^(1 / 3)
Sbille(K + 1) = 4 * Pi * rayon(K + 1) ^2
End If

J = J + 1

Worksheets("billeO2").Cells(1 + J, 1).Value = T
Worksheets("billeO2").Cells(1 + J, 2).Value = m0Si
Worksheets("billeO2").Cells(1 + J, 3).Value = m0P
Worksheets("billeO2").Cells(1 + J, 4).Value = x0P
Worksheets("billeO2").Cells(1 + J, 5).Value = dxP
Worksheets("billeO2").Cells(1 + J, 6).Value = minitSi(K)
Worksheets("billeO2").Cells(1 + J, 7).Value = dmSi
Worksheets("billeO2").Cells(1 + J, 8).Value = dt
Worksheets("billeO2").Cells(1 + J, 9).Value = xP
Worksheets("billeO2").Cells(1 + J, 10).Value = K
Worksheets("billeO2").Cells(1 + J, 11).Value = Tps(K)
Worksheets("billeO2").Cells(1 + J, 12).Value = Log(xPP(K)) / Log(10)
Worksheets("billeO2").Cells(1 + J, 13).Value = rayon(K)
Worksheets("billeO2").Cells(1 + J, 14).Value = Sbille(K)
Worksheets("billeO2").Cells(1 + J, 15).Value = Log(pSi) / Log(10)
Worksheets("billeO2").Cells(1 + J, 16).Value = Log(pSi2) / Log(10)
Worksheets("billeO2").Cells(1 + J, 17).Value = Log(pSi3) / Log(10)
Worksheets("billeO2").Cells(1 + J, 18).Value = Log(pP3) / Log(10)
Worksheets("billeO2").Cells(1 + J, 19).Value = Log(pO) / Log(10)
Worksheets("billeO2").Cells(1 + J, 20).Value = Log(pO2) / Log(10)
Worksheets("billeO2").Cells(1 + J, 21).Value = Log(pO3) / Log(10)
Worksheets("billeO2").Cells(1 + J, 22).Value = Log(pP) / Log(10)
Worksheets("billeO2").Cells(1 + J, 23).Value = Log(pP2) / Log(10)
Worksheets("billeO2").Cells(1 + J, 24).Value = Log(pP4) / Log(10)
Worksheets("billeO2").Cells(1 + J, 25).Value = Log(pPSi) / Log(10)
Worksheets("billeO2").Cells(1 + J, 26).Value = Log(pPSi2) / Log(10)
Worksheets("billeO2").Cells(1 + J, 27).Value = Log(pP2Si2) / Log(10)
Worksheets("billeO2").Cells(1 + J, 28).Value = Log(pSiO) / Log(10)
Worksheets("billeO2").Cells(1 + J, 29).Value = Log(pSiO2) / Log(10)
Worksheets("billeO2").Cells(1 + J, 30).Value = Log(pSi2O2) / Log(10)
Worksheets("billeO2").Cells(1 + J, 31).Value = Log(pPO) / Log(10)
Worksheets("billeO2").Cells(1 + J, 32).Value = Log(pPO2) / Log(10)
Worksheets("billeO2").Cells(1 + J, 33).Value = Log(pP2O3) / Log(10)
Worksheets("billeO2").Cells(1 + J, 34).Value = Log(pP2O4) / Log(10)
```

```
Worksheets("billeO2").Cells(1 + J, 35).Value = Log(pP2O5) / Log(10)
Worksheets("billeO2").Cells(1 + J, 36).Value = Log(pP4O6) / Log(10)
Worksheets("billeO2").Cells(1 + J, 37).Value = Log(pP4O7) / Log(10)
Worksheets("billeO2").Cells(1 + J, 38).Value = Log(pP4O8) / Log(10)
Worksheets("billeO2").Cells(1 + J, 39).Value = Log(pP4O9) / Log(10)
Worksheets("billeO2").Cells(1 + J, 40).Value = Log(pP4O10) / Log(10)
Worksheets("billeO2").Cells(1 + J, 41).Value = Rapp
Worksheets("billeO2").Cells(1 + J, 42).Value = xO1(K)
Worksheets("billeO2").Cells(1 + J, 43).Value = xP
Worksheets("billeO2").Cells(1 + J, 44).Value = EpsilonOP
Worksheets("billeO2").Cells(1 + J, 45).Value = EpsilonPP
Worksheets("billeO2").Cells(1 + J, 46).Value = GammaInfiniP
Worksheets("billeO2").Cells(1 + J, 47).Value = GammaInfiniO
Worksheets("billeO2").Cells(1 + J, 48).Value = GammaPter
Worksheets("billeO2").Cells(1 + J, 49).Value = GammaOter
Worksheets("billeO2").Cells(1 + J, 50).Value = aO
Worksheets("billeO2").Cells(1 + J, 51).Value = Lmax
Worksheets("billeO2").Cells(1 + J, 52).Value = pO2lim
K = K + 1
'Next L

'Stop

Next I

Line3:

J = J + 1

Next N

'Next T
End Sub
```

D

Choice of the enclosure constitution

The value of the surrounding environment pressure is different with an inert gas or under vacuum; it will impact the dephosphorization rate of silicon and thus shall be examined.

As the distillation process results in a large mass transfer from its liquid-to-gas phase, its subsequent overall mass flux Φ_m expressed in $\mathrm{mol.m^{-2}.s^{-1}}$ is studied. In the case of such an interface one can write:

$$\Phi_m = \overline{k}(C_\mathrm{d} - C_\infty) \tag{D.1}$$

where $\overline{k}$ is the global mass transfer coefficient in $\mathrm{m.s^{-1}}$, C_d and C_∞ are respectively the concentration of the droplet on the surface and far afield.

For such a liquid-to-gas mass transfer, both convection and diffusion mechanisms occur. The mean Sherwood number $\overline{\mathrm{Sh}}$ is an appropriate dimensionless number to consider in these circumstances:

$$\overline{\mathrm{Sh}} = \frac{\text{convective mass transfer}}{\text{diffusive mass transfer}} = \frac{\overline{k}L}{\mathcal{D}} \tag{D.2}$$

with L the characteristic length of the vessel in m and $\mathcal{D}$ the diffusion coefficient[1] expressed in $\mathrm{m^2.s^{-1}}$. Equation D.1 then becomes:

$$\Phi_m = \frac{\overline{\mathrm{Sh}}\mathcal{D}}{L}(C_\mathrm{d} - C_\infty) \tag{D.3}$$

Experimental correlations of $\overline{\mathrm{Sh}}$ exist as functions of Rayleigh number Ra and Prandtl number Pr. In the present case, it can be defined as [23]:

[1] To make clear the demonstration, this quantity will be properly defined afterwards.

$$\overline{\mathrm{Sh}} = 2 + \frac{0.589\mathrm{Ra}^{\frac{1}{4}}}{\left[1 + \left(\frac{0.469}{\mathrm{Pr}}\right)^{\frac{9}{16}}\right]^{\frac{4}{9}}} \qquad \text{for} \quad \begin{array}{l} \mathrm{Ra} = \dfrac{g_n \beta^* (C_\mathrm{d} - C_\infty) L^3}{\nu \alpha^*} \leq 10^{11} \\ \mathrm{Pr} = \dfrac{\nu}{\alpha^*} \geq 0.7 \end{array} \tag{D.4}$$

with $g_n \approx 9.81$ m.s^{-2} the standard gravity and β^* the coefficient of mass expansion expressed in m^3.mol^{-1}. The kinematic viscosity of the fluid ν and the mass diffusivity α^* (both in m^2.s^{-1}) are both inversely proportional to the surrounding pressure p. It means that Ra is proportional to p^2 and thus $\overline{\mathrm{Sh}} \propto 2 + \sqrt{p}$.

Thereby in equation D.3 the diffusion coefficient $\mathcal{D}$ is the remaining quantity that needs to unveil its relationship with the surrounding environment pressure p. This diffusion coefficient is described in the kinetic gas theory as a function of the mean velocity of the particles $\langle c \rangle$ defined in the previous chapter and their mean free path:

$$\mathcal{D} = \frac{1}{3} \ell \langle c \rangle \tag{D.5}$$

ℓ shall be conceived as the average distance traveled by a particle between two collisions with others. It is defined as:

$$\ell = \frac{k_B T}{\sqrt{2} \pi d^2 p} \tag{D.6}$$

where d is the particles diameter. Combining it with the mean velocity formula gives:

$$\mathcal{D} = \frac{2}{3pd^2} \sqrt{\frac{k_B^3 T^3}{\pi^3 m}} \tag{D.7}$$

Hereby $\mathcal{D} \propto p^{-1}$. It ultimately leads to:

$$\Phi_m \propto \frac{2 + \sqrt{p}}{p} \tag{D.8}$$

When the surrounding environment pressure p of the sample decreases, the diffusion flux Φ_m increases.
One can then conclude that working in a vacuum environment is preferred: it will facilitate the mass transfer phenomenon and therefore the dephosphorization process.

E

Measurements techniques

E.1 GDMS

A glow discharge is a plasma formed in an electrode cell filled with a reduced pressure of argon. A voltage of about 1 kV is applied between its anode and cathode so that the argon gas ionizes (Figure E.1).

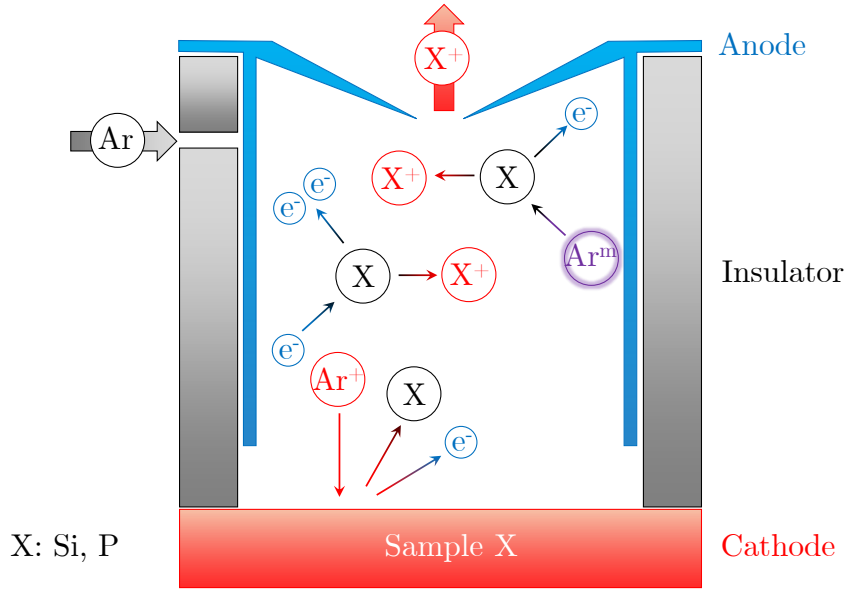

Figure E.1: Illustration of the GDMS principle

In the GDMS apparatus, the silicon sample assumes the cathode role. The argon cations are then accelerated towards the sample that therefore releases both

secondary electrons[1] and sample atoms X.

The sputtering of X are subject to direct electron impact and Penning ionization respectively defined by:

$$\begin{aligned} \mathrm{X} + \mathrm{e}^- &\rightarrow \mathrm{X}^+ + 2\mathrm{e}^- \\ \mathrm{X} + \mathrm{Ar}^\mathrm{m} &\rightarrow \mathrm{X}^+ + \mathrm{Ar} + \mathrm{e}^- \end{aligned} \tag{E.1}$$

X^+ ions are ultimately extracted and measured with a mass spectrometer.

E.2 Pirani and Penning vacuum gauges

The gauge used to measure the vacuum level inside the enclosure is a combination of a Pirani and a Penning gauge. This configuration enables a wide pressure range measurement: above $4 \cdot 10^{-3}$ mbar is activated the Pirani mode, and below the Penning mode.

□ The Pirani gauge measures the pressure via the thermal conductance of the atmosphere. Temperature of the gauge wire is increased by resistive heating when an electric current is applied (Figure E.2), while thermal losses occur due to the gas thermal conductivity. The measured cross voltage V_c is linked to the pressure in the gauge tube when connected to this Wheatstone bridge[2].

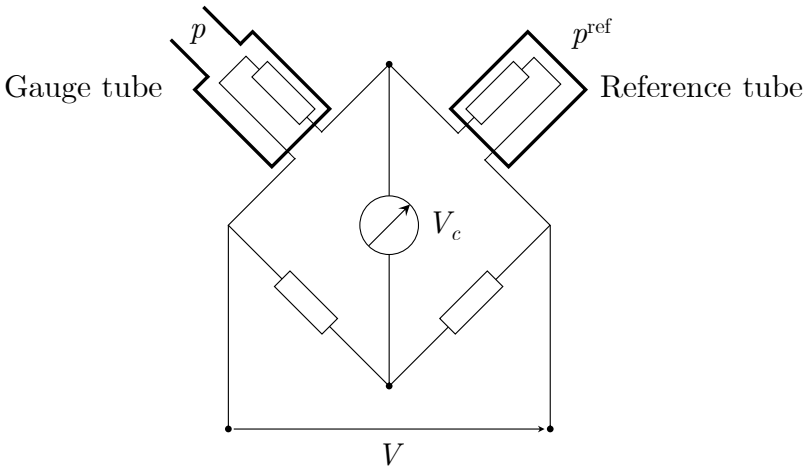

Figure E.2: Pirani gauge electrical model

In the present vacuum gauge, the reference tube is calibrated on argon conductivity. Its accuracy is assessed to be ± 50% in the range $5 \cdot 10^{-4}$ – 10^{-3} mbar, ± 15% in the range 10^{-3} – 10^{2} mbar and ± 50% in the range 10^{2} – 10^{3} mbar.

[1] These latter can collide and excite gas atoms Ar^m that subsequently emit light to lower their energy level, hence the name *glow* discharge.

[2] An electrical circuit used to measure an unknown resistance.

□ The Penning gauge[3] also indirecly measures the pressure, but through the ionic current produced from the gas particles. Ionization is obtained by applying an electric field between two electrodes. A magnetic field added in parallel promotes spiral trajectories of ions for producing a greater quantity of ions. The ionic current is finally detected and is linearly proportional to the pressure.

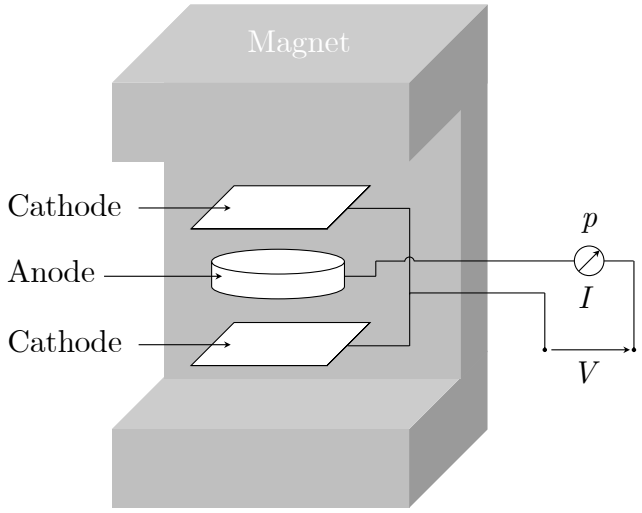

Figure E.3: Penning gauge illustration principle

Compared to Bayard-Alpert more classic gauges, modern Penning gauges have a lower accuracy of $\pm 30\%$, but are considered more reliable by preventing from degradation due to oxidizing atmosphere or sudden pressure increase.

[3]Also called cold cathode sensor.

Résumé en français

1. Le silicium dans le domaine de l'énergie

1.1 Contexte mondial de l'énergie

La consommation mondiale en énergie augmente exponentiellement (Figure 4.4): au début du XIX^{e} siècle elle était estimée à 0,25 Gtep. Au début du XX^{e} elle en valait 1 Gtep et a doublé en 1950. Aujourd'hui, l'humanité en consomme 13 Gtep.

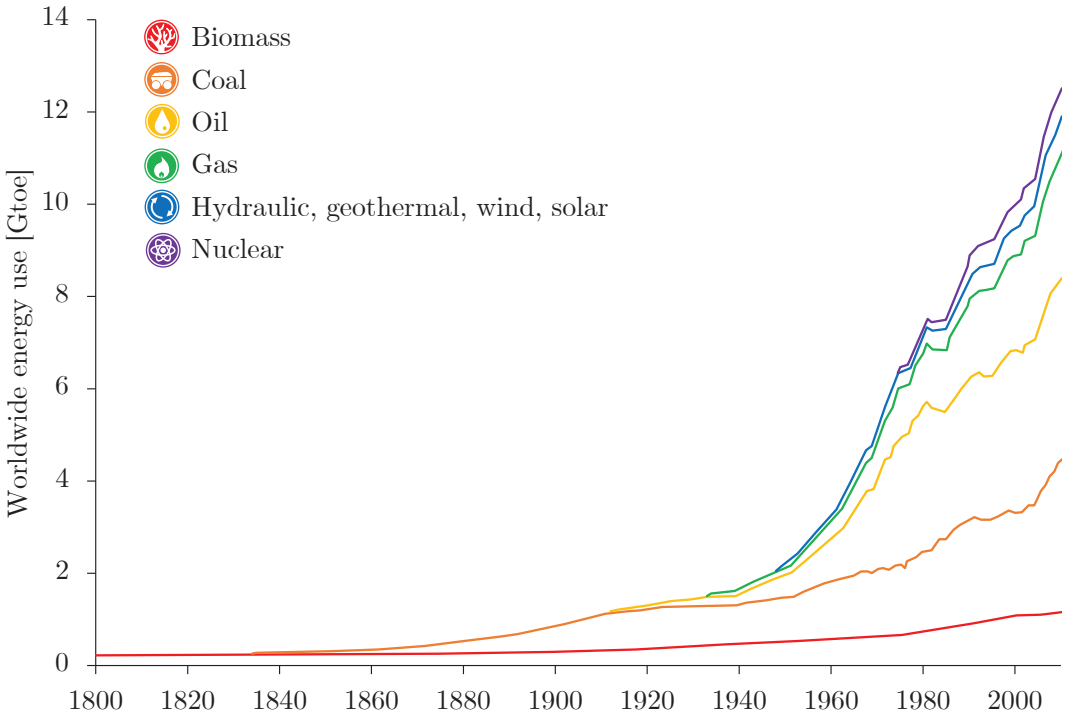

Figure 4.4: Consommation mondiale d'énergie cumulée entre 1800 et 2010 [16]

Malgré tous les efforts possibles de restrictions énergétiques, il faudra affronter une hausse de la demande : l'augmentation de la population mondiale est estimée à 30% d'ici 2050 [35].

1.2 Domaine du photovoltaïque

Parmi les ressources renouvelables, l'énergie solaire est prometteuse. Même s'ils ne représentent actuellement que 0,1% de la consommation mondiale, les panneaux photovoltaïques voient leur nombre augmenter de façon exponentielle comme la Figure 4.5 l'indique :

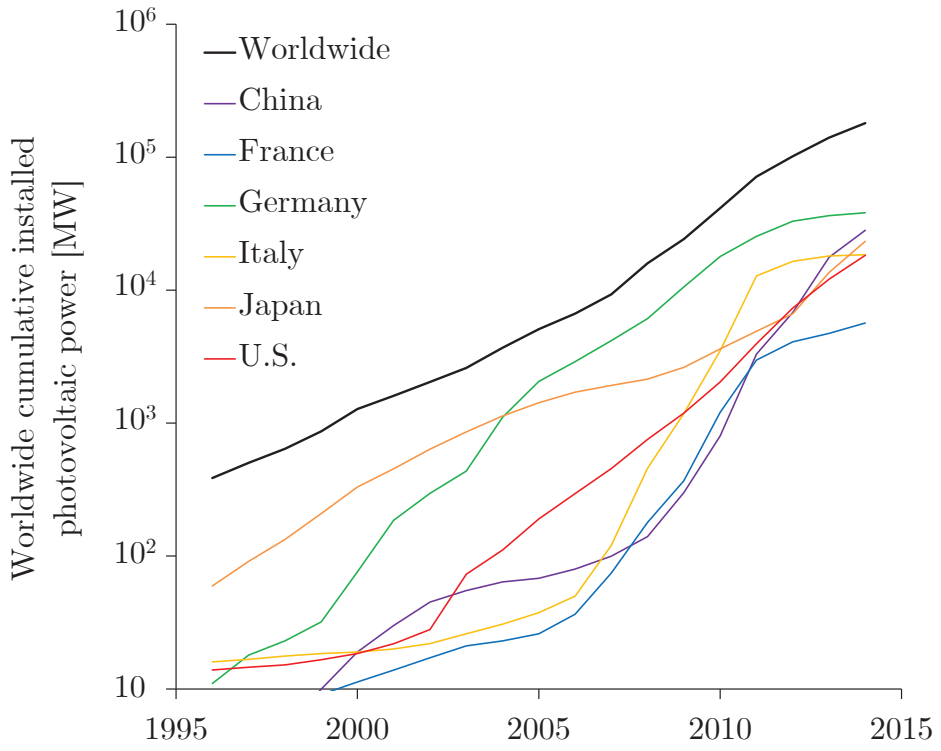

Figure 4.5: Croissance de l'installation de panneaux photovoltaïques [9]

Le soleil fournit annuellement 2,8 à 90,6 fois plus d'énergie thermique et lumineuse à la surface habitable terrestre que l'utilisation qui en est faite aujourd'hui. Pour ce qui est de sa lumière, elle peut être convertie en électricité par effet photoélectrique grâce à un semi-conducteur.

La bande interdite des semi-conducteurs est présente comme pour les matériaux conducteurs, en revanche elle est plus petite et peut être traversée par le biais d'une source d'énergie extérieure. Pour le silicium cette bande vaut $E_g = 1,1$ eV, donc l'énergie des photons est suffisante pour faire passer un électron de valence dans la bande de conduction. En d'autres termes, le silicium est conducteur seulement lorsqu'il est illuminé.

Pour créer un courant électrique, il faut créer d'un côté un excès en électron et de l'autre un défaut, ce qui est possible en dopant le silicium respectivement en phosphore (silicium de type n) et en bore (silicium de type p). Au contact de ces deux types de semi-conducteurs, les électrons diffusent dans le type p et les trous dans le type n. Des ions P^+ et B^- se forment de part et d'autre de la jonction créant

une zone de déplétion avec un champ électrique.

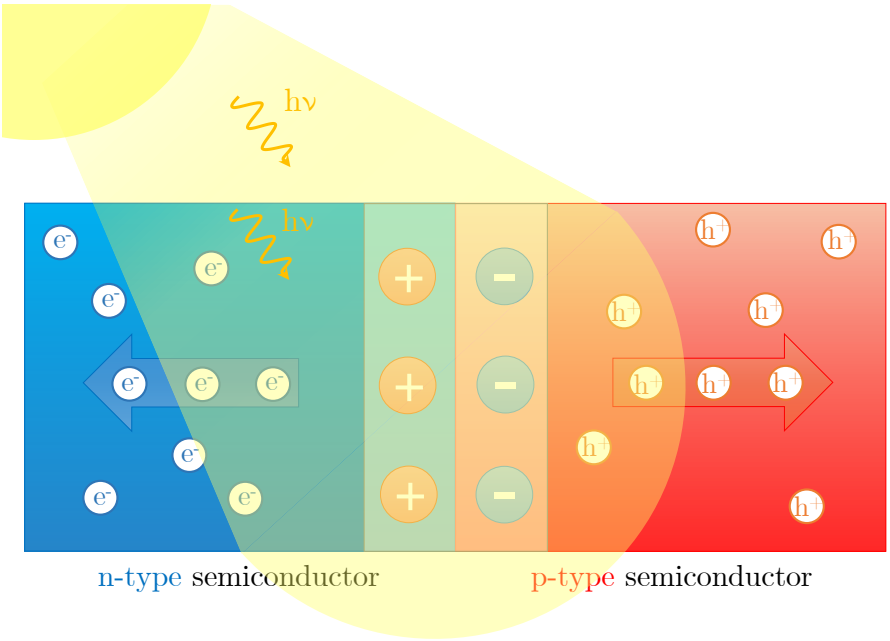

Figure 4.6: Zone de déplétion d'une jonction pn éclairée

Quand cette jonction pn est éclairée (Figure 4.6), les photons transfèrent des électrons du silicium de sa bande de valence à sa bande de conduction. Des paires électron-trou sont créées et le champ électrique de la zone de déplétion guide les électrons vers le type n et les trous vers le type p, créant ainsi de l'électricité.

La radiation solaire incidente est composée de photons aux longueurs d'onde comprises entre 250 et 2500 nm, pour la plupart dans le spectre visible. Seulement les photons d'une énergie plus grande que 1,1 eV sont absorbés et créent une paire électron-trou. Le rendement est alors théoriquement limité à 86%, mais en pratique il est loin d'être atteint.

En dehors des pertes de conversion dues à l'arrangement des cellules – par exemple leur ombrage – et leurs connexions – pertes ohmiques –, certaines pertes proviennent de la nature-même du semi-conducteur. Pour des cellules à jonction simple, 17% de photons ont une énergie inférieure à E_g par conséquent ne servent pas à la conversion. De plus, lorsque leur énergie excède E_g ils transfèrent leur surplus au réseau cristallin sous forme de chaleur en peu de temps : c'est le phénomène de thermalisation. En prenant en compte ces aspects, la limite de conversion théorique chute à 32% pour les cellules en silicium selon Shockley et Queisser [42].

Des réductions importantes en coût et une demande accrue en photovoltaïque ont été observées ces dernières années. Même si des recherches en cours se font sur d'autres types de matériaux, le silicium a la mainmise sur cette industrie.

Il s'agit de la première génération de matériau photovoltaïque à émerger. Prenant avantage de cette maturité technologique, les cellules en silicium représentent plus de 90% de la production mondiale (Figure 4.7). Des alternatives se créent peu à peu,

allant des couches minces – CdTe ou CIGS – aux organiques, des cellules solaires à colorant jusqu'aux pérovskites. Leurs performances sont prometteuses et en pleine croissance mais globalement restent à l'étape de développement.

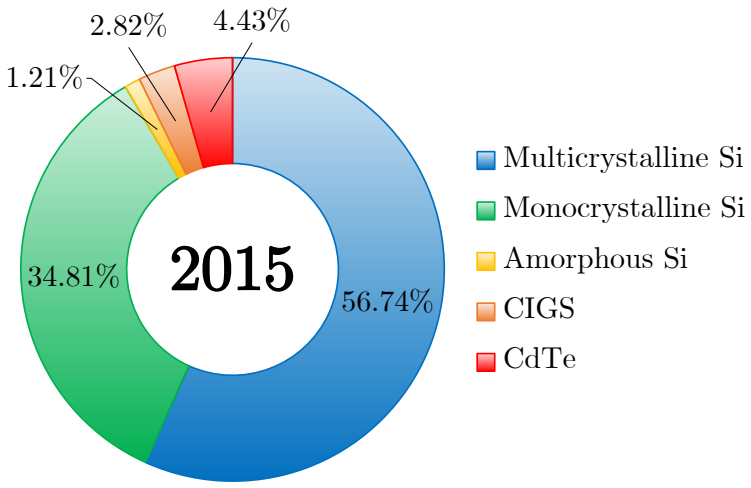

Figure 4.7: Parts de marché du photovoltaïque en W produits durant 2015 selon [18]

Selon le type de procédé employé, les cellules solaires en silicium peuvent être de plusieurs types:

- le silicium monocristallin est principalement obtenu par le procédé Czochralski. Un germe monocristallin est plongé dans un bain de silicium fondu; la solidification est initiée en le retirant lentement alors qu'il est en rotation, et elle reproduit l'orientation cristalline du germe. Les cellules en résultant oscillent généralement entre 18 et 20% de rendement, bien que certains laboratoires aient atteint 25,6% [19];
- le silicium polycristallin est constitué de cristaux de petite taille obtenus par solidification directionnelle à travers un four à deux zones, à savoir le procédé Bridgman. Les lingots obtenus héritent de la forme cubique de leur conteneur, ce qui permet de s'affranchir de l'étape de coupage des lingots cylindriques. Ce gain en temps et en énergie est compensé par son moindre rendement – de 16 à 18% – dû à ses défauts présents par essence;
- le silicium amorphe est par opposition non structuré à l'échelle nanoscopique avec des liaisons pendantes saturées par hydrogénation. Déposé en fines couches sur des substrats flexibles, le procédé est peu énergivore. Son rendement n'excède pas 10%, ce qui en fait un marché de niche pour les petits appareils telles les calculatrices.

1.3 Production de silicium de qualité solaire

Du silicium de grande pureté est nécessaire pour la fabrication des cellules photovoltaïques: le silicium de qualité dite solaire (SoG-Si) doit l'être à 99,999(9)%. Afin

de l'obtenir, plusieurs étapes sont nécessaires.

Le silicium est abondant dans la croûte terrestre : il s'agit du deuxième élément le plus présent – 25,7% – après l'oxygène. Il existe principalement sous forme de sable ou de quartz, à savoir la silice SiO_2. La première étape est alors de la réduire pour obtenir du silicium de qualité métallurgique – MG-Si. Le silicium liquide qui résulte de cette étape contiendra trop d'impuretés: une étape de purification est nécessaire, suivie d'une solidification.

Les 2% d'impuretés du MG-Si impactent le rendement de la cellule solaire (Figure 4.8) et doivent être drastiquement réduits en dessous du ppm. Il s'agit principalement d'impuretés métalliques, légères mais aussi dopantes comme le bore et le phosphore.

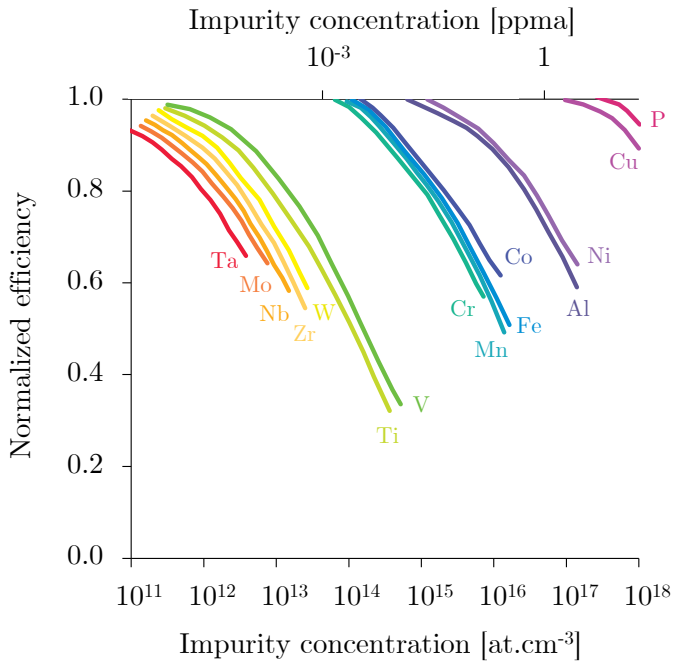

Figure 4.8: Impact des impuretés sur le rendement de cellules solaires en silicium de type p [12]

Le phosphore est inévitablement présent dans les matières premières utilisées pour la réduction de la silice. Il résulte de ce procédé un MG-Si qui présente une contamination en phosphore de 10 à 50 ppm. Sa purification est généralement effectuée par voie chimique, qui est initialement conçue pour l'industrie des semiconducteurs. Des alternatives émergent pour un procédé moins coûteux en énergie, comme la voie métallurgique.

Dans le cadre d'une telle méthode, le silicium subit différentes étapes de purification propres à certains contaminants. Le phosphore y est enlevé grâce à un four à induction sous vide, abaissant sa quantité en dessous de 0,1 ppm. Des travaux expérimentaux ont été menés ces vingt dernières années pour démontrer l'efficacité de ce procédé: Suzuki et al. [45] ont trouvé que le phosphore diminuait de 32 à 6-7 ppmw en une heure sous un vide de $2,7 \cdot 10^{-2}$ Pa entre 1723 et 1823 K, Yuge

et al. [58] l'ont abaissé en dessous des 0,1 ppm requis en deux heures, et Zheng et al. [60] de 15 à 0,08 ppmw après deux heures également.

Irradier la surface du silicium liquide avec un faisceau d'électrons est une alternative qui a été proposée [21, 22, 33, 38], mais le coût d'un tel procédé est son principal inconvénient.

Dans l'étude théorique de cette étape de déphosphoration sous vide, une hypothèse considérable a été faite [40, 61] : le modèle ne prend en compte aucun autre élément en dehors de Si et P.

Il est primordial de comprendre les phénomènes thermodynamiques mis en jeu dans ce processus pour en tirer les paramètres clés à l'échelle industrielle. L'oxygène est identifié comme un élément contaminant décisif, présent à la fois dans les creusets utilisés et dans l'atmosphère résiduelle du four. Son influence sur l'élimination du phosphore sera alors examinée.

La thermodynamique du système Si – P sera alors étudiée, puis en suivra une simulation de la déphosphoration du silicium en incluant au modèle l'oxygène. Enfin, la validation expérimentale de cette théorie sera abordée par le biais d'un appareil de lévitation électromagnétique.

2. Étude théorique du système Si – P

Étudier le procédé de déphosphoration du silicium demande de mettre en place une série de données thermodynamiques pertinentes sur le système Si – P. Un état de l'art a été réalisé, incluant des travaux expérimentaux et d'optimisation [2, 26, 28, 36, 39, 47].

Il en est ressorti certaines lacunes et inexactitudes dans des travaux de compilation. Cette constatation est l'occasion de procéder à une optimisation thermodynamique Calphad afin de contribuer à une meilleure compréhension de ce système.

2.1 Modélisation thermodynamique des phases

Les phases solides prises en compte sont le silicium de structure type diamant [52], le phosphore rouge [48], et les composés définis SiP [6, 55, 56] et SiP_2 [53, 54]. Pour ce qui est de la phase gazeuse, les espèces considérées sont Si, Si_2, Si_3, P, P_2, P_4 [11].

Les énergies libres de Gibbs des éléments purs Si et P proviennent de la base de données SGTE [13]. Celles des phases gazeuses sont calculées à partir des tables de JANAF [11]. La phase liquide est quant à elle exprimée par une solution régulière qui prend en compte les paramètres de Redlich-Kister suivants :

$$\begin{aligned} {}^0L^{(l)} &= -20801.04 + 4.1172 \cdot T \\ {}^1L^{(l)} &= 13982.31 - 2.7877 \cdot T \\ \\ {}^0L^{(\mathrm{Si})} &= -40498.48 + 21.8079 \cdot T \end{aligned} \tag{4.2}$$

Enfin, les G^{ϕ} des composés stœchiométriques sont calculés depuis les $\Delta_f H^0_{298\ \mathrm{K}}$ et $S^0_{298\ \mathrm{K}}$ de Philipp et Schmidt [37] et des C^0_p issus de la règle d'additivité de Neumann-Kopp.

Les différentes phases sont maintenant correctement modélisées pour le système Si – P. L'étape suivante consiste à examiner la littérature expérimentale qui s'y rapporte.

2.2 Analyse des données $p - T - x$

Les articles expérimentaux qui contiennent des données pertinentes d'équilibres de phase en $T - x$, ainsi qu'en $p - T$ et $p - x$ sont résumés dans le Tableau 4.1 :

Table 4.1: Résumé des données $T - x$, $p - T$ et $p - x$ dans le système Si – P

Premier auteur	**Méthode**	$\boldsymbol{T}$ **[K]**	$\boldsymbol{x_P}$ **[at.%]**
Giessen [1959]	Analyse thermique Métallographie	1400 – 1823	0 – 60
Ugai [1987]	Manométrie statique	1398 – 1450	40 – 77
Safarian [2011]	ATD-TG	1235 – 1684	0 – 6
		$\boldsymbol{T}$ **[K]**	$\boldsymbol{p}$ **[bar]**
Biltz [1938]	Manomètre à spirale	1273 – 1413	0.08 – 1
Korb [1976]	Manomètre de Bourdon	1173 – 1373	0.01 – 0.4
(1) Ugai [1981]	ATD sous p contrôlée	1410 – 1439	0.4 – 3.5
(2) Ugai [1987]	Manométrie statique ATD sous p contrôlée	1410 – 1450	0.4 – 43.3
(3) Ugai [1987]	Manomètre de Bourdon	1345 – 1470	0.3 – 2.7
		$\boldsymbol{p}$ **[bar]**	$\boldsymbol{x_P}$ **[at.%]**
Biltz [1938]	Manomètre à spirale	0.08 – 0.33	10 – 52
Ugai [1987]	Manométrie statique ATD sous p contrôlée	0.4 – 43.3	40 – 75
Miki [1996]	Méthode de transpiration	$8 \cdot 10^{-8}$ – $5 \cdot 10^{-6}$	0.013 – 0.10

Dans la zone riche en silicium du diagramme de phase, le problème de solubilité du phosphore dans le silicium $[\mathrm{P}]_{(\mathrm{Si})}$ s'avère être irrésolu. L'analyse de données faites par les précédents optimisateurs [2, 28, 36, 39, 47] étaient effectivement non spécifiées ou discutables.

Beaucoup d'auteurs ont étudié $[\mathrm{P}]_{(\mathrm{Si})}$ par diffusion ou procédé d'implantation ionique et sont listés dans le Tableau 4.2.

Table 4.2: Résumé des données de solubilités dans le système Si – P. Les acronymes sont explicités dans la nomenclature.

Premier auteur	Préparation	Mesure	Caractérisation
Trumbore [1960]	Diffusion		
Tannenbaum [1961]	Diffusion	NAA SR	
Abrikosov [1962]	Isobare	MH	OM
Mackintosh [1962]	Diffusion	SR	
Kooi [1964]	Diffusion	NAA	
Schmidt [1964]	Diffusion	NAA SR	TEM XRD
Joshi [1966]	Diffusion	NAA SR	TEM
Tsai [1969]	Diffusion	SR	
Schwettmann [1971]	Diffusion	SR	
Yoshida [1974]	Diffusion	NAA SR	
Mousty [1974]	Implantation P^+	NAA SR HE	TEM XRT
Ostoja [1976]	Laser à impulsion	SR	TEM
Fair [1977]	Diffusion	NAA SR	SIMS DC
Masetti [1977]	Diffusion	NAA SR HE	TEM XRT
Uda [1977]	Implantation P^+	SR	XRD EBSD
Tamura [1977]	Diffusion Implantation P^+	SR	TEM
Sunami [1978]	Diffusion Implantation P^+	SR	TEM
Wada [1978]	Implantation P^+	HE	TEM
Fogarassy [1980]	Diffusion Laser à impulsion	SR HE	SIMS RBS
Miyao [1980]	Implantation P^+ Laser à impulsion	SR HE	TEM PL
Finetti [1981]	Implantation P^+ Laser à impulsion	SR HE	TEM RBS
Itoh [1982]	Implantation P^+ Laser à impulsion	SR HE	TEM
Nobili [1982]	Implantation P^+ Laser à impulsion	SR HE	TEM RBS
Borisenko [1987]	Implantation P^+ Laser à impulsion	HE	
Solmi [1996]	Implantation P^+	SR HE	TEM SNMS
Safarian [2011]			TG-DTA

Une nouvelle grille de lecture a été apportée. Elle permet d'écarter certains résultats qui ont surestimé cette solubilité pour plusieurs raisons.

Leur expérience ont pu contenir trop d'oxygène et se retrouvent alors dans un cas de système ternaire Si – O – P [27, 30, 44]. Certains utilisaient des méthodes de mesure et d'observation qui ne permettaient pas en ce temps-là de déceler certains précipités SiP, ou considéraient qu'il s'agissait de phosphore dissous électriquement inactif [14, 15, 41, 57]. D'autres [25, 41, 46, 50, 57] ont basés leurs interprétations de mesures de résistivités à partir d'une courbe de résistivité/concentration d'impureté non spécifique au phosphore [24].

2.3 Analyse des autres propriétés thermodynamiques

Ont été également étudiés et incorporés dans l'optimisation les articles traitant de la capacité calorifique C_p, de l'entropie et de la variation d'enthalpie des composés stœchiométriques du système Si – P ainsi que des valeurs d'activité du phosphore a_P (Tableau 4.3).

Table 4.3: Résumé des données de C_p, a_P, $\Delta H^0_{298\ \mathrm{K}}$ et $S^0_{298\ \mathrm{K}}$ dans le système Si – P

Premier auteur	**Méthode**	**Type**	$\boldsymbol{T}$ **[K]**	$\boldsymbol{x_P}$ **[at.%]**
Zaitsev [2001]	KCMS Méthode statique	a_P	1507 – 1831	0.09 – 26.5
Ugai [1979]	Calorimétrie	C_p	5 – 300	SiP
Barin [1991]	Inconnue		298 – 1413	SiP
Jung [2012]	Barin modifié		298 – 1413	SiP
Philipp [2008]	DSC		–	SiP_2
			Valeur	**Composé**
Biltz [1938]	Manomètre à spirale	$\Delta H^0_{298\ \mathrm{K}}$	-79.03	SiP
Korb [1976]	Manomètre de Bourdon		-75.2	SiP
Philipp [2008]	DSC		-84.3	SiP_2
Jung [2012]	Optimisation		-63.3	SiP
			-79.3	SiP_2
Biltz [1938]	Manomètre à spirale	$S^0_{298\ \mathrm{K}}$	12.6	SiP
Korb [1976]	Manomètre de Bourdon		15.9	SiP
Ugai [1979]	Calorimétrie		34.78	SiP
Philipp [2008]	DSC		69.9	SiP_2
Jung [2012]	Optimisation		34.74	SiP
			67.0	SiP_2

2.4 Optimisation du système

L'optimisation du système binaire Si – P est réalisée avec les programmes de Lukas [29] BINGSS/BINFKT et la visualisation à l'aide du logiciel FactSage [3]. La Figure 4.9 représente le diagramme de phase optimisé pour une pression totale de 1 bar. Les points de solubilité y sont omis pour ne pas surcharger le graphique, et sont interprétés par la suite.

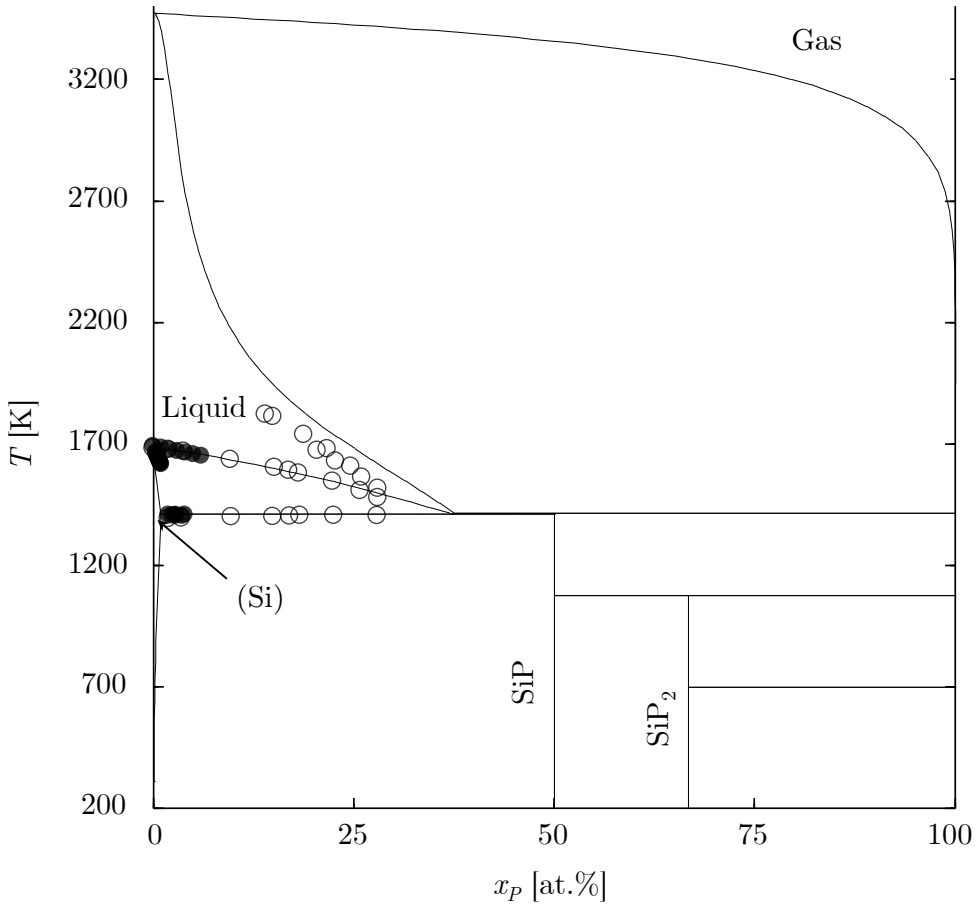

Figure 4.9: Diagramme de phase Si – P calculé pour une pression totale de $p = 1$ bar. Les données $T - x$ provenant de Giessen et Vogel [17] sont représentées en blanc, et celles de Safarian et Tangstad [39] en noir.

Les résultats sont en accord avec les points expérimentaux de Giessen et Vogel [17] ainsi que Safarian et Tangstad [39]. Par rapport aux dernières optimisations [26, 28], peu de changements sont à signaler ce qui s'explique par des choix similaires dans les données choisies et modèles de phases.

Une pression élevée est imposée au système pour révéler le liquidus qui culmine sur les fusions congruentes de SiP et SiP_2. Celle du SiP est observée pour des pressions supérieures à 6,5 bar, et à 36,5 bar pour le SiP_2. Comparé à Ugai et al. une faible différence de température respectivement de 11 K et 9 K est observée, ce qui témoigne d'un accord convenable. Ces valeurs sont cependant différentes

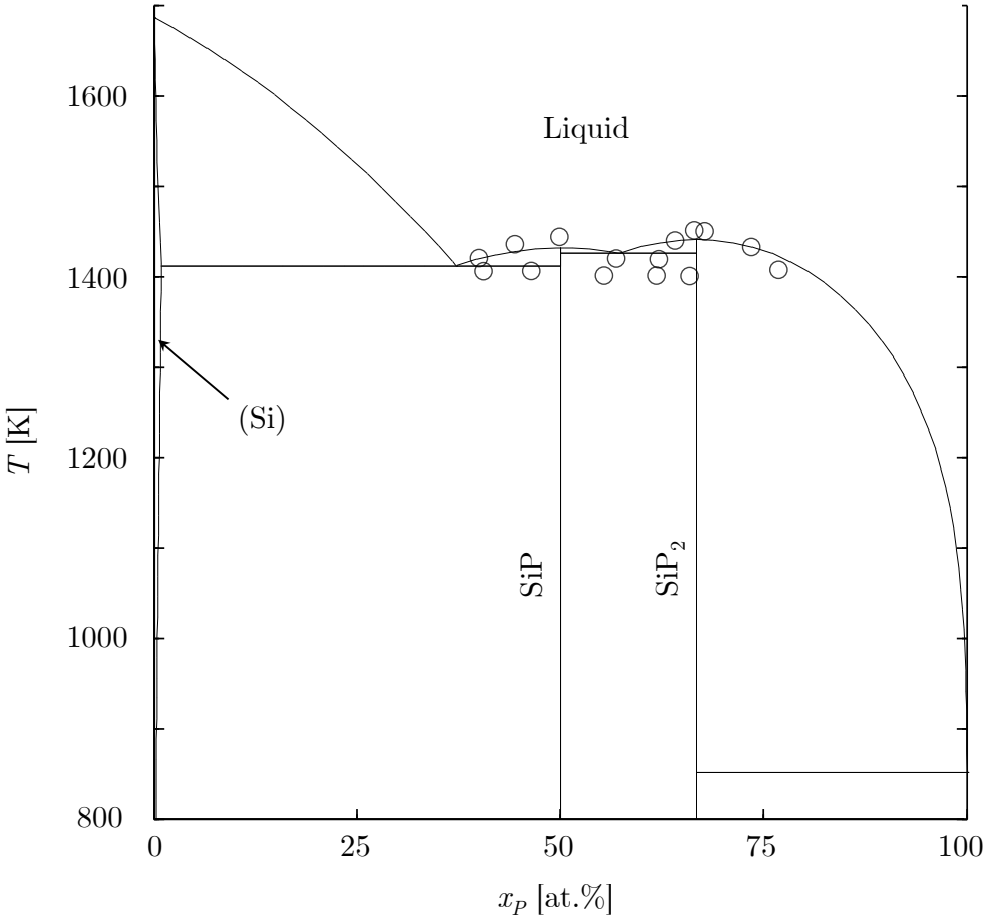

Figure 4.10: Diagramme de phase Si – P calculé pour des pressions élevées (figure valide pour $p \geq 450$ bar). Les données expérimentales $T - x$ de Ugai et al. [51] sont représentées.

des précédents travaux [26, 28] ce qui peut s'expliquer par l'utilisation de valeurs de potentiels chimiques de P calculées à partir des données de la littérature, ainsi qu'une description des C_p plus rigoureuse.

La ligne d'eutectique entre SiP et SiP_2 est une nouvelle fois au dessus de celle entre Si et SiP, ce qui est en contradiction avec les résultats expérimentaux de Ugai et al. [51]. Cela provient probablement de la description de la phase liquide en tant que solution régulière. Un modèle de solutions associées a bien été testé mais l'optimisation s'est avérée non cohérente. La précision des mesures de Ugai et al. est alors possiblement la cause de cet écart de tendance.

La solubilité optimisée $[P]_{(Si)}$ est présentée Figure 4.11. C'est cette partie qui a posé le plus de problèmes aux précédents auteurs (voir leurs diagrammes en Annexe A): Tang et al. [47] ont donné une solubilité limite à 2,3 at.% de P mais sans précisions sur leur méthode. Safarian et Tangstad [39] l'ont trouvé à 0,9 at.% mais une solubilité rétrograde ici irréaliste a été tracée à la main pour inclure leurs résultats expérimentaux d'ATD-TG. Arutyunyan et al. [2] l'a évalué à 2,3 at.% tandis que

Jung et Zhang [26] l'ont trouvé à 3,8 at.% : dans les deux cas leur analyse de la littérature n'est pas exhaustive. Deux modèles de solubilité sont proposés par Liang et Schmid-Fetzer [28] : un maximum à 1,1 at.% et un autre à 3,6 at.%. Ils privilégient le premier, mais déclarent ne pas pouvoir expliquer clairement la raison de cet écart.

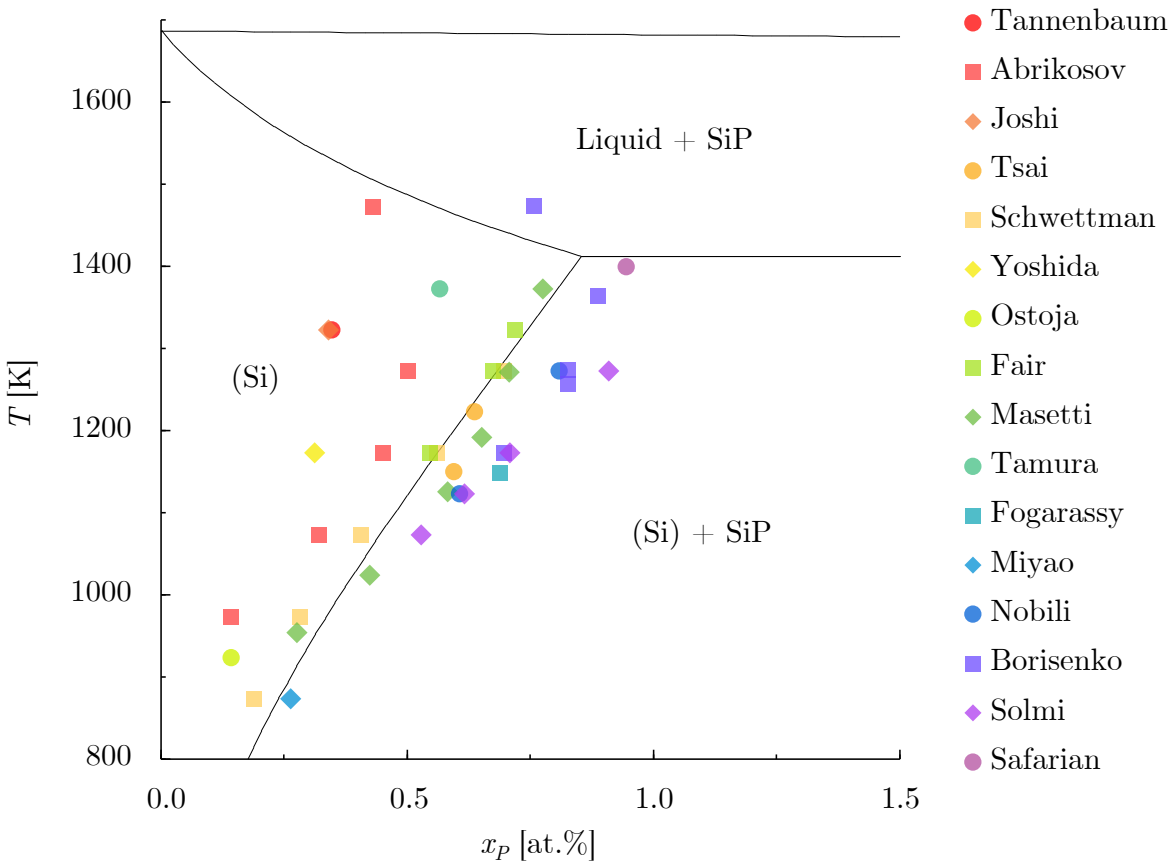

Figure 4.11: Diagramme de phase Si – P calculé dans la zone riche en Si pour une pression totale $p = 1$ bar

Ce problème est désormais élucidé : l'analyse donnée plus haut a rendu le nuage de données expérimentales plus cohérent (Figure 4.11) et permet d'évaluer la solubilité limite à 0,8 at.%.

2.5 Conclusions

Après une critique approfondie de la littérature thermodynamique disponible, une évaluation Calphad a été réalisée sur le système Si – P. Même si d'autres études de ce binaire ont été réalisées par le passé, certaines zones d'ombre se devaient d'être clarifiées.

La problématique de la solubilité du phosphore dans le silicium, liée à la celle de la déphosphoration du silicium, a été résolue. Elle était jusqu'alors restée en

suspens en raison de l'embrouillamini des interprétations données dans les articles expérimentaux. Désormais, la solubilité maximale est estimée à 0,8 at.%.

Cette solubilité $[P]_{(Si)}$ est étroitement corrélée à celle du coefficient d'activité de P en dilution infinie γ_P^{∞}. Celle-ci est une variable majeure qui va être calculée dans la simulation de la déphosphoration.

3. Simulation thermodynamique de la déphosphoration du silicium

Un algorithme est développé pour simuler le taux de déphosphoration d'une bille de silicium en prenant en compte la présence de l'oxygène. Plusieurs données de la littérature sont utilisées pour calculer le temps de distillation de l'échantillon. La perte de masse est également prise en compte : un tel processus est en effet inefficace si la bille en est trop réduite, même pour une distillation rapide.

3.1 Littérature sélectionnée

Déterminer le taux de déphosphoration du silicium est possible en utilisant l'équation de Hertz-Knudsen qui relie d'une part un flux s'apparentant à un taux de collision des particules, et d'autre part les pressions partielles des différentes espèces. Ces pressions sont obtenues en exprimant les constantes d'équilibre gazeux les liant par ailleurs aux activités des éléments.

Dans la littérature disponible du Si – P, plusieurs articles disposent de données adéquates. Les travaux précédemment utilisés de Miki et al. [32] et Zaitsev et al. [59] sont considérés, ainsi que la présente optimisation thermodynamique : leurs résultats permettent d'obtenir les coefficients d'activité γ.

L'influence de l'oxygène sur ces γ fait intervenir des paramètres d'interaction de Wagner ε, qui sont déterminés à partir d'un article de Narushima et al. [34].

3.2 Données thermodynamiques extraites

Les pressions partielles de la phase vapeur sont déterminées à partir des équilibres de phase dont les constantes K_p sont calculées à partir de tables thermodynamiques [20] et font le lien entre ces pressions et les activités des éléments Si, P et O (Tableau 4.4). Ces dernières sont obtenues via les coefficients d'activité en dilution infinie γ^{∞}.

L'interaction des éléments Si et P avec O se quantifie par le biais des paramètres de Wagner ε qui décrivent la solution diluée au delà de la gamme de composition donnée par la loi de Henry.

3.3 Calculs des flux de Hertz-Knudsen

La problématique de l'élimination du phosphore implique par sa nature un facteur temps que l'équation de Hertz-Knudsen fournit. Elle met en relation avec les pressions partielles un flux Φ qui correspond à un taux de collision de surface :

Table 4.4: Constantes d'équilibres des réactions d'évaporation exprimées par $\log K_P = \frac{A}{T} + B$

	Réaction d'évaporation	**Constante d'équilibre**	**A**	**B**	***T* [K]**
1	$Si_{(l)} = Si_{(g)}$	$K_p(1) = \frac{p_{Si}}{a_{Si}}$	-20436	5.8549	
2	$2Si_{(l)} = Si_{2(g)}$	$K_p(2) = \frac{p_{Si_2}}{a_{Si}^2}$	-23923	5.3439	
3	$3Si_{(l)} = Si_{3(g)}$	$K_p(3) = \frac{p_{Si_3}}{a_{Si}^3}$	-23194	4.3462	
4	$P_{(l)} = P_{(g)}$	$K_p(4) = \frac{p_P}{a_P}$	-16908	5.7147	1700 – 2500
5	$2P_{(l)} = P_{2(g)}$	$K_p(5) = \frac{p_{P_2}}{a_P^2}$	-5998.2	5.1931	
6	$3P_{(l)} = P_{3(g)}$	$K_p(6) = \frac{p_{P_3}}{a_P^3}$	-6941.8	-4.5460	
7	$4P_{(l)} = P_{4(g)}$	$K_p(7) = \frac{p_{P_4}}{a_P^4}$	-678.93	2.9330	
8	$Si_{(l)} + P_{(l)} = SiP_{(g)}$	$K_p(8) = \frac{p_{SiP}}{a_{Si}a_P}$	-17789	5.7825	
9	$2Si_{(l)} + P_{(l)} = Si_2P_{(g)}$	$K_p(9) = \frac{p_{Si_2P}}{a_{Si}^2 a_P}$	-15784	4.9735	
10	$2Si_{(l)} + 2P_{(l)} = Si_2P_{2(g)}$	$K_p(10) = \frac{p_{Si_2P_2}}{a_{Si}^2 a_P^2}$	-16962	5.1454	
11	$P_{(l)} + \frac{1}{2}O_{2(g)} = PO_{(g)}$	$K_p(11) = \frac{p_{PO}}{a_P a_O}$	2217.6	3.1949	
12	$P_{(l)} + O_{2(g)} = PO_{2(g)}$	$K_p(12) = \frac{p_{PO_2}}{a_P a_O^2}$	15500	-0.6823	
13	$2P_{(l)} + \frac{3}{2}O_{2(g)} = P_2O_{3(g)}$	$K_p(13) = \frac{p_{P_2O_3}}{a_P^2 a_O^3}$	36370	-5.0949	
14	$2P_{(l)} + 2O_{2(g)} = P_2O_{4(g)}$	$K_p(14) = \frac{p_{P_2O_4}}{a_P^2 a_O^4}$	48977	-10.104	900 – 1500
15	$2P_{(l)} + \frac{5}{2}O_{2(g)} = P_2O_{5(g)}$	$K_p(15) = \frac{p_{P_2O_5}}{a_P^2 a_O^5}$	58367	-12.016	
16	$3P_{(l)} + 3O_{2(g)} = P_3O_{6(g)}$	$K_p(16) = \frac{p_{P_3O_6}}{a_P^3 a_O^6}$	80744	-18.090	
17	$4P_{(l)} + 3O_{2(g)} = P_4O_{6(g)}$	$K_p(17) = \frac{p_{P_4O_6}}{a_P^4 a_O^6}$	83459	-22.538	
18	$4P_{(l)} + \frac{7}{2}O_{2(g)} = P_4O_{7(g)}$	$K_p(18) = \frac{p_{P_4O_7}}{a_P^4 a_O^7}$	102909	-26.452	
19	$4P_{(l)} + 4O_{2(g)} = P_4O_{8(g)}$	$K_p(19) = \frac{p_{P_4O_8}}{a_P^4 a_O^8}$	119188	-30.802	
20	$4P_{(l)} + \frac{9}{2}O_{2(g)} = P_4O_{9(g)}$	$K_p(20) = \frac{p_{P_4O_9}}{a_P^4 a_O^9}$	135154	-35.545	
21	$4P_{(l)} + 5O_{2(g)} = P_4O_{10(g)}$	$K_p(21) = \frac{p_{P_4O_{10}}}{a_P^4 a_O^{10}}$	150100	-40.704	
22	$Si_{(l)} + \frac{1}{2}O_{2(g)} = SiO_{(g)}$	$K_p(22) = \frac{p_{SiO}}{a_{Si}a_O}$	8539.0	2.3934	
23	$Si_{(l)} + O_{2(g)} = SiO_{2(g)}$	$K_p(23) = \frac{p_{SiO_2}}{a_{Si}a_O^2}$	19759	-1.6466	1700 – 2500
24	$2Si_{(l)} + O_{2(g)} = Si_2O_{2(g)}$	$K_p(24) = \frac{p_{Si_2O_2}}{a_{Si}^2 a_O^2}$	27326	-2.1191	
25	$O_{2(g)} = 2O_{2(g)}$	$K_p(25) = \frac{p_{O^2}}{p_{O_2}}$	-26678	6.9848	1700 – 2500
26	$O_{2(g)} = \frac{2}{3}O_{3(g)}$	$K_p(26) = \frac{p_{O_3}}{p_{O_2^{3/2}}}$	-5212.2	-2.2065	

$$\Phi_i = \frac{dn}{dt} = \frac{\nu_i p_i}{\sqrt{2\pi M_i RT}} \tag{4.3}$$

Le flux incident $\Phi^{\searrow}$ à la surface de l'échantillon liquide ainsi que le flux évaporant $\Phi^{\nearrow}$ sont calculés par cette formule. Seule la pression partielle de O_2 de l'enceinte est considérée dans le premier cas, tandis que toutes les pressions partielles des molécules du système Si – O – P sont incluses dans le second.

Lorsque le pompage à vide atteint l'état stationnaire, les deux flux $\Phi^{\searrow}$ et $\Phi^{\nearrow}$ sont égaux. Pour avoir cet équilibre, la quantité de phosphore et l'oxygène d'entrée de four p_{O_2} doivent être fixés.

Chaque pression partielle d'oxyde est calculée via les différents équilibres possibles entre $Si_{(l)}$ ou $P_{(l)}$ et le O_2 de surface. La pression maximale envoyée à la surface $p_{O_2}^{lim}$ est déterminée, pour laquelle se forme une couche de silice sur l'échantillon. À partir de cette valeur, la pression en oxygène est diminuée pas à pas jusqu'à atteindre l'égalité des deux flux.

3.4 Description de l'algorithme

Les calculs se réalisent pour une température d'échantillon et pour une pression en oxygène dans l'enceinte données.

Pour une itération z, les flux évaporants $\Phi_{Si}^{\nearrow}$, $\Phi_P^{\nearrow}$ et $\Phi_O^{\nearrow}$ sont évalués, et ce dernier est comparé au flux incident $\Phi_O^{\searrow}$.

La procédure commence à la pressure maximale $p_{O_2}^{lim}$ puis décroît. Si $\Phi_O^{\searrow} > \Phi_O^{\nearrow}$, la valeur du pas d'itération se réduit pour une évaluation plus précise jusqu'à atteindre une valeur limite. À ce moment la variation de poids de la bille dm_{Si} et le pas de temps dt sont calculés par les formules suivantes :

$$dm_{Si}(z) = \frac{m_{Si}(z) dx_P}{[1 - x_P(z) - x_O(z)] \left[\frac{\Phi_P}{\Phi_{Si}}(1 - x_P(z)) - x_P(z)\right]} \tag{4.4}$$

$$dt(z) = \frac{dm_{Si}(z)}{\Phi_{Si} M_{Si}} \tag{4.5}$$

3.4 Résultats et discussion

Les pressions partielles en oxyde de phosphore augmentent avec apport en p_{O_2} mais restent très faibles comparées aux phosphures de silicium et oxydes de silicium. $P_{2(g)}$ est l'espèce de phosphore prédominante pour des ratios élevés de P ($> 10^{-5}$) dans l'alliage liquide. En deçà il s'agit de $P_{(g)}$.

À la limite de Knudsen ($p_{O_2} = 10^{-4}$ bar) des oxydes de silicium émergent, comme le $SiO_{(g)}$ qui prédomine à quasiment 10^{-3} bar suivi de $Si_{(g)}$, $Si_{2(g)}$ puis $Si_2O_{2(g)}$. L'oxyde de phosphore le plus présent est $PO_{(g)}$, oscillant de 10^{-15} à 10^{-9} bar pour une gamme de x_P entre 10^{-8} et 10^{-2}. Ainsi lorsqu'une quantité importante d'oxygène se trouve dans l'enceinte et interagit avec le silicium fondu, il en ressort principalement sous forme d'oxyde de silicium.

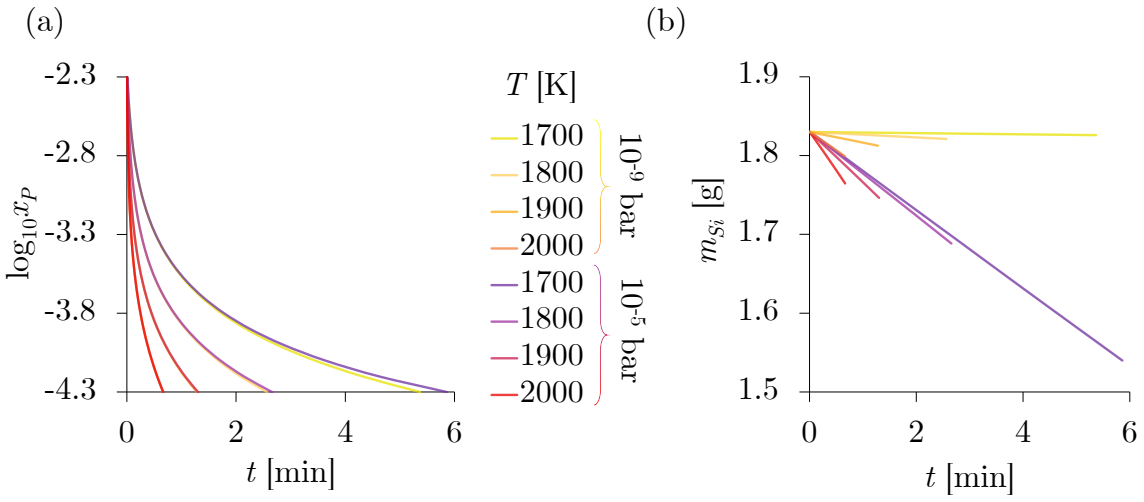

Figure 4.12: (a) Temps de déphosphoration et (b) perte de masse du silicium en fonction de la température pour une bille de 1,83 g contenant initialement 50 ppm éliminant jusqu'à 0,5 ppm de phosphore pour différentes pressions d'oxygène de l'enceinte

La Figure 4.12 révèle pour deux extremums de pression d'enceinte (a) le temps de déphosphoration et (b) la perte de masse d'une bille de silicium contenant 50 ppm, et chauffée à différentes températures.

Pour $p_{O_2} = 10^{-9}$ bar, le temps de distillation est identique à celui d'une simulation effectuée sans oxygène. En revanche lorsque la pression de l'enceinte monte à 10^{-5} bar, ces deux paramètres augmentent : nettement pour les basses températures, légèrement pour les hautes.

Une visualisation plus large du phénomène est donnée aux Figures 4.13 et 4.14 pour mieux le comprendre.

Dans la Figure 4.13 le temps de déphosphoration est donné pour $p_{O_2} \in \{10^{-10}; ...; 10^{-5}\}$ bar et $T \in \{1723; ...; 2123\}$ K. Il croît de manière exponentielle passant de 18 secondes à 2123 K à environ 271 secondes à 1723 K, et ce pour toute pression d'oxygène comprise entre 10^{-10} et 10^{-6} bar. Au-delà et jusqu'à 10^{-5} – l'ordre de grandeur sous la limite de Knudsen – ce temps de distillation est légèrement affecté pour les plus basses températures de bille : à 1723 K il est estimé à 290 secondes.

La perte de masse correspondante est donné Figure 4.14. Pour $p_{O_2} < 10^{-7}$ bar les résultats sont identiques : l'échantillon perd de 0,3 à 3,0% de sa masse de 1723 à 2123 K. Au-dessus de cette pression, la perte de matière augmente exponentiellement pour une bille approchant sa température de solidification. À 1723 K elle perd 13,2% de sa masse pour $p_{O_2} = 10^{-5}$ bar.

3.5 Conclusions

En utilisant des données thermodynamiques de la littérature ainsi que l'optimisation du système Si – P effectuée, il est possible de confirmer que l'élimination du phos-

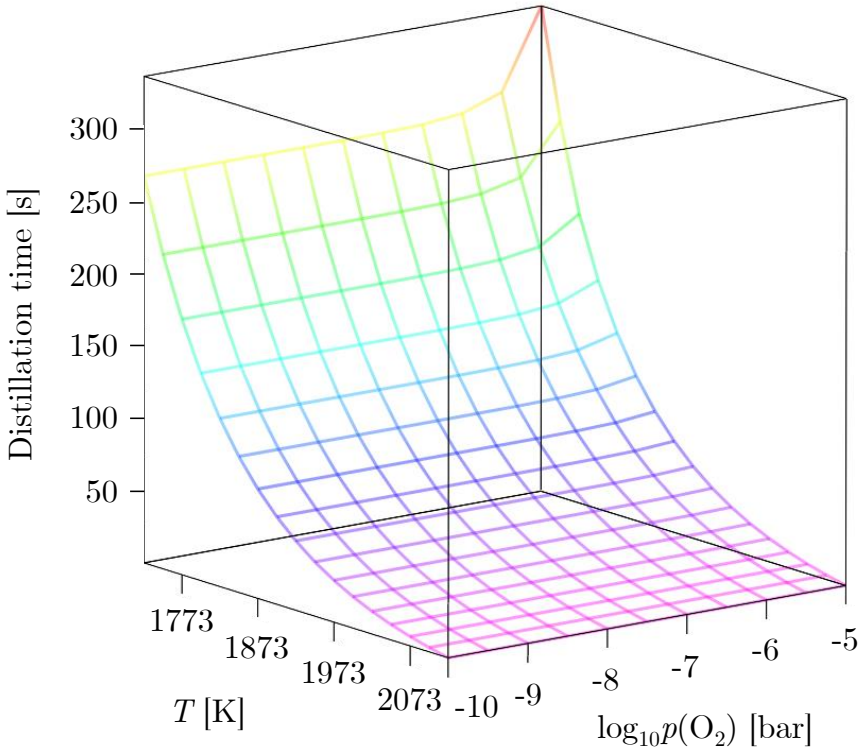

Figure 4.13: Temps de distillation d'un échantillon de silicium de 1,83 g contenant initialement 50 ppm éliminant jusqu'à 0,5 ppm de phosphore. Le pas de température est de 25 K et le pas de $\log_{10} p_{O_2}$ est de 0,5.

phore du silicium liquide est faisable.

Si l'on considère dans un système exempt d'oxygène une bille de silicium à 1800 K contaminé à 50 ppm en P, il a été démontré que ce phosphore s'évapore du liquide en tant que $P_{2(g)}$ jusqu'à ce que le ratio atteigne 10^{-3} auquel cas $Si_{(g)}$ devient l'espèce prépondérante.

Il faut 154 secondes pour distiller l'alliage jusqu'à 0,5 ppm de phosphore, et sa masse diminuera de 0,49%. Si une faible pression $p_{O_2} = 10^{-9}$ bar est appliquée dans l'enceinte, ces paramètres demeurent inchangés.

En revanche, à la limite de Knudsen, l'oxygène s'évapore sous forme d'oxydes de silicium plutôt que d'oxydes de phosphore : le $SiO_{(g)}$ est majoritaire dans ce cas.

Pour $p_{O_2} = 10^{-5}$ bar, le temps de distillation est de 160 secondes, ce qui n'est pas excessivement problématique, en revanche la bille perd 7,74% de son poids.

L'influence de ces paramètres sur le processus de déphosphoration doit être examiné expérimentalement avec un dispositif adapté. Pour ce faire, un appareil de lévitation électromagnétique est utilisé.

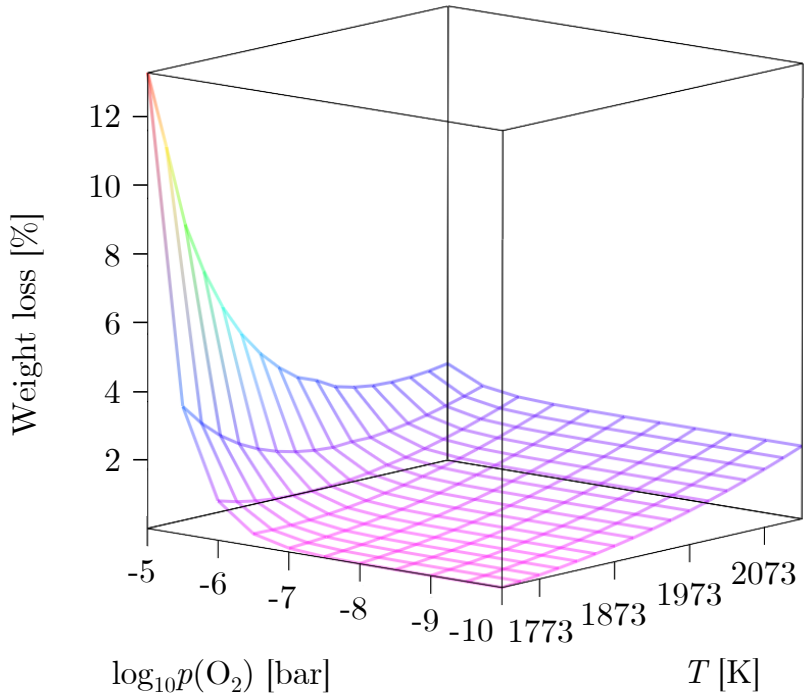

Figure 4.14: Perte de poids d'un échantillon de silicium de 1,83 g contenant initialement 50 ppm éliminant jusqu'à 0,5 ppm de phosphore. Le pas de température est de 25 K et le pas de $\log_{10} p_{O_2}$ est de 0,5.

4. Développement expérimental avec la lévitation électromagnétique

Au laboratoire SIMaP, Beaudhuin [4] a développé un dispositif de lévitation électromagnétique (EML) dénommé SPYCE[4] initialement pour déterminer la surfusion d'un composé en fonction de sa concentration en impureté.

Son utilisation initiale est détournée pour éliminer le phosphore du silicium liquide.

4.1 Spécificités de l'appareil

L'utilisation de la lévitation électromagnétique est justifiée avant tout pour s'affranchir de creuset contaminant : la validation de la simulation effectuée pourra se faire dans un environnement propre et contrôlé. Ceci est envisageable grâce à la lévitation électromagnétique de l'échantillon.

D'après le principe de la loi de Lenz-Faraday, une bobine en cuivre sous courant hautement alternatif induit des courants dans l'échantillon disposé en son sein. Il

[4] **S**ilicon **P**urit**Y** **C**ontrolled under **E**lectromagnetic levitation

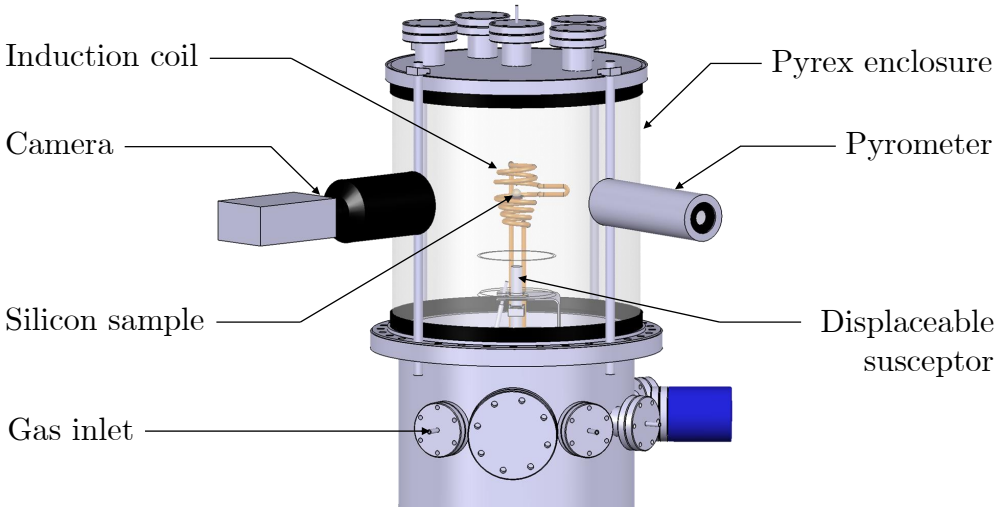

Figure 4.15: Conception initiale du cœur de SPYCE

lévite par la force de Lorentz qui en résulte et qui s'oppose à la force gravitationnelle.

La bille de silicium subit par la même occasion un effet Joule important, ce qui lui permet d'atteindre sa température de fusion.

Un autre avantage de cette technique est que la bille est brassée électromagnétiquement ce qui la rend homogène du point de vue thermique et chimique.

L'atmosphère de l'enceinte de l'installation peut être également contrôlée, en injectant par exemple un gaz inerte à 1 bar.

Un système de trois pompes est initialement utilisé. Une pompe à membrane est d'abord enclenchée à la pression atmosphérique pour atteindre 10^{-2} mbar. Par la suite, une pompe turbomoléculaire est activée permettant d'obtenir en pratique un vide à 10^{-5} mbar. Une pompe ionique complète occasionnellement le dispositif.

À basse température, la résistivité électrique du silicium est trop grande pour permettre à l'échantillon de coupler du point de vue électromagnétique. Une pastille de graphite encapsulée dans un capuchon en quartz est utilisée : sa résistivité est plus faible et va transférer sa chaleur à la bille. Une fois que celle-ci lévite, la canne sur laquelle est disposé le capuchon est retirée par l'opérateur.

Lorsque la distillation est terminée, un gaz inerte est injecté pour refroidir par convection l'échantillon.

4.2 Techniques de mesure

Le poids de l'échantillon est calibré par le fournisseur à 1,83 g pour satisfaire les besoins dimensionnels, et sera comparé au poids final pour connaître la variation de sa masse.

L'installation initiale est présentée Figure 4.16.

Au cours du temps sont synchronisés :

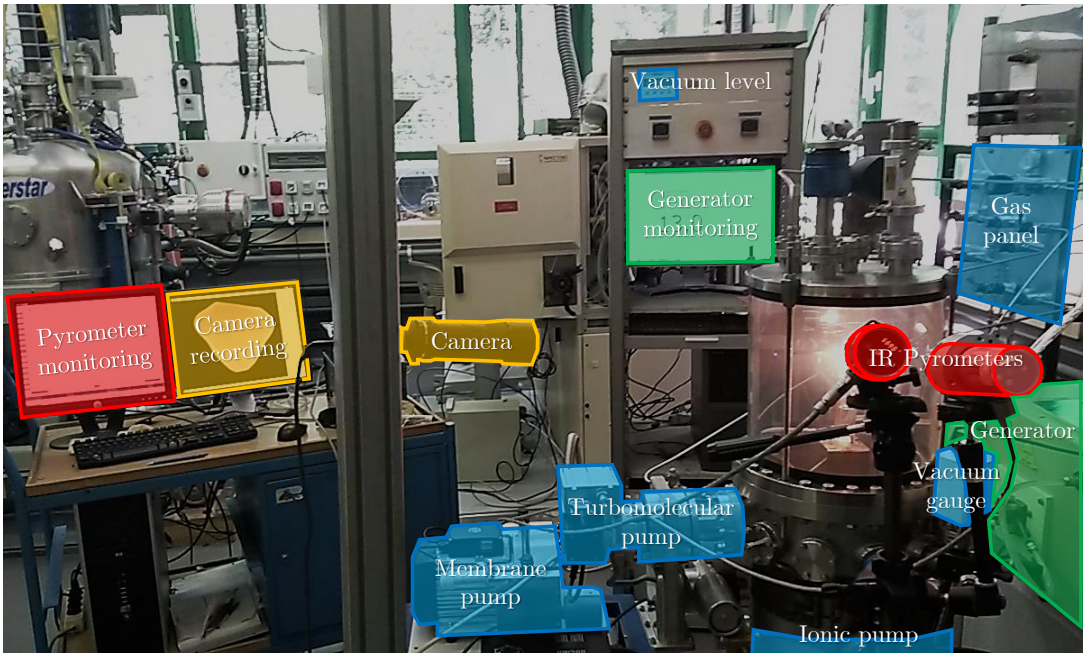

Figure 4.16: Photographie de l'installation initiale

- la température avec un pyromètre bichromatique;
- les changements de phase avec une caméra rapide;
- le niveau de vide avec une jauge Pirani/Penning;
- la pression de O_2 envoyée avec une pompe-jauge à oxygène qui sera installée ultérieurement;
- la puissance dans la bobine à induction avec un programme LabVIEW connecté au générateur à fréquence radio.

Une fois l'expérience terminée, l'échantillon sera analysé par spectrométrie de masse à décharge luminescente (GDMS). Cette méthode de caractérisation utilise lesdites décharges luminescentes comme source d'atomisation, excitation et ionisation de l'échantillon permettant d'analyser des éléments à l'état de trace comme le phosphore.

4.3 Mise en place de l'installation initiale

Dans la configuration initiale, l'échantillon doit traverser plusieurs étapes : sa mise en lévitation, sa fusion, le maintien de sa température, sa solidification et enfin sa chute.

L'installation ayant été inutilisée pendant une longue période puis déménagée, les premiers essais sont réalisés à 1 bar sous argon (Figure 4.17) : l'objectif est de retrouver les conditions d'expérience de Beaudhuin [5].

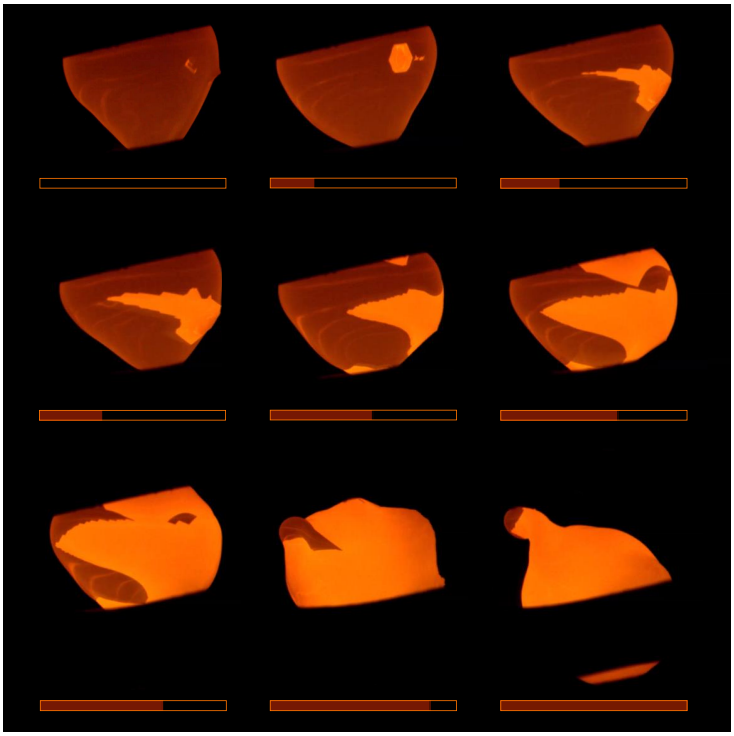

Figure 4.17: Solidification sous argon d'un échantillon de silicium d'environ 10 mm de diamètre avec l'installation initiale. L'échelle de temps sous chaque image est donnée pour une longueur totale de 52 s.

Chaque étape a été accomplie sous argon avec réussite. L'étape suivante est de faire fonctionner l'expérience sous vide, condition nécessaire pour valider la simulation thermodynamique.

Sous $2 \cdot 10^{-5}$ mbar, la mesure du pyromètre est instable du fait de l'importante distillation de l'échantillon qui opacifie l'enceinte en pyrex. L'installation d'un écran de vaporisation est nécessaire pour pallier ce problème. De plus, la récupération de l'échantillon n'a pas pu se faire correctement dans de telles conditions : il décroche du champ électromagnétique à l'état liquide, se répandant en plusieurs morceaux sur la canne en quartz. La pesée et l'analyse GDMS de la bille sont compromises.

Ces difficultés viennent renforcer le besoin d'adapter le dispositif de lévitation électromagnétique à des conditions de vide poussé.

4.4 Développement de l'installation

Trois améliorations nécessaires sont principalement identifiées pour réussir la déphosphoration du silicium sous vide avec O_2 résiduel : atteindre un niveau de vide plus important, récupérer l'échantillon intact et avoir le contrôle sur la pression partielle en dioxygène.

Une enceinte en inox à trois hublots élaborée sur mesure (Figure 4.18) remplace le pyrex qui était le principal limitant de vide. Une double paroi avec refroidissement

à eau lui assure une meilleure compatibilité à haute température et permet aux particules de condenser à sa surface.

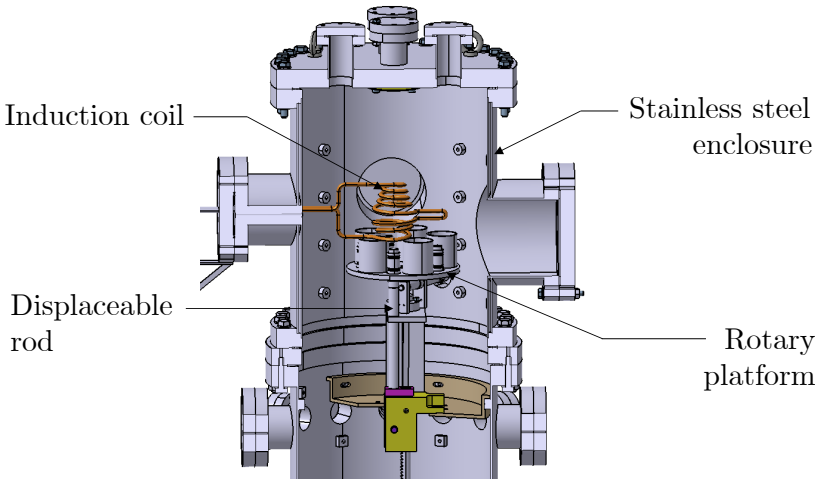

Figure 4.18: Plan de la nouvelle enceinte en inox

La pompe turbomoléculaire est alors fixée à côté de la bobine à induction pour maximiser son potentiel. Avec ce nouveau système, la pompe ionique est obsolète et donc retirée de l'installation.

Un plateau tournant est également mis en place : il peut contenir cinq échantillons et cinq réceptacles pour réaliser plusieurs expériences d'affilée.

La teneur en oxygène dans l'enceinte est un paramètre pris en compte dans la simulation et doit donc être ajustable. Un système de régulation en oxygène est installé pour contrôler la pression totale ainsi que p_{O_2}. Étant séparé de l'enceinte, la composition du gaz peut être affectée : leur connexion nécessite l'installation d'une vanne à pointeau. Un analyseur de gaz résiduels (RGA) est enfin installé pour estimer avec précision ces pressions.

Le schéma de l'installation finale comprenant ces nouveaux composants est présenté Figure 4.19.

4.5 Mise en place de l'installation modifiée

Un niveau de vide de $1,5 \cdot 10^{-8}$ mbar est atteint pour un pompage de 40 h, ce qui rend la gamme d'étude 10^{-8} – 10^{-4} mbar atteignable.

Une perturbation électromagnétique est observée dans les premières mesures de RGA. Le problème se règle en fixant l'analyseur sur bride plus éloignée de la bobine à induction.

Une sélectivité des gaz est d'abord observée pour une entrée de gaz trop importante lors des premiers essais. En réglant alors le flux d'argon entrant à 1 L.min^{-1}, la vanne variable pour obtenir $p^{\text{up}} = 3.35$ mbar et la vanne à pointeau pour $p \approx 10^{-5}$ mbar, seuls les signaux de O et O_2 sont affectés dans l'enceinte par la variation de $p^{\text{up}}_{O_2}$ de la pompe-jauge à oxygène (Figure 4.20).

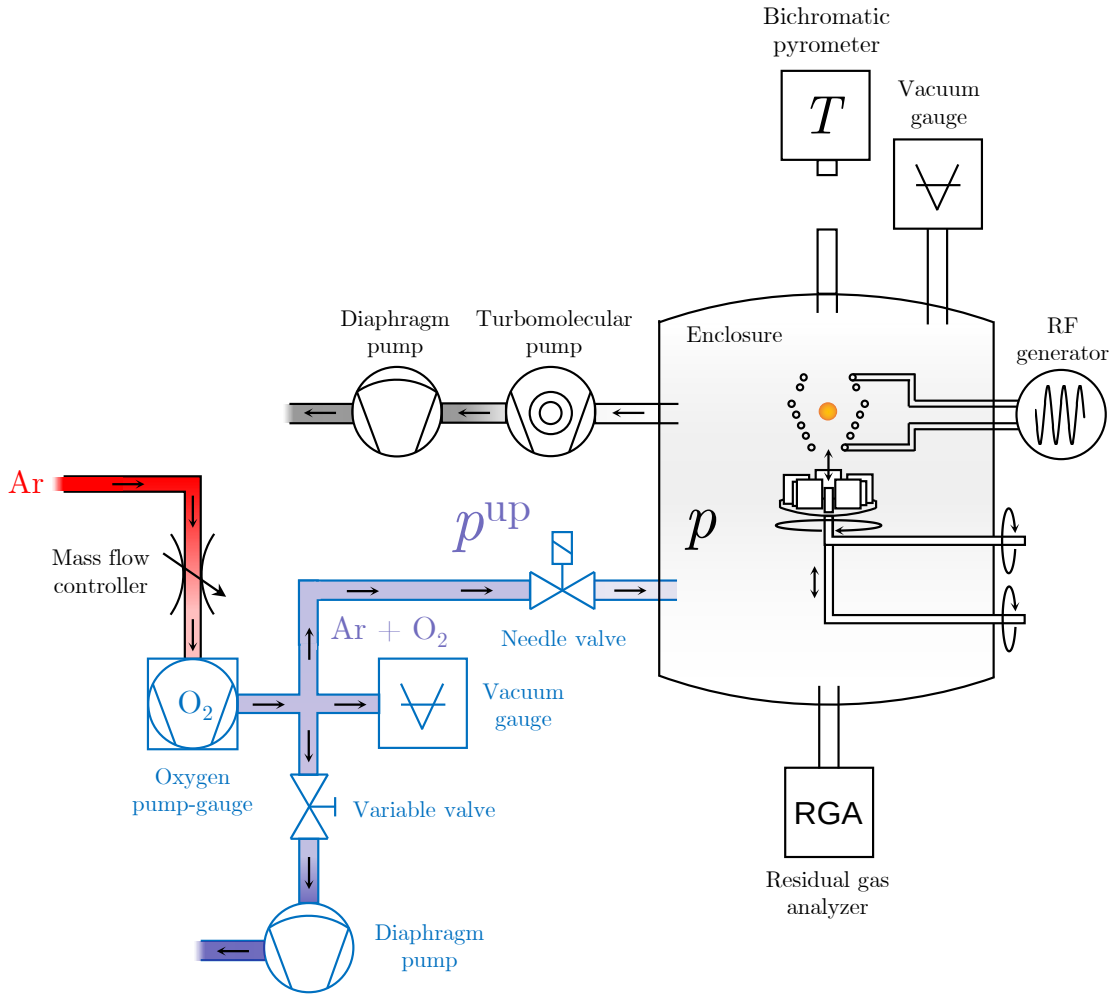

Figure 4.19: Schéma général de l'installation modifiée

4.6 Conclusions

La lévitation électromagnétique est une technique totalement adaptée pour l'étude de la déphosphoration du silicium à l'échelle laboratoire. L'échantillon est manipulé sous vide et sans creuset contaminant durant l'expérience, et est électromagnétiquement brassé lorsque qu'il est liquide.

Cependant, il a été nécessaire de modifier considérablement l'installation déjà existante pour pouvoir valider la simulation thermodynamique. Pour cela, un vide limite plus poussé (de l'ordre de 10^{-8} mbar), un contrôle de p et p_{O_2} dans l'enceinte ainsi que leurs mesures au cours du temps ont été obtenus.

Des améliorations supplémentaires concernant la récupération de l'échantillon de silicium liquide sont nécessaires pour pouvoir aller au bout du protocole expérimental. Comparer les résultats obtenus avec le modèle théorique sera alors possible.

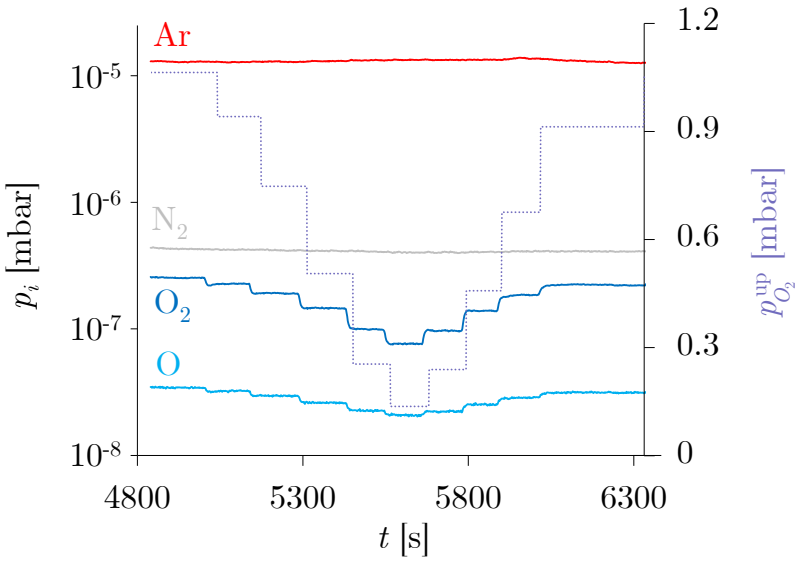

Figure 4.20: Mesures RGA dans des conditions optimisées

Conclusion générale

La relation thermodynamique complexe entre le silicium et le phosphore a été étudiée dans le contexte du domaine photovoltaïque. La quantité de phosphore déjà faible dans le silicium métallurgique doit être diminuée pour satisfaire les critères de pureté de l'industrie. Dans l'approche métallurgique, des fours à induction sous vide sont utilisés à cet égard. Jusqu'à présent, la problématique de la déphosphoration n'avait pas été abordée en prenant en compte l'influence de l'oxygène présent dans les creusets et l'atmosphère résiduelle des fours.

La bibliographie disponible sur le système Si – P s'est avérée incomplète, particulièrement dans la région riche en Si qui décrit la solubilité du phosphore dans le silicium $[P]_{(Si)}$.

Une modélisation Calphad a alors été réalisée en sélectionnant des articles pertinents d'équilibres de phases et de propriétés thermodynamiques, puis en optimisant ce système binaire avec les programmes de Lukas BINGSS/BINFKT.

Grâce à une évaluation critique d'articles de diffusions et d'implantations ionique de phosphore dans le silicium, la solubilité $[P]_{(Si)}$ a été correctement estimée. Les modélisations précédentes donnaient un solubilité maximum allant de 1,0 à 3,8 at.%. Dans la présente étude, $[P]^{max}_{(Si)}$ est évalué à 0,8 at.%. Cette valeur plus faible s'explique par l'exclusion de travaux expérimentaux contenants une quantité non négligeable d'oxygène, des précipités SiP non détectés, ou bien des conversions de données de résistivité en teneur en impureté recalculées. Cette solubilité est intimement liée au coefficient d'activité à dilution infinie du phosphore γ_P^∞, un élément clé pour la description thermodynamique de l'élimination du phosphore.

En se basant sur ces résultats, le procédé de déphosphoration du silicium liquide

en présence d'oxygène a pu être modélisé. Son rendement est évalué en comparant le temps de distillation à la perte de masse de l'échantillon.

Un algorithme a été développé en prenant en compte γ_P^∞ de même que d'autres quantités thermodynamiques.

À 1800 K et pour une faible quantité d'oxygène résiduel ($p_{O_2} = 10^{-9}$ bar), $P_{2(g)}$ est l'espèce prédominante qui s'évapore. Pour des quantités plus importantes, les atomes de Si et de P sont progressivement oxydés. À la limite de Knudsen ($p_{O_2} = 10^{-4}$ bar), l'oxygène s'évapore principalement sous forme de $SiO_{(g)}$.

Le facteur temps a été incorporé en utilisant des flux condensants et évaporants de Hertz-Knudsen qui dépendent des pressions partielles et de la nature des espèces constituantes, mais également de la température. Pour distiller de 50 à 0,5 ppm de phosphore à $p_{O_2} = 10^{-9}$ bar et 1800 K, il a été démontré que l'échantillon utilisé a besoin de 154 secondes et perd 0,5% de sa masse. En dessous de la limite de Knudsen cela ne prend seulement que 6 secondes de plus, mais il en perd 7,7%.

De ces résultats, il alors été prouvé que l'oxygène résiduel est un obstacle au procédé d'élimination du phosphore.

Un appareil de lévitation électromagnétique présent dans le laboratoire a été amélioré pour pouvoir corroborer cette simulation thermodynamique.

Cette méthode remplit tous les critères demandés pour faire évaporer le phosphore du silicium liquide dans un environnement propre et contrôlé. En revanche, l'installation initiale a été conçue pour une utilisation sous atmosphère d'argon.

Après plusieurs essais avec l'expérience originale, des modifications ont été réalisées. Une enceinte en inox avec hublots remplace le pyrex pour atteindre un vide limite plus poussé de 10^{-8} mbar, et un plateau tournant contenant cinq réceptacles maximise le nombre d'échantillons à faire léviter pour une seule expérience. De plus, un système de régulation de p_{O_2} comprenant une pompe-jauge à oxygène et vanne à pointeau est installé pour contrôler séparément pression totale et partielle en oxygène. Enfin, un analyseur de gaz résiduels permet d'estimer avec précision les différentes pressions partielles dans l'enceinte évoluant au cours du temps.

Quand un gaz inerte est injecté pour refroidir par convection la bille de silicium, elle chute avant de pouvoir se solidifier. La récupérer en entier et non contaminée est la principale perspective de ces travaux expérimentaux pour pouvoir comparer sa perte de masse et son temps de distillation avec la théorie proposée.

Pour résumer, il a été prouvé que même si l'oxygène a un impact mineur sur le temps de déphosphoration, il réduit le rendement du procédé en faisant évaporer le silicium sous forme d'oxydes. Un vide poussé est alors nécessaire à l'échelle industrielle pour éviter de perdre trop de matière. Si cette condition de vide ne peut pas être satisfaite, une température élevée pourra compenser cette contamination en oxygène.

En dehors de la validation expérimentale de la simulation thermodynamique, la perspective de cette étude serait de considérer d'autres éléments contaminants dans le système Si – P en dehors de l'oxygène. Durant l'étape de purification du silicium, de l'azote, du carbone ou encore du bore résiduel sont présents dans le

bain: leur impact sur l'élimination du phosphore pourrait alors être déterminé avec les outils thermodynamiques développés ici, ainsi qu'avec le dispositif de lévitation électromagnétique.

Bibliography

[1] N. K. Abrikosov, V. Glazov, and L. Chen-Yuan, *Individual and joint solubilities of aluminium and phosphorus in germanium and silicon*, Russian journal of inorganic chemistry, 7 (1962), pp. 429–431.

[2] N. Arutyunyan, A. Zaitsev, and N. Shaposhnikov, *Analysis of thermodynamic properties and phase equilibria in the si-p system*, Russian Journal of Physical Chemistry A, 85 (2011), pp. 911–915.

[3] C. Bale, E. Belisle, P. Chartrand, S. Decterov, G. Eriksson, K. Hack, I.-H. Jung, Y.-B. Kang, J. Melancon, A. Pelton, et al., *Factsage thermochemical software and databases - recent developments*, Calphad, 33 (2009), pp. 295–311.

[4] M. Beaudhuin, *Etude expérimentale et numérique de la précipitation d'impuretés et de la formation des grains dans le silicium photovoltaïque*, PhD thesis, Institut National Polytechnique de Grenoble-INPG, 2009.

[5] M. Beaudhuin, K. Zaidat, T. Duffar, and M. Lemiti, *Silicon purity controlled under electromagnetic levitation (spyce): influences on undercooling*, Journal of materials science, 45 (2010), pp. 2218–2222.

[6] C. Beck and R. Stickler, *Crystallography of sip and sias single crystals and of sip precipitates in si*, Journal of Applied Physics, 37 (1966), pp. 4683–4687.

[7] A. Bentzen, J. Christensen, B. Svensson, and A. Holt, *Understanding phosphorus emitter diffusion in silicon solar cell processing*, in Proceedings of the 21th European Photovoltaic Solar Energy Conference, Dresden, Germany, 2006, pp. 1388–1391.

[8] V. Borisenko and S. Yudin, *Steady-state solubility of substitutional impurities in silicon*, physica status solidi (a), 101 (1987), pp. 123–127.

[9] BP, *Bp statistical review of world energy*, 2015.

[10] A. Carabelas, D. Nobili, and S. Solmi, *Grain boundary segregation in silicon heavily doped with phosphorus and arsenic*, Le Journal de Physique Colloques, 43 (1982), pp. C1–187.

[11] M. W. Chase, *NIST-JANAF Thermochemical tables*, no. 4, american chemical society and the american institute of physics for the national institute of standards and technology ed.

[12] J. Davis, A. Rohatgi, R. H. Hopkins, P. D. Blais, P. Rai-Choudhury, J. R. Mccormick, and H. Mollenkopf, *Impurities in silicon solar cells*, IEEE Transactions on Electron Devices, 27 (1980), pp. 677–687.

[13] A. Dinsdale, *Sgte data for pure elements*, Calphad, 15 (1991), pp. 317–425.

[14] R. B. Fair and J. Tsai, *A quantitative model for the diffusion of phosphorus in silicon and the emitter dip effect*, Journal of the Electrochemical Society, 124 (1977), pp. 1107–1118.

[15] E. Fogarassy, R. Stuck, J. Muller, A. Grob, J. Grob, and P. Siffert, *Effects of laser irradiation on phosphorus diffused layers in silicon*, Journal of Electronic Materials, 9 (1980), pp. 197–209.

[16] R. Fouquet et al., *A brief history of energy*, International Handbook on the Economics of Energy, (2009).

[17] B. Giessen and R. Vogel, *Uber das system silizium-phosphor*, Zeitschrift FuHhr Metallkunde, 50 (1959), pp. 274–277.

[18] M. A. Green, *Commercial progress and challenges for photovoltaics*, Nature Energy, 1 (2016).

[19] M. A. Green, K. Emery, Y. Hishikawa, W. Warta, and E. D. Dunlop, *Solar cell efficiency tables (version 45)*, Progress in photovoltaics: research and applications, 23 (2015), pp. 1–9.

[20] L. V. Gurvich and I. Veyts, *Thermodynamic Properties of Individual Substances: Elements and Compounds*, vol. 2, CRC press, 1990.

[21] K. Hanazawa, N. Yuge, and Y. Kato, *Evaporation of phosphorus in molten silicon by an electron beam irradiation method*, Materials Transactions, 45 (2004), pp. 844–849.

[22] T. Ikeda and M. Maeda, *Purification of metallurgical silicon for solar-grade silicon by electron beam button melting*, ISIJ international, 32 (1992), pp. 635–642.

[23] F. P. Incropera and D. P. De Witt, *Fundamentals of heat and mass transfer*, 1985.

[24] J. C. Irvin, *Resistivity of bulk silicon and of diffused layers in silicon*, Bell Labs Technical Journal, 41 (1962), pp. 387–410.

[25] M. Joshi and S. Dash, *Dislocation-induced deviation of phosphorus-diffusion profiles in silicon*, IBM Journal of Research and Development, 10 (1966), pp. 446–454.

[26] I.-H. Jung and Y. Zhang, *Thermodynamic calculations for the dephosphorization of silicon using molten slag*, JOM, 64 (2012), pp. 973–981.

[27] E. Kooi, *Formation and composition of surface layers and solubility limits of phosphorus during diffusion in silicon*, Journal of the Electrochemical Society, 111 (1964), pp. 1383–1387.

[28] S.-M. Liang and R. Schmid-Fetzer, *Modeling of thermodynamic properties and phase equilibria of the si-p system*, Journal of Phase Equilibria and Diffusion, 35 (2014), pp. 24–35.

[29] H. Lukas, E. T. Henig, and B. Zimmermann, *Optimization of phase diagrams by a least squares method using simultaneously different types of data*, Calphad, 1 (1977), pp. 225–236.

[30] I. Mackintosh, *The diffusion of phosphorus in silicon*, Journal of The Electrochemical Society, 109 (1962), pp. 392–401.

[31] G. Masetti, D. Nobili, and S. Solmi, *Profiles of phosphorus predeposited in silicon and carrier concentration in equilibrium with sip precipitates'*, Semiconductor silicon 1977, (1977), pp. 648–657.

[32] T. Miki, K. Morita, and N. Sano, *Thermodynamics of phosphorus in molten silicon*, Metallurgical and Materials Transactions B, 27 (1996), pp. 937–941.

[33] V. M. Miyake, T. Hiramatsu, and M. Maeda, *Removal of phosphorus and antimony in silicon by electron beam melting at low*, Journal of the Japan Institute of Metals, 70 (2006), pp. 43–46.

[34] T. Narushima, K. Matsuzawa, Y. Mukai, and Y. Iguchi, *Oxygen solubility in liquid silicon*, Materials Transactions, JIM, 35 (1994), pp. 522–528.

[35] U. Nations, *World population 2015 wallchart*, Department of Economic and Social Affairs, Population Division, (2015).

[36] R. Olesinski, N. Kanani, and G. Abbaschian, *The p- si (phosphorus-silicon) system*, Journal of Phase Equilibria, 6 (1985), pp. 130–133.

[37] F. Philipp and P. Schmidt, *The cationic clathrate si 46- 2 xp 2 xtex crystal growth by chemical vapour transport*, Journal of Crystal Growth, 310 (2008), pp. 5402–5408.

[38] J. Pires, J. Otubo, A. Braga, and P. Mei, *The purification of metallurgical grade silicon by electron beam melting*, Journal of Materials Processing Technology, 169 (2005), pp. 16–20.

[39] J. Safarian and M. Tangstad, *Phase diagram study of the si–p system in si-rich region*, Journal of Materials Research, 26 (2011), pp. 1494–1503.

[40] ——, *Kinetics and mechanism of phosphorus removal from silicon in vacuum induction refining*, High Temperature Materials and Processes, 31 (2012), pp. 73–81.

[41] F. Schwettmann and D. Kendall, *Carrier profile change for phosphorus-diffused layers on low-temperature heat treatment*, Applied Physics Letters, 19 (1971), pp. 218–220.

[42] W. Shockley and H. J. Queisser, *Detailed balance limit of efficiency of p-n junction solar cells*, Journal of applied physics, 32 (1961), pp. 510–519.

[43] S. Solmi, A. Parisini, R. Angelucci, A. Armigliato, D. Nobili, and L. Moro, *Dopant and carrier concentration in si in equilibrium with monoclinic sip precipitates*, Physical Review B, 53 (1996), p. 7836.

[44] H. Sunami, *Thermal oxidation of phosphorus-doped polycrystalline silicon in wet oxygen*, Journal of The Electrochemical Society, 125 (1978), pp. 892–897.

[45] K. Suzuki, K. Sakaguchi, T. Nakagiri, and N. Sano, *Gaseous removal of phosphorus and boron from molten silicon*, Journal of the Japan Institute of Metals, 54 (1990), pp. 161–167.

[46] M. Tamura, *Dislocation networks in phosphorus-implanted silicon*, Philosophical Magazine, 35 (1977), pp. 663–691.

[47] K. Tang, E. J. Ovrelid, G. Tranell, and M. Tangstad, *Thermochemical and kinetic databases for the solar cell silicon materials*, in Crystal growth of Si for solar cells, Springer, 2009, pp. 219–251.

[48] H. Thurn and H. Krebs, *Uber struktur und eigenschaften der halbmetalle. xxii. die kristallstruktur des hittorfschen phosphors*, Acta Crystallographica Section B: Structural Crystallography and Crystal Chemistry, 25 (1969), pp. 125–135.

[49] F. A. Trumbore, *Solid solubilities of impurity elements in germanium and silicon*, Bell System Technical Journal, 39 (1960), pp. 205–233.

[50] J. C. Tsai, *Shallow phosphorus diffusion profiles in silicon*, Proceedings of the IEEE, 57 (1969), pp. 1499–1506.

[51] Y. A. Ugai, L. Sokolov, and E. Goncharov, *P-t-x state diagram and thermodynamics of phase equilibria in the silicon - phosphorus system*, Zhurnal Neorganicheskoi Khimii, 32 (1987), pp. 1198–1200.

[52] P. Villars, L. Calvert, and W. Pearson, *Pearson's handbook of crystallographic data for intermetallic phases. volumes 1, 2, 3*, American Society for Metals, 1985„ (1985), p. 3258.

[53] T. Wadsten, *Crystal structures of sip2 sias2 and gep*, 1967.

[54] T. Wadsten, *Synthesis of a pyrite-type modification of sip2*, Acta Chem. Scand, 21 (1967), pp. 1374–1376.

[55] T. Wadsten, *Synthesis and structural data of sip*, 1969.

[56] T. Wadsten, *Preparative and crystal-structure studies on orthorhombic silicon monophosphide*, Chemica Scripta, 8 (1975), pp. 63–69.

[57] M. Yoshida, E. Arai, H. Nakamura, and Y. Terunuma, *Excess vacancy generation mechanism at phosphorus diffusion into silicon*, Journal of Applied Physics, 45 (1974), pp. 1498–1506.

[58] N. Yuge, K. Hanazawa, K. Nishikawa, and H. Terashima, *Removal of phosphorus, aluminum and calcium by evaporation in molten silicon*, Journal of the Japan Institute of Metals(Japan), 61 (1997), pp. 1086–1093.

[59] A. I. Zaitsev, A. D. Litvina, and N. E. Shelkova, *Thermodynamic properties of si–p melts*, High Temperature, 39 (2001), pp. 227–232.

[60] S.-S. Zheng, W.-H. Chen, J. Cai, J.-T. Li, C. Chen, and X.-T. Luo, *Mass transfer of phosphorus in silicon melts under vacuum induction refining*, Metallurgical and Materials Transactions B, 41 (2010), pp. 1268–1273.

[61] S.-S. Zheng, T. A. Engh, M. Tangstad, and X.-T. Luo, *Separation of phosphorus from silicon by induction vacuum refining*, Separation and purification technology, 82 (2011), pp. 128–137.

List of Figures

List of Tables

Publications in peer-reviewed journals

[1] S. Favre, I. Nuta, G. Chichignoud, K. Zaidat, C. Chatillon, *Removing phosphorus from molten silicon: a thermodynamic evaluation of distillation.*, ECS Journal of Solid State Science and Technology, 5(3) (2016), pp. 129-137.

Abstract: Within the framework of purification of molten silicon for solar cells, phosphorus is one of few impurities that remains problematic. The present purpose is to develop a new method that leads to a final phosphorus concentration around 0.5 wppm. We have first focused on the main thermodynamic parameters that control the process: relevant thermodynamic parameters are taken from literature, such as activities, partial pressures and interaction coefficients. According to our results, distillation of phosphorus under vacuum occurs at high temperatures. Yet, the residual oxygen present in the vacuum is a hindrance to the distillation, since it evaporates in the form of silicon oxides.

[2] S. Favre, E. Fischer, I. Nuta, G. Chichignoud, K. Zaidat, C. Chatillon, *Removing phosphorus from molten silicon: solubility prediction of P in Si.*, To be submitted.

Abstract: After a thorough critical literature review of the available thermodynamic data, a Calphad assessment has been performed on the Si – P binary system. Although it has already been quite accurately investigated in the past, some gray areas needed to be clarified. The main ensuing outcome is the resolution of the $[P]_{(Si)}$ issue. Up to now it has been left in abeyance because of the complex entanglement of the related diffusion articles. Some authors misinterpretations has been noticed every so often: irrelevant adopted resistivity curves or else disregarded SiP precipitates biased the solid solubility results. After revising the concerned data points, its maximum limit is henceforth estimated to be 0.8 at.%. With this solubility problematic solved, the present modeling of the liquid phase is more accurately described. The related Redlich-Kister interaction parameters are needed to calculate the activity coefficient at infinite dilution of phosphorus γ_P^∞. This variable is essential for the simulation of the dephosphorization of silicon.

Orals at international conferences

[3] I. Nuta, *Removing phosphorus from molten silicon: a thermodynamic evaluation of distillation*, in the 45th International Conference on "Computer Coupling of Phase Diagrams and Thermochemistry" CALPHAD XLV, Awaji Island, Hyogo, Japan. May 29 – June 3 (2016).

[4] G. Chichignoud, *Electromagnetic levitation method for silicon purification*, in the 18th International Conference on "Crystal Growth and Epitaxy" (ICCGE18), Nagoya, Japan. 7 – 12 August (2016).

Posters at international conferences

[5] S. Favre, *Thermodynamic and experimental study of the dephosphorization of molten silicon for photovoltaic applications*, in 8^{th} *International Conference on "Electromagnetic Processing of Materials"* Cannes, France. October 12 – 16 (2015).

Abstract

Purifying silicon to a certain degree is needed in the photovoltaic industry. In the metallurgical route, phosphorus is removed from molten silicon in an induction vacuum refining furnace. This study presents the simulation of the silicon dephosphorization process that takes into account a neglected factor thus far, namely the residual oxygen amount.

A thermodynamic assessment is performed for the Si – P system, and the phosphorus solubility in silicon is determined. Resulting activity coefficients are incorporated in an algorithm created to simulate this phenomenon. By also using other literature data, this program predicts the distillation time of a n-type silicon sample as well as its weight loss as a function of the oxygen pressure in the enclosure.

The experimental validation of those results is intended with an electromagnetic levitation device. It enables to melt a silicon sample without any contaminant crucible and under a controlled atmosphere.

Keywords: photovoltaic silicon, dephosphorization, thermodynamic assessment, Hertz-Knudsen equation, electromagnetic levitation.

Résumé

La purification du silicium à un certain degré est requis pour l'industrie photovoltaïque. Par voie métallurgique, le phosphore est éliminé du silicium fondu dans un four à induction sous vide. Cette étude présente la simulation du processus de déphosphoration du silicium en prenant en compte un facteur jusqu'alors négligé, à savoir la présence d'oxygène résiduel.

Un travail d'optimisation thermodynamique du système Si – P est effectué, où la solubilité du phosphore dans le silicium est notamment déterminée. Les coefficients d'activité qui découlent de celle-ci sont incorporés dans un algorithme créé pour simuler ce phénomène. En s'appuyant également sur des données issues de la littérature, ce programme prédit le temps de distillation d'un échantillon de silicium de type n ainsi que sa perte de masse en fonction de la pression d'oxygène dans l'enceinte.

La validation expérimentale de ces résultats est envisagée en utilisant un dispositif de lévitation électromagnétique. Il permet de faire fondre un échantillon de silicium sans creuset contaminant et avec une atmosphère contrôlée.

Mots-clés : silicium photovoltaïque, déphosphoration, modélisation thermodynamique, équation de Hertz-Knudsen, lévitation électromagnétique.